Investigating the Interstellar Medium Conditions of Star Formation in High Redshift Galaxies by studying Dust Emission and Emission lines.

Jorge González López

Instituto de Astrofísica, Facultad de Física
Pontificia Universidad Católica de Chile

Universität Heidelberg

Max Planck Institute für Astronomie, Heidelberg

Santiago – Heidelberg 2015

Dissertation

submitted to the
Instituto de Astrofísica, Facultad de Física
Pontificia Universidad Católica de Chile, Chile
for the degree of
Doctor in Astrophysics

submitted to the
Combined Faculties for the Natural Sciences and for Mathematics
of the Ruperto-Carola University of Heidelberg, Germany
for the degree of
Doctor of Natural Sciences

presented by

Jorge González López
Born in Santa Cruz, Chile

Oral examination: January 28rd 2015

Investigating the Interstellar Medium Conditions of Star Formation in High Redshift Galaxies by studying Dust Emission and Emission lines.

Referees: Prof. Dr. Leopoldo Infante
Prof. Dr. Henrik Beuther

Abstract.

This thesis presents the search for the [C II] 158 μm emission line, one of the brightest far-infrared (FIR) emission lines, in a selection of $z > 6$ (the Universe was less than 1 Gyr old) galaxies. These galaxies have been observed with CARMA and PdBI millimeter interferometers and no [C II] nor continuum emission is detected. The estimated upper limits show that the [C II] line in these galaxies is not as bright as in some galaxies with similar values of star formation rates at lower redshifts. These results indicate that the low metallicity expected for these type of galaxies could be the reason of the non-detection of [C II] .

For a lensed multiple-imaged galaxy (MACS0329-iD) observed with the ALMA millimeter interferometer a tentative detection of the [C II] emission line with a 3.7σ significance has been detected. This detection would put the galaxy at a spectroscopic redshift of $z = 6.17722 \pm 0.00005$, in agreement with the photometric redshift previously estimated. The galaxy is not detected in the continuum, with a 3σ upper limit of 1.8 mJy at 158 μm restframe. The ratio between the tentative observed [C II] emission line and the far-infrared luminosity of $> 5.0 \times 10^{-4}$ puts this galaxy near what is typically found in the local star-forming galaxies. In conclusion, significantly deeper [C II] observations than previously thought are need in the future to securely detect [C II] emission in the highest redshift galaxies.

This work also presents the search for lensed submillimeter galaxies with the goal of studying the faint population of dusty starbursting galaxies. Observations were made of 15 galaxy clusters using the bolometers LABOCA at APEX telescope and GISMO at IRAM 30 meters telescope. Of the 62 unique sources detected, we were able to find the galaxy counterpart to the far-infrared emission when was possible. Our sample of lensed submillimeter galaxies appears to be within the range of observed infrared luminosities at $z < 2$ and being lower than other samples at $z > 2$. When comparing the stellar masses and the SFR of our sample, they appear to agree well with the main-sequence of galaxies at $z \sim 2$.

This thesis presents the efforts of studying high redshift galaxies with submillimeter and millimeter observations and some techniques to better analyze and understand them.

Zusammenfassung.

Diese Doktorarbeit beschreibt sensitive Beobachtungen der [C II] 158 μm Emissionslinie, eine der hellsten Emissionslinien im Ferninfraroten (FIR), in Galaxien bei Rotverschiebungen von $z > 6$ (Alter des Universums: weniger als 1 Gyr). Die Galaxien wurden mit den CARMA und PdBI Millimeterinterferometern beobachtet, und es wurde weder die die [C II] Linie noch Kontinuumsemission detektiert. Die erzielte Empfindlichkeit zeigt, dass diese Galaxien nicht so hell in [C II] Emission sind, wie Galaxien bei geringeren Rotverschiebungen mit ähnlichen Sternentstehungsraten. Diese Ergebnisse lassen darauf schliessen, dass eventuell die geringe Metallizität der Galaxien der Grund für die schwache [C II] Emission ist.

Im Fall der vielfach vergrösserten Galaxy MACS0329-iD haben Beobachtungen mit dem ALMA Interferometer ergeben, dass die Quelle mit einer Signifikanz von 3.7σ detektiert wurde. Diese Detektion entspricht einer spektroskopischen Rotverschiebung von $z = 6.17722 \pm 0.00005$, diese stimmt der zuvor bestimmten photometrischen Rotverschiebung überein. Die Galaxie wurde nicht im Kontinuum detektiert (mit einem 3σ Flusslimit von 1.8 mJy bei 158 μm). Das Verhältnis der Leuchtkraft der [C II] Emissionslinie und der Ferninfrarot Leuchtkraft ist $> 5.0 \times 10^{-4}$, d.h. die Galaxie verhält sich so wie typische Galaxien im lokalen Universum.

Diese Doktorarbeit beschreibt ausserdem die Suche nach Submillimetergalaxien, deren Helligkeit durch Gravitationslinsen verstärkt wird, um die schwache Population von sternbildenden Galaxien zu untersuchen, die reich an Staub sind. Hierzu wurden Beobachtungen von 15 Galaxienhaufen durchgeführt, und zwar mit Hilfe der LABOCA (APEX)

und GISMO (IRAM 30m) Bolometerkameras. Von den insgesamt 62 Quellen, die im FIR detektiert wurden, konnten die entsprechenden Galaxien bestimmt werden. Die hier untersuchten Submillimeter Galaxien sind denen bei Rotverschiebungen von $z < 2$ ähnlich, sind allerdings schwächer als die bei $z > 2$. Ein Vergleich der stellaren Massen und Sternentstehungsraten zeigt, dass die hier untersuchten Galaxien den 'Main-Sequence' Galaxien bei ~ 2 sehr ähneln.

Diese Doktorarbeit beschäftigt sich daher mit den Schwierigkeiten, Galaxien bei hohen Rotverschiebung im Submillimeter und Millimeterbereich zu untersuchen, und beschreibt mögliche Beobachtungsansätze diese besser zu analysieren und zu verstehen.

A Andrea y mi familia.

Acknowledgements

I am sure that this acknowledgments section will never be finished, I apologize for any person that deserves to be here and that is missing.

First of all, I need to thank my parents, Rosa y Fernando, and my siblings Nando and Belen for all the support. *Gracias por el apoyo en este viaje de convertirme en astrónomo, es obvio que no lo habría logrado de no ser por ustedes. También me gustaría agradecer a mi familia en Lolol y a la familia Corvillón Grez en Santiago, que han sido como una segunda casa lejos de casa.*

Now, I would like to thank my wife Andrea for all the support these years we have been together, you have been the light in all the good and bad moments.

I am very grateful to Leopoldo Infante, for the guidance, ideas and patience all these years. You know how important you were in the design and completion of this work. I also want to thank Fabian Walter, for receiving me at MPIA and taking the time for teaching me all that I needed and still need to learn. Manuel Aravena, I really want to thank you for the patience you had all these years while you helped me with my work and for always being so positive and kind.

I would like to thank Dr. Infante, Dr. Beuther, Dr. Bartelmann, Dr. Díaz and Dr. Aravena for accepting being referees and examiners for this thesis.

I need to acknowledge Mauricio Carrasco for making the magnification maps of the CLASH clusters and Livia Vallini for providing the [C II] simulation data. Both of you were crucial in solving doubts, thank you for taking the time.

Thank you to all the professors at PUC, specially to Felipe Barrientos, Franz Bauer, Rolando Dunner, Nelson Padilla, Márcio Catelan, Andreas Reisenegger and Gaspar Galaz. I cordially thank to Harold Francke and Felipe Menanteau for their support in my first years of the PhD and to Juan Veliz, Mariela Villanueva, Giselle Ulloa, Lilena Montenegro and Carmen Cordovez for helping me many times.

To my fellow students at PUC and MPIA; Juan Carlos Beamin, Cristina Garcia, Sergio Vásquez, Alejandra Muñoz, Alejandra Rojas, Cristobal Sifón, Nicolas González, Pablo Marchant, Elena Manjavacas, Eduardo Bañados, Mauricio Ortiz it was very fun sharing this journey with you.

To my friends from Lolol and Santa Cruz, I want you thank you for helping me in the 'relieving stress section' of the thesis; Exequiel, Francisco, Benjamin, Alonso, Luis, Nicolas, Mauricio, Arturo, Ramón, Tere, Olayo, Jaime, José and Humberto.

Contents

Acknowledgements **xii**

Contents **xiv**

1 Motivation **1**
1.1 Motivation. . . . 1
1.2 Concepts of studying high redshift galaxies. . . . 5
1.2.1 Cosmic star-formation history 5
1.2.2 Far-Infrared Continuum Emission 6
1.2.3 Far-Infrared Emission Lines 8
1.3 Outline. . . . 10

2 Search for [C II] emission in $z = 6.5 - 11$ star-forming galaxies. **11**
2.1 Introduction 11
2.2 Observations 13
2.2.1 Source Selection 13
2.2.2 CARMA Observations 14
2.2.3 PdBI Observations 14
2.3 Results 15
2.3.1 Line Emission 15
2.3.2 Continuum Emission 15
2.4 Discussion 19
2.4.1 Width of the [C II] emission line. . . . 19
2.4.1.1 [C II] detection on a LAE z=4.7. . . . 19
2.4.1.2 Himiko simulations. . . . 22
2.4.2 CMB effects. . . . 22
2.4.3 Spectral energy distribution of the galaxies. . . . 25
2.4.4 Ratio $L_{[C\,II]}/L_{\rm FIR}$ 26
2.4.5 SFR-$L_{[C\,II]}$ Relation 27
2.4.6 IOK-1 Models 27
2.4.7 Spectral Resolution 30
2.4.8 Atomic Mass Estimation 30

3 Search for [C II] emission in a normal star-forming lensed galaxy at the end of the reionization epoch. **35**
3.1 Introduction 35
3.2 Observations 38

3.2.1 Target Selection . . . 38
3.2.2 ALMA observations . . . 38
3.3 Result . . . 39
3.3.1 Continuum Emission . . . 39
3.3.2 [C II] emission in MACS0329-iD. . . . 41
3.4 Discussion. . . . 42
3.4.1 Constrains in MACS0329-iD . . . 43
3.4.1.1 FIR Continuum. . . . 43
3.4.1.2 Constraints on the [C II] emission line. . . . 46
3.4.1.3 SFR-$L_{[CII]}$ Relation . . . 49
3.4.1.4 Ratio $L_{[CII]}/L_{FIR}$ . . . 53
3.4.2 Other continuum detections. . . . 53
3.4.3 Stacking . . . 56
3.4.4 Other Emission lines . . . 61
3.4.4.1 Line 1 . . . 62
3.4.4.2 Line 2 . . . 67
3.4.4.3 Line 3 . . . 67
3.4.4.4 Line 4 . . . 69
3.4.5 Positional Offsets . . . 71

4 Submillimeter Galaxies behind the CLASH galaxy clusters. 75
4.1 Introduction . . . 75
4.2 Observations . . . 77
4.2.1 LABOCA . . . 77
4.2.2 GISMO . . . 77
4.2.3 Complementary data. . . . 77
4.3 Results . . . 78
4.3.1 Source Extractor . . . 96
4.3.2 Flux deboosting . . . 97
4.4 Counterparts . . . 103
4.4.1 MAGPHYS . . . 104
4.4.2 Counterpart candidates. . . . 104
4.5 Discussion . . . 107
4.5.1 MACS1931 BCG . . . 107
4.5.2 Lensed SMGs . . . 108
4.5.2.1 Infrared Luminosity. . . . 113
4.5.2.2 Star Formation Rate and Stellar mass . . . 114
4.5.2.3 Dust Mass and Stellar mass . . . 118

5 Summary and Future Work 127
5.1 Summary. . . . 127
5.1.1 Search for [CII] emission in $z = 6.5 - 11$ star-forming galaxies. . . . 127
5.1.2 Search for [C II] emission in a normal star-forming lensed galaxy at the end of the reionization epoch. . . . 128
5.1.3 Submillimeter Galaxies behind the CLASH galaxy clusters. . . . 131
5.2 Future Work. . . . 132

Bibliography **135**

List of Figures **158**

List of Tables **170**

Chapter 1

Motivation

1.1 Motivation.

One of the main subject of interest in astrophysics are the high redshift galaxies. Redshift, z, is a quantification of the ratio of the observed wavelength (λ_o) to the emitted wavelength (λ_e) of light:

$$1 + z = \frac{\lambda_o}{\lambda_e}. \tag{1.1}$$

The redshift can also be associated to the recession velocity associated to the longitudinal relativistic Doppler effect:

$$1 + z = \frac{\lambda_o}{\lambda_e} = \sqrt{\frac{1 + v/c}{1 - v/c}}, \tag{1.2}$$

where v is the recession velocity for a given redshift z (c is the speed of light in vacuum). In a cosmological context, the redshift of the light is mainly produced by the expansion of the Universe, i.e.

$$1 + z = \frac{\lambda_o}{\lambda_e} = \frac{R(t_{now})}{R_e}, \tag{1.3}$$

where $R(t)$ is the scale factor which describes the time evolution of the Universe (**?**). When we observe a galaxy at $z = 6$, we are actually observing the light emitted when the Universe was 1/7th of its present size. When we assume some cosmological parameters like $\Omega_m = 0.3$, $\Omega_\Lambda = 0.7$ and $\mathrm{H}_0 = 70\,\mathrm{km\,s^{-1}Mpc^{-1}}$ a galaxy at $z = 6$ is emitting its

light when the Universe was ≈ 0.9 Gyr old. Because the expansion of the Universe is a function of distance, observing high redshift galaxies means that we are observing distant galaxies as well.

The high redshift galaxies do not just represent a population of very distant galaxies, but also show how were the younger version of the galaxies observed in the local Universe. From this point of view, observing and studying the high redshift galaxies can reveal critic information about the evolution of galaxies as a whole. From the moment that we realized that those 'nebulae' in the sky were in fact extragalactic objects we began to note differences among them. These differences can be morphological (Elliptical and Spiral galaxies), of colors (red and blue galaxies), of size (dwarf and Cd galaxies), activity (high and low star formation rates). To know how these galaxies end up as they are observed in the local Universe, we need to understand they evolution throw cosmic time, by looking to different stages in the evolution of similar galaxies at high redshift.

The study of high redshift galaxies have revealed several interesting facts about galaxy evolution. One of the facts is that the star formation rate density of the Universe peaks at redshift ~ 2, ~ 3.2 Gyr after the Big Bang. Another interesting fact is how mergers appear to have a very important role in the growth and evolution of galaxies. How the environment where the galaxies are located can play an important role in quenching or activating the process of star formation, just to name a few. The more we learn about high redshift galaxies, the more we understand galaxies as a whole and therefore our own Galaxy.

One of the bases of the study of galaxies is having large samples. As we go to higher redshifts we are actually observing larger volumes to where galaxies can be located, which is good for the purpose of having large samples. The problem with this is that we also are observing farther and therefore the capacity to observed faint galaxies decreases at the same time. The current machinery for observing high redshift galaxies is based in large photometric surveys of regions in the sky, and then by different criteria select galaxies that are either interesting, bright, or are believed to be distant throw different estimators (colors for example). For the selected galaxies, the next step is to obtain deep spectroscopy to first, constraint the redshift, and to study the state of the interstellar medium in the galaxies. The main problem with this process is that deep spectroscopy is expensive and is limited to a number of galaxies per pointing, although the latter is improving with the later instruments advances.

With the goal of complementing the current methods of observations, some alternatives have arise for the study of high redshift galaxies. Here we explain the alternative methods that will be used in this thesis with the purpose of studying high redshift galaxies.

The first alternative is related with the fact that we need deep spectroscopy to obtain several critical properties from the galaxies, such as redshift, metallicity, star formation rate, etc. In the cases when the galaxies are bright and the continuum can be detected, the observation of emission and absorption lines reveal most of the critical information that we want to obtain. The true is that not all the observed galaxies are bright enough to be detected in such detail with optical spectroscopy, as we go higher in redshift, smaller is the amount of bright galaxies to be observed. Because of this luminosity plus instrumentation limitation, most of the information that we obtain from high redshift galaxies comes from the observation of one bright emission line, the Lyman-α emission line. The Lyman-α line is produced by hydrogen (H) when one electron falls from the orbital $n = 2$ to $n = 1$, emitting a photon at $1215.67\mathring{A}$. The process that allows the Lyman-α photon escape the galaxies after the light scatters between the hydrogen atoms manages to excite the electrons and then emit the energy in the form of Lyman-α photon is very complex and not fully understood yet, making the analysis of the observed Lyman-α line not a trivial task.

As complement to the Lyman-α line, it has been used the bright emission lines that are emitted in far infrared (FIR) of the spectra of galaxies. These emission lines are emitted by different processes and region in the galaxy, resulting in that far-infrared emission lines are not affected by some limitations as it is sometimes the Lyman-α line. One of the brightest emission lines in the far infrared is the [C II] emission line that at 157.7 μm and it is already a very good complement to the Lyman-α line in the study of the highest redshift galaxies.

The second alternative that we will use is the observation of the continuum of high redshift galaxies in submillimeter wavelength instead of in the optical. The choice to observe galaxies in the submillimeter comes from two simple reasons. First, the farther the galaxy, the fainter it looks, as product of the flux being inversely proportional to the distance. Second, if a galaxy emits in the red part of the spectrum, when observed, the redshift is going to shift the emission from the red to the near infrared, where the observations are not so easy from most of the current telescopes. In the submillimeter, specifically at 870 μm rest frame, we observe the Rayleigh-Jeans region of the spectrum produced by the cold dust present in most of galaxies. In the submillimeter, as product of the negative K-correction, as the redshift of the galaxies increases the observed flux density at 870 μm increases as well. The peak of the dust emission is usually around 100 μm, higher the redshift the peak of the dust emission is going to be shifted to longer wavelengths, closer to 870 μm . When we observe high redshift galaxies at 870 μm , the fact that they should be fainter is countered by the fact that we are observing closer to the peak of the emission as well, resulting in that higher redshift galaxies are brighter

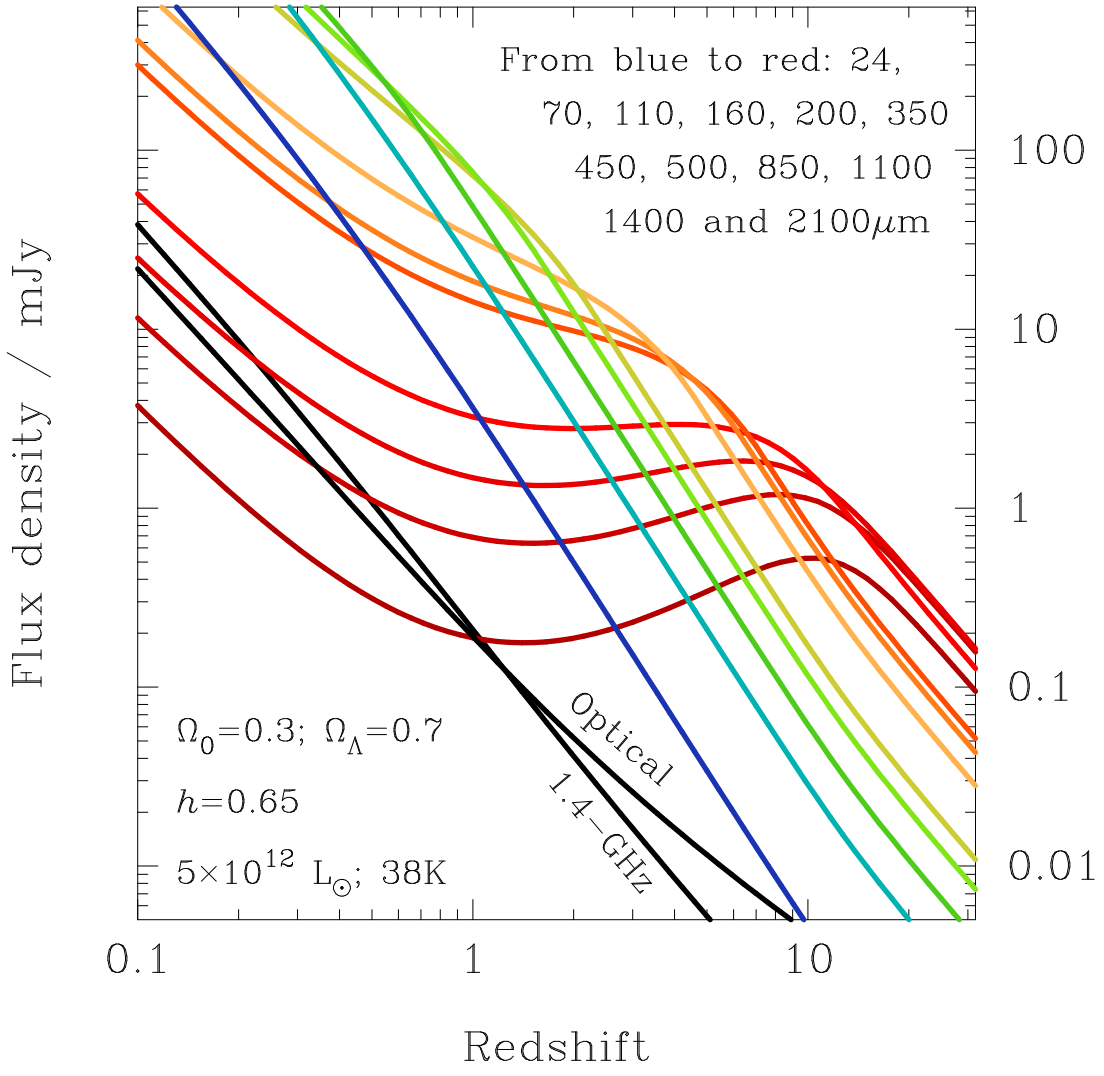

Figure 1.1 Example of how the negate K-correction affects the observation of high redshift galaxies. The predicted flux density of a dusty galaxy template as a function of redshift in various submm atmospheric windows. Each color line represent the flux density observed at a given wavelength. For observations at wavelength longer than 250 μm the flux density is almost independent of redshift (**?**).

at 870 μm than galaxies at lower redshift, making the observation at these wavelength a very good method to obtain information about high redshift galaxies (Fig. 1.1).

The third alternative method that we will use is related to where to search for high redshift galaxies. Galaxy clusters provide a natural lens that amplify the light emitted by galaxies in the background and they are observed several times brighter than they truly are. The magnification produced by the galaxy cluster can make a galaxy appear up to $\sim 100\times$ brighter, therefore revealing galaxies that would be impossible to observed if not thanks to the galaxy clusters. The magnification produced by galaxy clusters and even by galaxies has been used for years to observed distant galaxies. The main problem

with this method is that the magnification produced by the galaxy clusters is a quantity difficult to estimate, and without an accurate value it is impossible to know if the intrinsic flux is half of even a tenth of the observed flux as an example. The magnification values depend of many factors, the redshifts of the sources and the clusters, but mainly in the mass distribution of the galaxy clusters. In some cases, surveys are designed to observed galaxy clusters field with the purpose of modeling the mass distribution of them and also to have accurate photometric redshifts of the lensed galaxies, allowing the fast identification of lensed galaxies and by how much magnified. We will take advantage of such surveys to observed line and continuum emission is lensed galaxies.

The combination of these alternatives method in the study of high redshift galaxies, makes the motivation and core of this doctoral thesis.

1.2 Concepts of studying high redshift galaxies.

In this section I will familiarize the reader with some of the concepts used throw this thesis work. The concepts describe below are in close relation to the observations of high redshift galaxies. The far-infrared emission of the galaxies consists mainly of two sources, the continuum emission and emission lines. Both of the emission are emitted by different processes and deliver complementary information about the physical properties of the galaxies.

1.2.1 Cosmic star-formation history

The star-formation process is crucial in the evolution of galaxies through cosmic time. Observations of galaxies at different redshifts have have been used to estimate the co-moving UV luminosity density. These UV luminosities densities can be converted to star-formation densities, resulting in a global view of the evolution of star-formation activity per unit comoving volume over cosmic time (**?**). The conversion from UV luminosity to star-formation rate is not a robust calculation, since is based in several extrapolation and assumptions, one of the most important being the amount of UV extinction produced by dust absorption at different redshift. Despite of that, the results have been broadly accepted as a good indicator of the star-formation activity across time.

In Fig. 1.2 we show the star-formation density versus redshifts for the latest studies, going even up to $z \sim 10$ (Bouwens et al., 2014). This plot shows how the star-formation activity increases from z=0 to $z \simeq 2$, stays stable up to $z \sim 3$ and then decreases for

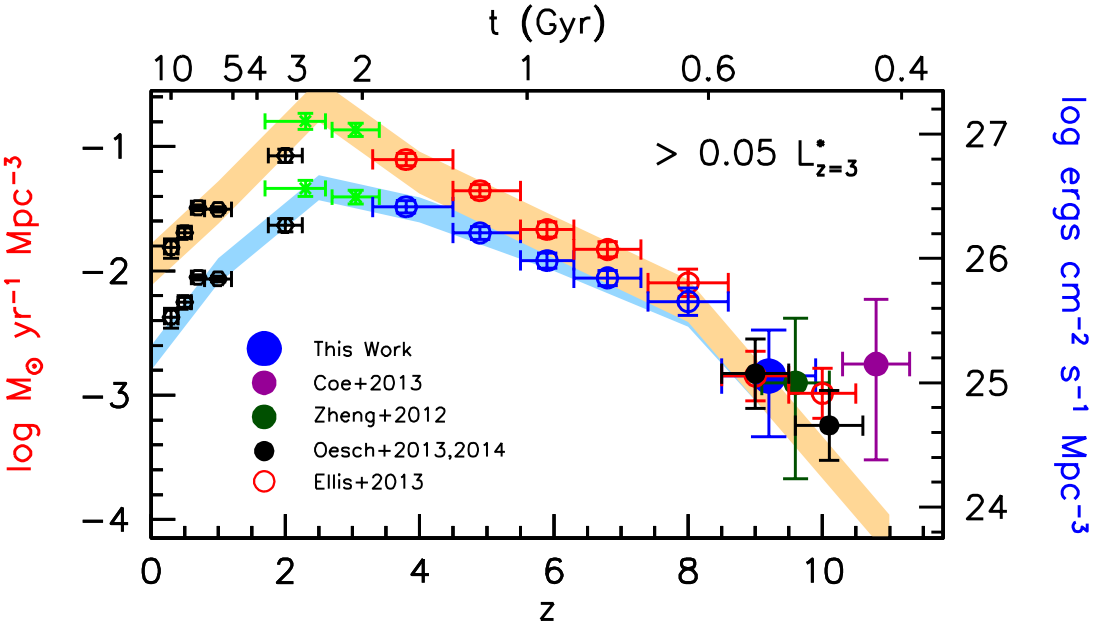

Figure 1.2 The *UV* luminosity density (*right axis*) and star formation rate density (*left axis*) versus redshift (extracted from Bouwens et al. (2014)). These luminosity densities and SFR densities are only considered down to a limiting luminosity of −17.7 AB mag. The *UV* luminosity is converted into a star formation rate using the canonical *UV*-to-SFR conversion factors. The upper set of points at every given redshift and orange contour show the dust-corrected SFR densities, while the lower set of points and blue contours show the inferred SFR densities before dust correction. The data is been taken from Bouwens et al. (2007, 2011b); Coe et al. (2013); Ellis et al. (2013); Oesch et al. (2012, 2013, 2014); Reddy and Steidel (2009); Schiminovich et al. (2005); Zheng et al. (2012).

higher redshifts. The two sets of points from $z = 0$ to $z = 8$ show the difference between the dust-corrected and observed values of star-formation rate densities. The amount of dust in high redshift galaxies is still a topic of debate, since no many dust observations of normal star-forming galaxies have been made at high redshift.

The evolution rate of the star-formation density appears fairly constant between $z \sim 2$ and $z \sim 8$, showing how the different process at $z > 2$ trigger star formation in galaxies (e.g. mergers and gas accretion). The discovery of candidates to galaxies at $z > 8$ show that the evolution in star-formation density would be faster at $z > 8$ than in the lower redshift range. The sample of galaxies at $z > 8$ is still low and not statistically strong to confirm this tendency.

1.2.2 Far-Infrared Continuum Emission

The Far-Infrared of the spectrum is usually defined as the emission corresponding to wavelength at $\lambda > 30$Å restframe. This emission is associated to the interstellar dust

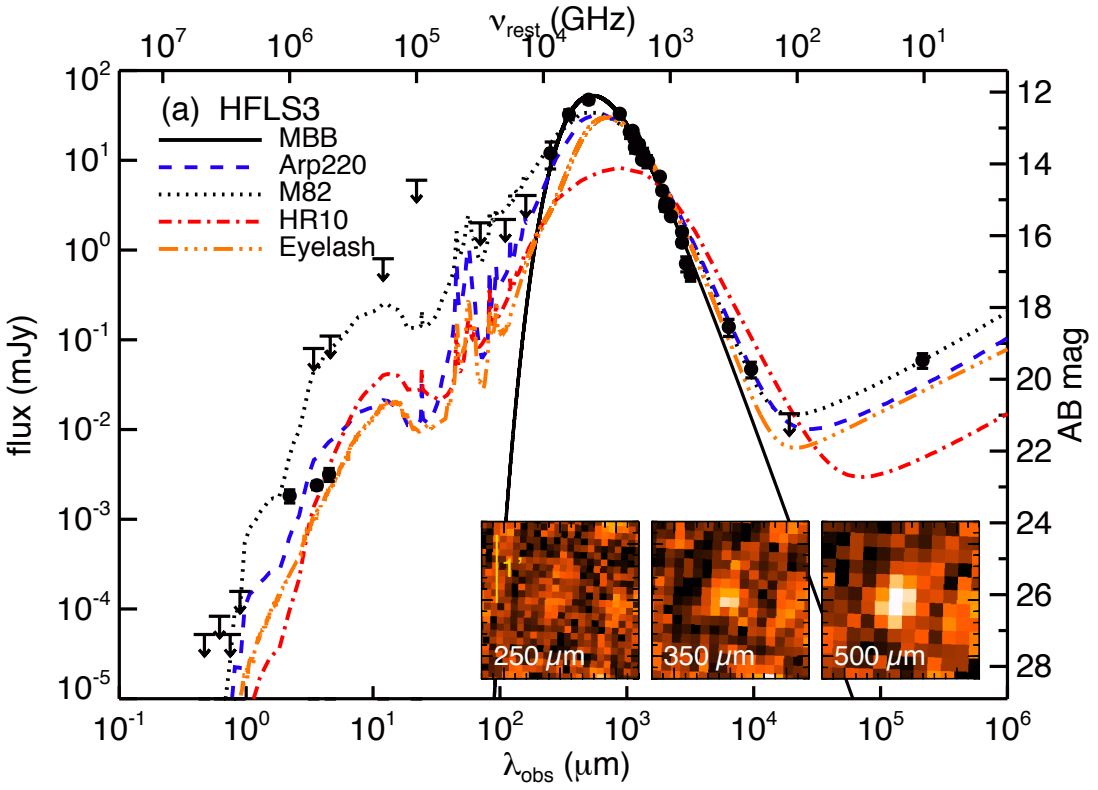

Figure 1.3 Example of a fit to the FIR continuum emission in a submillimeter galaxy HFLS3 at $z = 6.34$. HFLS3 was identified as a very high redshift candidate, as it appears red between the Herschel/SPIRE 250, 350, and 500 μm bands (inset). The SED of the source (black data points) is fitted with a modified black body (MBB; solid line) and spectral templates for the starburst galaxies Arp 220, M82, HR10, and the Eyelash (broken lines, see key) (Riechers et al., 2013).

present in galaxies that consists of the combination of dust grains of different sizes and composition.

The emission that we are interest in is that emitted at the longer wavelength, $\lambda > 100$Å, which is generally dominated by dust grains in thermal equilibrium at low temperatures. The dust grains that emit at this wavelength have sizes between 0.01-0.25 μm , they are heated to temperatures about $20-200$ K, depending in the spectrum and intensity of the interstellar radiation field (ISRF). The dust grains emit the absorbed energy as thermal radiation until they reach an equilibrium temperature T_d.

For a particular galaxy, there will be a distribution of dust temperatures, reflecting the different nature and environment of the dust grain (Blain et al., 2002). When working with unresolved dust emission it is usually assumed that all the dust grains have similar size and composition and that they reach a similar equilibrium temperature T_d. In this case, the emission is equivalent to that of a single temperature blackbody (MBB, Fig. 1.3), which is the Planck function for a given temperature multiplied by the dust

absorption cross section (Bianchi, 2013). In this approach, the peak of the FIR emission is a good indicator of the dust heating in the interstellar medium (ISM). In the cases when FIR emission is observed with high spectral resolution it is also good to model the emission with different dust grain sizes reaching different dust temperatures (da Cunha et al., 2008).

The study of the dust emission in the FIR can be used as an indicator of some galaxies properties as the dust mass and the star formation rate (SFR). If you have more dust the emission associated to it will be higher, and if you have more SFR, the ISRF will be higher and there will more energy heating the dust grains and therefore more thermal emission. Details of the usage of the FIR observations will be discussed below.

1.2.3 Far-Infrared Emission Lines

We already know that with the continuum FIR emission we are observing the emission of the diffuse dust in the ISM, with the observation of FIR emission lines we explore the emission of the gas (atomic or molecular) in the ISM.

The gas in the ISM can be found in different phases, depending strongly in the environment (density, temperature, radiation field). We already pointed out that the gas in the ISM can be atomic or molecular form, and the atomic gas can also be in ionized or neutral form. The complexity of the ISM as its different phases can be studied by the observations of the different emission lines that are emitted in each of the different phases.

The molecular gas mass is dominated by the presence of molecular Hydrogen, H_2 and in second place by carbon monoxide CO (Carilli and Walter, 2013). The molecular gas forms giant clouds where the high gas density, the dust and H_2 protect the molecules of being destroyed by UV photons. The cold molecular clouds is where the star formation process is thought to happen, therefore the importance of characterize them to understand the galaxy evolution.

The main source of study of the molecular gas are the CO rotational emission lines. The CO molecules have quantized rotational states that are exited by collision with H_2, protons, electrons or by the radiation field. The decay of the rotational states release photons of a fixed frequency associated to the rotational level J. The emission of different rotational level lines depend strongly in the density and temperature of the medium, therefore, the observations of the different CO rotational lines can reveal the physical properties of the molecular clouds. The excitation of CO is mainly triggered by the collision with H_2 molecules, and because of these molecules being the fuel of star

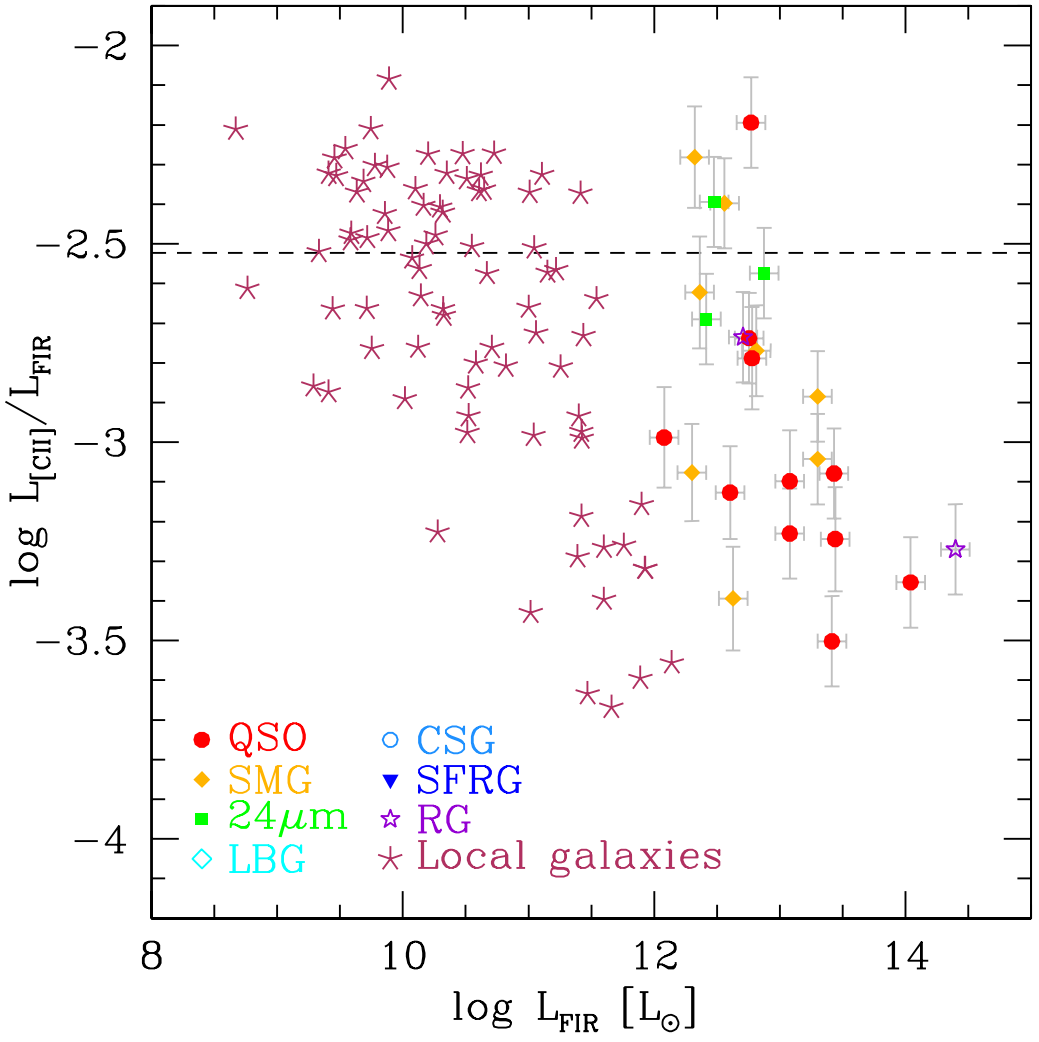

Figure 1.4 The ratio L[CII]/L_{FIR} as a function of L_{FIR} for some observed galaxies. The dashed horizontal line indicates a value of $3 \times 10^{-3} \sim$ Milky Way value. This plot shows how bright is the [CII] emission with respect to the total FIR emission of some galaxies. (Carilli and Walter, 2013).

formation, it is normal to use CO emission lines as good tracer of star formation rate in the ISM of distant galaxies.

The atomic gas is mainly studied by the fine structure emission lines (e.g. [C I], [C II], [N II], [O I] and [O III]). These emission lines are produced when the fine-structure energy levels (given by total angular momentum) are collision excited and decay emitting photons at a given frequency for each element and energy level.

In the ionized ISM, where Hydrogen is in the form of H II , the tracer emission lines correspond to [C II] , [N II] and [O III] . In the neutral ISM, the emission lines [C I] , [C II] and [O I] are produced. These fine structure lines have been noted to be the main dominant

coolant of the ISM, being [C II] the brightest emission lines in FIR for a wide range of galaxy population and has been used to observed the ISM of high redshift galaxies (Fig. 1.4).

These emission lines are important because can reveal more information about the ISM. Observations of the different emission lines of [C I] at 370 and 609 μm can give information about the excitation temperature, neutral carbon column density and mass. The combination of observations of [C I] , [O I] and CO can reveal more information about the molecular gas and the neutral medium. In the other hand, the observations of the emission lines associated to the ionized medium ([N II] and [O III]) can reveal the hardness of the radiation field. Because of the ionization level of [C II] (11.3 eV) being lower than the one of the Hydrogen (13.6 eV), the [C II] emission can be produces in the neutral and in the ionized medium. The observation of [N II] can be used to estimate how much of the [C II] is produced in the ionized medium.

1.3 Outline.

This thesis is divided in three projects. The first project, that will be discussed in Chapter 2 consists in the search for [C II] and continuum emission in three Lyman-α emitters at $z > 6.5$ and in one lensed Lyman break galaxy at $z \sim 11$. We discuss what can we learn from the non detection of such emission from those galaxies. The second project, that is a continuation of the first project, will be discussed in Chapter 3 and consists on the search for [C II] emission in a multiple imaged lensed Lyman break galaxy with $z_{\rm phot} = 6.18^{+0.05}_{-0.07}$ discovered behind the galaxy cluster MACS0329.6-0211 and the search for other continuum and line emissions in the field. The third project, that will be discussed in Chapter 4 consists in the search for lensed submillimeter galaxies behind galaxy clusters using submillimeter and millimeters observations. In Chapter 4 we present a summary and conclusion of our work.

Throughout this thesis we use a Λ-Cold Dark Matter cosmology with $H_0 = 70$ km s^{-1} Mpc^{-1}, $\Omega_\Lambda = 0.7$ and $\Omega_{\rm m} = 0.3$.

Chapter 2

Search for [C II] emission in $z = 6.5 - 11$ star-forming galaxies.

This project corresponds to the publication González-López et al. (2014)

2.1 Introduction

Lyman-alpha Emitters (LAE) are galaxies selected through strong Lyα emission and are among the most studied galaxy populations at high redshift. The use of narrow band filters over a wide area on the sky has proven to be a very effective method to find galaxies up to $z \sim 7$ (Fontana et al., 2010; Iye et al., 2006; Ono et al., 2012; Rhoads et al., 2012; Schenker et al., 2012; Shibuya et al., 2012; Vanzella et al., 2011). The possibility of finding LAEs from $z \sim 1$ to $z \sim 7$ shows that this type of galaxies can be used to understand galaxy evolution over cosmic time. It has been observed that the LAE fraction in UV selected galaxies increases with redshift up to $z \sim 6$ (Stark et al., 2010), which is expected due to the decreasing dust content at higher redshifts. Beyond $z \sim 6$ it is expected that the LAE fraction decreases as the amount of neutral Hydrogen (H I) increases, due to the incomplete reionization of the Intergalactic Medium (IGM) (Ono et al., 2012; Ota et al., 2008; Pentericci et al., 2011; Schenker et al., 2012; Stark et al., 2010). This is consistent with the comparatively low success rate of detection of Lyα emission at $z \gtrsim 7$.

If Lyman-alpha photons from redshifts $z \geq 7$ are absorbed by H I in the IGM (Dayal and Ferrara, 2012), it will be difficult to spectroscopically confirm the candidates at high redshift, such as the candidate $z \sim 12$ galaxy UDFj-39546284 discovered in the Hubble Space Telescope (HST) Ultra Deep Field (UDF) (Bouwens et al., 2011a; Brammer et al.,

2013; Capak et al., 2013; Ellis et al., 2013), and the candidates found behind galaxy clusters at $z \sim 9.6$ MACS1149-JD and ~ 10.7 MACS0647-JD (Coe et al., 2013; Zheng et al., 2012).

Among the usual Interstellar medium (ISM) tracers at optical/UV wavelengths, the only line that has been observed at $z > 4$ in galaxies is Ly-alpha. The emission of Ly-alpha is complicated by its high optical depth in the emission region and its escape through resonant scattering, by dust absorption, and by the contribution from outflows. Therefore direct constrains on the gas properties from the Ly-alpha line strength and shape are difficult to derive. This motivates the exploration of alternative means to study the highest redshift galaxies. Promising candidates include far-infrared fine structure emission lines, e.g., [C II] ($^2P_{3/2} \rightarrow {}^2P_{1/2}$) at 157.74 μm, which is not affected by the increasingly neutral IGM at $z > 7$ and can account for up to 1% of the total infrared luminosity in some galaxies, especially in those with low luminosity and metallicity (Crawford et al., 1985; Israel et al., 1996; Madden et al., 1997; Stacey et al., 1991).

The [C II] line traces photo-dissociation (a.k.a. photon-dominated) regions (PDRs), as well as diffuse H I and H II regions. In PDRs, the far-UV radiation produced by OB stars heats the surface layers of molecular clouds, which cool preferentially through [C II] emission. It has been observed that most of the [C II] emission in IR-bright galaxies is coming from PDRs, and that the PDR gas mass fraction can be up to 50% in starbursts like M82 (Crawford et al., 1985).

Modeling of FIR emission lines observed in starburst galaxies showed that at least 70% of the [C II] emission is produced in PDRs (Carral et al., 1994; Colbert et al., 1999; Lord et al., 1996). In the low-metallicity system Haro 11, on the other hand, at least 50% of the [C II] emission arises from a more diffuse, extended ionized medium (Cormier et al., 2012). The different conditions in which the [C II] emission is produced, and the direct or indirect relation of these conditions with the star formation process, suggest that [C II] emission should be a good tracer of the global galactic star formation activity (de Looze et al., 2011), at least for galaxies with low $T_{\rm dust}$ or low $\Sigma_{\rm IR} = L_{\rm IR}/\pi r^2_{\rm mid-IR}$ (Díaz-Santos et al., 2013). [C II] is found to be the strongest emission line, stronger than CO, and thus is the most promising tracer of the dense, star forming regions in distant galaxies where [C II] can be detected with ground-based telescopes due to the redshift into observable atmospheric windows.

In the past years, the [C II] 158 μm emission line has been established as a promising observable in high-redshift galaxies (Carilli et al., 2013; Cox et al., 2011; De Breuck et al., 2011; Gallerani et al., 2012; Hailey-Dunsheath et al., 2010; Iono et al., 2006; Ivison et al., 2010; Maiolino et al., 2009, 2005; Riechers et al., 2013; Stacey et al., 2010; Valtchanov et al., 2011; Venemans et al., 2012; Wagg et al., 2010, 2012; Walter et al.,

2012a, 2009; Wang et al., 2013; Willott et al., 2013). Most of the high-z detections were for infrared-luminous starbursts, many of which also show signatures of AGN. See the review by Carilli and Walter (2013) for more details.

With star formation rates of a few tens $M_{\odot}yr^{-1}$, based on the Lyα and UV continuum emission, LAEs are classified as "normal" star forming galaxies. Different studies claim that LAEs are young, dust free, starbursting galaxies, supported by UV observations (Finkelstein et al., 2007; Gawiser et al., 2006; Lai et al., 2008). Recent MIR detection of LAEs at $z \sim 2.5$ and $z < 0.3$ show that a significant fraction of the star formation in these galaxies is strongly obscured by dust (Oteo et al., 2012a,b). Thus, LAEs are promising targets for the detection of [C II] at high redshift.

Previous attempts to detect [C II] in a small sample of LAEs at $z \sim 6.6$ were unsuccessful (Kanekar et al., 2013; Ouchi et al., 2013; Walter et al., 2012b).

Here we present the result of a search for [C II] in three LAEs at $z > 6.5$ and in a lensed galaxy at $z \sim 11$. In Sect. 2 we describe the target selection and observations. The data is shown in Sect. 3 together with some implications and analysis in Sect. 4. A summary of the paper is presented in Sect. 5. Throughout this paper we use a Λ-Cold Dark Matter cosmology with $H_0 = 70$ km s^{-1} Mpc^{-1}, $\Omega_\Lambda = 0.7$ and $\Omega_m = 0.3$.

2.2 Observations

2.2.1 Source Selection

The three Lyman-α emitters targeted in this study were discovered in the Subaru Deep Field (SDF). Two of the LAEs observed belong to the sample of LAEs at $z \sim 6.6$ discovered by Taniguchi et al. (2005). The targets are the brightest LAEs (sources 3 and 4 in their catalog) and have a narrow and bright Lyman-α emission line. The third LAE (IOK-1) was discovered at $z \sim 7$ by Iye et al. (2006). It is one of the brightest and most distant LAEs known to date.

The fourth target, MACS0647-JD, is a lensed Lyman-break galaxy (LBG) discovered behind the galaxy cluster MACSJ0647.7+7015 at $z = 0.591$ (Coe et al., 2013). The galaxy was discovered as a J-Dropout galaxy lensed into 3 magnified images as part of The Cluster Lensing And Supernova survey with Hubble (CLASH) (Postman et al., 2012). The three images of the galaxy MACS0647-JD1, MACS0647-JD2 and MACS0647-JD3, have a magnification of $\sim$8,$\sim$7 and $\sim$2 respectively. The photometric redshift of the galaxy is $10.7^{+0.6}_{-0.4}$ (95% confidence limits). This is one of the highest redshift galaxy candidates known to date.

2.2.2 CARMA Observations

Observations of the three $z \sim 6.5-7$ LAEs were carried out using the Combined Array for Research in Millimeter-wave Astronomy (CARMA) between 2008 July and 2010 July. The array configurations used were the most compact, D and E, to minimize phase decoherence and maximize point source sensitivity. The [C II] line has a rest frequency of 1900.54 GHz (157.74 μm). For the redshifts of the targets, the line is shifted to the 1 mm band. The receivers were tuned to a frequency $\sim$150 $\mathrm{km\,s^{-1}}$ bluer than the expected frequency from the redshift determined by the peak of the Lyman-α line. This is for taking into account the possible absorption by the IGM in the Lyman-α line. The setups provide an instantaneous bandwidth of $\sim$ 1.5 GHz ($\sim 1800\,\mathrm{km\,s^{-1}}$) with a spectral resolution of 31.25 MHz ($\sim 37 - 39$ $\mathrm{km\,s^{-1}}$).

The observations were processed using MIRIAD (Sault et al., 1995). The absolute flux calibrators used are 3C84, MWC349, 3C273 and Mars, the latter being the most used. As passband calibrators the QSOs 3C273, 3C345 and 0854+201 were used. As gain calibrator the QSO 1310+323 was used. The time on source for IOK-1 was 58.5 hours, for SDF J132415.7+273058 was 15.9 hours and for SDF J132408.3+271543 4.6 hours. The final cubes were made using natural weighting to maximize point source sensitivity. The observations resulted in the following beamsizes: IOK-1: 1.86" $\times$1.33", PA= $-0.34°$, SDF J132415.7+273058: 1.92" $\times$ 1.56", PA= 83.45°, SDF J132408.3+271543: 2.54" $\times$ 2.01", PA= 88.02° (all targets: D and E configurations). For D configuration the minimum baseline is 11 meters and the maximum is 150 meters. For E configuration the minimum baseline is 8 meters and the maximum is 66 meters. Table 2.1 summarizes the sensitivities reached for the observations of the LAEs.

2.2.3 PdBI Observations

All MACS0647-JD observations were carried out in 2012 November as part of a DDT (Director's Discretionary Time) program with the Plateau de Bure Interferometer (PdBI). The target was observed with 4 WideX frequency setups (3.6 GHz bandwidth each), covering 80% of the photometric redshift range ($z = 10.1 - 11.1$). Two of the three lensed images (JD1 and JD2) are within 18" of each other and they were covered in a common 2 mm pointing. The absolute flux calibrators used are MWC349, 2200+420, 3C279 and 0716+714. As gain calibrator the QSO 0716+714 was used. The total on source time for all tunings was 7.4 hours (6-antennas equivalent). The observations were processed using GILDAS. The beamsize of the observations is the following: MACS0647-JD :

2.10" × 1.76", PA= 102.0° (C configuration). For C configuration the minimum baseline is 22 meters and the maximum is 184 meters. Table 2.2 summarizes the sensitivity reached for the observations of MACS0647-JD .

2.3 Results

2.3.1 Line Emission

The spectra of the three $z \sim 6.5 - 7$ LAEs are presented in Fig. 2.1 and the spectrum of MACS0647-JD is shown in Fig.2.2. No significant emission is detected at the redshifted line frequencies or close to them. The observations were sampled to a channel resolution of 50 $\mathrm{km\,s^{-1}}$ similar to the expected FWHM of the [C II] emission line (see Sect. 2.4.1). We use our non-detections to put constrains on the luminosities of the [C II] lines for all targets. The results for the LAEs can be seen in the Table 2.1 and for the MACS0647-JD in Table 2.2. The upper limits were estimated assuming that the sources were unresolved. For MACS0647-JD the spectra of the two images were corrected by the primary beam pattern before combination. The [C II] luminosities were estimated assuming that the velocity integrated flux of the line is $I_{\rm line}$=$S_{\rm line}\,\Delta v$, with $S_{\rm line}$ being 3 times the r.m.s. of the 50 $\mathrm{km\,s^{-1}}$ channel and $\Delta v = 50\,\mathrm{km\,s^{-1}}$ the range in velocity (details on Tab. 2.1 notes). Using 3σ over a 50 $\mathrm{km\,s^{-1}}$ channel to estimate the upper limit in the luminosities can result in a underestimation. We point out that for a more conservative estimation the luminosities should be multiplied by a factor 2. (i.e. 3σ over 200 $\mathrm{km\,s^{-1}}$ channel). Assuming a channel width of 200 $\mathrm{km\,s^{-1}}$, our IOK-1 [C II] limit is $\sim 10\%$ deeper than the previous PdBI limit (Walter et al., 2012b).

2.3.2 Continuum Emission

No continuum emission is detected in our observations of the three LAEs and the $z \sim 11$ LBG. The sensitivity reached for the continuum observations is given in the Tab. 2.1 for the LAEs and a continuum map for the three LAEs is shown in Fig. 2.3. The results for the MACS0647-JD are given in Tab. 2.2 and the continuum map is shown in Fig. 2.4. In Sect. 2.4.2 we discuss how the CMB affects our continuum observations and in Sect. 2.4.3 we use our continuum measurements to constrain the nature of our targets.

Table 2.1. Summary of Observations and Results for the LAEs

source	RA J2000.0	DEC J2000.0	z[a]	ν_{obs}[b] GHz	σ_{cont}[c] mJy b^{-1}	σ_{line}[d] mJy b^{-1}	$L_{[CII]}$[e] 10^8 L$_\odot$	$L_{IR,CMB}^{N6946}$[f] 10^{11} L$_\odot$	$SFR_{dust,CMB}$[g] M$_\odot$ yr^{-1}	SFR_{UV}[h] M$_\odot$ yr^{-1}
IOK–1	13:23:59.80	+27:24:56.0	6.965	238.881	0.19	1.17	<2.05	<6.34	<109.1	∼24
SDF J132415.7	13:24:15.70	+27:30:58.0	6.541	252.154	0.37	2.82	<4.52	<10.3	<177.2	∼34
SDF J132408.3	13:24:08.30	+27:15:43.0	6.554	251.594	0.75	5.67	<10.56	<21.0	<360.9	∼15

Note. — All luminosities upper limits are $3\,\sigma$.

[a]References: IOK–1:Iye et al. (2006); Ono et al. (2012) –SDF J132415.7+273058 and SDF J132408.3+271543 : Taniguchi et al. (2005)

[b]Observing Frequencies; tuned ∼125 MHz blueward of the Ly–α redshifts for all targets.

[c]1σ continuum sensitivity at 158μm rest wavelength.

[d]1σ [C II] line sensitivity over a channel width of 50 km s^{-1}.

[e]3σ [C II] luminosity limit over a channel width of 50 km s^{-1} assuming $L_{\rm line} = 1.04 \times 10^{-3}\, I_{\rm line}\, \nu_{\rm rest} (1+z)^{-1}\, D_{\rm L}^2$, where the line luminosity, $L_{\rm line}$, is measured in $L_\odot$; the velocity integrated flux, $I_{\rm line}$=$S_{\rm line}\,\Delta v$, in Jy km s^{-1}; the rest frequency, $\nu_{\rm rest} = \nu_{\rm obs}(1+z)$, in GHz; and the luminosity distance, $D_{\rm L}$, in Mpc. (e.g. Solomon et al. (1992)

[f]3σ limit based on the SED of NGC 6946 and including the effect of the CMB.

[g]3σ limit based on $L_{\rm IR}^{\rm N6946}$ including the effect of the CMB.

[h]UV–based SFR from Jiang et al. (2013)

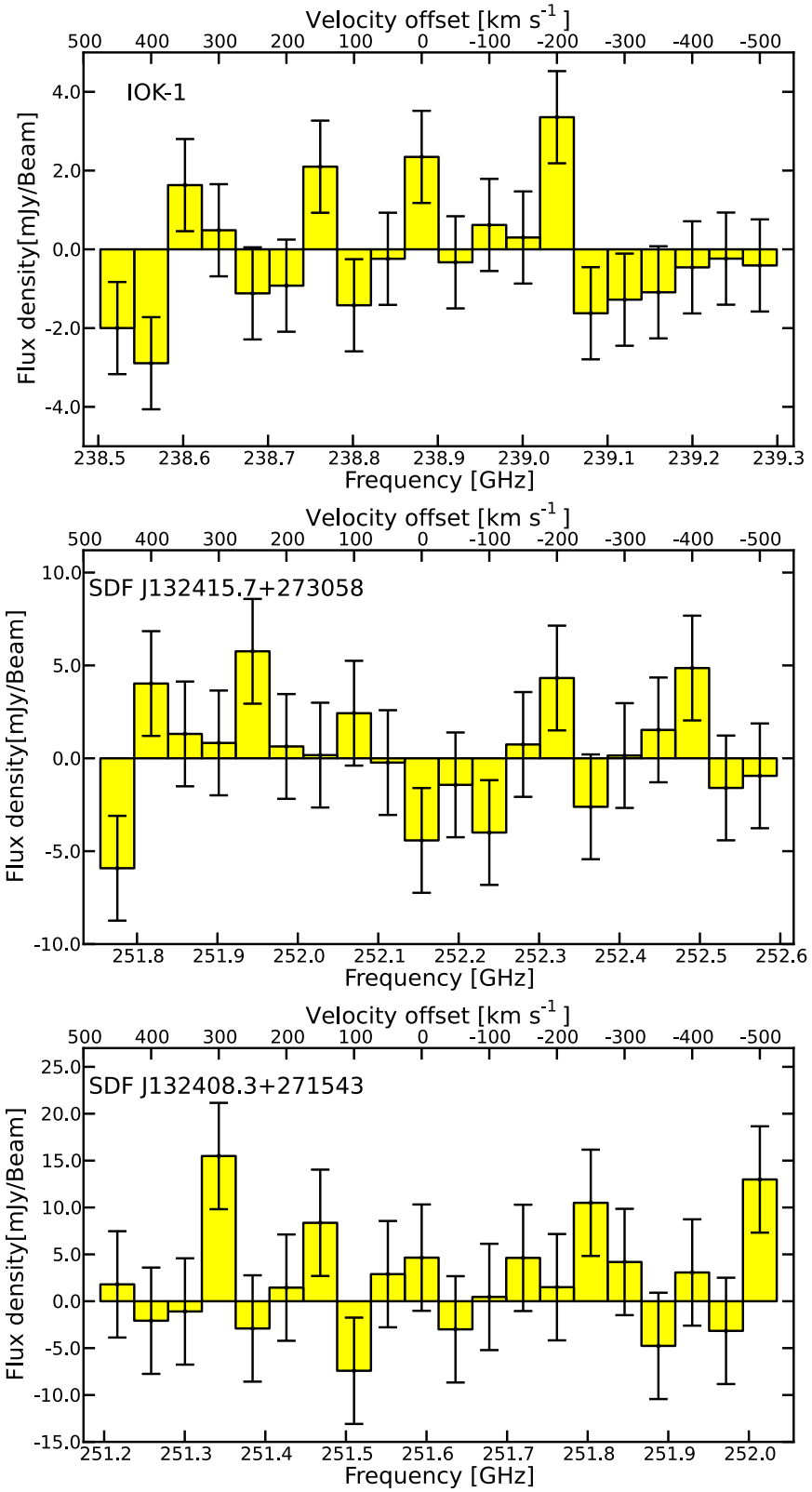

Figure 2.1 Spectra of the LAEs with a velocity resolution of 50 $\mathrm{km\,s^{-1}}$. The relative velocities are with respect to the frequency expected for the [C II] line including absorption by the IGM (150 $\mathrm{km\,s^{-1}}$ to the blue of $z_{\mathrm{Ly}\alpha}$). The redshifts of the target are z=6.965 for IOK-1, z=6.541 for SDF J132415.7+273058 and z=6.554 for SDF J132408.3+271543 .

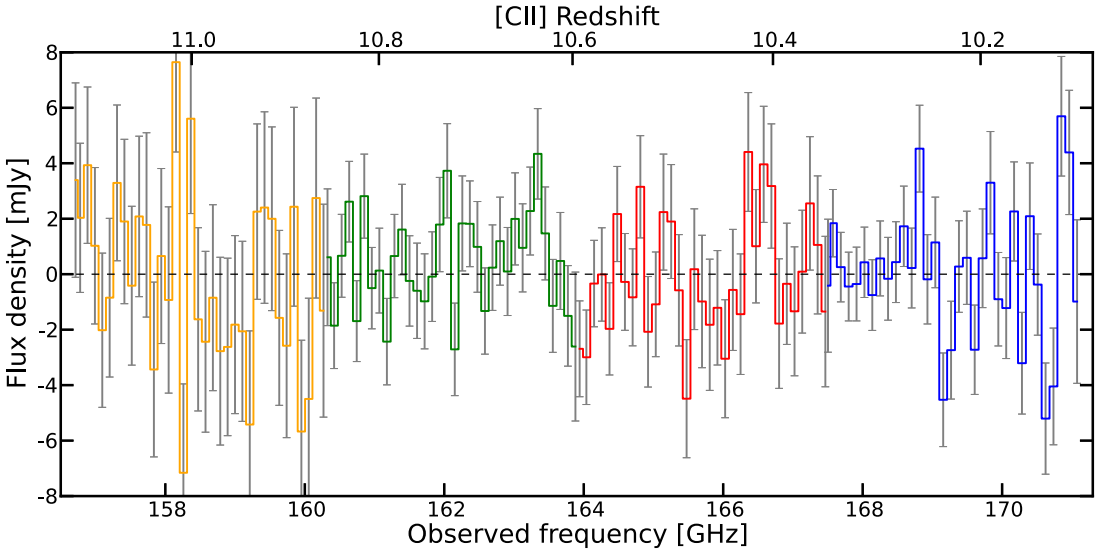

Figure 2.2 Spectrum of MACS0647-JD . The spectrum shows the added fluxes measured on the positions of the two lensed images JD1 and JD2 (combined magnification $\mu \sim 15$). The spectra of the two images were corrected by the primary beam pattern before combination. The 4 setups are plotted in different colors, blue, red, green and orange the colors for the setups A, B, C and D respectively. The error bars correspond to the quadrature of the errors of the individual measurement of the fluxes for JD1 and JD2 in each frequency channel. For display purposes, the spectrum is sampled at a channel resolution of 200 $\mathrm{km\,s^{-1}}$, but the search of the [C II] line as well as the analysis was made with the spectrum sampled to 50 $\mathrm{km\,s^{-1}}$.

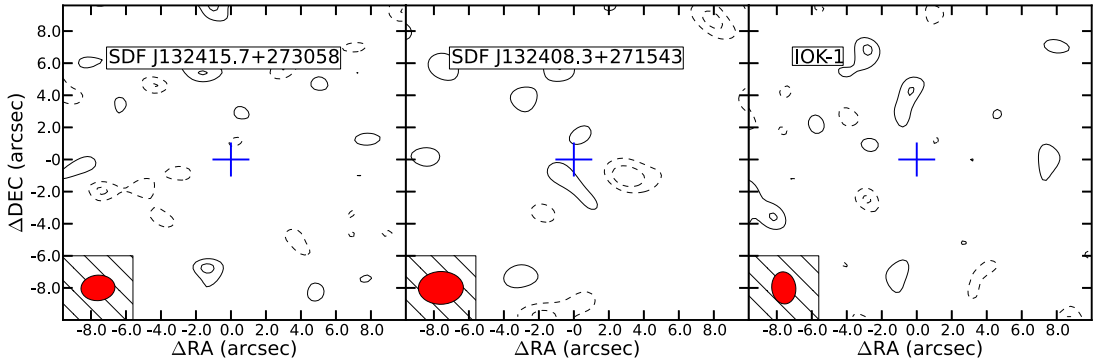

Figure 2.3 Rest-frame 158 μm continuum maps of the LAEs. Each contour level represents 1σ steps ($\pm 1\sigma$ levels are not shown). Solid contours are positive signal and dashed contour are negative signals. The 1σ levels are 0.75 $\mathrm{mJy\,beam^{-1}}$ for SDF J132408.3+271543 , 0.37 $\mathrm{mJy\,beam^{-1}}$ for SDF J132415.7+273058 and 0.19 $\mathrm{mJy\,beam^{-1}}$ for IOK-1. The blue crosses represent the position of each LAE as given in Tab. 2.1.

Table 2.2. Summary of Observations and Results for MACS0647JD

Parameter	MACS0647-JD1, JD2
Coordinates (J2000) JD1	06:47:55.731,+70:14:35.76
Coordinates (J2000) JD2	06:47:53.112,+70:14:22.94
μ (JD1+JD2)	~ 15
Redshift	$10.7^{+0.6}_{-0.4}$
UV SFR	~ 1 [$M_\odot yr^{-1}$]
ν	156.7-171.1 [GHz]
$\sigma_{\rm cont}$ [a]	0.17 mJy b^{-1}
$\sigma_{\rm line}$ (Setup A)[b]	3.31 mJy b^{-1}
$\sigma_{\rm line}$ (Setup B)[b]	4.12 mJy b^{-1}
$\sigma_{\rm line}$ (Setup C)[b]	3.19 mJy b^{-1}
$\sigma_{\rm line}$ (Setup D)[b]	6.42 mJy b^{-1}
$L_{\rm [CII]}$ (Setup C)[c]	$< 6.78 \times 10^7 \times (\mu/15)^{-1}$[$L_\odot$]
$L_{\rm [CII]}$ (Setup D)[c]	$< 1.36 \times 10^8 \times (\mu/15)^{-1}$[$L_\odot$]
$L_{\rm IR}^{\rm N6946}$[d](Corrected CMB)	$< 1.65 \times 10^{11} \times (\mu/15)^{-1}$[$L_\odot$]
SFR ($L_{\rm IR}$) (Corrected CMB)[e]	$< 28 \times (\mu/15)^{-1}$ [$M_\odot yr^{-1}$]
SFR ($L_{\rm [CII]}$) (Setup C)[f]	$< 5 \times (\mu/15)^{-1}$ [$M_\odot yr^{-1}$]
SFR ($L_{\rm [CII]}$) (Setup D)[f]	$< 9 \times (\mu/15)^{-1}$ [$M_\odot yr^{-1}$]

Note. — All luminosities upper limits are $3\,\sigma$.
References: Coordinates, magnification, redshift and UV-SFR from Coe et al. 2013.
All the luminosities and SFR are corrected by magnification.

[a] 1σ continuum sensitivity at 158μm rest wavelength.

[b] 1σ [C II] line sensitivity over a channel width of 50 km s^{-1}.

[c] 3σ [C II] luminosity limit over a channel width of 50 km s^{-1} as in Tab. 2.1. The two results correspond to the most sensitive and the least sensitive setups.

[d] 3σ limit based on the SED of NGC 6946 and including the effect of the CMB.

[e] 3σ limit based on $L_{\rm IR}^{\rm N6946}$ including the effect of the CMB.

[f] Based on the De Looze et al., 2011 $L_{\rm [CII]} - SFR$ relation. The two results correspond to the most sensitive and the lest sensitive setups.

2.4 Discussion

2.4.1 Width of the [C II] emission line.

Previous studies have presented the non-detection of [C II] (Ouchi et al., 2013; Walter et al., 2012b) with a channel resolution of 200 km s^{-1}, a choice motivated by the width of the Lyα emission line. We argue that recent observations and models of [C II] in LAEs suggest that the [C II] line could be narrower that the previously assumed value.

2.4.1.1 [C II] detection on a LAE z=4.7.

In support of a the narrow emission line is the detection of [C II] in a LAE at $z = 4.7$ (Lyα -1) with ALMA (Carilli et al., 2013). The FWHM of the emission line is 56 km s^{-1},

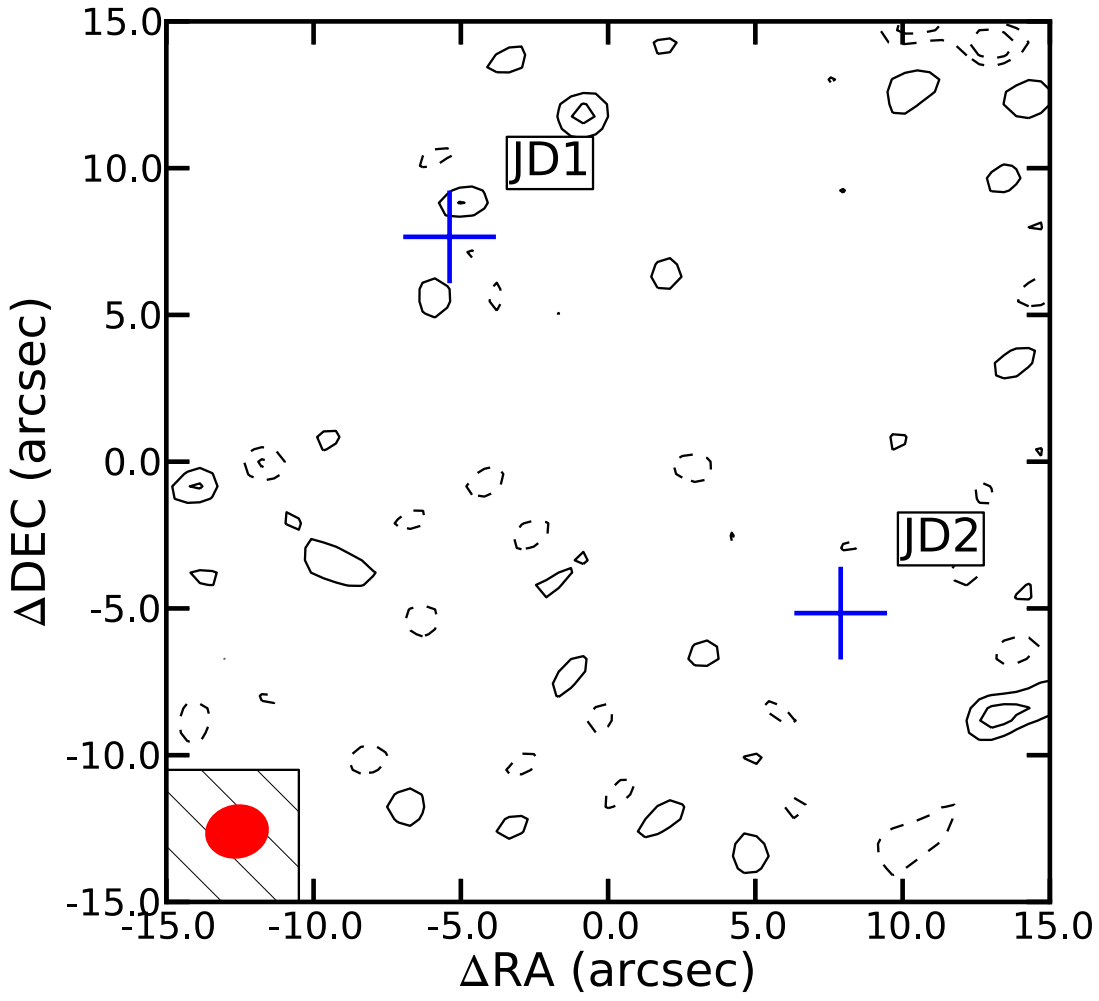

Figure 2.4 Continuum map of the field of MACS0647-JD . Each contour level represents 1σ steps ($\pm 1\sigma$ levels are not shown). Solid contours are positive signal and dashed contour are negative signals. The 1σ level is 93 μmJy beam^{-1}. The blue plus signs represent the positions of the two lensed images MACS0647-JD1 and MACS0647-JD2 as given in Tab. 2.2.

which is one order of magnitude narrower than the width of the Lyα emission line of ~ 1100 km s^{-1} of the same source (Ohyama et al., 2004; Petitjean et al., 1996). Despite of the LAE being at a separation of 2.3″ (~ 15 kpc) to the quasar BRI 1202-0725, there is no evidence for a significant influence of the quasar on the properties of the LAE from the observations. Carilli et al. (2013) tried to model the emission of the LAE taking into account the radiation coming from the luminous nearby quasar. All the models that reproduce the [C II] and Lyα luminosities predict higher luminosities for other UV lines that are not detected (Ohyama et al., 2004). Given this results, they conclude that the quasar is unlikely the source of heating and ionization in the LAE.

Based on deep, spatially resolved optical spectroscopy of the LAE, Ohyama et al. (2004) argue that the LAE is likely the composition of a normal star-forming galaxy and an

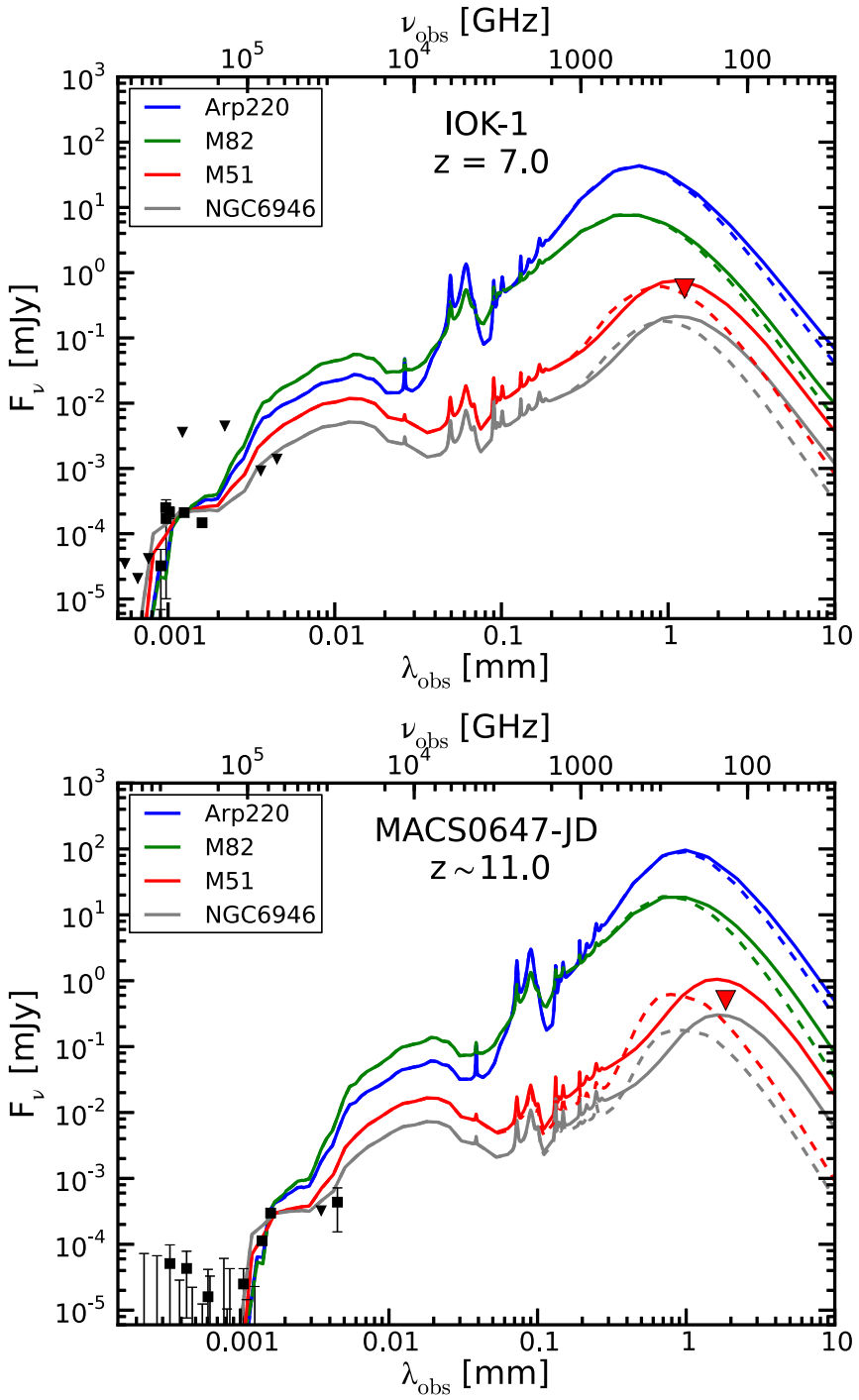

Figure 2.5 *Top:* Spectral energy distribution of IOK-1. The photometric points correspond to those measured by Cai et al. (2011); Iye et al. (2006); Ono et al. (2012); Ota et al. (2010). The red triangle corresponds to the 3σ upper limit given by the CARMA observations. The colored lines correspond to the SEDs of local galaxies shifted to the redshift of IOK-1 and scaled to the observations in the UV band. The dashed lines correspond to the observed SED of the local galaxies after the effects of the CMB on the observations are taken into account. *Bottom:* Spectral energy distribution of MACS0647-JD. The photometric points correspond to those presented by Coe et al. (2013). The SED of the galaxies follow the same prescription as in the upper panel. The red triangle corresponds to the 3σ upper limit calculated as the quadrature of the errors of the individual fluxes of JD1 and JD2, in the same way as the errors presented by Coe et al. (2013). The 1σ photometric uncertainty of the observations is 0.093 mJy, and the error of the added fluxes is 0.13 mJy.

extended nebula with violent kinematic status. This nebula emission would produce a broadening of the Lyα emission. This nebula can be explained, at least in a qualitative way, as a superwind caused by the supernovae explosion of OB stars in the late phase of the evolution of a starburst.

In conclusion, this LAE is not intrinsically different from the general population of LAE. The [C II] detection in this LAE can thus be used as a reference for [C II] searches in other LAEs at high redshift.

2.4.1.2 Himiko simulations.

Simulations also suggest narrow [C II] emission lines at high redshift for LAEs. Vallini et al. (2013) combine a high resolution cosmological simulation with a sub-grid multi-phase model of the interstellar medium to simulate the [C II] emission in a halo similar to the LAE Himiko at $z = 6.6$. They find that 95% of the [C II] emission is generated in the Cold Neutral Medium (CNM), mainly in clumps of individual size ≤ 3 kpc. They present a spectrum for the simulated [C II] emission, where the FWHM of the main peak is ~ 50 km s^{-1}, very similar to the 56 km s^{-1} of the LAE at z=4.7. This suggests that the width of the [C II] line is to first order determined by the gravitational potential of the clumps. The [C II] emission produced in the CNM follows the gravitational potential of the clumps, resulting in narrow emission lines associated with each clumps. An ensemble of emitting clumps moving through the galaxy following the potential of the galaxy could combine and produce a broader line. Such behavior is not observed in the simulations, where just a small number of clumps dominate the [C II] emission.

We conclude that the adopted width of ~ 50 km s^{-1} for the [C II] line in LAEs agrees with recent observations and simulations. Nevertheless, we do not discard the possibility of [C II] lines being broader than our assumption, but that the occurrence of unusually narrow lines in this population appears plausible.

2.4.2 CMB effects.

The Cosmic Microwave Background Radiation (CMB) emits as a black body with a temperature of $T_{\rm CMB}^{z=0} = 2.7$ K. The temperature of the CMB increases linearly with $(1 + z)$, becoming an important factor to take into account for observations of objects at high redshift. da Cunha et al. (2013) showed the effect of the CMB on observations of high-redshift galaxies. Here we will follow the prescription formulated by da Cunha et al. (2013) to take into account the effects of the CMB in the continuum observations

of galaxies at high redshift in the mm and sub-mm. We will apply this prescription to the SED of the local galaxies, as if they would be observed at a given redshift z.

The templates that we use are those presented by Silva et al. (1998) for the galaxies Arp 220, M82, M51 and NGC 6946. For the galaxies assume cold dust with temperature $T_{\rm dust}^{z=0}$ and an emissivity index β. For Arp 220 we used $T_{\rm dust}^{z=0} = 66.7$ K and $\beta = 1.86$ (Rangwala et al., 2011), for M82 $T_{\rm dust}^{z=0} = 48$ K and $\beta = 1$ (Colbert et al., 1999), for M51 $T_{\rm dust}^{z=0} = 24.9$ K and $\beta = 2$ (Mentuch Cooper et al., 2012) and for NGC 6946 we used $T_{\rm dust}^{z=0} = 26$ K and $\beta = 1.5$ (Skibba et al., 2011). At a given redshift the CMB contributes to the dust heating such that the equilibrium temperature is:

$$T_{\rm dust}(z) = \left((T_{\rm dust}^{z=0})^{4+\beta} + (T_{\rm CMB}^{z=0})^{4+\beta} \left[(1+z)^{4+\beta} - 1 \right] \right)^{\frac{1}{4+\beta}}. \tag{2.1}$$

$T_{\rm dust}^{z=0}$ is a measurement of the mean dust temperature as determined by a modified black-body fit to an observed galaxy IR SED at $z = 0$, representing the total IR luminosity of the galaxy. As a representative fit, this is equally applicable to both optically thin galaxies and optically thick as in Arp 220. So long as the galaxy is transparent to the CMB radiation (true for even Arp 220), Eq. 1 holds. The additional heating by the CMB affects the SEDs such that the peak of the emission is shifted to a shorter wavelength and the total luminosity associated to the cold dust is higher by $[T_{\rm dust}(z)/T_{\rm dust}^{z=0}]^{(4+\beta)}$. We need to modify the intrinsic SED of the galaxies to include this new $T_{\rm dust}(z)$. The flux density depends on the black body radiation for the given temperature,

$$F_{\nu/(1+z)} \propto B_\nu(T_{dust}(z)), \tag{2.2}$$

To include $T_{\rm dust}(z)$ we have to apply the following factor to convert the intrinsic SED flux density to the emission associated with the new temperature $F^*_{\nu/(1+z)}$.

$$F^*_{\nu/(1+z)} = F^{\rm int}_{\nu/(1+z)} \times \frac{B_\nu(T_{\rm dust}(z))}{B_\nu(T_{\rm dust}^{z=0})}. \tag{2.3}$$

This factor will only apply to the part of the SED that correspond to the emission of the cold dust. To accomplish this, we scale a modified black body (MBB) to the peak of the FIR emission of the SED at $T_{\rm dust}^{z=0}$, and then use this MBB emission to estimate the ratio (R_ν) of emission associated with the cold dust at a given frequency,

$$R_\nu = \frac{K\nu^\beta B_\nu(T_{\rm dust}^{z=0})}{F_\nu^{\rm int}}, \tag{2.4}$$

where K is just the scaling factor. The flux density associated to the new temperature of the cold dust will be:

$$F^{*}_{\nu/(1+z)} = M_{\nu} \times F^{\rm int}_{\nu/(1+z)} \tag{2.5}$$

with

$$M_{\nu} = \left[(1 - R_{\nu}) + R_{\nu} \times \frac{B_{\nu}(T_{\rm dust}(z))}{B_{\nu}(T^{z=0}_{\rm dust})}\right]. \tag{2.6}$$

Finally, following da Cunha et al. (2013), we have to take into account the effect of the CMB as an observing background. For this we have to multiply the flux associated with $T_{\rm dust}(z)$ by C_{ν},

$$C_{\nu} = \left[1 - \frac{B_{\nu}(T_{\rm CMB}(z))}{B_{\nu}(T_{\rm dust}(z))}\right], \tag{2.7}$$

resulting in the flux observed of the galaxies as:

$$F^{\rm obs}_{\nu/(1+z)} = C_{\nu} \times M_{\nu} \times F^{\rm int}_{\nu/(1+z)}, \tag{2.8}$$

with $C_{\nu} \times M_{\nu}$ representing the effect of the CMB in the observations at a given frequency. The same corrections are derived when an optically thick emission is assumed, as in the case of Arp 220.

As we can see in Fig. 2.5, the effect of the CMB decreases the observable flux density at 2 mm by up to a factor of 5× (in the case of M51) for the galaxy at $z \sim 11$, when the temperature of the CMB is higher, as expected. Also, the effect is higher for galaxies with a lower temperature of the cold dust. Galaxies with temperature of order of 25-30 K are more affected than those with temperature of 40-50 K. The CMB effects will be important for estimations of the flux densities of these type of galaxies in the continuum and for the correct interpretation of the observations.

The CMB effects on the [C II] line observations are similar to those on the continuum. The flux of an emission line observed against the CMB is:

$$\frac{S^{\rm obs}_{\nu/(1+z)}}{S^{\rm int}_{\nu/(1+z)}} = \left[1 - \frac{B_{\nu}(T_{\rm CMB}(z))}{B_{\nu}(T_{\rm exc})}\right], \tag{2.9}$$

with $T_{\rm exc}$ being the excitation temperature of the transition. For the case of local thermal equilibrium (LTE), when collisions dominate the excitation of the [C II] line, the excitation temperature of the transition is equal to the kinetic temperature of the gas ($T_{\rm kin}$). The kinetic temperature varies for the different [C II] emission regions. Gas temperatures within PDRs are typically $T \sim 100 - 500$ K (Stacey et al., 2010), for the CNM $T \approx 250$ K, for the WNM $T \approx 5000$ K and for the ionized medium $T \approx 8000$ K(Vallini et al., 2013). Since the CMB temperature at $z = 6.5 - 11$ is much lower than the gas temperature of the [C II] emitting region, it will not contribute significantly to the [C II] excitation, but must be taken into account as the background against which the line flux is measured. In most of the [C II] emission regions, the temperatures are so high that the observed flux of the line against the CMB is similar to the intrinsic flux ($S^{\rm obs}_{\nu/(1+z)}/S^{\rm int}_{\nu/(1+z)} \approx 1$). For the extreme case where all the [C II] emission is being produced in PDRs with temperature of 100 K in a galaxy at $z = 11$, the observed flux (using Eq. 2.9) would be 90% of the intrinsic flux. We found this case very unlikely, since in low redshift galaxies the [C II] emission produced in PDRs is 50-70% of the total [C II] luminosity and the gas temperatures associated to the PDRs are higher (Carral et al., 1994; Colbert et al., 1999; Crawford et al., 1985; Lord et al., 1996). We conclude that the CMB effects on the [C II] line observations are negligible for our observations.

2.4.3 Spectral energy distribution of the galaxies.

Using the upper limits on the continuum, we compare the targets with the spectral energy distribution templates of local galaxies (SEDs). For the LAEs, the SEDs of the local galaxies are scaled to the flux of a near-IR filter that is not contaminated by the Lyα emission line. For MACS0647-JD , the filter used for the scaling is the one next to the Lyman Break. The photometry of IOK-1 and MACS0647-JD together with the SED of local galaxies are shown in Fig. 2.5. For SDF J132415.7+273058 and SDF J132408.3+271543 (not shown) the situation is very similar: the sources have a similar redshift, the continuum upper limits are comparable and the CMB effects are of the same order. Our upper limit for IOK-1 is comparable to the upper limit found by Walter et al. (2012b) using PdBI observations.

Using the SED of NGC 6946 as a template, we estimate the IR luminosity given the upper limit flux densities, similar to the approach shown by Walter et al. (2012b). We scale the SED of NGC 6946 to the 3 sigma upper limits of the mm observations and integrate from 8 μm to 1 mm (rest frame) to compute the IR luminosity.

The IR luminosity corresponding to this intrinsic SED and the SFR associated (Kennicutt, 1998) are given in Tab. 2.1 for the LAEs and in Table 2.2 for MACS0647-JD .

We note that estimating the IR luminosity using NGC 6946 without taking into account the CMB result in a significant underestimation of the luminosity upper limits. The IR luminosity limit corrected by the CMB of the LAEs at $z \sim 6.6$ is 35% higher than without correcting by the CMB. For IOK-1 at $z \sim 7$, the IR luminosity limit is a 50% higher than the estimation without correcting by the CMB. For MACS0647-JD at $z \sim 10.7$, the IR luminosity limit corrected for the CMB is ~ 3.5 times the IR luminosity limit not corrected by the CMB. For galaxies with cold dust temperature of ~ 25 K, the effect of the CMB on the observations is very important at high redshift, and it will significantly limit the feasibility of detecting not extremely starbursting galaxies in the IR continuum, it will not greatly affect the detectability of [C II] emission.

2.4.4 Ratio $L_{[\mathrm{CII}]}/L_{\mathrm{FIR}}$

Figure 2.6 presents our upper limits to $L_{[\mathrm{CII}]}/L_{\mathrm{FIR}}$ and L_{FIR} together with detections of [C II] in other galaxies. The arrows represent the region of possible values for $L_{[\mathrm{CII}]}/L_{\mathrm{FIR}}$ and L_{FIR} (integrated from 42.5μm to 122.5μm rest frame). If we used UV-based SFR estimates to infer L_{FIR}, our data points would move across the diagonal arrows towards the region where local galaxies are, putting our $L_{[\mathrm{CII}]}/L_{\mathrm{FIR}}$ upper limits close to the average value found for the local galaxies. The ratio $L_{[\mathrm{CII}]}/L_{\mathrm{FIR}}$ is a measure of how efficient the [C II] emission is in cooling the gas. The values presented for our targets, $\log(L_{[\mathrm{CII}]}/L_{\mathrm{FIR}}) \sim -2.9$, do not necessarily imply that [C II] is not efficient in cooling the gas in these galaxies, it is most likely a consequence of the galaxies having much lower FIR luminosities than our conservative upper limits. Different processes can affect the ratio $L_{[\mathrm{CII}]}/L_{\mathrm{FIR}}$. In galaxies with low extinction and low metallicity, like in Haro 11, about 50% of the [C II] emission arises from the diffuse ionized medium (Cormier et al., 2012). Variations on the fraction of [C II] emission associated with the ionized medium will also affect the ratio $L_{[\mathrm{CII}]}/L_{\mathrm{FIR}}$. In some galaxies, the internal dust extinction can affect the ratio $L_{[\mathrm{CII}]}/L_{\mathrm{FIR}}$. In Arp 220, the dust is optically thick at 158 μm and can absorb part of the [C II] emission, decreasing the ratio $L_{[\mathrm{CII}]}/L_{\mathrm{FIR}}$ (Rangwala et al., 2011).

Díaz-Santos et al. (2013) present the results of a survey of [C II] in luminous infrared galaxies (LIRGs) observed with the PACS instrument on board the *Herschel Space Observatory*. They found a tight correlation between the ratio $L_{[\mathrm{CII}]}/L_{\mathrm{FIR}}$ and the far-IR $S_\nu(63\mu m)/S_\nu(158\mu m)$ continuum color, independently of their L_{IR}. They found that the ratio decreases as the average temperature of dust increases, suggesting that the main observable linked to the variation of $L_{[\mathrm{CII}]}/L_{\mathrm{FIR}}$ is the average dust temperature. For the galaxies with dust temperatures $\sim 20K$ the average ratio is $\log(L_{[\mathrm{CII}]}/L_{\mathrm{FIR}}) \sim 10^{-2}$, suggesting that for galaxies like NGC 6946 with a dust temperature of ≈ 26 K, the ratio

$L_{[\mathrm{CII}]}/L_{\mathrm{FIR}}$ should be on the same order of magnitude. Díaz-Santos et al. (2013) also found a correlation between $L_{[\mathrm{CII}]}/L_{\mathrm{FIR}}$ and luminosity surface density of the mid-IR emitting region ($\Sigma_{\mathrm{IR}} = L_{\mathrm{IR}}/\pi r^2_{\mathrm{mid-IR}}$). LIRGs with lower $L_{[\mathrm{CII}]}/L_{\mathrm{FIR}}$ ratios are warmer and more compact. We can use this relation to find a rough estimation for $L_{[\mathrm{CII}]}/L_{\mathrm{FIR}}$ of our targets. As $r_{\mathrm{mid-IR}}$ we use the size found in the UV observations of the targets. The half-light radius of IOK-1 is ≈ 0.62 kpc (Cai et al., 2011). The full width at half maximum size of SDF J132415.7+273058 and SDF J132408.3+271543 are ≈ 4.0 and 3.2 kpc respectively (Taniguchi et al., 2005). For MACS0647-JD the delensed half-light radius is $\lesssim 0.1$ kpc (Coe et al., 2013). Using our L_{IR} upper limits as an approach to L_{IR} we can estimate Σ_{IR}. For IOK-1 the estimated ratio is $\log(L_{[\mathrm{CII}]}/L_{\mathrm{FIR}}) \sim -2.9$, for SDF J132415.7+273058 is $\log(L_{[\mathrm{CII}]}/L_{\mathrm{FIR}}) \sim -2.5$ and for SDF J132408.3+271543 is $\log(L_{[\mathrm{CII}]}/L_{\mathrm{FIR}}) \sim -2.6$. For the LAEs the average of $L_{[\mathrm{CII}]}/L_{\mathrm{FIR}}$ is similar to the average value for the local galaxies (Fig. 2.6). For MACS0647-JD the estimated ratio is $\log(L_{[\mathrm{CII}]}/L_{\mathrm{FIR}}) \sim -3.2$.

2.4.5 SFR-$L_{[\mathrm{CII}]}$ Relation

In Fig. 2.7 we present our $L_{[\mathrm{CII}]}$ upper limits with the UV-SFR estimated for the targets together with upper limits detections for published LAEs (Carilli et al., 2013; Kanekar et al., 2013; Ouchi et al., 2013). The black solid lines corresponds to the relation found by de Looze et al. (2011), with the gray area corresponding to 2σ scatter in the relation. Our upper limits for the [C II] luminosity fall within the scatter of the SFR-$L_{[\mathrm{CII}]}$, with the exception of SDF J132408.3+271543 , where the upper limit falls above the relation due to the moderate depth of its observations. The detection of the LAE at z=4.7 (Lyα -1) agree very well with the relation found by de Looze et al. (2011) using the UV-SFR estimated by Ohyama et al. (2004). The upper limits for the lensed LAE at $z = 6.56$ HCM 6A and Himiko suggest that LAEs at $z > 6$ could fall below the relation found at low redshift. More observations are needed to clarify if there is an intrinsic difference between the LAEs at $z \sim 4.5$ with the higher redshift population. The high magnification of MACS0647-JD allows us to explore an UV-SFR one order of magnitude lower than the ones of the LAEs, showing the advantage of observing lensed galaxies to cover the intrinsically faint population at high redshift.

2.4.6 IOK-1 Models

Using the same procedure presented in Vallini et al. (2013) for the [C II] emission of Himiko, we estimate the emission of [C II] for IOK-1 at $z \sim 7$. For this simulation, the star formation rate was set to 20 $\mathrm{M}_{\odot} yr^{-1}$ and a stellar population age of 10 Myr. The

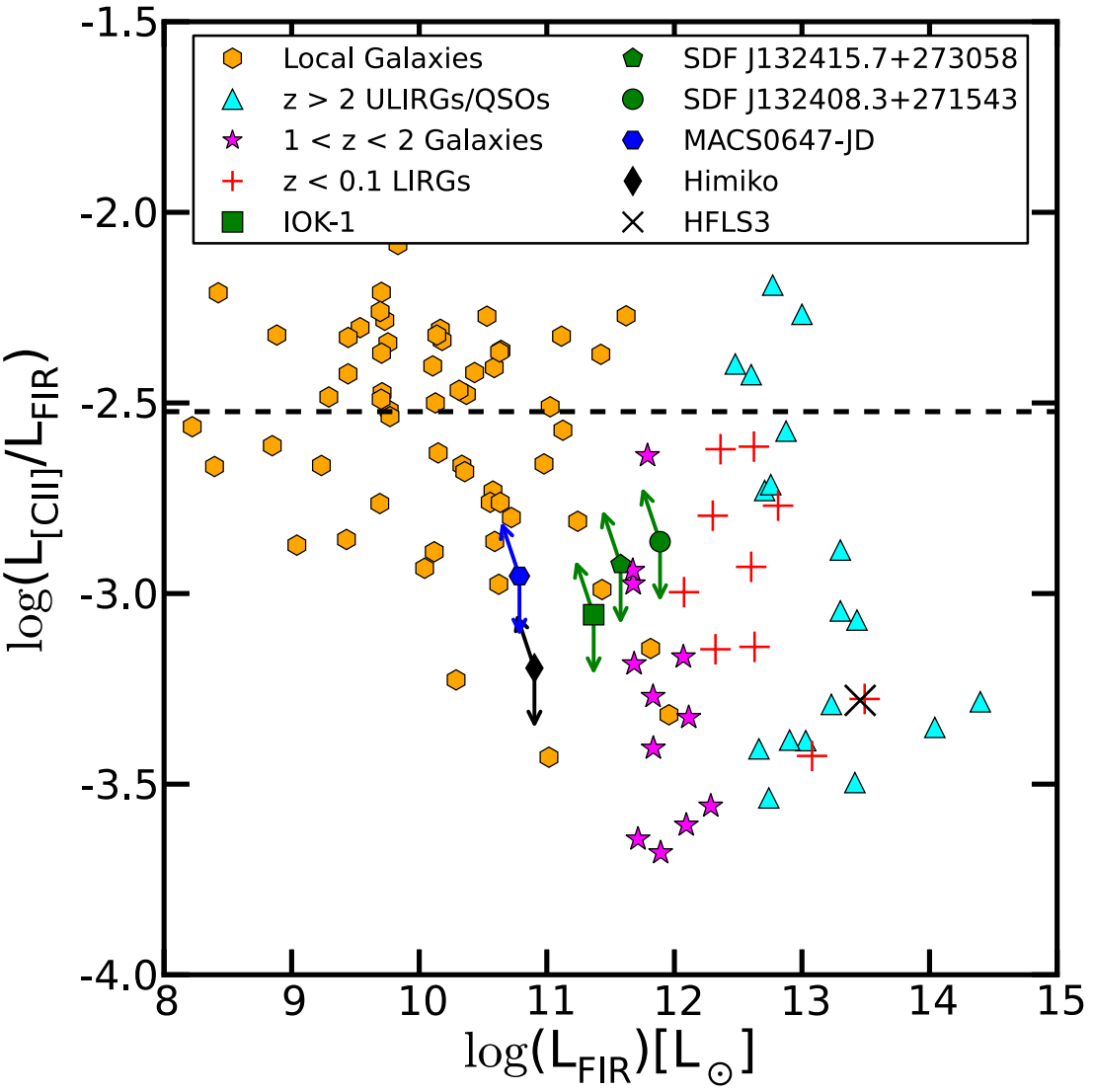

Figure 2.6 Ratio of the [C II] luminosity to the FIR luminosity vs the FIR luminosity (integrated from 42.5μm to 122.5μm rest frame) for galaxies at different redshifts. The green symbols correspond to the upper limits of the LAEs presented here. The blue hexagon corresponds to the upper limit of MACS0647-JD using the most sensitive setup. The FIR luminosities for the galaxies are upper limits estimated from the observations including the CMB effects. The black diamond corresponds to the upper limit for Himiko with ALMA observations (Ouchi et al., 2013). The horizontal dashed line is the average value for $L_{[\mathrm{CII}]}/L_{\mathrm{FIR}}$ on the local galaxies. (Cox et al., 2011; De Breuck et al., 2011; Iono et al., 2006; Ivison et al., 2010; Luhman et al., 2003; Maiolino et al., 2009; Malhotra et al., 2001; Negishi et al., 2001; Ouchi et al., 2013; Riechers et al., 2013; Stacey et al., 2010; Swinbank et al., 2012; Venemans et al., 2012; Wagg et al., 2010; Walter et al., 2012a, 2009; Wang et al., 2013)

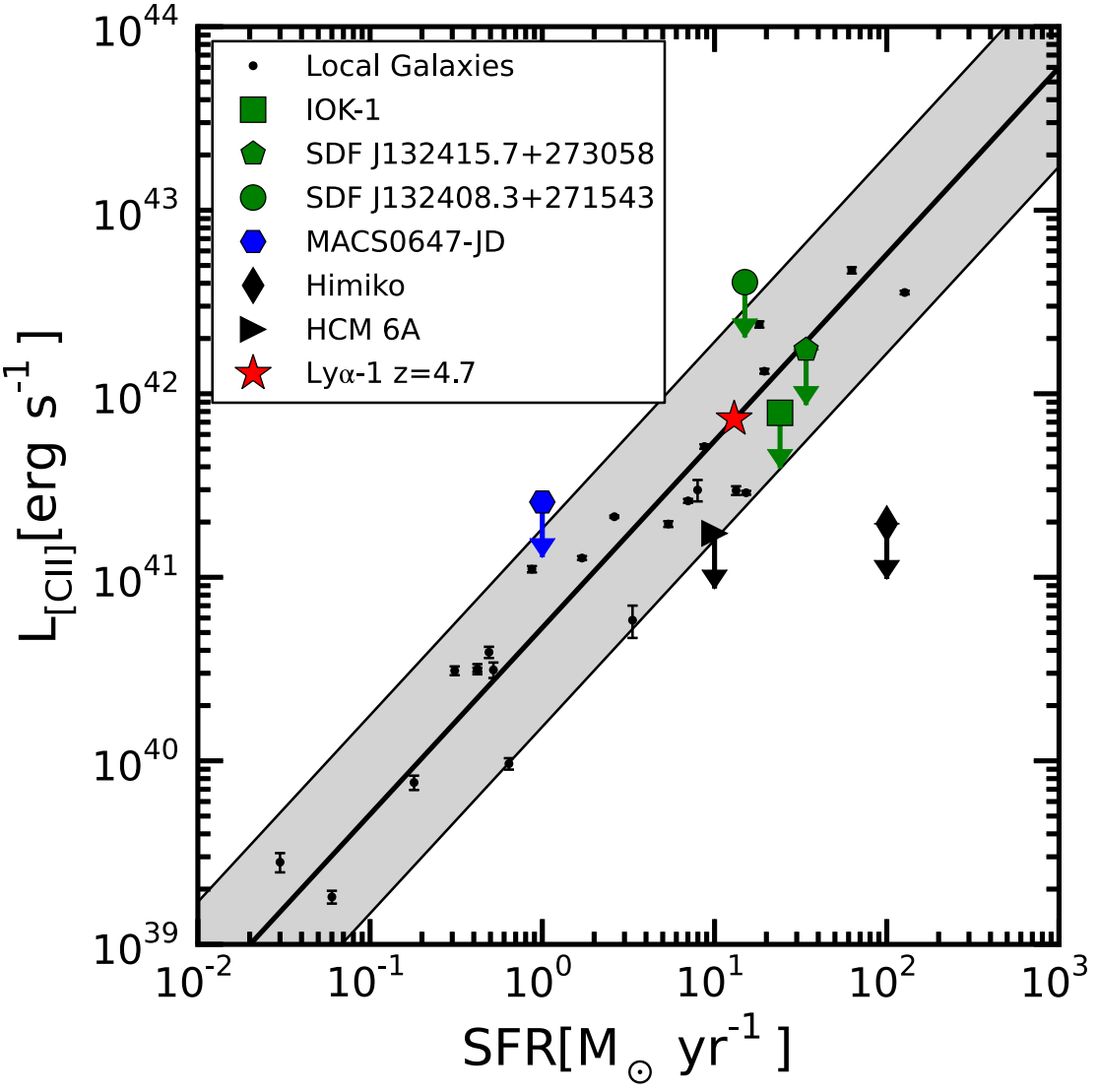

Figure 2.7 Relation of the [C II] luminosity with the UV-derived star formation rate of galaxies. The black solid lines correspond to the relation found by de Looze et al. (2011), with the gray area corresponding to 2σ of the scatter in the relation. The black dots with error bars correspond to the data used to find the relation of [C II] - SFR. The green circle, square and pentagon correspond to the LAEs with the [C II] upper limits presented in this paper assuming the star formation rate estimated from the UV fluxes. The blue hexagon corresponds to the [C II] upper limit of MACS0647-JD with based in the most sensitive setup and the star formation rate estimated from the UV fluxes. The red star corresponds to the LAE detected with ALMA at $z \sim 4.7$ (Carilli et al., 2013). The black triangle corresponds to the upper limit of the [C II] emission found for HCM-6A by Kanekar et al. (2013). The black diamond corresponds to the upper limit of the [C II] emission found for Himiko by Ouchi et al. (2013).

metallicity was set to solar to have a conservative estimation of the [C II] emission. The simulation does not include the emission from PDRs and should be seen as a lower limit. In Fig. 2.8, we show the [C II] emission produced by the three modeled phases, cold neutral medium (CNM), warm neutral medium (WNM) and the ionized medium. Most of the [C II] emission comes from the CNM ($\sim 50\%$), the rest is coming from the WNM ($\sim 20\%$) and from the ionized medium ($\sim 30\%$). For comparison, in Himiko, 95% of the emission is produced in the CNM and the rest in the WNM. No emission from the ionized medium was modeled in the simulation of Himiko (Vallini et al., 2013). We can also see in the emission that the FWHM of the main peak is ~ 50 km s^{-1}, just as expected.

In Fig. 2.9, we present the integrated flux of [C II] for a different combination of metallicities and stellar population ages. This shows a strong dependency on the metallicity, which is expected, since it is treated linearly with the abundance of [C II] in the gas. The second main feature of this results is the dependency with the stellar population age. Here we assumed a continuum star formation rate of 20 $M_{\odot} yr^{-1}$, for the older stellar populations there is a higher amount of heating photons coming from the UV part of the spectrum. This is a result of using a continuum star formation mode, for a given SFR, older populations have more time generating young UV emitting stars. These extra heating photons avoid the cooling of the gas, which decrease the amount of gas in the cold neutral medium, where most of the [C II] emission is produced.

2.4.7 Spectral Resolution

For a Gaussian emission line, with a FWHM of 50 km s^{-1} observed at a channel resolution of 200 km s^{-1}, emission lines will be significantly diluted. In the best case scenario of the line falling completely in one channel, we will recover 38% of the peak flux density of the line. This suggests to carry out observations a sufficiently high spectral resolution. E.g. with a line of FWHM of 50 km s^{-1} and a channel resolution of 10 km s^{-1}, we expect to recover 97% of the peak flux density of the line.

2.4.8 Atomic Mass Estimation

We use Equation 1 from (Hailey-Dunsheath et al., 2010) to give rough upper limits to the atomic mass associated with PDRs in our targets (Assuming all [C II] would arise from PDRs). As approach to the PDRs conditions we use the result of Vallini et al. (2013) for the temperature and density in the CNM of Himiko, $n = 5 \times 10^4$ cm^{-3} and T=250 K. Using our upper limits for [C II] we obtain the following upper limits to the atomic mass: For IOK-1 $M_{\rm HI} \lesssim 2 \times 10^8 M_{\odot}$, for SDF J132415.7+273058 $M_{\rm HI} \lesssim 4 \times 10^8 M_{\odot}$, for

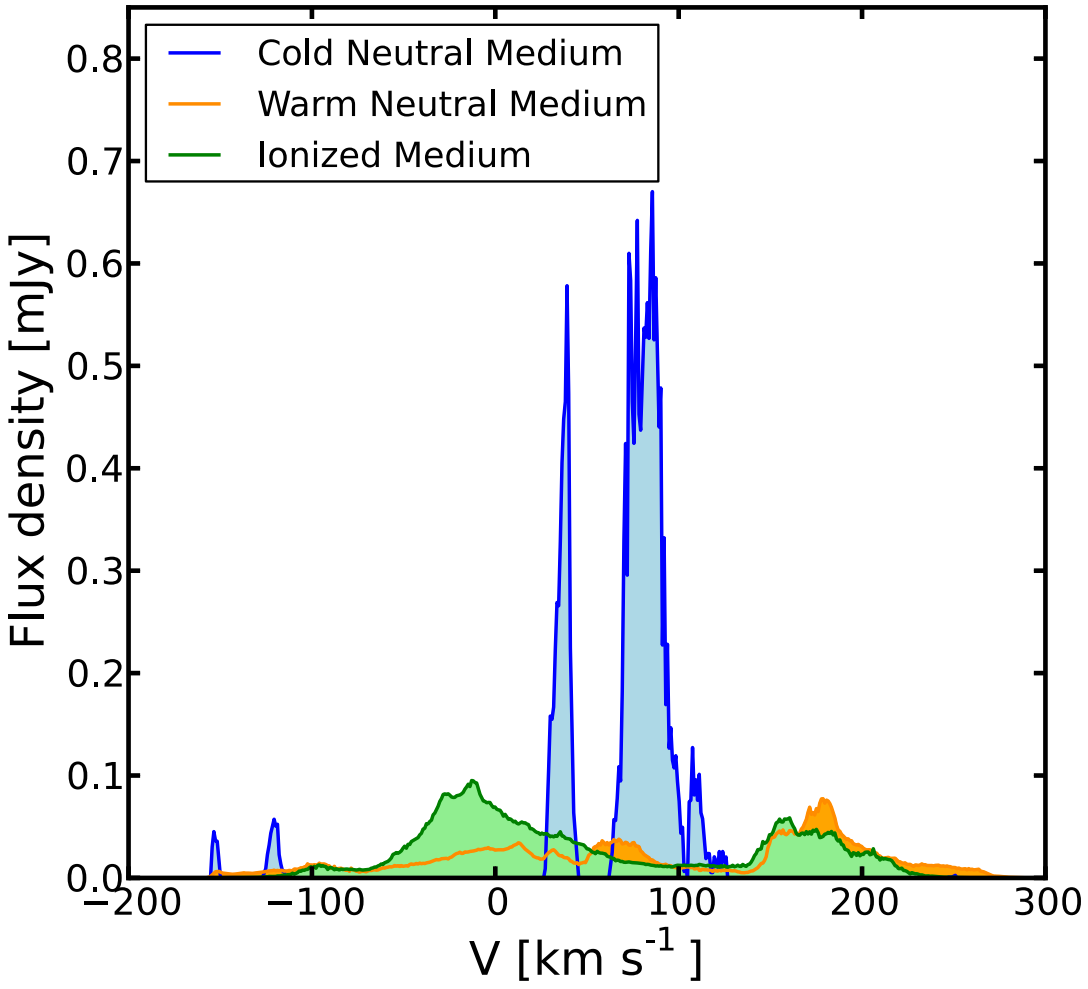

Figure 2.8 Simulated [C II] spectrum of a galaxy similar to IOK-1 at $z \sim 7$. The parameters set for this simulation were a SFR of $20 M_{\odot} yr^{-1}$, and stellar population age of 10 Myr and a solar metallicity. The blue spectrum corresponds to the emission produced in the cold neutral medium, the orange spectrum corresponds to the emission produced in the warm neutral medium and the green spectrum corresponds to the emission produced in the ionized medium. The main peak (at ~ 80 km s^{-1}) of the cold neutral medium has a FWHM of ~ 50 km s^{-1}. For more details on the simulations of [C II] emission in high redshift galaxies see Vallini et al. (2013).

SDF J132408.3+271543 $M_{\rm HI} \lesssim 1 \times 10^9 M_{\odot}$ and for MACS0647-JD $M_{\rm HI} \lesssim 6 \times 10^7 M_{\odot}$. Assuming that the mass of atomic gas is similar to the mass of molecular gas, we can compare our upper limits with the measurements of similar galaxies at lower redshift.

The only molecular gas masses measured in high redshift UV-selected star-forming galaxies come from the detection of CO transition lines in lensed LBGs. The measured values are, $\sim 4 \times 10^8 M_{\odot}$, $\sim 9 \times 10^8 M_{\odot}$ and $\sim 1 \times 10^9 M_{\odot}$ for MS 1512–cB58 ($z = 2.73$), the cosmic eye ($z = 3.07$) and MS1358–arc ($z = 4.9$) respectively (Coppin et al., 2007; Livermore et al., 2012; Riechers et al., 2010). Our upper limits for the LAEs are similar to

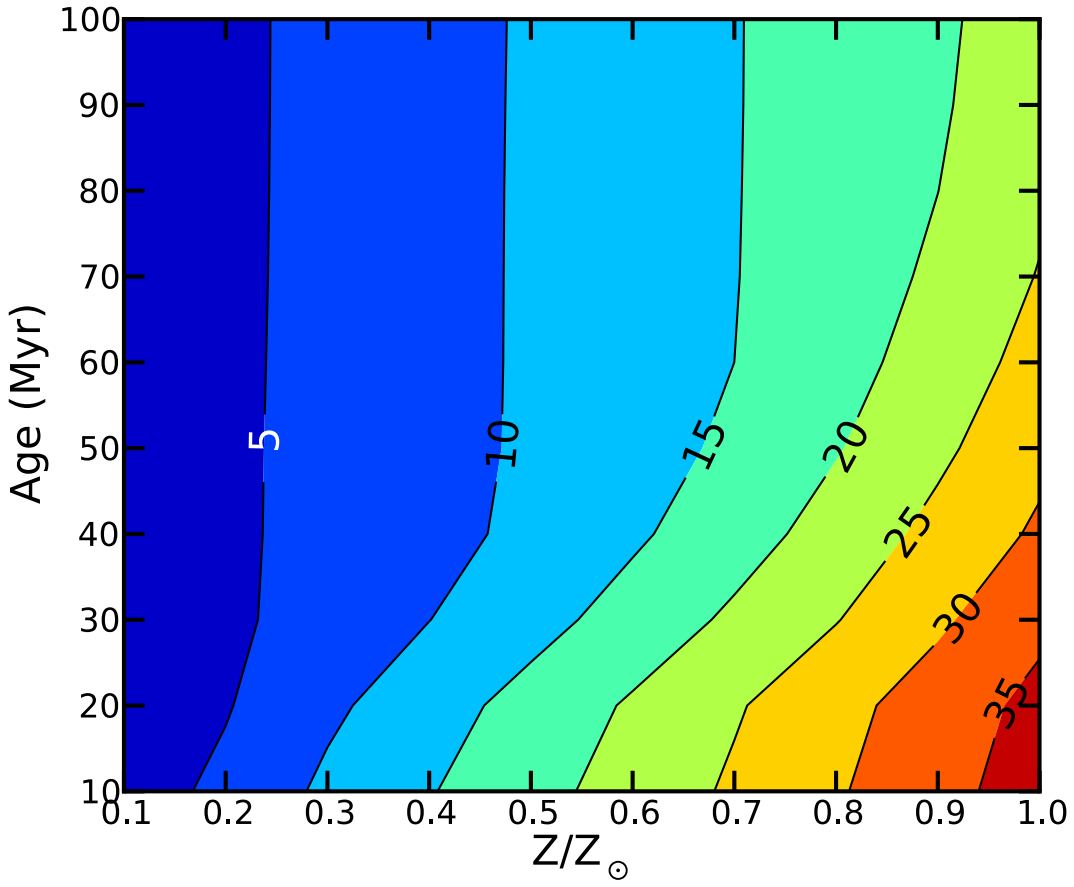

Figure 2.9 Contour plot of the integrated [C II] flux of IOK-1 in mJy km s^{-1} for different simulation conditions. As comparison, our upper limit for integrated flux of IOK-1 is 175 mJy km s^{-1}. The two independent parameters are the stellar population age and the metallicity of the gas. The flux is integrated over the whole area of the cube and in a channel resolution of 500 km s^{-1} around the peak of the emission. The integrated flux is a conservative upper limit for the different parameters. We can see from the contour plot that the [C II] emission is very sensitive to the metallicity of the galaxy, and in a less significant way to the age of the stellar population. The different ages correspond to a different amount of heating photons coming from the young stars, which is critical for the cooling of the gas.

the values estimated for the observed LBGs. For MACS0647-JD our upper limit for the molecular mass is at least 8× lower than in the observed LBGs.

Using the UV-SFR relation we can estimate the gas depletion timescales for our targets, assuming $\tau_{\rm dep} = M_{\rm gas}/{\rm SFR}_{\rm UV}$. We estimate upper limits for the depletion time of $\lesssim$ 8Myr, $\lesssim$ 11Myr and $\lesssim$ 66Myr for IOK-1, SDF J132415.7+273058 and SDF J132408.3+271543 respectively. For MACS0647-JD the depletion time is $\lesssim$ 60Myr. The estimated depletion times for the observed lower redshift lensed LBGs are within the range of $\sim 7 - 24$ Myr, similar to our upper limits. The depletion times for the LAEs are consistent with the ages estimated for the young population of LAEs at $z \sim 4.5$ of < 15 Myr found by Finkelstein et al. (2009) and to the simulated LAEs at ~ 3.1 with

ages < 100 Myr (Shimizu et al., 2011). The depletion times of the LBGs are consistent with the LBG-phase predicted duration of $20 - 60$ Myr (González et al., 2012).

Saintonge et al. (2013) presented molecular gas masses and depletion timescales for a sample of lensed star forming galaxies at $z = 1.4 - 3.1$. The range of measured molecular gas masses is $5.6 \times 10^9 - 4 \times 10^{11} \mathrm{M}_\odot$ and of depletion timescales is $127 - 1089$ Myr. The longer depletion timescales measured for the lower-z sources could indicate that they experience less 'extreme' bursts of star formation in comparison to our $z > 6.5$ sample. Although, assuming a higher molecular-to-atomic gas ratio (of at least 5) would put our upper limits within the values measured by Saintonge et al. (2013).

Chapter 3

Search for [C II] emission in a normal star-forming lensed galaxy at the end of the reionization epoch.

3.1 Introduction

We are beginning the exploration of the faint normal star-forming galaxies population at high redshift. We refer to normal star-forming galaxies as those galaxies that follow the relation between star formation rate (SFR) ans stellar mass found up to $z \sim 2$ (Daddi et al., 2007; Elbaz et al., 2007; Noeske et al., 2007). Generally, these galaxies have SFR $\lesssim 100 M_{\odot} yr^{-1}$ and they dominate the star formation density in the universe, at least at $z \sim 2$(Rodighiero et al., 2011). The fact that the peak of the universe star formation density is at $z \sim 2$ and that the star formation process is dominated by these type of galaxies, makes important the study of them in detail. Until now, most of our knowledge of high redshift normal star-forming galaxies come from the observation of the UV-optical emission and the study of stars, star formation and ionized gas. We need to study the interstellar medium (ISM) and cool gas, which are the fuel of star formation (Carilli and Walter, 2013, and references therein).

Two complementary approaches have been taken to study the cold gas in galaxies at high redshift. First, the observation of the dust emission can reveal the amount of dust present in the galaxies and give indication of the obscured star formation and the dust attenuation present in the optical observations. Secondly, the study of emission lines

produced in the interstellar medium (ISM) can reveal physical properties as density, temperature, radiation intensity and the amount of molecular gas available for star formation (Carilli and Walter, 2013, and references therein).

These methods have been used to study normal star-forming galaxies at high redshift since more than 10 years ago. Chapman et al. (2000) detected a Lyman-break galaxy (LBG) at 450μm and 850μm using the bolometric array SCUBA revealing a real star formation rate (SFR) ten times higher than the one estimated from the UV observations. Peacock et al. (2000) showed that LBGs in the *Hubble Deep Field* (HDF) with the highest UV-SFR ($\sim 1 M_{\odot} yr^{-1}$) are detected statistically at 850μm, indicating that the total star formation activity is on average six times higher than the one estimated from the UV observations. A big step forward was taken when Baker et al. (2001) detected the 1.2 mm dust continuum emission in the gravitationally lensed LBG MS $1512+36-$cB58, a system with an intrinsic SFR$\sim 24 M_{\odot} yr^{-1}$ (Baker et al., 2004).

Several posterior searches for continuum dust emission in $z \sim 5$ Lyα emitters (LAE) and LBGs in well studied fields resulted in non detections (Carilli et al., 2007; Davies et al., 2012; Stanway et al., 2010). Davies et al. (2013) investigated the far-infrared (FIR) emission in LBGs $z \sim 3$ using the Large Apex Bolometer Camara (LABOCA) in the Extended Chandra Deep Fields South (ECDFS) and detected the composite emission of the three samples of galaxies at 870μm. Together with *Herschel* SPIRE observations of the field, they were able to do spectral energy distribution (SED) fitting of the galaxies and reached to the conclusion that, although their sample falls in the main sequence relation, the detected subsample likely represent the high obscuration end of the LBG population at that epoch. These results show that the search for dust continuum emission in normal star-forming galaxies is still bias to very obscured systems.

In the case that the observations of faint galaxy population are restricted by the current instrumentation, the best approach is to use the gravitational lensing to study, at least in a small numbers, these elusive targets. With this in mind, Sklias et al. (2014) studied 7 lensed galaxies as part of the *Herschel Lensing Survey* and they were able to study the physical properties of individual normal star-forming galaxies between $z \sim 1.5 - 3$ up to a factor ~ 10 fainter that the search achieved with blank field observations. The importance of these studies is that they are able to extend the range of dust mass down to $\sim 2 \times 10^7 M_{\odot}$, lower than previous studies at the same redshift. Recently, Boone et al. (2013) presented the 870μm LABOCA detection of a possible lensed dusty normal star-forming galaxy at $z = 6.1$. Although the possibility of this detection being a substructure of the Sunyaev-Zel'dovich effect produced by the lensing galaxy cluster is not rejected, the possibility of the emission being related to the lensed galaxy makes the study of such type of galaxy at the end of the reionization epoch unique.

As stated above, the second approach to study high redshift galaxies is by the observation of FIR emission lines. The most observed emission lines are the different transition of the molecule of CO, such lines have been observed in many galaxies at $z > 1$, see Carilli and Walter (2013) for a complete list of CO detections. As expected, these lines were the first to be targeted to be observed in normal star-forming galaxies in lensed and not lensed galaxies, resulting in several detections (Baker et al., 2004; Coppin et al., 2007; Daddi et al., 2010; Tacconi et al., 2013). Due to the low luminosity of the CO emission lines, other emission lines have been focused to study these type of galaxies at high redshift. The main emission line that has been searched in high redshift galaxies is [C II] ($^2P_{3/2} \rightarrow {}^2P_{1/2}$), one of the brightest FIR emission lines, accounting for up to 1% of the FIR luminosity in some galaxies (Malhotra et al., 2001). This line has been observed in local and high redshift galaxies up to $z = 7.1$ (Carilli et al., 2013; Cox et al., 2011; De Breuck et al., 2011; Gallerani et al., 2012; Hailey-Dunsheath et al., 2010; Iono et al., 2006; Ivison et al., 2010; Maiolino et al., 2009, 2005; Riechers et al., 2013; Stacey et al., 2010; Valtchanov et al., 2011; Venemans et al., 2012; Wagg et al., 2010, 2012; Walter et al., 2012a, 2009; Wang et al., 2013; Willott et al., 2013). Most of the high-z detections were for quasars and infrared-luminous starbursts. Many efforts have been made in the search of [C II] in galaxies with star formation rate (SFR) less than 100 $M_\odot yr^{-1}$ at $z > 4$. Until now, most of the searches have resulted in non-detections (González-López et al., 2014; Kanekar et al., 2013; Ota et al., 2014; Ouchi et al., 2013; Schaerer et al., 2014; Walter et al., 2012b). The only detections are of a LAE at $z = 4.7$ (Carilli et al., 2013), of a triplet of LBGs in a protocluster associated with the submillimeter galaxy (SMG) AzTEC-3 at $z = 5.3$ (Riechers et al., 2014). Both detections were made in systems where very bright and starbursting galaxies are surrounded by these normal star-forming galaxies. No continuum was detected in the galaxies, suggesting that these galaxies are significantly metal-enriched, but not heavily dust-obscured. The fact that most of the non-detections correspond to LAEs at $z > 6.5$ with very strong Lyman-α emission open the possibility that those galaxies correspond to a different population than those LAE and LBG at $z < 6$, although, more observations are needed to confirm that hypothesis as pointed out by Ota et al. (2014).

In complement to [C II] , the lines [N II] and [O III] produced in the ionized medium are starting to be observed in submillimeter galaxies (SMG) and starbursting galaxies at high redshift (Combes et al., 2012; Decarli et al., 2014, 2012; Ferkinhoff et al., 2011, 2010; Nagao et al., 2012). Of particular importance is the detection of [N II] in the transition $^3P_1 \rightarrow {}^3P_0$ in the LAE at z4.7 in Decarli et al. (2014). The ratio [C II] /[N II] $\sim 1-2$ in the LAEs suggest that, at least in these sources, most of the [C II] emission is associated with the ionized medium (H II regions) rather than the neutral medium (photon-dominated regions). These results show the importance of observing several emission lines in these

galaxies to constraint the physical properties of the ISM in high redshift galaxies and also that emission lines produced in the ionized medium rise as a good alternative to [C II] to be observed in normal star-forming galaxies at high redshift.

Here we present the result of a search for [C II] in a multiple imaged lensed LBG with $z_{\rm phot} = 6.18^{+0.05}_{-0.07}$ discovered behind the galaxy cluster MACS0329.6-0211 (Zitrin et al., 2012), hereafter MACS0329-iD. In Sect. 2 we describe the target selection and observations. The data is shown in Sect. 3 together with some implications and analysis in Sect. 4. A summary of the paper is presented in Sect. 5. Throughout this paper we use a Λ-Cold Dark Matter cosmology with $H_0 = 70$ km s^{-1} Mpc^{-1}, $\Omega_\Lambda = 0.7$ and $\Omega_{\rm m} = 0.3$.

3.2 Observations

3.2.1 Target Selection

The galaxy MACS0329-iD was discovered as a high-redshift dropout as part of The Cluster Lensing And Supernova survey with Hubble (CLASH) (Postman et al., 2012). The galaxy is lensed into four images by the galaxy cluster MACSJ0329.6-0211 ($z_l = 0.45$), the mass model for the cluster shows that the galaxy has a total magnification across the multiple images of $\mu \approx 37$ (Zitrin et al., 2012). The combination of the 4 images photometry yields a secure photometric redshift of $z_{\rm phot} = 6.18^{0.05}_{0.07}$ (95% confidence level). The best-fit to the spectral energy distribution (SED) of HST and Spitzer photometry results in a demagnified stellar mass of $\sim 10^9$ M$_\odot$, low dust content ($A_V \sim 0.1$ mag), a SFR-weighted age of ~ 180 Myr and an intrinsic SFR of ~ 3.2 M$_\odot$yr^{-1}. The stellar metallicity is not well constrained, but the distribution of best-fit models has a median of Z ~ 0.5Z$_\odot$, being Z ~ 0.2Z$_\odot$ the one with the highest probability.

The SED fit shows that this galaxy can be a very evolved galaxy at the end of the reionization epoch, and with a very well constraint photometric redshift, small enough to do a search for [C II] in the 2σ range of the photometric redshift in just one tuning with the Atacama Large Millimeter/sub-millimeter Array (ALMA).

3.2.2 ALMA observations

The galaxy MACS0329-iD was observed in March 23 2014 as part of the ALMA cycle-1 early science. To cover the 2σ range in the photometric redshift, we positioned 4 spectral windows (SPW) in the upper sideband, covering the frequency range of 262.6-267.5 GHz, mapping the [C II] emission line between $z = 6.105 - 6.237$, more extended

than the photometric redshift range of $z_{\rm phot} = 6.11 - 6.23$ that is estimated by the photo-z. The correlator was setup to use the Frequency Division Modes (FDM) with an averaging channel factor of N=16, resulting in a channel resolution of 7.812 MHz ($\approx$ 8.85 km s^{-1}). We used the averaging channels feature to have a higher spectral resolution than using Time Division Mode (TDM) but still having a low data rate. The total on source integration time was of 10 minutes using 38 antennas (some of them were flagged in the reduction process).

The observations were reduced using the Common Astronomy Software Applications (CASA). As passband calibrator was used J0457-2324, and as phase calibrator was used J0339-0146. As flux calibrator was used Callisto. The flux calibration resulted in an error of 4% in the phase calibrator flux. The images were produced using 'natural' weighting.

The galaxy was observed in low elevation, resulting in a very elongated synthesized beam. Because of this, for the clean task we used the uv-taper option to select the short baselines to obtain a less elliptical beam. In the 'nominal' resolution, with no uv-tapering, the resulting synthesized beam: $1.85'' \times 0.55''$. When we request for a uv-taper (requested: $1.5''$), hereafter 'extended' resolution, a resulting synthesized beam of $2.23'' \times 1.26''$ is obtained. The continuum depth reached are of 121.3 μJy b^{-1} for the nominal resolution and 176.5 μJy b^{-1} for the extended resolution. For the 7.812 MHz channels, a sensitivity of 2 mJy b^{-1} is reached in the central channels with the nominal resolution and 3 mJy b^{-1} for the extended resolution. All the shown maps are corrected by the primary beam (PB).

3.3 Result

3.3.1 Continuum Emission

In the continuum map of Fig. 3.1, where no uv-tapering was used, there are two positive signal that have significance higher than any negative signal. The one with the highest signal-to-noise is outside the half-power beam width (HPBW) and there is no optical counterpart, which do not necessary means that it is not real rather that it is more difficult to find the redshift of the source.

The second detection, and most reliable, is detected with 3.3σ (Fig. 3.13), with $S_{1,1\rm mm} = 550 \pm 167$ μJy. The galaxy is detected in the observations made as part of the HST CLASH survey (Postman et al., 2012). The photometric redshift of the galaxy is $z_{\rm phot} = 3.54^{+0.14}_{-0.19}$ (1σ errors), we can see the in probability density function (pdf) for

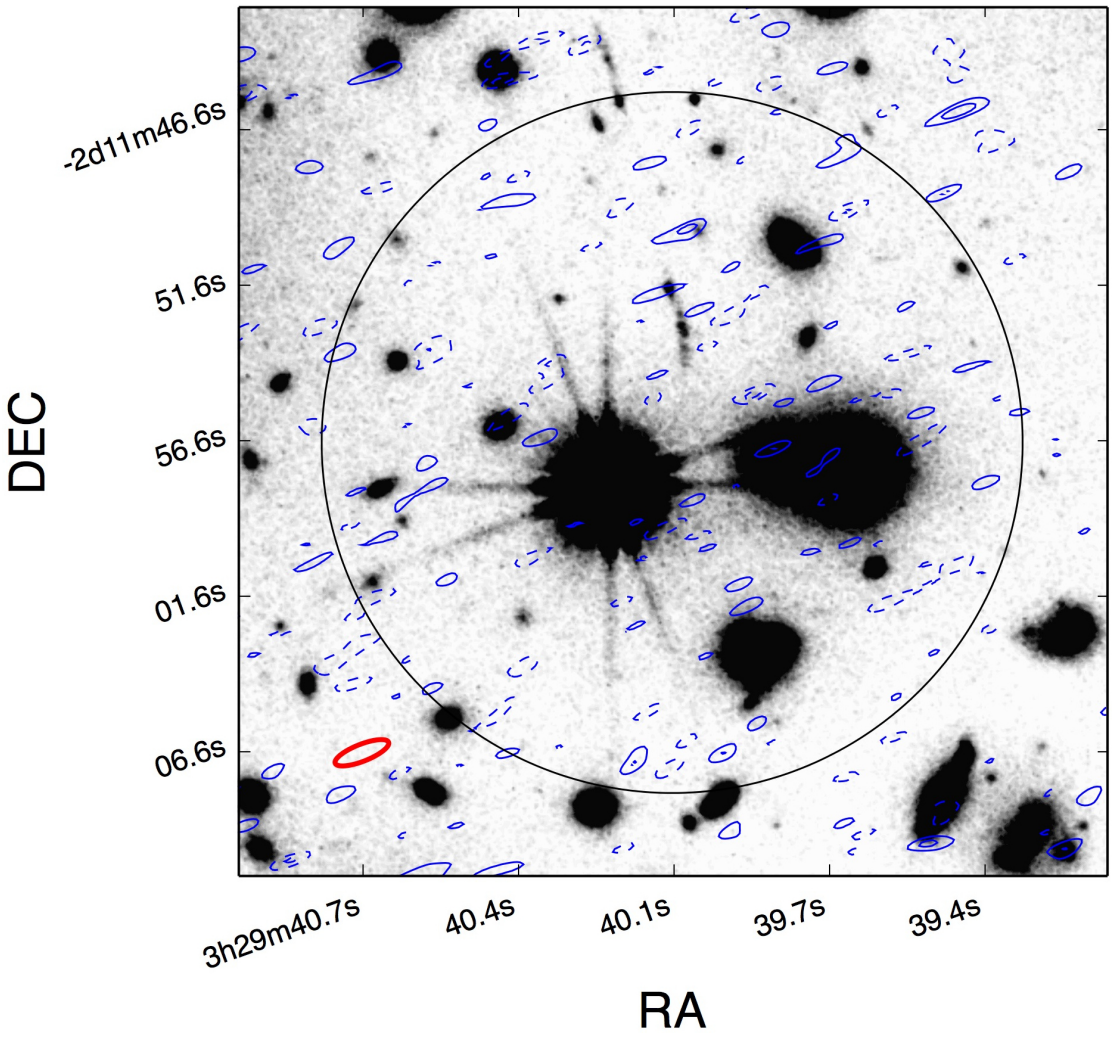

Figure 3.1 Continuum map of one pointing in the galaxy cluster MACS0329. The synthesized beam is of $1.85'' \times 0.55''$. The contour levels are in step of 1σ, starting in $-2\sigma, 2\sigma$, with $\sigma = 121.3$ μJy b^{-1} in the phase center. The contours are corrected by the primary beam sensitivity. Two detections are found with $sn > 3\sigma$ and no negative detection of similar significance. One of them is outside the HPBW and no optical counterpart is found. The second detection corresponds to a lensed galaxy at $z \sim 3.5$.

the photometric redshift that there is a secondary peak around $z \sim 0.5$. That secondary peak is small in comparison to the one at higher redshift. The ALMA detection puts a prior for the galaxy being at high redshift. In the search for continuum emission in the galaxy MACS0329-iD, the continuum maps for the two angular resolutions are shown in Fig. 3.2. No continuum emission is detected in either of the lensed images of the galaxy. Although, two peaks of 2σ each are located just in the location of the brightest regions of the lensed image in the bottom (MACS0329-iD2), they are not strong enough to be considered as detection, and they are not observed in the upper image D1. In the right panel, we show red crosses at the position of the brightest region of the galaxy together with the synthesized beam, with the purpose of showing that by combining the emission

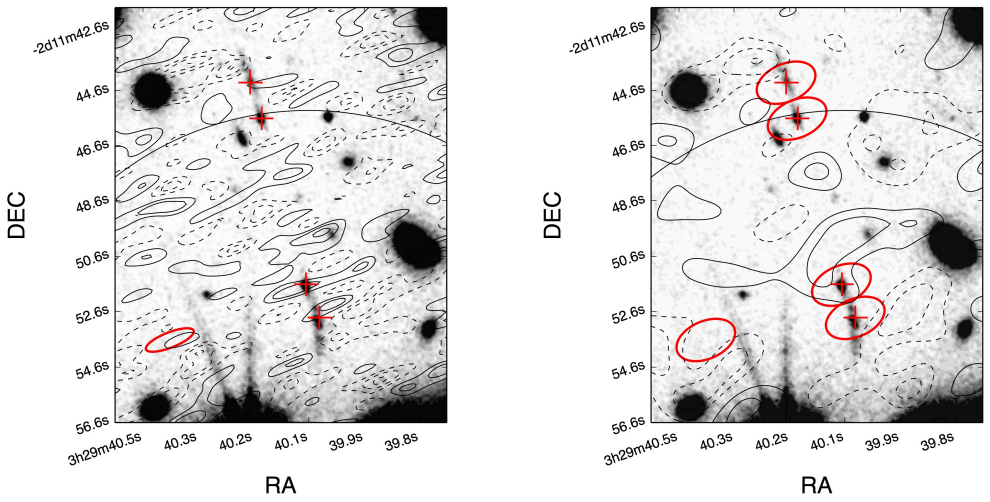

Figure 3.2 Rest-frame 158 μm continuum map of the region around MACS0329-iD. Each contour level represents 1σ steps. Solid contours represent positive signal and dashed contour represent negative signal. The panel to the left shows the nominal resolution and the one in the right shows the extended resolution. In the left panel, the 1σ levels are of 121.3 μJy b^{-1}in the phase center and are corrected by the PB. In the right panel, the 1σ levels are of 176.5 μJy b^{-1}in the phase center and are corrected by the PB as in the left panel. The black solid line represent the ALMA HPBW. The red crosses are the position of the brightest regions of each image of the lensed galaxy. The red ellipse is the synthesized beam, $1.85'' \times 0.55''$ for the left panel and $2.23'' \times 1.26''$ for the right panel.

of the 4 points we can put constrains to the total emission of the galaxy. There is a extended 2σ signal just to the north of the image D2, this is not related to the galaxy, but it is related to the 3σ continuum that can be seen in the left panel. That continuum signal correspond to a lensed galaxy described above. By stacking the continuum emission of the 4 crosses position, no continuum is detected, resulting in a final rms for the continuum non-detection of 0.62 mJy b^{-1} using the extended resolution.

3.3.2 [C II] emission in MACS0329-iD.

For the search of [C II] emission, we combine the signal of the two lensed images as we did for the continuum emission. The final spectrum is the sum of the emission in the position of the brightest region of the lensed images (red crosses in Fig. 3.2). The rms of the spectrum is calculated as the addition in quadrature of the rms (PB corrected) in each position. The rms for the central channels of the spectrum is of 6mJy. The upper lensed image is located just in the edge of the HPBW, where the noise is higher than the one near the phase center.

The signal-to-noise spectra extracted is shown in Fig. 3.3. No clear detection of [C II] is observed in the spectrum, putting a 3σ upper limit of $L_{[CII]} < 3.0 \times 10^7 \times (\mu/29.2)^{-1} L_\odot$,

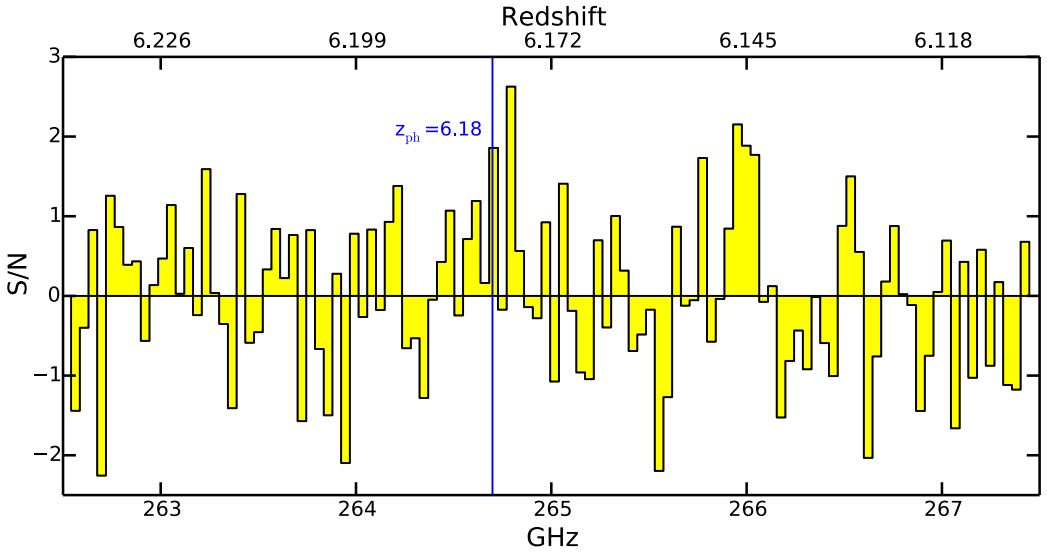

Figure 3.3 Signal-to-noise spectrum of the combination of the two lensed images (D1 and D2) of the galaxy. Using the a channel resolution of 50 km s^{-1} and the extended resolution. The blue line correspond to the photometric redshift of 6.18 estimated for the galaxy. We recall two features that need further study; the channel with a $sn = 2.3$ just to the right of the line that represents the frequency expected for the [C II] emission line for the photometric redshift and what appears to be an emission line at 266 GHz.

despite of that, we will further explore the two features that are observed. It is important to note that we are assuming that the [C II] emission line would fall within the frequencies range observed. The possibility of the systemic redshift being outside the 2σ range allowed by the photometric redshift is not discarded by our observations. A positive signal is detected just to the right of the expected photometric redshift of $z_{\rm phot} \sim 6.18$, the signal has 2.6σ and it is located at a frequency 264.8 GHz. No other positive or negative signal are found with the similar significance. The second feature corresponds to the channels at frequency 266 GHz that appear to resemble an emission line.

More details about these features are in Sec. **??**.

3.4 Discussion.

The discussion about the results will be separated into two parts. In the first part we will analyze the constraints on the emissions from MACS0329-iD and in the second part we will analyze the other detections in the field.

Table 3.1. Summary of Observations and Results for MACS0329-iD

Parameter	MACS0329-iD
Coordinates (J2000) D1	03:29:40.18,–02:11:45.60
Coordinates (J2000) D2	03:29:40.06,–02:11:51.72
μ (D1+D2)	≈ 29.2
Photometric Redshift	$z_{\rm phot} = 6.18^{+0.05}_{-0.07}$
$\sigma_{\rm cont}$ [a]	0.62 [mJy b^{-1}]
UV SFR	~ 3.2 [M$_\odot$yr^{-1}]
ν range	262.6-267.5 [GHz]
L$_{\rm [CII]}$ [b]	$< 3.0 \times 10^7 \times (\mu/29.2)^{-1} L_\odot$
$\nu_{\rm obs}$ [c]	264.8012 ± 0.0023 [GHz]
[CII] Redshift[c]	6.17722 ± 0.00005
L$_{\rm [CII]}$ [c]	$(3.7 \pm 1.0) \times 10^7 \times (\mu/29.2)^{-1} L_\odot$
FWHM[c]	14.6 ± 4.9 [km s^{-1}]
peak of the line[c]	55.4 ± 17.4 [mJy]
L$_{\rm IR}^{\rm N6946,d}$	$< 1.5 \times 10^{11} \times (\mu/29.2)^{-1} [L_\odot]$
SFR (L$_{\rm IR}$)	$< 26.9 \times (\mu/29.2)^{-1}$ [M$_\odot$yr^{-1}]
L$_{\rm FIR}^{\rm N6946,d}$	$< 5.7 \times 10^{10} \times (\mu/29.2)^{-1} [L_\odot]$

Note. — All luminosities upper limits are $3\,\sigma$.
References: Coordinates, magnification, redshift and UV-SFR from Zitrin et al. 2012.
All the luminosities and SFR are corrected by magnification.

[a] 1σ continuum sensitivity at 158μm rest wavelength.

[b] For the case of non detection.

[c] For the tentative detection in Fig. 3.7

[d] 3σ limit based on the SED of NGC 6946 and including the effect of the CMB.

3.4.1 Constrains in MACS0329-iD

3.4.1.1 FIR Continuum.

We use the continuum non-detection to put constraints to the FIR continuum and therefore to the properties of MACS0329-iD. In Fig. 3.4 we show the CLASH photometry and the ALMA upper limit to the FIR continuum. For comparison, the sed of local galaxies scaled to the reddest HST filter are also plotted. The sed of Arp 220, M82, M51 and NGC6946 were extracted from Silva et al. (1998), the sed of the Wolf–Rayet region of the Gamma-Ray Burst GRB980425 was extracted from Michałowski et al. (2009) and the Spiral, dwarfs and Irregulars galaxies were extracted from Dale et al. (2007). For GRB980425WR a $T_{\rm dust}^{z=0} = 92$ K and $\beta = 1.3$ was used (Michałowski et al., 2009). For the other sed the temperature correspond to the ones used in González-López et al. (2014) and Ota et al. (2014).

We used the sed of NGC6946 to estimate the upper limit to the FIR luminosity. We scale the NGC6946 sed to the ALMA upper limit and then integrated between 42.5 and 122.5 μm restframe to estimate the upper limit to the FIR luminosity. We found that $L_{\rm FIR} < 5.7 \times 10^{10} \times (\mu/29.2)^{-1} L_\odot$, after correcting by the magnification of $\mu = 29.2$.

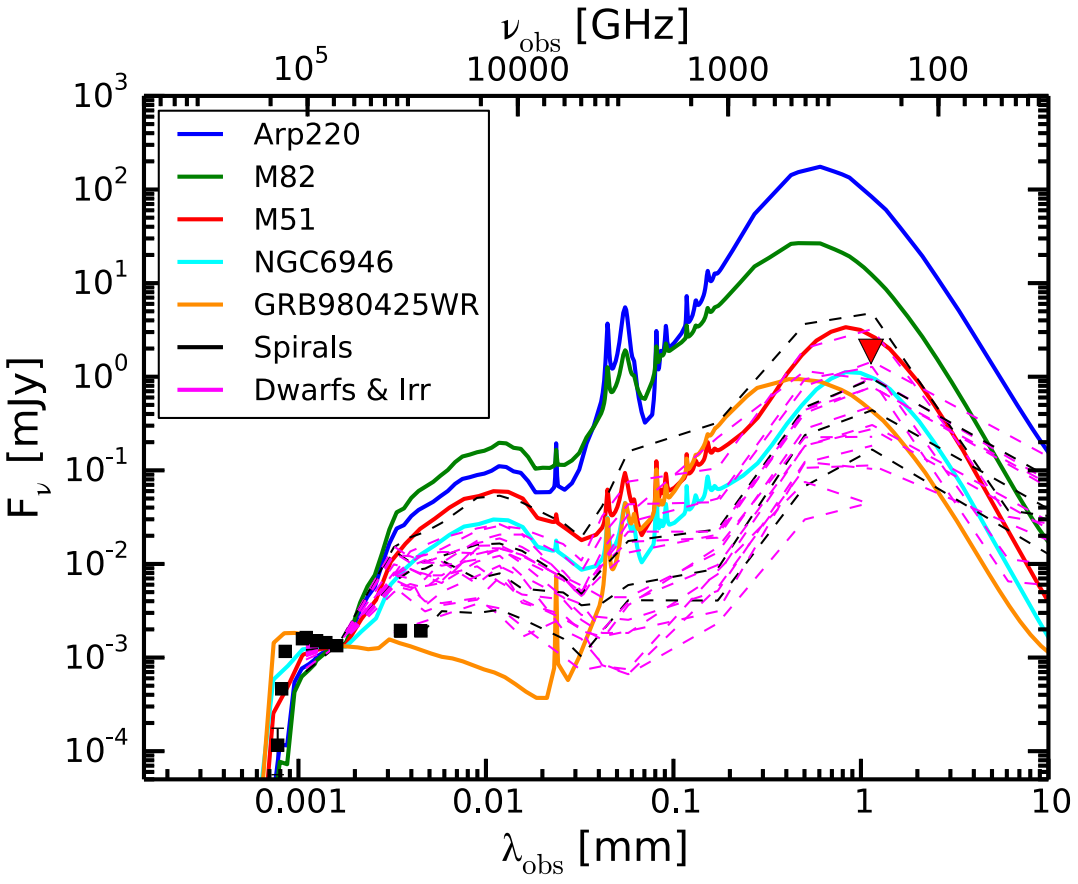

Figure 3.4 Spectral energy distribution of MACS0329-iD together with several templates of local galaxies. The black points represent the HST and Spitzer photometry while the red triangle is the ALMA upper limit to the FIR continuum. All the templates has been corrected by the effect of the CMB following the procedures presented in da Cunha et al. (2013) and extended in González-López et al. (2014). The dashed line correspond to the sed templates of local galaxies.

The IR luminosity is calculated by integrating between 8 and 1000 μm, $L_{\rm IR} < 1.5 \times 10^{11} \times (\mu/29.2)^{-1} L_\odot$.

We note that much more deeper continuum observations will be needed to detect this type of galaxies at this redshift. It is interesting to note that, the Spitzer photometry at 3.6 and 4.5 μm already is rejecting most of the local SED templates. Because of this, we include the SED template of the Wolf-Rayet (WR) region in the galaxy host of GRB980425, one of the closest known GRBs (z=0.0085) (Michałowski et al., 2009). The WR region is where most of the star formation is occurring in the GRB host. its SED is blue in the optical and luminous in the mid-IR, indicating a very hot dust content. Despite of the similitude in the optical, the starbursting nature of the WR region is not shared by MACS0329-iD.

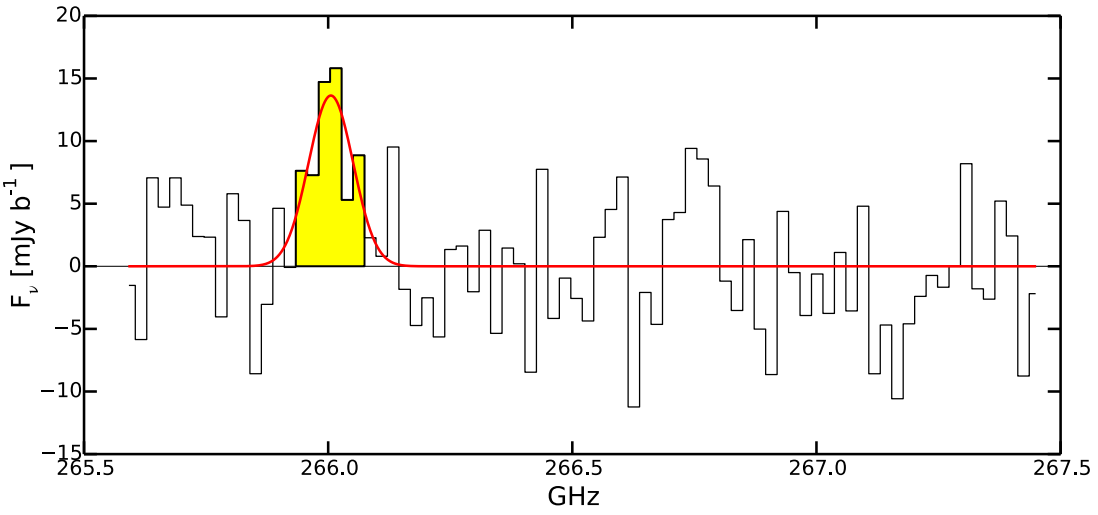

Figure 3.5 Spectrum extracted in the the position of the emission found at 266 GHz in Fig. 3.3 using the a channel resolution of 26.5 km s^{-1} and the extended resolution.

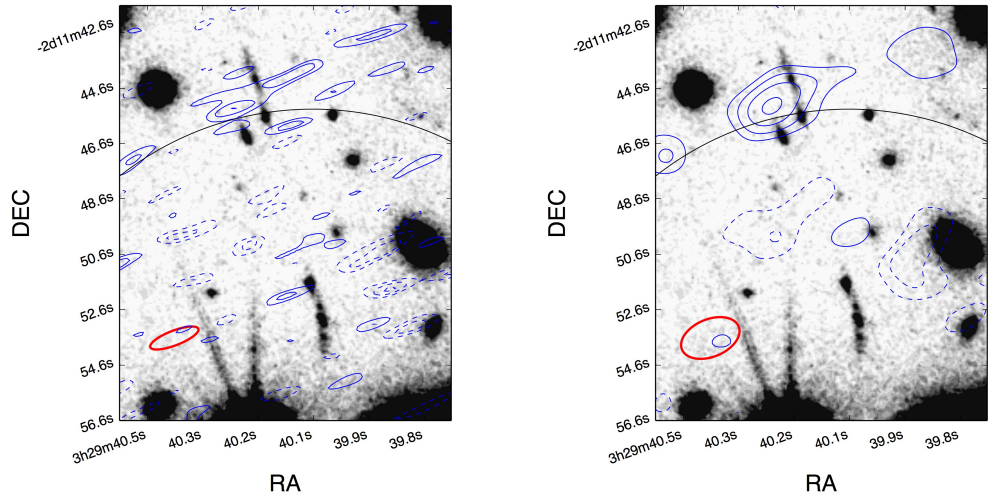

Figure 3.6 Map of the emission associated with the yellow channels in Fig. 3.5 with the two spatial resolutions. The left panel shows the nominal resolution and the right panel shows the extended resolution. Each line corresponds to a 1σ level starting at -2σ and $+2\sigma$. The emission appears to be related to a galaxy near the MACS0329-iD2. The fact that the emission is not observed in MACS0329-iD1 discards the possibility of this emission being [C II] for the MACS0329-iD. The emission in the left panel appear to not be related with any optical detected galaxies, making difficult to associated the possible emission to a galaxy and therefore identifying the emission line.

We can conclude the MACS0329-iD is not a galaxy with a large amount of dust, and that has a similar SED to local spiral and dwarfs galaxies.

3.4.1.2 Constraints on the [C II] emission line.

We will explore the two features observed in the spectrum presented in Fig. 3.3. For the feature around 266 GHz, we found that when integrating over the channels around 266 GHz the emission is not centered in MACS0329-iD. Whe plot the spectrum extracted at the position of the feature emitting at 266 GHz in Fig. 3.5, for the plot we used 1 spectral window and combining three channels, resulting in a channel width of $\approx 26.5\,\mathrm{km\,s^{-1}}$. The red line corresponds to the fit of a gaussian function, resulting in a peak of 13.6 ± 3.3 mJy $\mathrm{b^{-1}}$, a central frequency of 266.01 ± 0.01 GHz and a FWHM of $120.1 \pm 33.2\,\mathrm{km\,s^{-1}}$. In Fig. 3.6 we show the integrated maps over the yellow channelos of Fig. 3.5, in the left panel we show the nominal resolution and in the right panel the extended resolution. In the right panel we see that the emission could be coming from the MACS0329-iD2, but the fact that the emission is not found in MACS0329-iD1 discards the possibility of the emission being associated with MACS0329-iD. The second option is that the emission is related to the galaxy just to the left of MACS0329-iD2, altought that possibility is allowed by the emission in the right panel, the left panel shows that the emission is centered to the north of that galaxy. If this emission is real, we will not be able to associate it to a galaxy detected in the optical.

The second feature corresponds to a channel with the highest signal-to-noise in the $50\,\mathrm{km\,s^{-1}}$ channels. In Fig. 3.7 we see the frequencies where the channels is but this time with a spectral resolution given by the default channel width of $\approx 8.85\,\mathrm{km\,s^{-1}}$. There is a signal that could correspond to the [C II] emission of the galaxy. We will explore the possibility of this positive emission being just a product of random noise. When we stack the emission of the 4 red crosses in Fig. 3.2 and integrate in the velocity space of the 4 channels marked in Fig. 3.7 we obtain the map in Fig. 3.9, which would be the [C II] emission associated to the images D1 and D2 of MACS0329-iD. The peak of the emission has a signal-to-noise of 3.64σ. To estimate what are the odds of finding a positive signal with this significance we use the same procedure to map Fig. 3.9 but using 4 random position and a random frequency as center for a 5 channels emission line. After performing 10^6 iteration, we find that in 0.026% of the times we observed a signal-to-noise equal or higher than the observed of 3.64σ. When we do the same experiment, but just using the 3 central channels, which carry out most of the signal associated with the line, the observed significance is of 3.78σ, and the result of performing 10^6 iterations is of 0.014% of the times observing a signal-to-noise equal or higher than the observed of 3.78σ for the 3 channels. We explore the scenario where the proximity of the regions used to search for the emission could be causing some correlation that could increase the possibility of getting a fake emission line. We did the same experiment that before but this time fixing the distance between the two closest positions to the distance

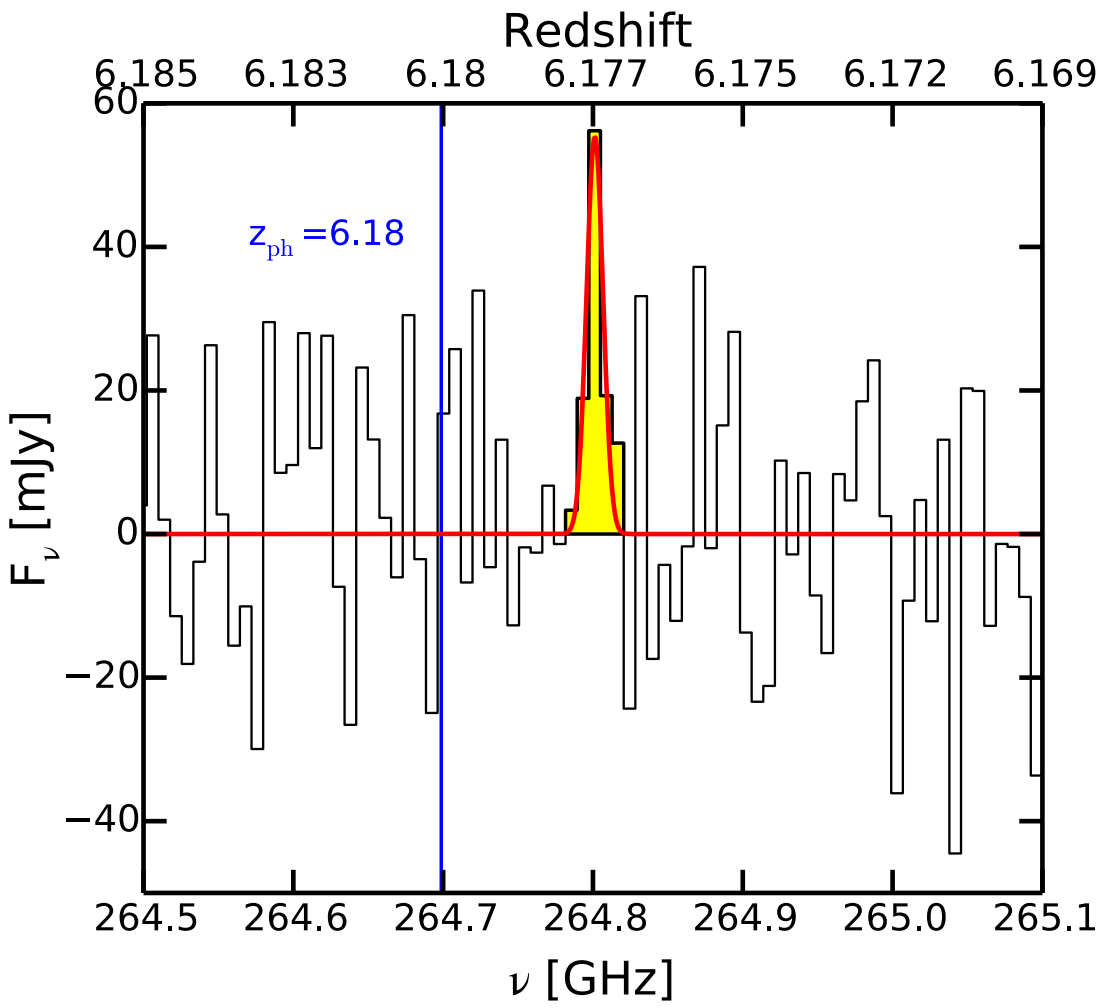

Figure 3.7 Zoom in to the positive signal found in Fig. 3.3 but showing the flux density units instead of signal-to-noise. The red line correspond to a gaussian function adjusted to the data. The best-fit parameters of the gaussian function are in Table 3.1.

between the brightest regions in each of the lensed images. We obtain fraction values similar to the ones for the 4 random positions, indicating that by using two position per lensed image do not increase the chances of the positive emission being fake. From the total frequency coverage of the observations we obtain 623 channels with native spectral resolution. When we combine 5 channels as for our tentative emission line we obtain 124 channels. Assuming that the probability of obtaining a signal-to-noise of our tentative line is of 0.026% per channel, the total probability of obtaining 1 signal as the observed in any of the observed frequencies is of $\approx 3.2\%$.

We find that the possibility of the positive emission shown in Fig. 3.7 being a product of just random association is not small enough for us to consider the line as a real detection of [C II]. From hereafter we will considered our observations as a non detection of [C II] with a tentative detection corresponding to this feature.

When we fit a gaussian function to the possible emission line, we find an amplitude of 55.4±17.4 mJy, a central frequency of 264.8012±0.0023 GHz, a full width half maximum (FWHM) of 14.6 ± 4.9 km s^{-1}, resulting in a possible z = 6.17722 ± 0.00005. The spec-z of 6.17722 ± 0.00005 is at less than 0.1σ from the photometric redshift of $z_{\rm phot} = 6.18$. We believe that the closeness of our tentative line and the expected frequency for the photometric redshift increases the odds that this feature could correspond to [C II] emission. The probability of having the measured signal-to-noise so close to the photometric redshift is of $< 0.2\%$. Another indicator that this feature could be in fact [C II] coming from the galaxy is that it is emitted in both images D1 and D2 as we can see in Fig 3.8, where the 2d map is plotted for the 3 central channels of the tentative emission line.

To check whether the width and the amplitude of the emission line are consistent with galaxies at the end of the reionization epoch we used the simulations of [C II] emission in high redshift galaxies described in Vallini et al. (2013). This models present [C II] emission produced in ionized and neutral medium. One of the main result of Vallini et al. (2013), is that, without including the emission from photo-dissociation (a.k.a. photon-dominated) regions (PDRs) most of the emission is produced in the cold neutral medium (CNM), and in less intensity in the warm neutral medium (WNM). Secondly, the CNM emission is primary produced in small clumps of cold dust, where the shielding is enough to prevent the heating of the gas by the UV radiation coming from hot stars. The [C II] emission is dominated by the several very narrow emission lines associated to each of the clumps.

Using that model, we use the simulation of the [C II] emission in a galaxy at similar redshift as comparison to our observations (Models delivered by Livia Vallini, private communication). For the simulation, we use a SFR= 3.2 $M_{\odot}$yr^{-1}, a magnification of $\mu = 29.2$, and a metallicity of $0.2Z_{\odot}$. We use a metallicity of $0.2Z_{\odot}$ instead of the median value of $0.5Z_{\odot}$ estimated by Zitrin et al. (2012) because the former is the one with the highest probability in the SED fitting and a lower metallicity is favored at this redshift.

Figure 3.10 show the simulated [C II] emission, we will compare our observation with the narrow emission that has the highest peak. The emission is binned to match the spectral resolution of our observations (~ 8.85 km s^{-1}), the fit of a gaussian function result in a line width of ~ 30 km s^{-1}, two times the value of the FWHM we found for our possible emission line. Such narrow line would indicate that the line could be produced in one of the clumps mentioned in Vallini et al. (2013). The fact that the peak of the line is at a flux density similar to the one observed could be interpret as that the metallicity of the galaxy is similar to the one proposed by the SED fitting of the optical photometry.

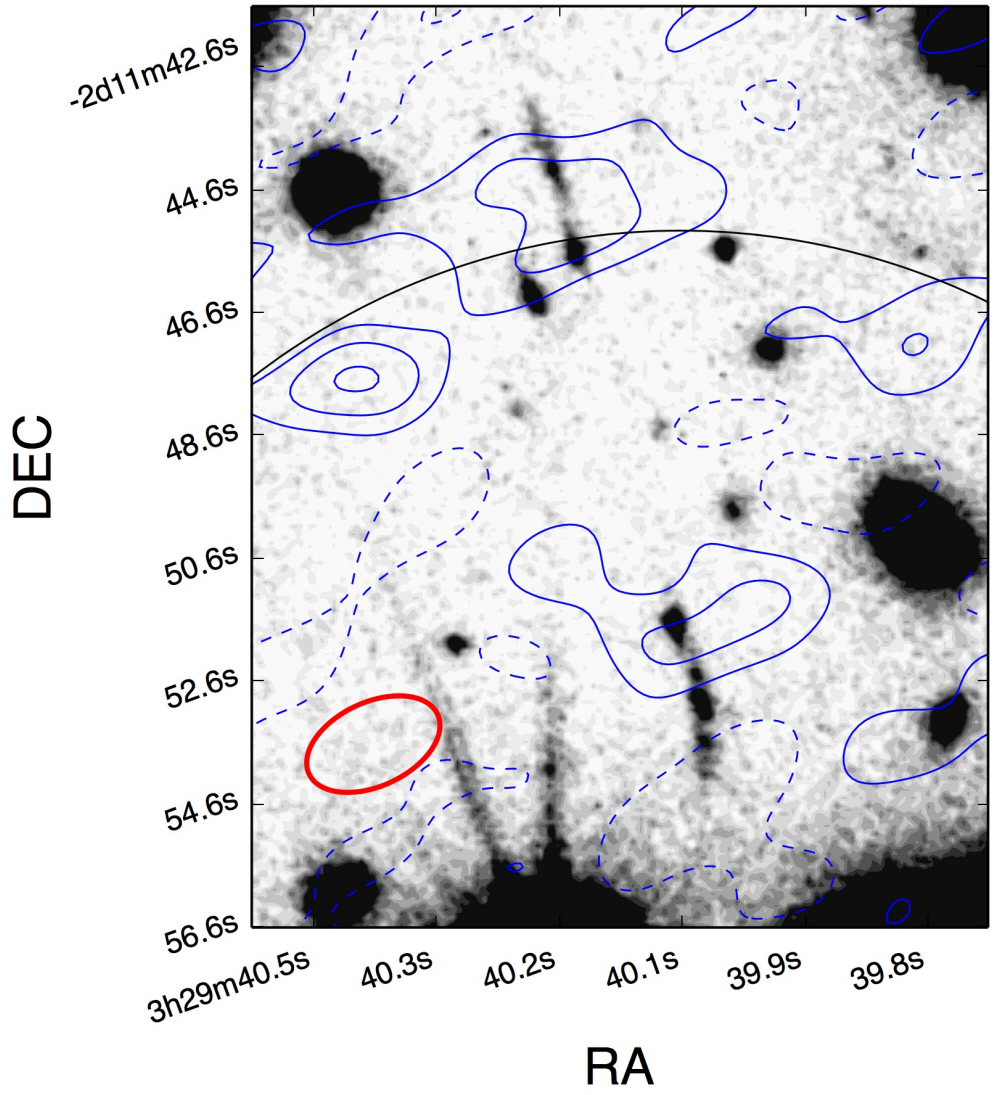

Figure 3.8 Map of the three central channels of the tentative [C II] emission shown in Fig. 3.7. The contour levels are in step of 1σ, starting in $-1\sigma, 1\sigma$. The tentative emission line is observed, at least in low signal-to-noise, in both lensed images D1 and D2, supporting the hypothesis that this emission could correspond to the [C II] in MACS0329-iD.

We believe that the characteristics of the observed line; frequency, width and amplitude, support the assumption that we are detecting in fact [C II] emission but we can not confirm it without more observations. The observed luminosity of the line would be $\mathrm{L}_{[\mathrm{CII}]} = (3.7 \pm 1.0) \times 10^7 \times (\mu/29.2)^{-1} L_{\odot}$. Thanks the the cluster light magnification, this line is would be one of the faintest [C II] emission line observed at high redshift.

3.4.1.3 SFR-$L_{[\mathrm{CII}]}$ Relation

Figure 3.11 shows the results of the search for [C II] emission in normal star-forming galaxies at high redshift. The black solid lines corresponds to the relation found by de

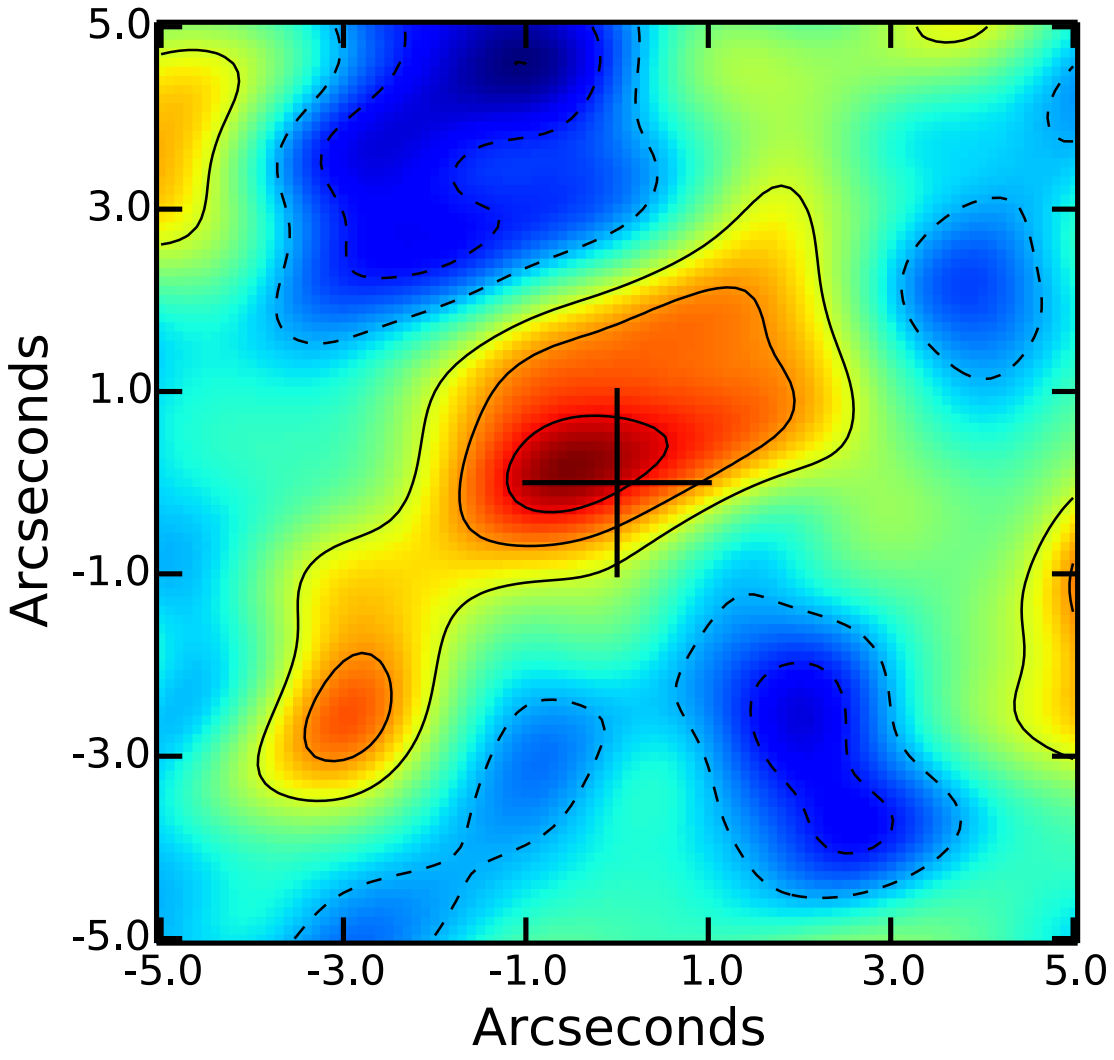

Figure 3.9 Stack of the four position of the brightest regions of the lensed images in the channels around the tentative [C II] detection (marked as yellow channels in Fig. 3.7). The total signal-to-noise of the line is of 3.64σ.

Looze et al. (2011), with the gray area corresponding to 2σ scatter in the relation. For the galaxies we plot the UV-based SFR and the range of possible obscured SFR allowed by the FIR continuum upper limits.

All the previous searches for [C II] in LAEs and LBGs at $z > 6$ have resulted in non-detections (Carilli et al., 2013; González-López et al., 2014; Kanekar et al., 2013; Ota et al., 2014; Ouchi et al., 2013; Schaerer et al., 2014). The only detections correspond to the a LAE at z=4.7 and a LBG at z=5.3 (Carilli et al., 2013; Riechers et al., 2014). The deepest searches for [C II] correspond to the lensed LAE HCM 6A at z=6.5, the two bright LAEs Himiko at z=6.6 and IOK-1 at z=7, the lensed LBG A1703-zD1 at $z_{\rm phot} \approx 6.8$ discovered behind the galaxy cluster Abell-1703 and the LAE z8-GND-5296

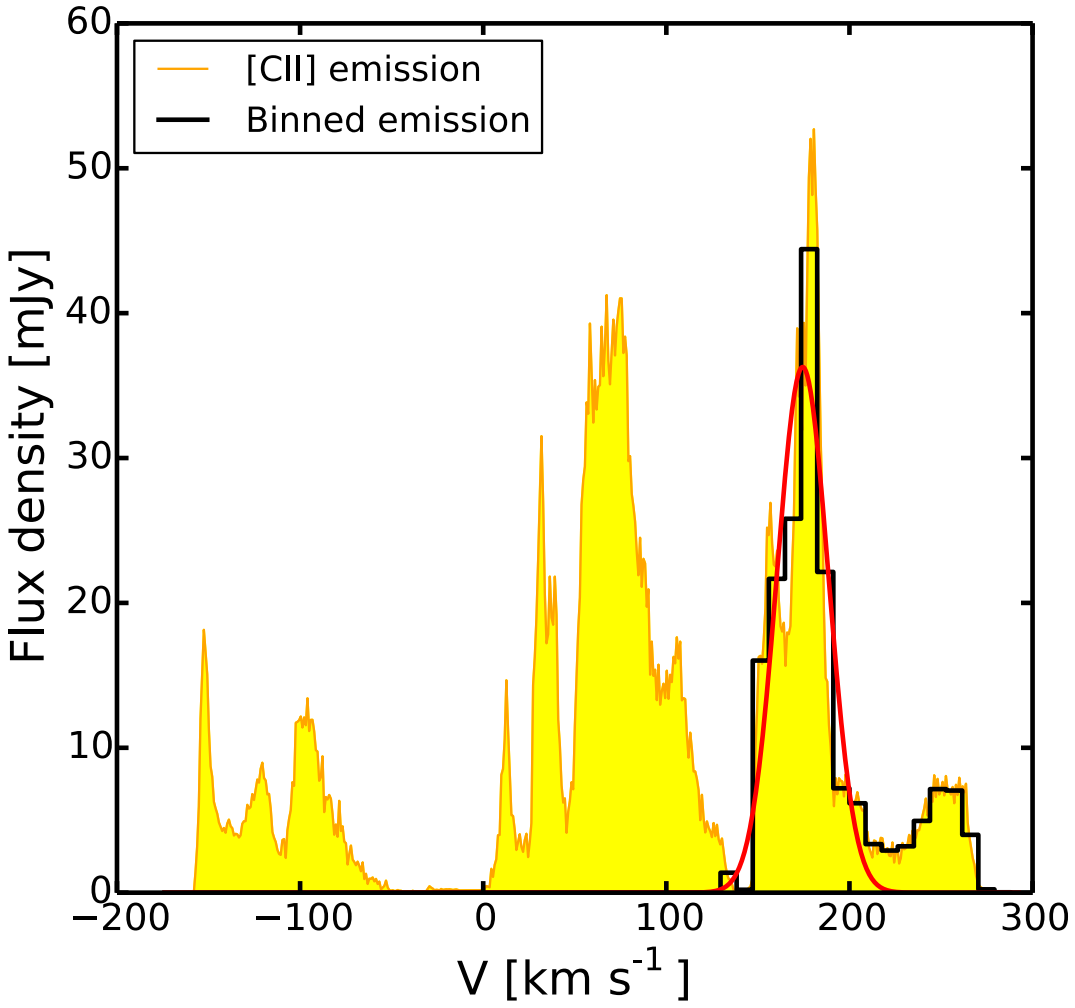

Figure 3.10 Simulated [C II] emission for a galaxy at a similar redshift of MACS0329-iD and with similar characteristics. We use a SFR= 3.2 $M_{\odot}yr^{-1}$, a magnification of $\mu = 29.2$, and a metallicity of $0.2Z_{\odot}$. The yellow lines represent the simulated emission, the black lines is the emission binned to match the observed spectral resolution of ~ 8.85 km s^{-1}. The red line is the best fit gaussian function to the binned emission, resulting in a line width of ~ 30 km s^{-1}.

at $z = 7.508$ discovered in the COSMOS-N field. The upper limits for [C II] put HCM 6A 2σ below the SFR-$L_{[CII]}$ relation, and Himiko, IOK-1 and A1703-zD1 directly off the relation. These results have suggested that the LAEs population at $z > 6.5$ could show different characteristic than low redshift normal star-forming galaxies. The three current detections, show different behavior. LAE-1 shows a perfect agreement with the relation, LBG-1 is 2σ above the relation based in the UV-SFR, although, the range allowed by the obscured star formation still could place it close the relation. MACS0329-iD is represented with the upper limit in [C II] (red circle, displaced to the left) and with the tentative detection (red star). Within the errors, the galaxy is in agreement with the relation, the possible obscured star formation could move the galaxy to the region where the upper limits for the LAEs are located. Deepest observations are needed

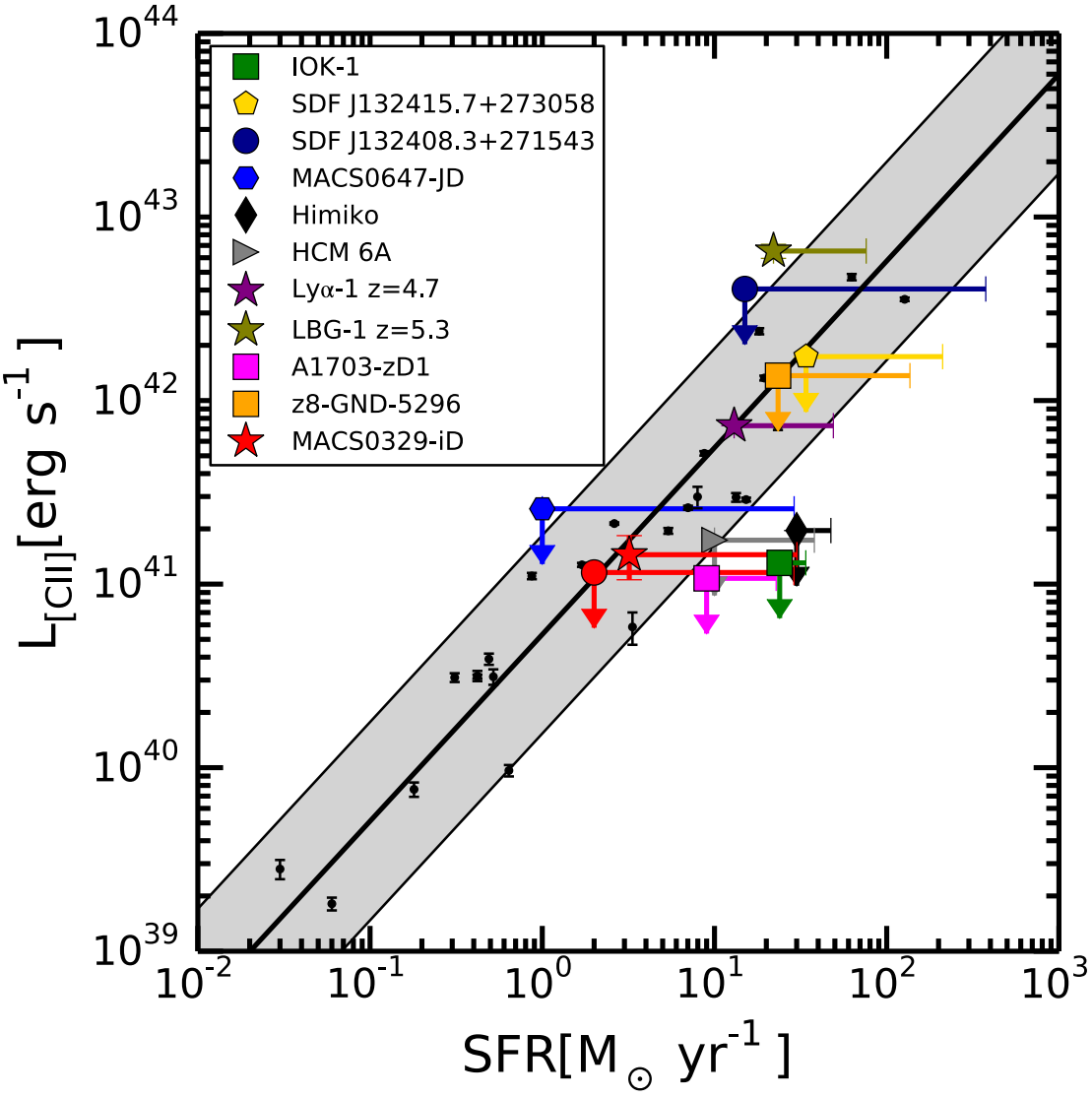

Figure 3.11 Relation of the [C II] luminosity with the UV-derived star formation rate of galaxies. The black solid lines correspond to the relation found by de Looze et al. (2011), with the gray area corresponding to 2σ of the scatter in the relation. The black dots with error bars correspond to the data used to find the relation of [C II] - SFR. We present our tentative detection in MACS0329-iD (red star) together with the 3σ upper limit (red square, displaced for display purposes). We also present the upper limits and observations of [C II] in normal star-forming galaxies at $z > 4$ (Carilli et al., 2013; González-López et al., 2014; Kanekar et al., 2013; Ota et al., 2014; Ouchi et al., 2013; Riechers et al., 2013; Schaerer et al., 2014). For each galaxy, the symbol correspond to the SFR estimated from the UV observations and the error bar in SFR correspond to the range of values allowed by the FIR non detections.

to constraint the obscured star formation in the galaxy and the the [C II] emission and therefore whether it follows the local relation. The measured luminosity for the tentative line in MACS0329-iD is at least one order of magnitude lower than the previous detected line, showing the importance of using magnification to study the faint population of galaxies at high redshift.

3.4.1.4 Ratio $L_{[CII]}/L_{FIR}$

In Fig. 3.12 we present the ratio $L_{[CII]}/L_{FIR}$ for a number of galaxies. The tentative detected [C II] emission in MACS0329-iD has a ratio of $L_{[CII]}/L_{FIR} > 5.7 \times 10^{-4}$ and the upper limit has a similar ratio. This ratio does not necessary means that [C II is not a good cooling of the gas, it is a result of the continuum observation being not deep enough. If we assume a L_{FIR} based in the UV-SFR we obtain a ratio of $\sim 1.6 \times 10^{-3}$, similar to some of the local star-forming galaxies. It would be very interesting to detect the continuum in MACS0329-iD and put real constrains to the ratio $L_{[CII]}/L_{FIR}$ for normal galaxies at high redshift for the first time. Despite of the continuum non-detection in the normal star-forming galaxies at high redshift, [C II] emission line appears to be a good alternative to study the high redshift population in short amount of time, at least for a certain type of galaxies.

3.4.2 Other continuum detections.

Using HST, Spitzer, Herschel, LABOCA and ALMA observations we are able to constraint some properties for the galaxy. For this purpose, we used the Multi-wavelength Analysis of Galaxy Physical Properties (MAGPHYS), which is a versatile model that is capable of interpreting the spectral energy distribution (SED) of galaxies from the UV up to the FIR in a consistent way. The best fit SED is shown in Fig. 3.15 with the physical parameters distribution in Fig. 3.16 and in Tab. 3.2. Figure 3.15 shows that some parameters, as the temperature for the cold and warm dust are not well constrained by our observations. The star formation rate is estimated in SFR=$6.2^{+4.4}_{-2.4}$ $M_\odot yr^{-1}$, very low in comparison to previous detection in continuum of galaxies at high redshift. The dust-to-mass ration is ~ 0.03, being the former of $M_d = 4.5^{+16.0}_{-3.5} \times 10^7 M_\odot$ and $M_* = 1.6^{+1.2}_{-0.57} \times 10^9 M_\odot$. When we do a fit with MAGPHYS but just using the CLASH photometry, the dust mass is estimated in $M_d = 3.4^{+7.3}_{-2.2} \times 10^7 M_\odot$ a value in well agreement, within the errors, to the value estimated using the ALMA detection. This similarity between the values estimated supports the fact that the continuum detection is real and that is not just a peak of the noise.

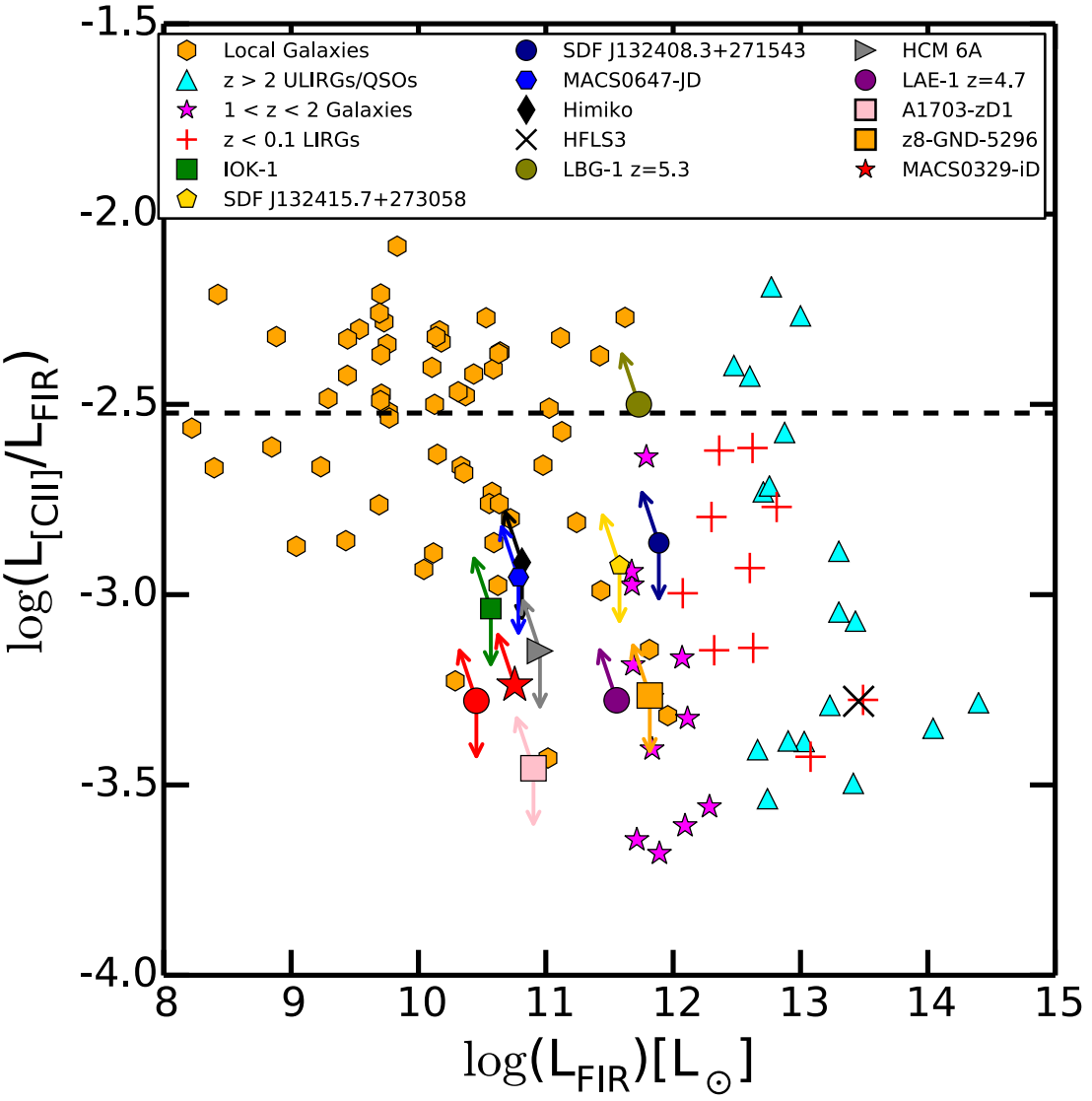

Figure 3.12 Ratio of the [C II] luminosity to the FIR luminosity vs the FIR luminosity (integrated from 42.5μm to 122.5μm rest frame) for galaxies at different redshifts. The horizontal dashed line is the average value for $L_{[CII]}/L_{FIR}$ on the local galaxies. The galaxy MACS0329-iD is represented with the red star together with the 3σ upper limit (red circle, displaced for display purposes). (Carilli et al., 2013; Cox et al., 2011; De Breuck et al., 2011; González-López et al., 2014; Iono et al., 2006; Ivison et al., 2010; Kanekar et al., 2013; Luhman et al., 2003; Maiolino et al., 2009; Malhotra et al., 2001; Negishi et al., 2001; Ota et al., 2014; Ouchi et al., 2013; Riechers et al., 2013, 2014; Schaerer et al., 2014; Stacey et al., 2010; Swinbank et al., 2012; Venemans et al., 2012; Wagg et al., 2010; Walter et al., 2012a, 2009; Wang et al., 2013)

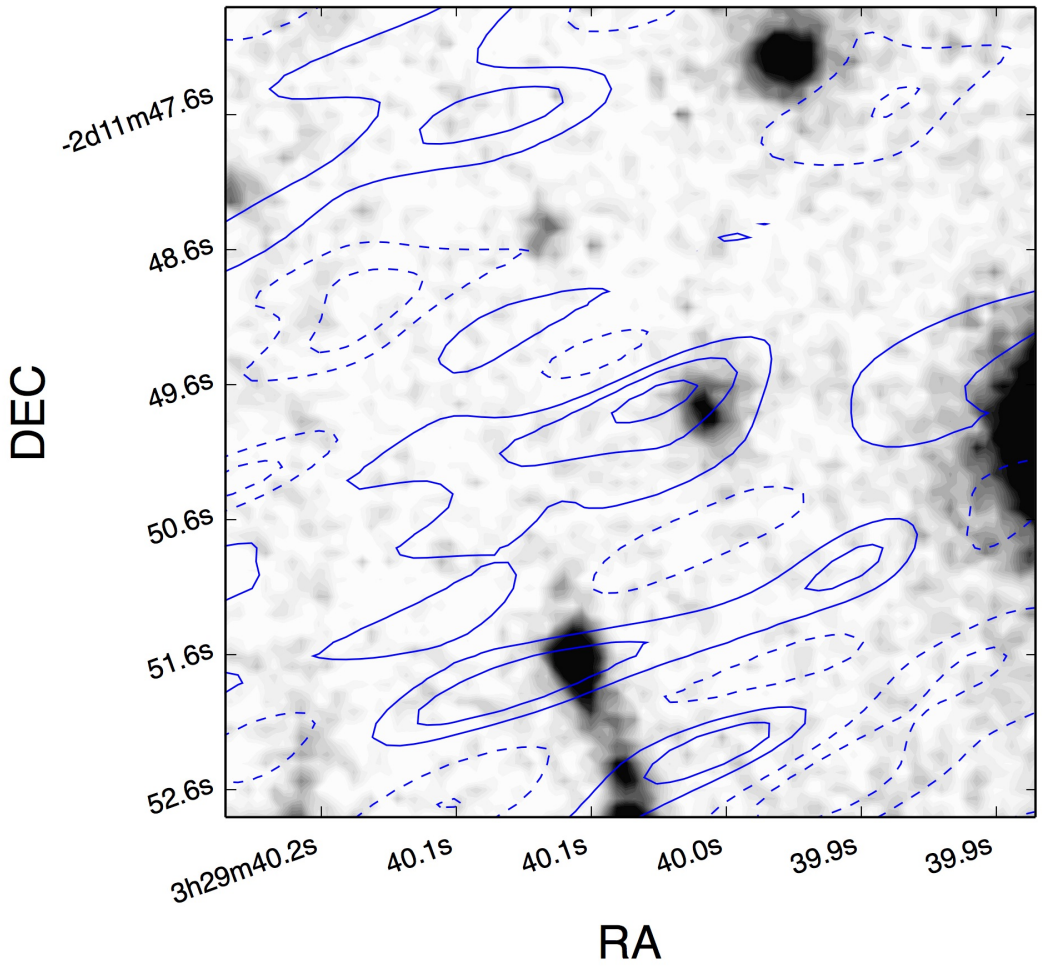

Figure 3.13 Continuum detection of a galaxy at $z \sim 3.5$. The contour levels are in step of 1σ, starting in $-1\sigma, 1\sigma$.

The magnification estimated for the galaxy using the mass distribution of the cluster is of $\mu \sim 21$ (The magnification values were estimated by Mauricio Carrasco, member of the CLASH team). The FWHM of the detection in the CLASH catalog is of 0.759′′, when we take this to the source plane we obtain a size of 0.16" which represents a physical size of $\sim$ 1.2 kpc at $z = 3.54$, putting this galaxy in the category of dwarf galaxy. The dust-to-stellar mas ratio is a bit high for the stellar mass, but it is similar to the ratios found in the local universe. Figure 3.17 shows SFR, dust mass and stellar mass of our galaxy corrected by the cluster magnification and for the sample of galaxies studied by the KINGFISH survey (Skibba et al., 2011). We also plot some low-metallicity blue compact dwarf galaxies (Hunt et al., 2005) and some lensed galaxies studied with Herschel (Sklias et al., 2014). We see that our galaxy falls just in the middle of the local population when we compare the SFR with the dust mass, but it falls a bit higher than the local population when we compare the stellar mass and the dust mass. This galaxy appears to have a higher amount of dust than local galaxies with similar stellar mass

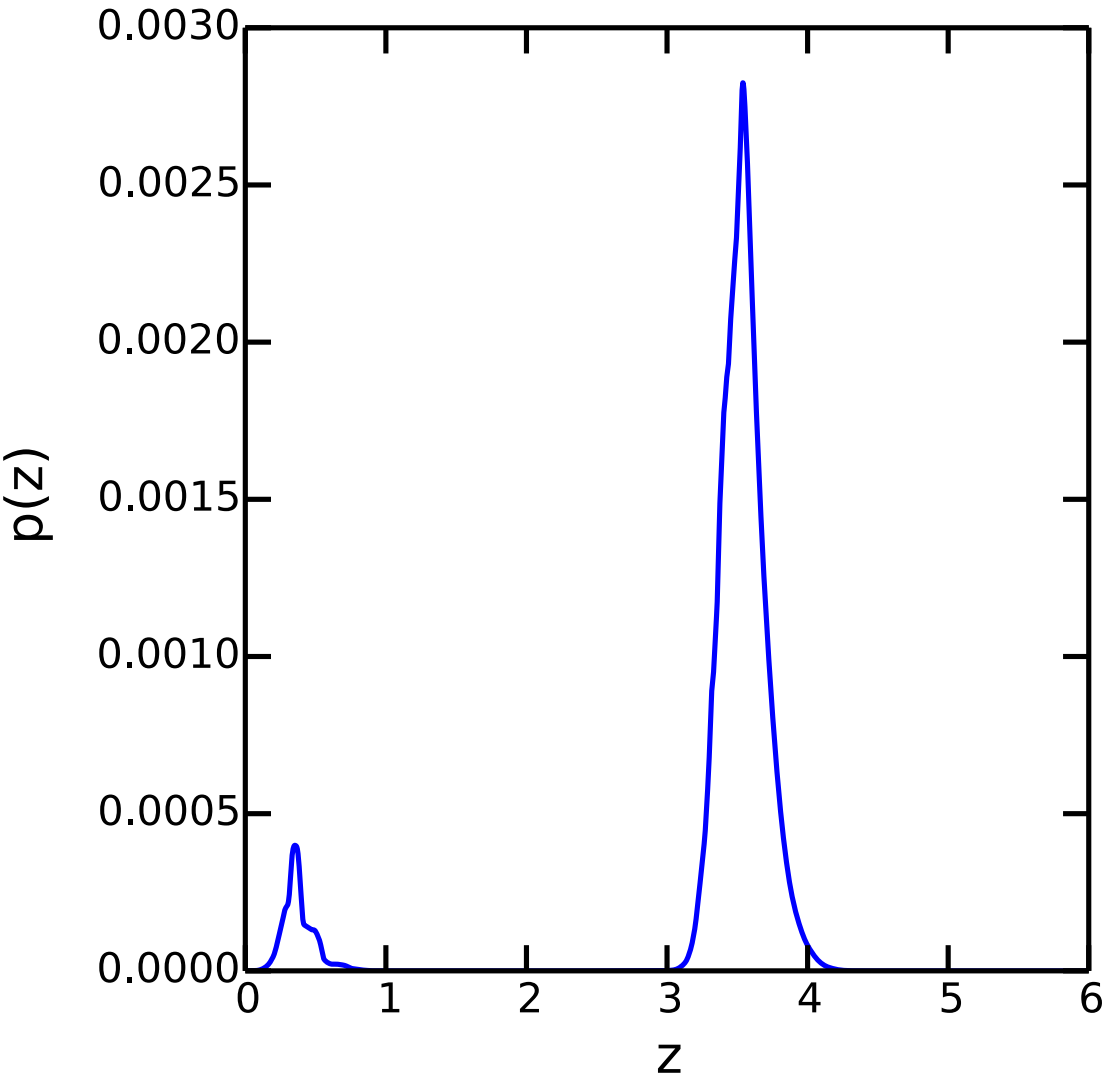

Figure 3.14 Probability distribution of the redshift for the galaxy detected in continuum with ALMA. The distribution was calculated using Bayesian Photometric Redshifts and the 16 HST filters used in the CLASH survey. The low redshift secondary peak is low in comparison to the main higher redshift peak. The high redshift peak is also supported by the ALMA 1.1 mm detection.

but the large errors in the estimated dust mass still can put the galaxy near the local galaxy population. This detection is one of the first detection of a dusty dwarf galaxy at high redshift and it is only possible because of the galaxy cluster light magnification.

3.4.3 Stacking

The number of galaxies detected in the CLASH survey within the pointing of the ALMA observation is 32. We will do a stacking to search for continuum in the members of the

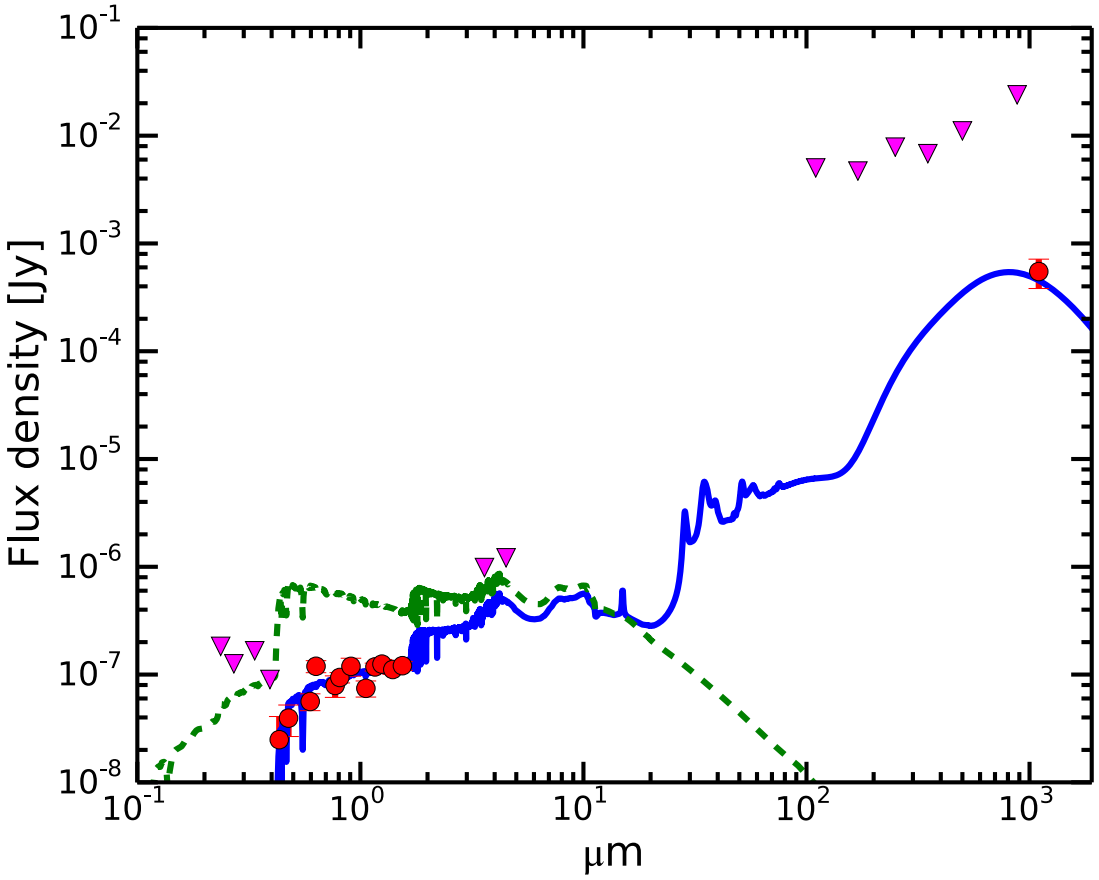

Figure 3.15 Spectral energy distribution of the galaxy detected with ALMA. The red points are the detection in each filter, from HST and ALMA. The upper limits are plotted as downward triangles, and correspond to the UV filter from HST, Spitzer channels 1 and 2 at 3.6 and 4.5 μm, Herschel cameras PACS and SPIRES, and APEX/LABOCA bolometer. The red dashed line corresponds to the stellar emission in the galaxy and the blue continuum line corresponds to the stellar emission absorbed by dust and re-emitted in the FIR. The physical quantities distribution obtained from the fit can be found in Table 3.2.

clusters, and in galaxies by range of redshift. The bpz photometric redshift of the 32 galaxies inside the HPWB are in Fig. 3.18. We will stack the continuum emission of each of the group marked as G1 to G5. The group G1 correspond to the members of the galaxy cluster MACS0329. The group G5 corresponds to the photometry of the galaxy at z=6.17 discussed in González-López et al. 2014b. No continuum emission is detected in the stacked continuum images, a 3σ signal is found at 2" from the center of the stacked image for G1, we think treat it as a non detection. The results of the stacking are in Tab. 3.3, for the nominal resolution as well as for the extended resolution. No stacked

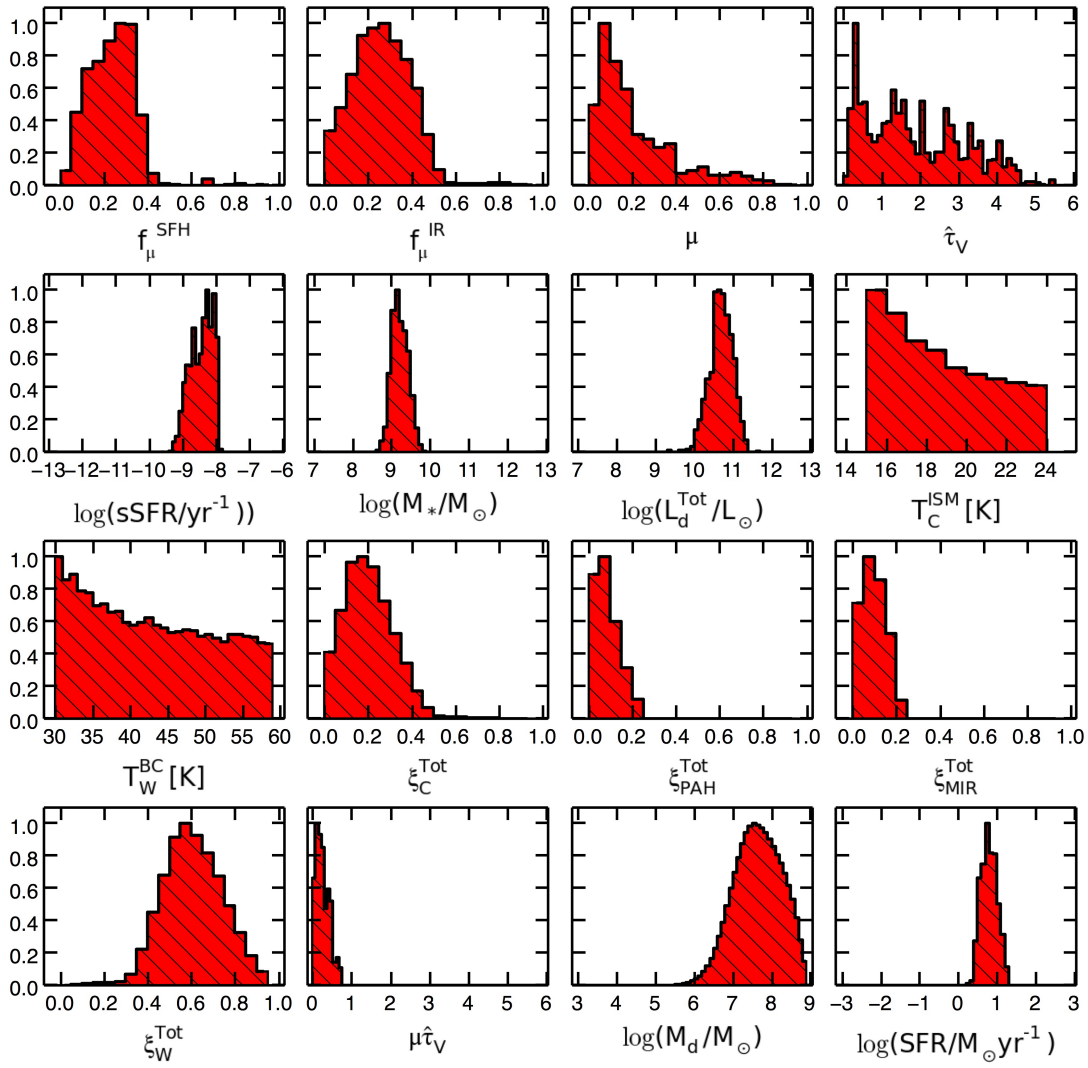

Figure 3.16 Likelihood distribution of the physical parameters fitted by MAGPHYS to photometry of the galaxy at $z \sim 3.5$. The parameters are, first row in the top; fraction of the total infrared luminosity contributed by dust in the ambient inter stellar medium (ISM) associated to the stellar population ($f_\mu^{\rm SFR}$); fraction of the total infrared luminosity contributed by dust in the ambient ISM associated to the IR spectrum ($f_\mu^{\rm IR}$), the total fraction of the total infrared luminosity contributed by dust in the ambient ISM (f_μ) is estimated as the average of the previous values, $f_\mu = 0.5 \times (f_\mu^{\rm SFR} + f_\mu^{\rm IR})$; fraction of the total V-band absorption optical depth of the dust contributed by the ambient ISM (μ); total effective V-band absorption optical depth of the dust ($\hat{\tau}_{\rm V}$); second row from the top; specific star formation rate (sSFR); stellar mass (M_*); total infrared luminosity of the dust (L_d^{Tot}); equilibrium temperature of cold dust in the ambient ISM ($T_{\rm C}^{\rm ISM}$); third row; equilibrium temperature of warm dust in stellar birth clouds ($T_W^{\rm BC}$); contribution by cold dust in thermal equilibrium to the total infrared luminosity ($\xi_{\rm C}^{\rm Tot}$); global contributions (i.e. including stellar birth clouds and the ambient ISM) by polycyclic aromatic hydrocarbons (PAHs); global contributions by the hot mid-infrared continuum ($\xi_{\rm MIR}^{\rm Tot}$); fourth row; global contributions by the warm dust in thermal equilibrium ($\xi_{\rm W}^{\rm Tot}$); effective V-band absorption optical depth of the dust in the ambient ISM ($\mu\hat{\tau}_{\rm V}$); dust mass ($M_{\rm d}$); Star formation rate (SFR).

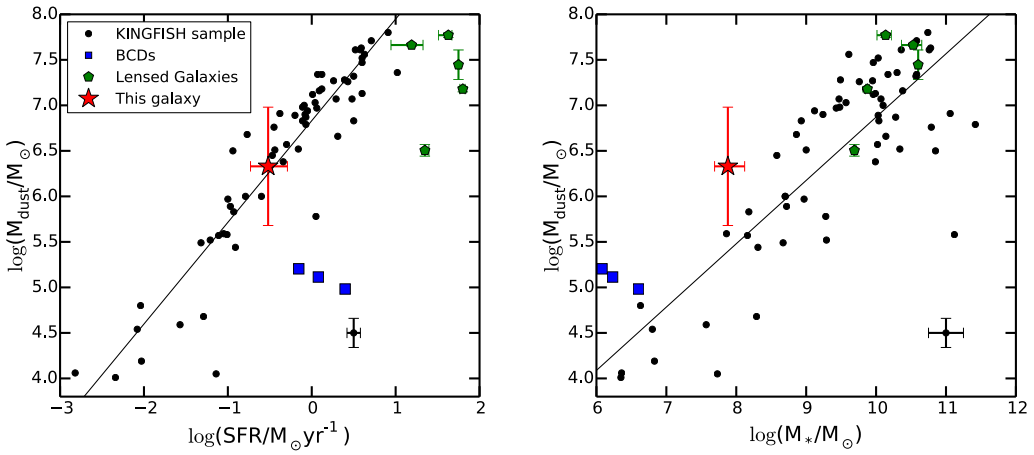

Figure 3.17 Comparison of the dust mass, stellar mass and star formation rate for the detected galaxy (red star) with the local galaxies of the KINGFISH survey sample (black dots). In the lower red corner is the median of the errors for the KINGFISH sample. The blue squares are the low-metallicity blue compact dwarfs (BCDs) studied in Hunt et al. (2005). The green pentagons are the lensed galaxies studied as part of the Herschel Lensing Survey (Sklias et al., 2014), we are only showing the galaxies that have similar values to the KINGFISH sample. The galaxy detected in our observations agrees very well with the fit to the KINGFISH sample (black line) in the dust mass to SFR relation. In the lower panel, the dust mass appears to be slightly higher in comparison to the galaxies of the KINGFISH sample with similar stellar mass. In general, the BCDs sample, the lensed galaxies appears to be above the relation found between dust mass and stellar mass for the KINGFISH sample.

Table 3.2. Best fit parameters from MAGPHYS for the galaxy detected in continuum

Parameter	Value
f_{μ}^{SFH}	$0.24^{+0.09}_{-0.12}$
f_{μ}^{IR}	$0.26^{+0.14}_{-0.13}$
μ	$0.15^{+0.22}_{-0.09}$
$\hat{\tau}_V$	$1.62^{+1.73}_{-1.17}$
$\log(sSFR/yr^{-1}))$	$-8.37^{+0.35}_{-0.45}$
$\log(M_*/M_\odot)$	$9.2^{+0.25}_{-0.19}$
$\log(L_d^{Tot}/L_\odot)$	$10.7^{+0.3}_{-0.3}$
T_C^{ISM}[K]	$18.6^{+4.0}_{-2.6}$
T_W^{BC}[K]	$42.4^{+11.6}_{-9.2}$
ξ_C^{Tot}	$0.19^{+0.13}_{-0.10}$
ξ_{PAH}^{Tot}	$0.08^{+0.07}_{-0.04}$
ξ_{MIR}^{Tot}	$0.10^{+0.07}_{-0.05}$
ξ_W^{Tot}	$0.60^{+0.15}_{-0.13}$
$\mu\hat{\tau}_V$	$0.23^{+0.23}_{-0.14}$
$\log(M_d/M_\odot)$	$7.65^{+0.65}_{-0.63}$
$\log(SFR/M_\odot yr^{-1})$	$0.79^{+0.24}_{-0.21}$

Note. — All the errors correspond to 1σ errors.

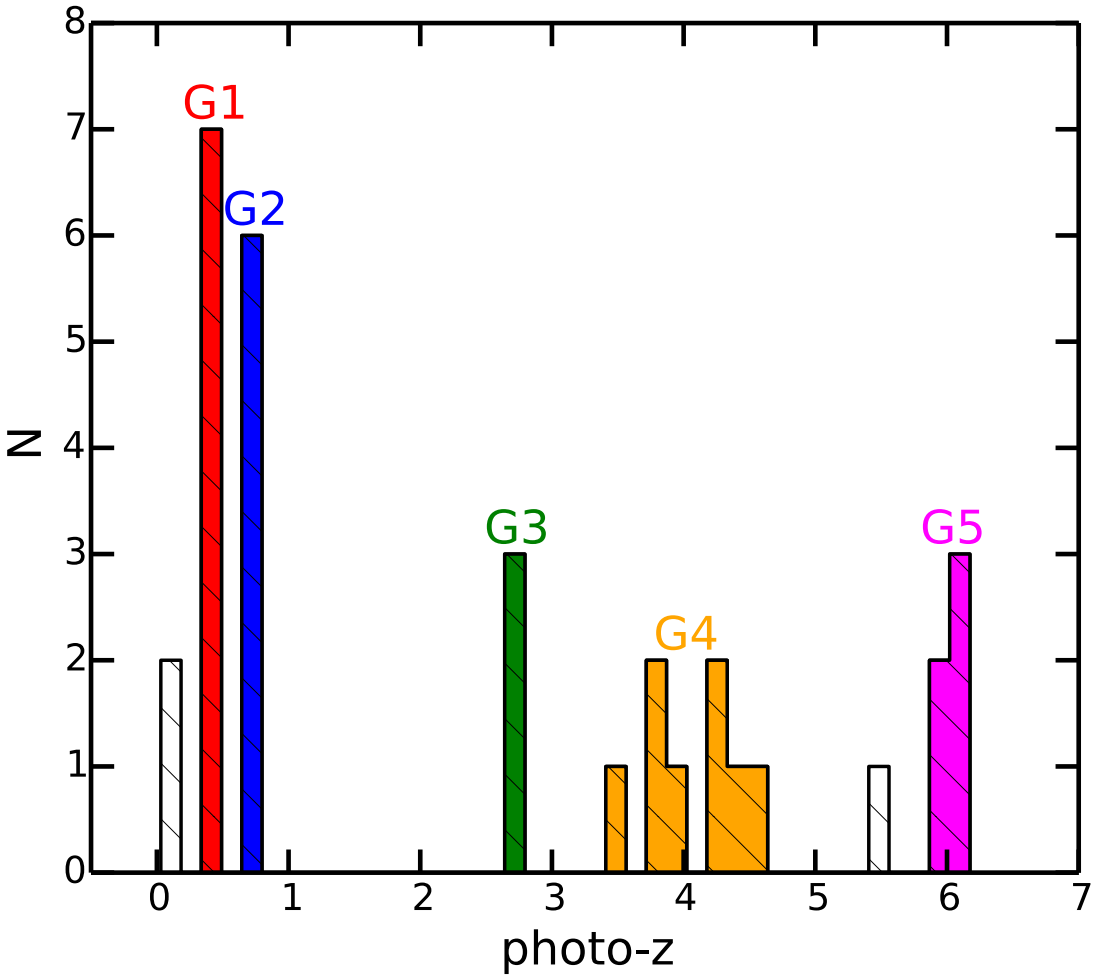

Figure 3.18 Distribution of photometric redshift of the galaxies found within the ALMA HPWB. We separate the group to do a stacking searching for continuum emission. The group G5 is the galaxy found at $z = 6.17$ discussed above. G1 corresponds to the members of the galaxy cluster.

Table 3.3. Groups of galaxies searched for stacked continuum emission.

Group	z	F^1_ν [μJy b^{-1}]	F^2_ν [μJy b^{-1}]
G1, N=7	0.3-0.5	< 182	< 268[a]
G2, N=6	0.65-0.8	< 229	< 3268
G3, N=3	2.6-2.8	< 276	< 431
G4, N=8	3.4-4.6	< 235	< 333
G5, N=5	5.8-6.2	< 238	< 332[a]

Note. — All upper limits are $3\,\sigma$.

[a]There is a 3.1σ peak at 2" from the center of the stacked image. It could be related to the galaxies but we treat it as a non detection. This group corresponds to the members of the galaxy cluster.

[a]This group corresponds to the galaxy at z=6.17 discussed above. The CLASH photometry breaks the galaxy in 5 small portions that is why 5 galaxies are found at this redshift range.

continuum detection is found in any of the groups of galaxies.

3.4.4 Other Emission lines

Given the large amount of galaxies within the ALMA pointing, we did a simple search for candidate to emission lines in the data cube. For the search, we made a simple assumption, that the emission lines are well represented by gaussian functions. We created data cubes with two spectral resolution; the native with $dv = 8.85\,\mathrm{km\,s^{-1}}$ and one with $dv = 50\,\mathrm{km\,s^{-1}}$. To help in the search, we also used a third uv-taper configuration, apart from the two presented above. The synthesized beam for the third configuration is of 3.2" × 2.5" with a PA=-65.65 degree.

The search was performed in the data cubes without correction by the primary beam. We took the data cube and made a gaussian convolution in the spectral axis. For each data cube the σ values for the gaussian convolution ranged from 0 to 5 times the channel resolution. Covering from $0-45\,\mathrm{km\,s^{-1}}$ for the native resolution and from $0-250\,\mathrm{km\,s^{-1}}$ with the channel resolution of $50\,\mathrm{km\,s^{-1}}$. After the convolution, in each spectral channel, we took the rms of the pixels and search for peaks with signal to noise at least of 4σ. The same exercise is made to look for negative peaks. For each significance, (hereafter SN), we count the number of positive ($\mathrm{N_{pos}}$) and negative ($\mathrm{N_{neg}}$) peaks. We calculate the parameter $R = (\mathrm{N_{pos}} - \mathrm{N}_{neg})/\mathrm{N_{pos}}$, which should be around zero for when the peaks are representative of the noise for a given significance and a given value of σ used in the convolution. For a given data cube, if emission lines are found, the parameter R should trend to unity while increasing the values of SN. In Fig. 3.19 we show the R values for each of the three synthesized beams and the 2 spectral resolutions. The values are calculated until no positive peak are found for the given SN. For a positive peak to be assigned as candidate to emission line needs to meet the following criteria:

1. The R value for that positive signal needs to be unity. Meaning that no negative peaks are found with the same line width and significance SN.

2. The R value needs to reach unity before the final SN. For each σ, R has to be 1 for a value of SN<max(SN).

3. The position of the positive peak has to be located in the map where the sensitive of the primary beam is at least 10% of the one in the phase center.

4. The emission line when integrated in frequency has to have a signal-to-noise higher than 5σ. This has to be done in the data cube corrected by the primary beam.

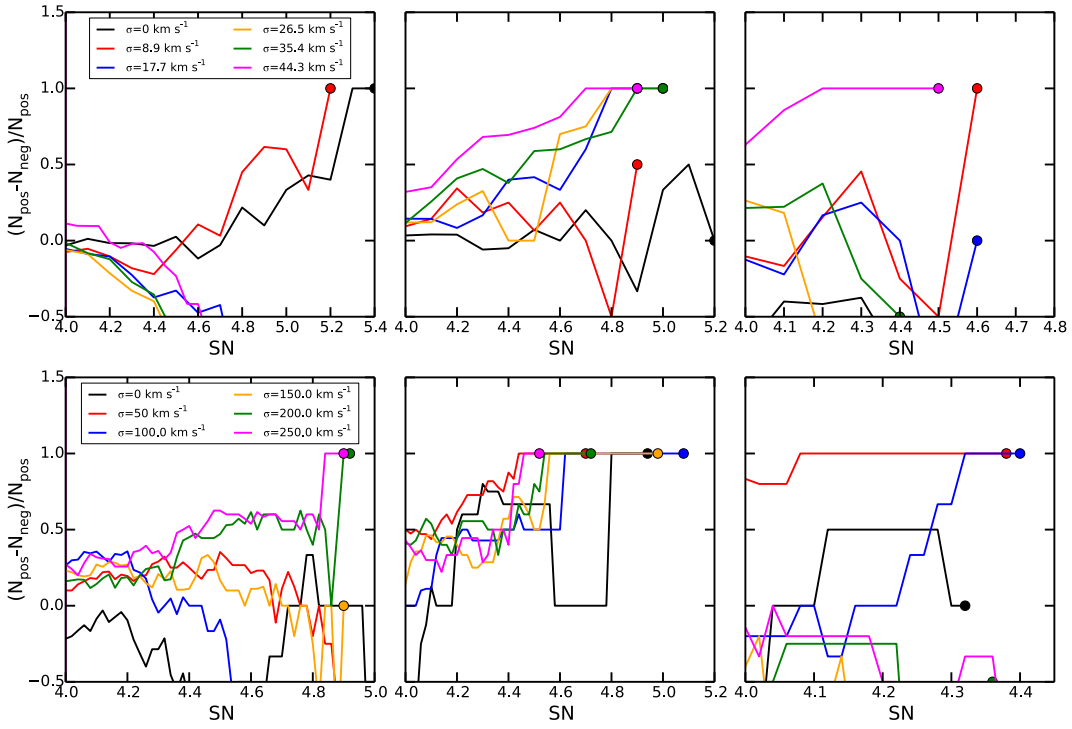

Figure 3.19 R values for different channel resolutions and different angular resolution. The top row represent the native spectral resolution and the bottom row the search in the data cube where the channel resolution was set to 50 $\mathrm{km\,s^{-1}}$. For each row, each color represents the search for emission lines with a given line width, set by the σ value assigned in the legend of the plot. For each row, the left panel is the one with the nominal resolution, the middle is the one with the extended resolution and the right panels are for the third angular resolution reached by using a smaller uv-tapering. In the top row, the green and magenta lines in the middle and right panel follow the trends that indicate a possible emission line. The same behavior is observed for some lines in the bottom row. It is important to note that one candidate to emission line can be detected in several panels at the same time.

Once these criteria are fulfilled, the positive signal passes to be a candidate to emission line. A list with the candidate to emission lines is in Tab. 3.4. The lines are shown in Fig. 3.20.

Below we describe each of the possible emission lines.

3.4.4.1 Line 1

The emission line L1 in the top left panel in Fig. 3.20 is clearly detected with two peaks. This line has a signal-to-noise of 7.4 when the emission is integrated in the yellow channels. In Fig. 3.21 we see the integrated emission line with the two spatial resolution used. In the left is the extended resolution and in the right is the nominal resolution.

Table 3.4. List of candidates to emission lines.

Line	S/N	Coordinates [RA, DEC]	Central Frequency [GHz]	FWHM [$\mathrm{km\,s^{-1}}$]	Amplitude [$\mathrm{mJy\ b^{-1}}$]
L1-red	5.1[a]	03:29:39.796, -2:11:46.508	264.718 ± 0.007	24.5 ± 13.5	14.6 ± 6.4
L1-blue	5.1[a]	03:29:39.796, -2:11:46.508	264.782 ± 0.008	62.9 ± 21.8	16.5 ± 4.5
L2	5.6	03:29:38.929, -2:12:03.708	263.894 ± 0.007	65.7 ± 17.6	75.8 ± 17.6
L3	5.2	03:29:40.650, -2:11:51.708	265.829 ± 0.006	52.6 ± 14.8	12.4 ± 3.1
L4	5.8	03:29:40.737, -2:11:50.408	264.27 ± 0.03	252.8 ± 81.7	10.0 ± 2.8

Note. — Results of fitting gaussian function to the emission lines.

[a]signal-to-noise of the emission combined of the two component red and blue.

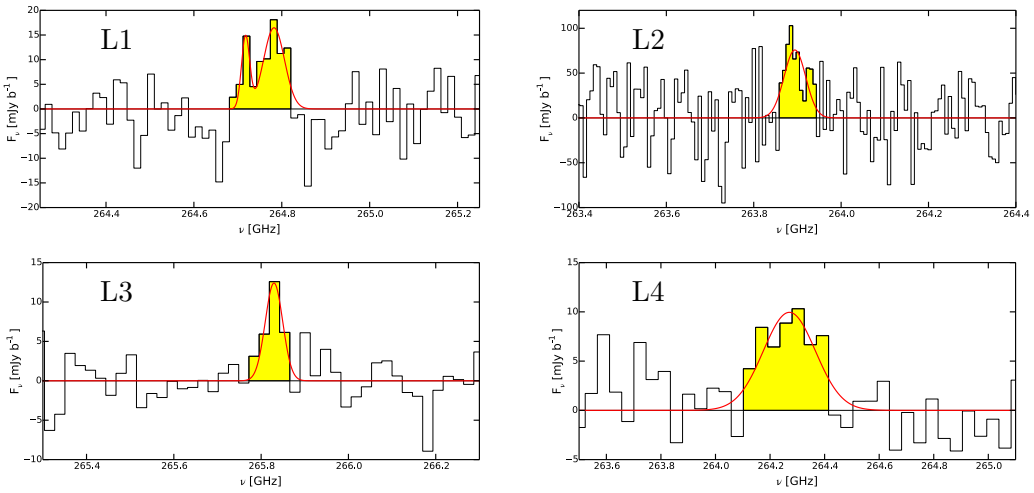

Figure 3.20 Spectra of the 4 candidate to emission lines found in the data cube. The list from L1 to L4 is in decreasing signal to noise value.

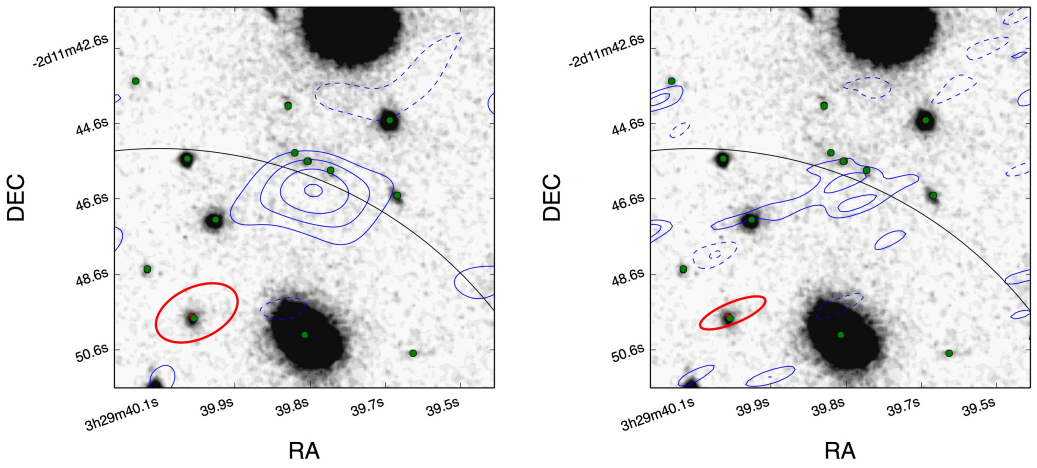

Figure 3.21 Emission line 1. Each contour represent 1σ (starting in $\pm 2\sigma$) of the emission integrated in the yellow channels in Fig. 3.20. The red and green circles are the positions of the detection made with CLASH. The red circles represent the detections made using the optical images and the green circles the ones made with the IR images in the CLASH survey.

The line was first discovered in the extended resolution. The nominal resolution is shown to see the spatial distribution of the emission and to find the counterparts.

The double peak feature can be explained by three scenarios. i) we are seeing a merger of galaxies; ii) this is the superposition of two emission lines of two galaxies at different redshifts and iii) this is the resolved emission of a rotating disk. The third scenario is not supported by the fact that the width of the two component are very different. Daddi et al. (2010) presented the resolved emission of CO(2-1) on rotating disk at $z \sim 1.5$, one of the main results from they observations and numerical simulations is that in the case

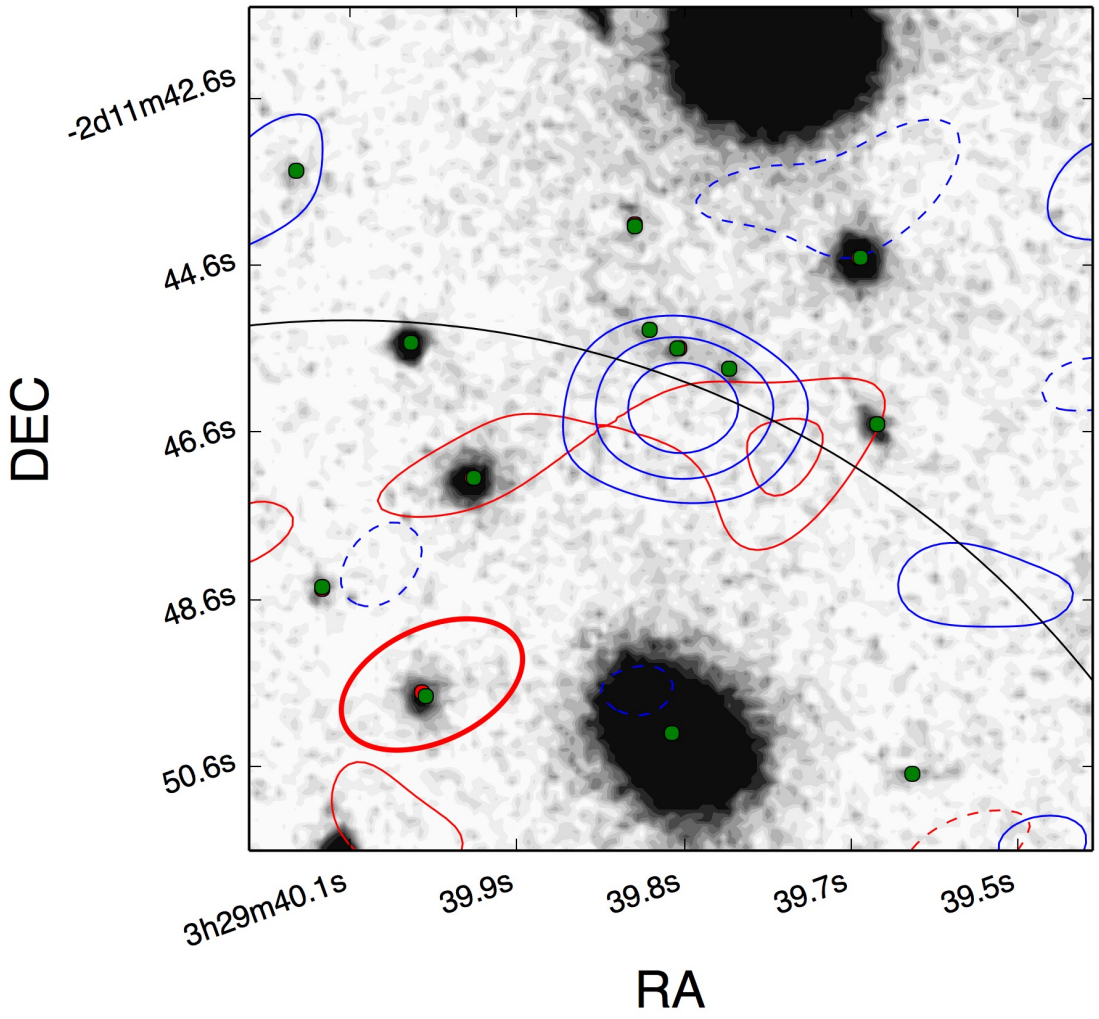

Figure 3.22 Map of the two peaks found in Line 1 in Fig. 3.20. The contours are in step of 1σ starting in $\pm 2\sigma$. The blue contours represent the line with the peak at the higher frequency.

of rotating disk, the emission from the peak can have different peaks values, but they velocity distribution (width of the line) needs to be similar. Similar results is found in the observations of H I in nearby local galaxies, where the two peaks show similar widths (Walter et al., 2008). The blue component shows a FWHM at least three time larger than the one in the red component, showing that the velocity distribution is different and therefore discouraging the rotating disk scenario.

The spatial distribution of the two peaks is shown in Fig. 3.22, we see how the emission from the red peak is more extended than the blue peak. If we compare the emission from Fig. 3.21 right panel and the map of the two peaks, we that that the emission extends to the left, to a galaxy that is not close to the peak of the emission. We see

that the extension is only shown in the red peak, indicating a possible emission coming from that galaxy. Still, we see that the peak of the emission associated to the red peak is not located in the other galaxy, so we can not say that the red peak is coming from that galaxy, but may be just part of it. The scenario of the merger can not be discarded until we have optical spectra of the possible galaxies counterpart.

For the search of counterparts, we will explore the possibility of the emission coming from one or two of the closest galaxies to the peak of the emission. In Fig. 3.26 we plot the probability distribution of the photometric redshift for the possible counterparts to the detected emission lines. The vertical lines are the redshifts that the counterparts should be if the detected line is the one in the name. In the first row of Fig. 3.26 we have the two possible counterparts for L1. The galaxy 1 has a $z_{\rm photo} = 0.87^{+0.17}_{-0.18}$ and if the emission line is CI($^3P_1 \rightarrow ^3 P_0$) the redshift of the galaxy would be $z = 0.86$. For galaxy 2 the photometric redshift is $z_{\rm photo} = 3.97^{+0.23}_{-0.26}$, the emission line closest to the peak of the redshift distribution for this galaxy is CO(11-10), which would put this galaxy at $z = 3.79$. The emission line CO(11-10) has been observed at high redshift just in the quasar APM 08279+5255 at $z = 3.9$ (Bradford et al., 2011; Weiß et al., 2007), which is one of the brightest object in the universe. The gas properties of APM 08279+5255 differ from those seen in in other high-z quasar and local starburst (Weiß et al., 2007), showing that the chances of this line being C(11-10) are very low.

The small difference between the photometric redshift for galaxy 1 and the redshift obtained if we assume that the emission line is CI(1-0) strongly suggest galaxy 1 as the counterpart to the emission line. The next step is to see if the photometry for galaxy 1 is according with having the detected flux for CI(^{3}P1-^{3}P0). When we do a SED fitting to galaxy 1 using MAGPHYS we obtain a SFR $\sim 0.06 M_\odot yr^{-1}$. We will use the results from Walter et al. (2011) where a ratio of CI(1-0)/CO(3-2)$\approx$ 0.32 is found for a sample of quasar and submillimeter galaxies and the relation between CO(3-2) and $L'_{\rm FIR}$ found by Iono et al. (2009) to estimate the expected line luminosity for the galaxy. Using the relation $L'_{\rm FIR} = 5.8 \times 10^9 \times$ SFR we obtain a $L'_{\rm CO(3-2)} \sim 2.9 \times 10^6$ K km s^{-1}pc^2 and $L'_{\rm CI(1-0)} \sim 9.3 \times 10^5$ K km s^{-1}pc^2. The observed luminosity is of 3.2×10^9 K km s^{-1}pc^2. The ratio between the observed and the estimated luminosity is of $\log(L'^{\rm obs}_{\rm CI(1-0)}/L'^{\rm est}_{\rm CI(1-0)}) \sim 4.4$, more than 4 order of magnitude higher. Is is difficult to conciliate our observed luminosity with the estimated luminosity, resulting than either, our detected emission line is fake, or the photometric redshift is not accurate. It is important to note that the average AB magnitude for the galaxy is 28 and that it is detected with 5σ in just 2 out of the 16 CLASH filters, which make the photometric redshift not reliable.

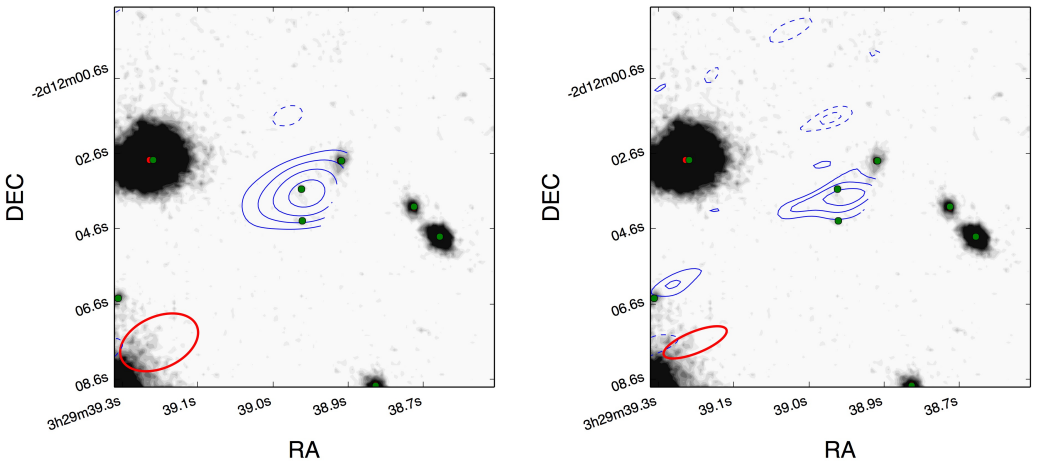

Figure 3.23 Emission line 2. Each contour represent 1σ (starting in $\pm 2\sigma$) of the emission integrated in the yellow channels in Fig. 3.20. The red and green circles are the positions of the detection made with CLASH. The red circles represent the detections made using the optical images and the green circles the ones made with the IR images.

3.4.4.2 Line 2

The emission line L2 top right panel in Fig. 3.20. The range of frequencies between 263.6 and 263.8 GHz has a higher noise than the other channels because the emission is affected by an atmospheric water line. This line is detected in the edge of the data cube, the cut of the emission is because the data cube is used up to where the sensitivity is 10% of the one in the phase center. In Fig. 3.23 left panel, we see that in the center of the emission there is a detection made with HST. That galaxy is detected in the combination of all the images, but is none of the filter the galaxy is detected with more than 5σ, which makes the photometry and therefore redshift probability distribution not reliable. For completion, we show the redshift probability distribution in Fig 3.26 middle row left panel. The closest lines to the peak of the distribution is CO(7-6) and CI(1-0). If this line is CI(1-0), then CO(7-6) falls in the observed range of frequency, but is not detected and as CO(7-6) is always brighter than CI(1-0), this discards the possibility of the observe line being CI(1-0). The another possibility is CO(7-6), resulting in a redshift of $z = 2.05$, close to the $z_{\rm photo} = 1.89^{+0.54}_{-0.66}$. The luminosity for CO(7-6) would be $L_{\rm CO(7-6)} = 3.6 \times 10^8 L_\odot$.

3.4.4.3 Line 3

The emission line L3 is in the bottom left panel in Fig. 3.20. In the left panel in Fig. 3.24 is the emission where the line was discovered, and in the right panel is the emission for the same channels but in the nominal resolution. The emission is clearly related to the

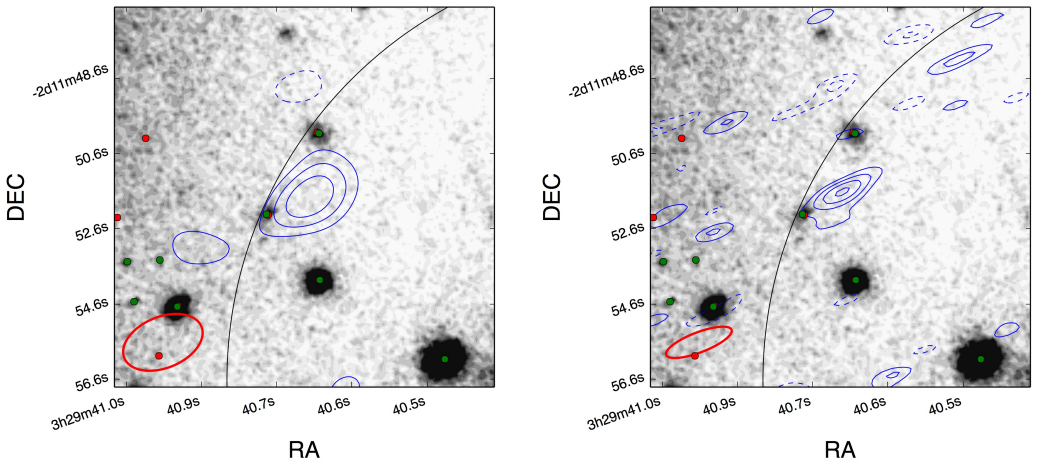

Figure 3.24 Emission line 3. Each contour represent 1σ (starting in $\pm 2\sigma$) of the emission integrated in the yellow channels in Fig. 3.20. The red and green circles are the positions of the detection made with CLASH. The red circles represent the detections made using the optical images and the green circles the ones made with the IR images.

galaxy to the left of the peak of the emission. The photometric redshift of that galaxy is $z_{\rm phot} = 4.4^{+0.2}_{-0.3}$. When we check for the possible emission lines that could account for the one observed we see that there are two possible lines, in Fig. 3.26 middle row right panel we have the redshift probability distribution for the galaxy and the two lines CO(12-11) and [N II] . The CO lines is discourage to be the one observed because the probability of observing that line are very low, as stated above. The second possibility is that the line is [N II] in the transition $^3P_1 \rightarrow {}^3P_0$, which together with the other transition $^3P_2 \rightarrow {}^3P_1$ has been observed a few times before at high redshift (Combes et al., 2012; Decarli et al., 2014, 2012; Ferkinhoff et al., 2011; Nagao et al., 2012). In the case of the line being [N II] , the redshift of the galaxy would be $z = 4.5$. The two detection in normal star-forming galaxies correspond to two Lyman-alpha emitters (LAE) at z=4.7 (Decarli et al., 2014), we will be using those galaxies as reference to check weather the detected line can correspond to the [N II] in the galaxy at z=4.4.

From the sed fitting of the galaxy using MAGPHYS we obtain a SFR $= 10.3^{+4.0}_{-2.8} {\rm M}_\odot {\rm yr}^{-1}$. The observed luminosity of the line is $L_{[NII]} = 3.0 \pm 0.5 \times 10^8 L_\odot$, if we compare the emission found in LAE-1, where the [N II] luminosity is $L_{[NII]} = 1.4 \pm 0.6 \times 10^8 L_\odot$ for a SFR=$13 {\rm M}_\odot {\rm yr}^{-1}$(Petitjean et al., 1996) we find that the luminosities are very similar, indicating that the observed line flux is consistent with a galaxy a high redshift and such star formation rate. The magnification estimate for the galaxy is of $\mu \sim 23.5$, indicating that we are exploring the very faint population of galaxies at high redshift. We conclude that the observed line corresponds to a lensed galaxy at $z = 4.4965 \pm 0.0001$ with a SFR$= 0.44^{+0.17}_{-0.11} \times (\mu/23.5) {\rm M}_\odot {\rm yr}^{-1}$ and a [N II] luminosity of $L_{[NII]} = 1.6 \pm 0.2 \times 10^7 \times$

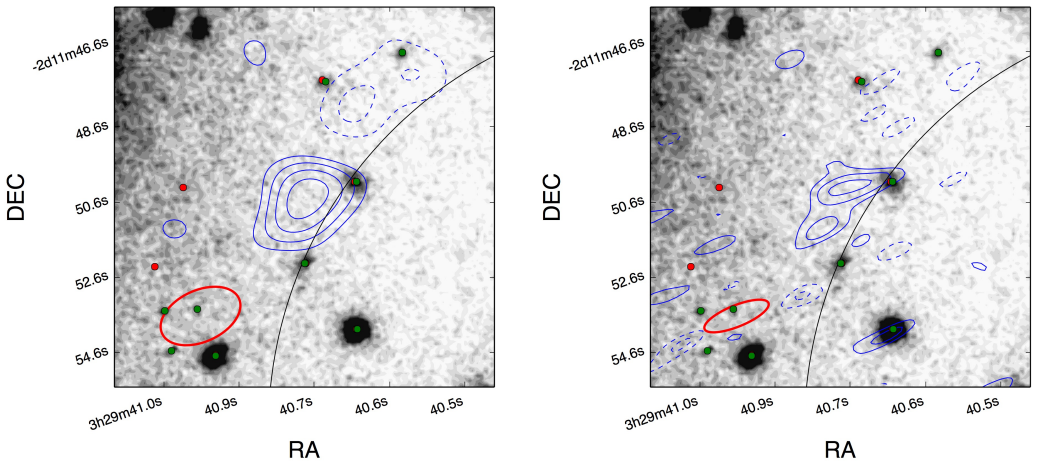

Figure 3.25 Emission line 4. Each contour represent 1σ (starting in $\pm 2\sigma$) of the emission integrated in the yellow channels in Fig. 3.20. The red and green circles are the positions of the detection made with CLASH. The red circles represent the detections made using the optical images and the green circles the ones made with the IR images.

$(\mu/23.5)L_{\odot}$. We will need [C II] observations for this galaxy to put constraints to the ionization medium in the ISM.

3.4.4.4 Line 4

The emission line L4 is in the bottom right panel in Fig. 3.20. In the left panel in Fig. 3.25 is the emission where the line was discovered, and in the right panel is the emission for the same channels but in the nominal resolution. The emission is clearly related to the galaxy to the right of the peak of the emission. The photometric redshift of that galaxy is not well constrained and has two peaks with similar probability, one at high redshift and other at low redshift. When we check for the possible emission lines that could account for the one observed we see in Fig. 3.26 bottom row the two peak of the redshift probability distribution. The peak around $z \sim 3.6$ has possible CO emission lines but the transition are too high to be easily observed and associated to the observed line, also the lines are not too close to the peak of the redshift distribution. For the low redshift peak around $z \sim 0.4$, the possible line are HCN are HCO, but those are usually faint in comparison to the usually observed emission lines at high redshift. The combination of the double peak redshift distribution and that none strong emission line appears to be in the peaks of the distribution makes difficult to disentangle which line corresponds to the observed one. We do not attempts to assign a redshift to the galaxy based in the observed emission line.

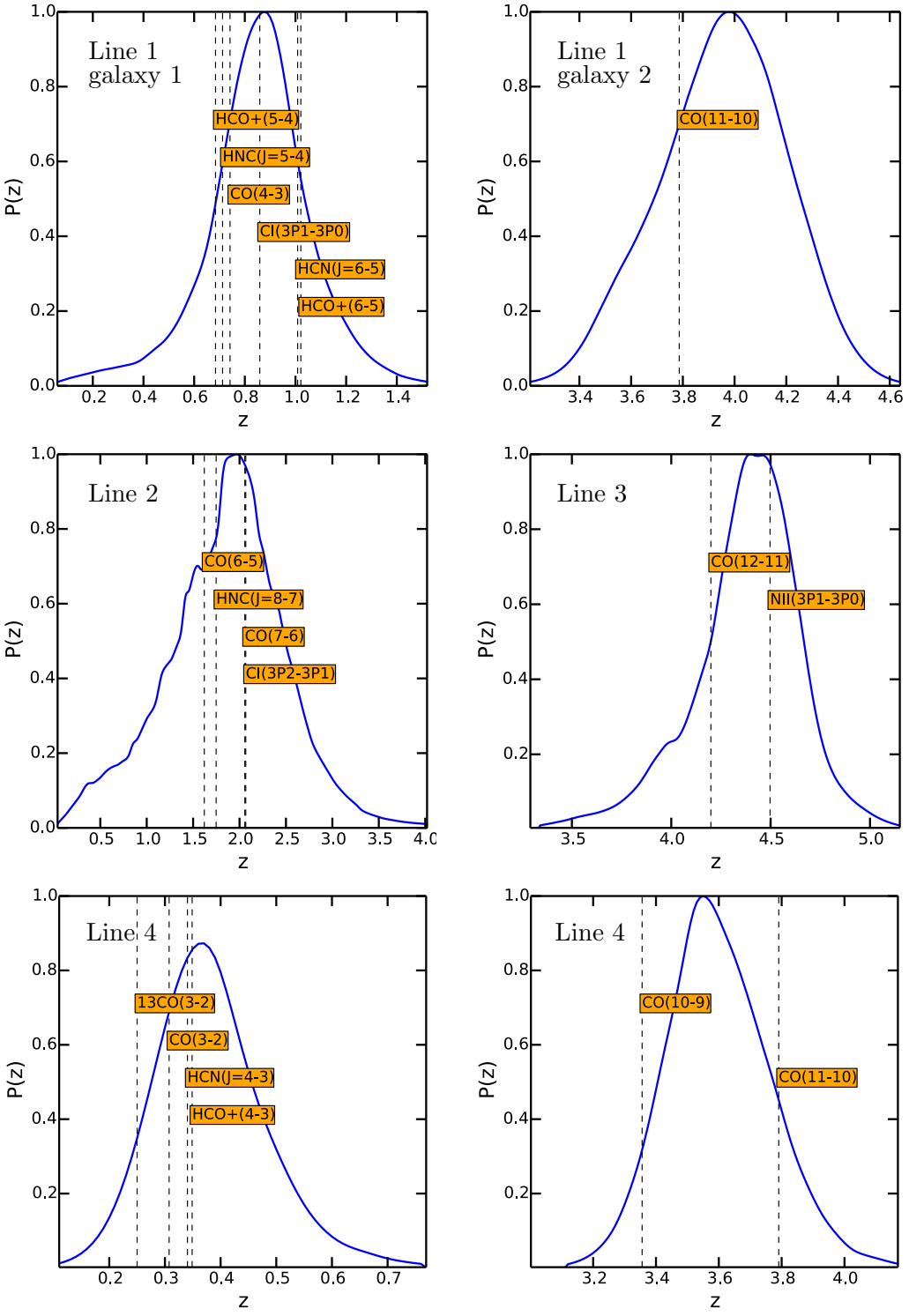

Figure 3.26 Redshift probability distribution of the possible counterparts to the emission lines detected in the data cube. Each probability distribution is normalized to the peak of the distribution. For each distribution, the vertical lines corresponds to the redshift that the galaxy would be if the detected line corresponds to the one in the label. The closest the line to the peak of the distribution higher are the chances that the observed line corresponds to that.

3.4.5 Positional Offsets

As we can see in Fig. 3.13, 3.21, 3.23, 3.24 and 3.25, there are clear offsets of up to 1.3" between the continuum and line emission and the optical detected galaxies. That offsets can be explained if there are no relation between the mm observed signals and the optical galaxies, meaning that the counterpart correspond to very obscured galaxies or that all the mm signals are fake, both options very unlikely but not impossible. Offsets between FIR emission lines and optical or new infrared counterparts have been observed before in lensed galaxies behind galaxy clusters. Johansson et al. (2012) observed CO(3-2) and CO(1-0) emission lines in a lensed galaxy behind the bullet cluster finding offsets of up to $\sim$ 2". They claim that the observed offsets could be the results of the combination of pointing uncertainties, low signal-to-noise ratio and the elongated beam. Such effects could be also producing our observed offsets.

To check weather the offsets corresponded to a pointing error we checked if there was a privileged direction for the offset shifting. There is a small tendency of the offset toward the axis of the elongated axis of the synthesized beam but in both directions, the other offsets have different directions. We concluded that the offsets are not produced by a pointing error. We also checked if there was a dependency of the offsets with the observed signal-to-noise but not dependency was observed. Finally, we noted that the emission lines showed a higher offset value while closer to the region of maximum magnification, as the cases for L1, L3 and L4. Because of this, we explore the relation between the offsets and the magnification.

The offsets of the galaxies were measured as the the distance between the brightest pixel in either the continuum emission or in the line emissions of our ALMA observations with the nearest galaxy detected in CLASH. To estimate the magnification, we can not use the value of magnification given by the models because for three of the emission lines, the nearest galaxies have not a well defined photometric redshift so the magnification can not be constrained. As an alternative to the magnification, we use the distance to the critical curve of the galaxy cluster for a source at $z = 2$. The critical curve represent the region where the magnification is maximum for a given source redshift. The critical curves for sources at different redshift are different, but should be located very close, as we can see in Zitrin et al. (2012) where the critical curves for sources at z=2 and z=6 are very similar for the cluster MACS0329. The normal distance between a lensed galaxy and the critical curve at $z = 2$ should be a good indicator of its magnification. For our measurement and for practical reasons, we used the critical curve as the region where the magnification is $\mu > 500$, while the real critical curve is where the magnification trends to infinity. In Fig. 3.27 we plot the offsets of our ALMA detected sources (continuum and line emission) and the distance to the critical curve at $z = 2$. We see that the points

show a clear trend to have higher offset values while closer to the critical curve (smaller distance), where the magnification is higher. In blue is shown the power law function that best fit the points, with the purpose of showing the observed trend.

The observed behavior could be explained if the continuum and line emissions are not produced in the exact region of the lensed galaxies, meaning that there is an intrinsic offset between the optical and the submm emission. Such offsets should be amplified by the magnification of the galaxy cluster by a value $\sim \sqrt{\mu}$, resulting in an offset higher for the most magnified galaxies. The magnification μ can be defined as the ratio of the observed and the intrinsic area of a lensed galaxy, $\mu \propto A$. The intrinsic offset is a linear distance in the galaxy, such linear distance l can be roughly proportional to the area, meaning that $l \propto \sqrt{A}$ and therefore $l \propto \sqrt{\mu}$. Because we are using the normal distance (d) of the galaxy to the critical curve we used the fact that $\mu \propto 1/d$ to find that $l \propto 1/\sqrt{d} \propto d^{-0.5}$. The fact that the power law that best fit the two quantities in Fig. 3.27 has an index of $\alpha = -0.46 \sim -0.5$ could support our explanation for the observed offset. This hypothesis can not be confirmed with our current observations. Obtaining optical spec-z for the nearest optical galaxies could confirm the association between the observed FIR emission lines and the optical galaxies, therefore confirming the offsets. Deeper ALMA observations could also help disentangle the reason of the observed offsets.

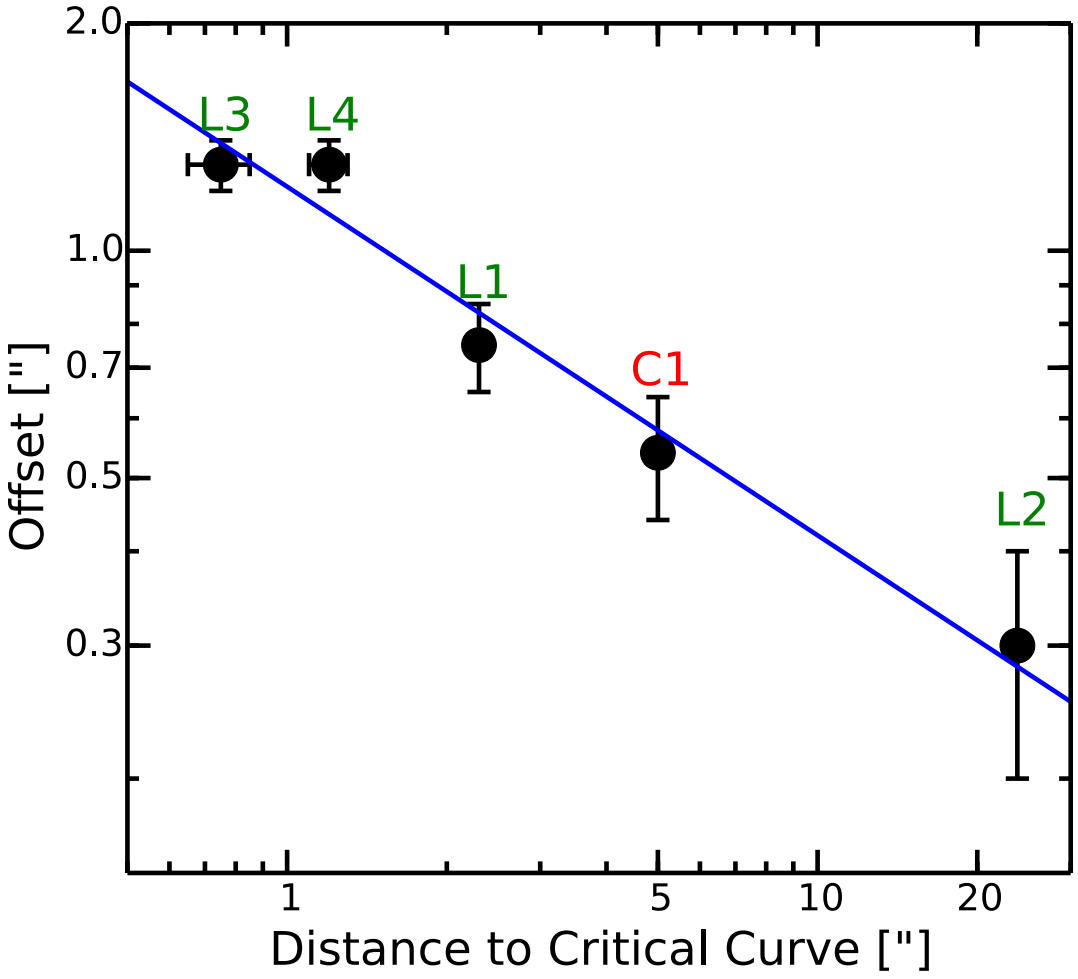

Figure 3.27 Offset between the optical detected galaxies nearest to the continuum and line emission detected in our ALMA observation vs the distance to the critical curve of the galaxy cluster at $z = 2$. The offsets and distances were calculated between the center of the optical galaxies and the brightest pixel of the mm source. The errors of the points correspond to the size of the pixel in the ALMA observations of 0.1". The point label as C1 corresponds to the continuum detection of the galaxy at $z_{\rm ph} = 3.5$ and the other points correspond to the emission lines. The blue line correspond to a power law fit with an index of -0.46.

Chapter 4

Submillimeter Galaxies behind the CLASH galaxy clusters.

4.1 Introduction

Submillimeter galaxies (SMG) represent a population of dusty, highly star-forming, high-redshift galaxies. They were first observed as part of blind surveys with Submillimeter Common-User Bolometer Array (SCUBA) (Eales et al., 1999; Hughes et al., 1998; Smail et al., 1997). Their large infrared (IR) luminosities ($> 10^{12} L_{\odot}$) make them important contributors to the luminosity density at early epochs (Le Floc'h et al., 2005). These SMGs are heavily obscured objects that often co-exist with active galactic nucleus (AGN) of minor luminosity, despite of that, their are powered mainly by star-formation activity of ~ 1000 $M_{\odot}$ yr^{-1} (Alexander et al., 2005).

The starbursting nature of SMGs appears to be driven by major gas-rich mergers (Combes et al., 2012; Engel et al., 2010; Riechers et al., 2011; Tacconi et al., 2008; Wang et al., 2011) or by the accretion of cold gas (Davé et al., 2010; Dekel et al., 2009; van de Voort et al., 2011). SMGs usually have stellar masses of $\sim 10^{10}$ $M_{\odot}$ and dust masses of 10^{8-9} $M_{\odot}$ (Hainline et al., 2011; Magdis et al., 2012; Magnelli et al., 2012; Santini et al., 2010; Simpson et al., 2014)

Despite of some SMGs being extreme objects with high star formation rates (SFRs) that contribute largely to the star formation in the Universe, even at the high redshift (Riechers et al., 2013), they are not the representative of the SMGs population. The steep number count distribution shows that the number of SMGs increases for low flux densities, being most of them at sub-mJy flux densities (Chapman et al., 2001; Hughes et al., 1998; Knudsen et al., 2008; Smail et al., 2002).

It is difficult to study this sub-mJy population because of the low resolution of the used bolometers and the confusion limit. Massive galaxy clusters at $z < 1$ have been largely used to find intrinsically faint star forming galaxies in the submm/mm regime, aided by the gravitational lensing magnification (Boone et al., 2013; Chapman et al., 2002; Egami et al., 2010; Johansson et al., 2012, 2010, 2011; Knudsen et al., 2006, 2005, 2008; Rex et al., 2009; Sklias et al., 2014; Smail et al., 1997, 2002; Wardlow et al., 2010). In such way, the lower end of the submillimeter flux density number counts can be probed and the properties of these galaxies can be studied in much more detail than possible for 'blank-field' selected SMGs. Although most cluster fields studied so far count with important ancillary multi-wavelength datasets, few of them are able to produce detailed lensing models that enable to reconstruct the background sources in the image plane, and hence study their morphologies. This is a critical requirement in order to disentangle the major channel for galaxy growth: i.e. galaxy mergers vs. cold mode accretion scenarios.

In the case of galaxy mergers, the distribution of stars and gas is centrally concentrated, as observed in local ULIRGs (Mihos and Hernquist, 1996); while in the latter, the gas and stars are distributed across the disk, punctuated by kpc-regions of enhanced star-formation and gas density (Dekel et al., 2009). For this, high-angular resolution multi-wavelength imaging to resolve internal structure within the lenses (particularly giant arc lenses) are needed, thus benefiting from the increase in spatial resolution provided by lensing, is crucial.

One of the most interesting cases is the lensed SMG SMMJ0658 at $z = 2.79$ discovered behind the Bullet Cluster with a magnification of ~ 100 (Gonzalez et al., 2010; Johansson et al., 2010, 2011; Rex et al., 2009). SMMJ0658 was observed as a bright source with APEX LABOCA at 870 μm but corresponds to the combined emission of two lensed images, which were observed in CO emission lines with a interferometer afterward. This corresponds to a good example of how to use galaxy clusters to study the faint population of SMGs. In this work we do a search for similar lensed bright SMGs behind a sample of galaxy clusters belonging to the CLASH survey.

In section 2 we present the observations used for this project, in Section 3 we present the results of the observations together with source extraction and flux deboosting. In section 4 we present how we search for candidates to the observed sub and mm sources, in section 5 we present the implication of that counterparts and finally in section 6 we present a summary and conclusion of our work. Throughout this paper we use a Λ-Cold Dark Matter cosmology with $H_0 = 70$ km s^{-1} Mpc^{-1}, $\Omega_\Lambda = 0.7$ and $\Omega_m = 0.3$.

4.2 Observations

4.2.1 LABOCA

Thirteen galaxy clusters were observed with The Large Apex BOlometer CAmera (LABOCA) (Siringo et al., 2009) in the Atacama Pathfinder EXperiment (APEX). The data was taken in July, August and December of 2012 and in May and June of 2013. The data was reduced using the Comprehensive Reduction Utility for SHARC-2 (CRUSH) using the calibrations provided by the APEX telescope team. CRUSH uses the combination of the skydips observations together with the radiometer data taken during the observation to calibrate the data. As flux calibrators were used primary planets observed together the targets. The reduction configuration was set to look for point sources within the beam of LABOCA of 19.2″.

4.2.2 GISMO

Three Galaxy clusters were observed using the Goddard-IRAM Superconducting 2 Millimeter Observer (GISMO) (Staguhn et al., 2008) in Institut de radioastronomie millimétrique (IRAM) 30 meters telescope. The data was taken in October 2013 and April 2014. The data was also reduced using CRUSH. The reduction configuration was set to look for point sources within the beam of GISMO of 16.7″. In both cases the pointing model used was the ones provided by the instruments support members and included in the latest version of the CRUSH package.

4.2.3 Complementary data.

The HST CLASH collaboration is a survey to map 25 galaxy clusters with 16 HST filters. The photometry is public as well as the photometric redshift estimated for each detected galaxy. Herschel Space Observatory images of the galaxy cluster were acquired from the archive when available, corresponding to The Photodetector Array Camera and Spectrometer (PACS) and The Spectral and Photometric Imaging REceiver (SPIRE) instruments. The images were already calibrated in Jyb^{-1} or in $\mathrm{Jypixel}^{-1}$. The images calibrated in $\mathrm{Jypixel}^{-1}$ were transformed to Jyb^{-1}.

The three bands of SPIRE correspond to the 250, 350 and 500 μm , with beam sizes of FWHM of $18.1, 25.2, 36.6''$ respectively (Griffin et al., 2010). The two bands of PACS correspond to the 100 and 160 μm , with beam sizes of 6.5 and 10.3″ respectively (Poglitsch et al., 2010). For the search for counterparts for the LABOCA and GISMO sources they

where assumed as point sources in the PACS and SPIRE observations. A summary of the depth of the PACS and SPIRE images is in Tab. 4.3.

4.3 Results

The depth reached for each cluster can be found in Tab. 4.1 for the LABOCA observations and in Tab. 4.2 for the GISMO observations. Not all the galaxy clusters have the same exposure time therefore the difference between the rms reached. In Fig. 4.1 we plot the histogram of all the pixels signal-to-noise belonging to the LABOCA observations and compare the distribution with a gaussian distribution. In the bottom of the figure we also plot the ratio between the histogram observed and the gaussian function for the corresponding signal-to-noise value, we see how the ratio is constant between $S/N = -4$ and $S/N = 2$, beyond that point the ratio begins to raise as product of the real sources. We see how the distribution of errors is well described for a gaussian function.

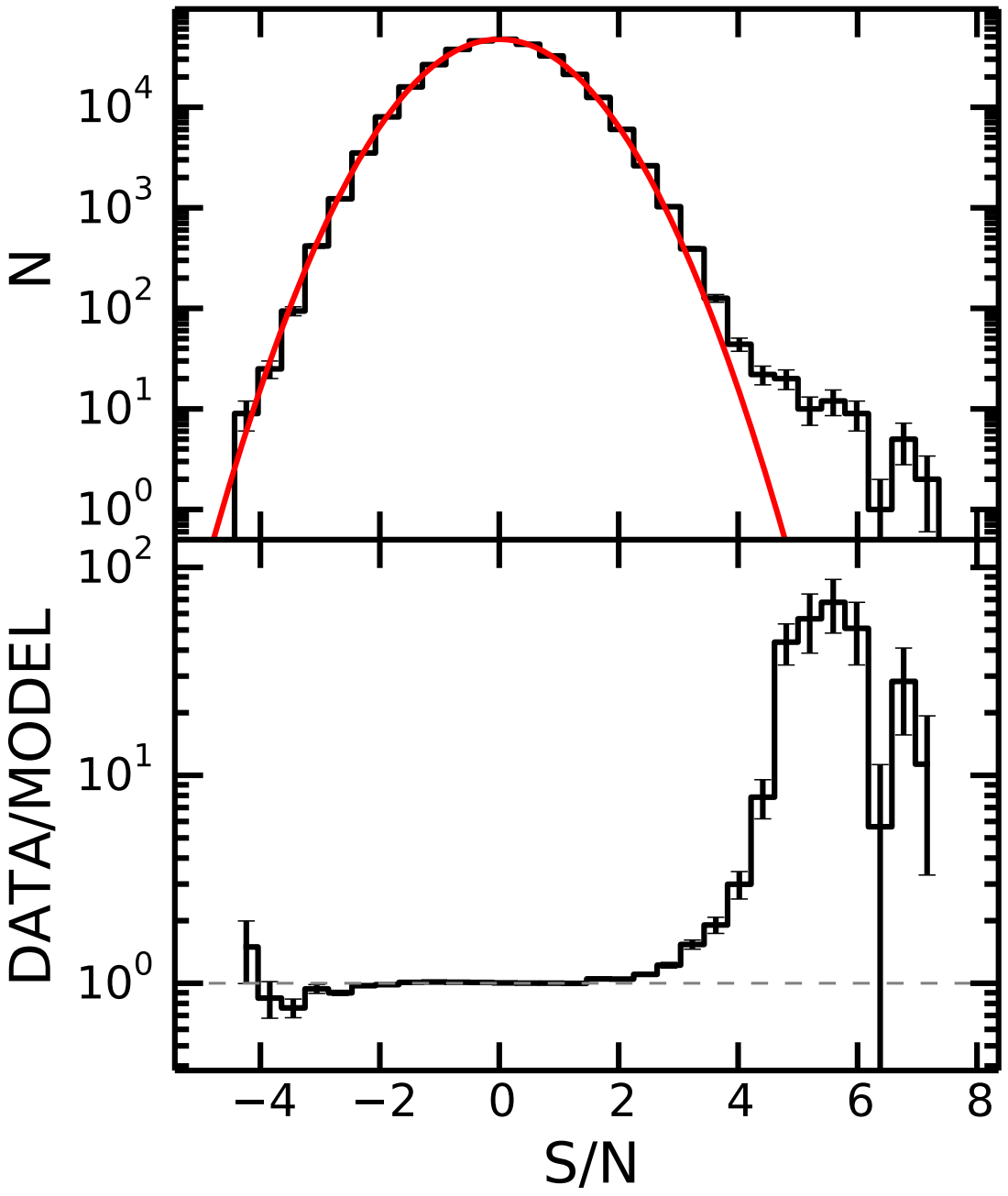

Figure 4.1 Histogram of the pixels in signal-to-noise for the LABOCA observations. The red line corresponds to a gaussian noise. In the bottom of the plot we can see the ratio of the data and the gaussian noise. The error bars in the upper plot correspond to the square root of the number of pixel per interval. The error bars in the bottom plot correspond to the error propagation of the errors in the counts. At signal-to-noise higher to 3 we can see how the data is clearly departing from the gaussian model, indicating the existence of real sources.

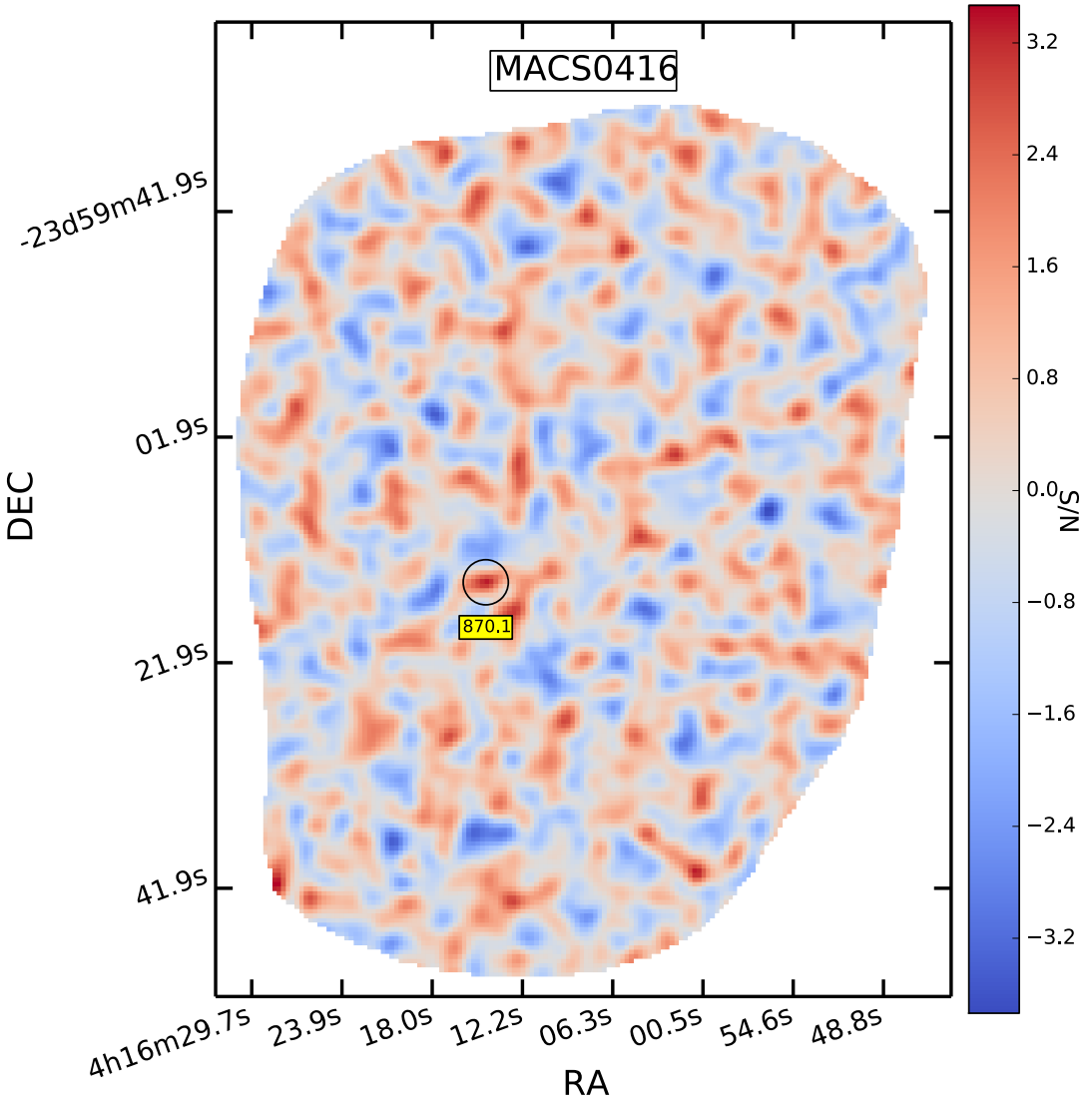

Figure 4.2 LABOCA signal-to-noise map towards the galaxy cluster MACS0416. Each detected source is marked as black circle with the corresponding name.

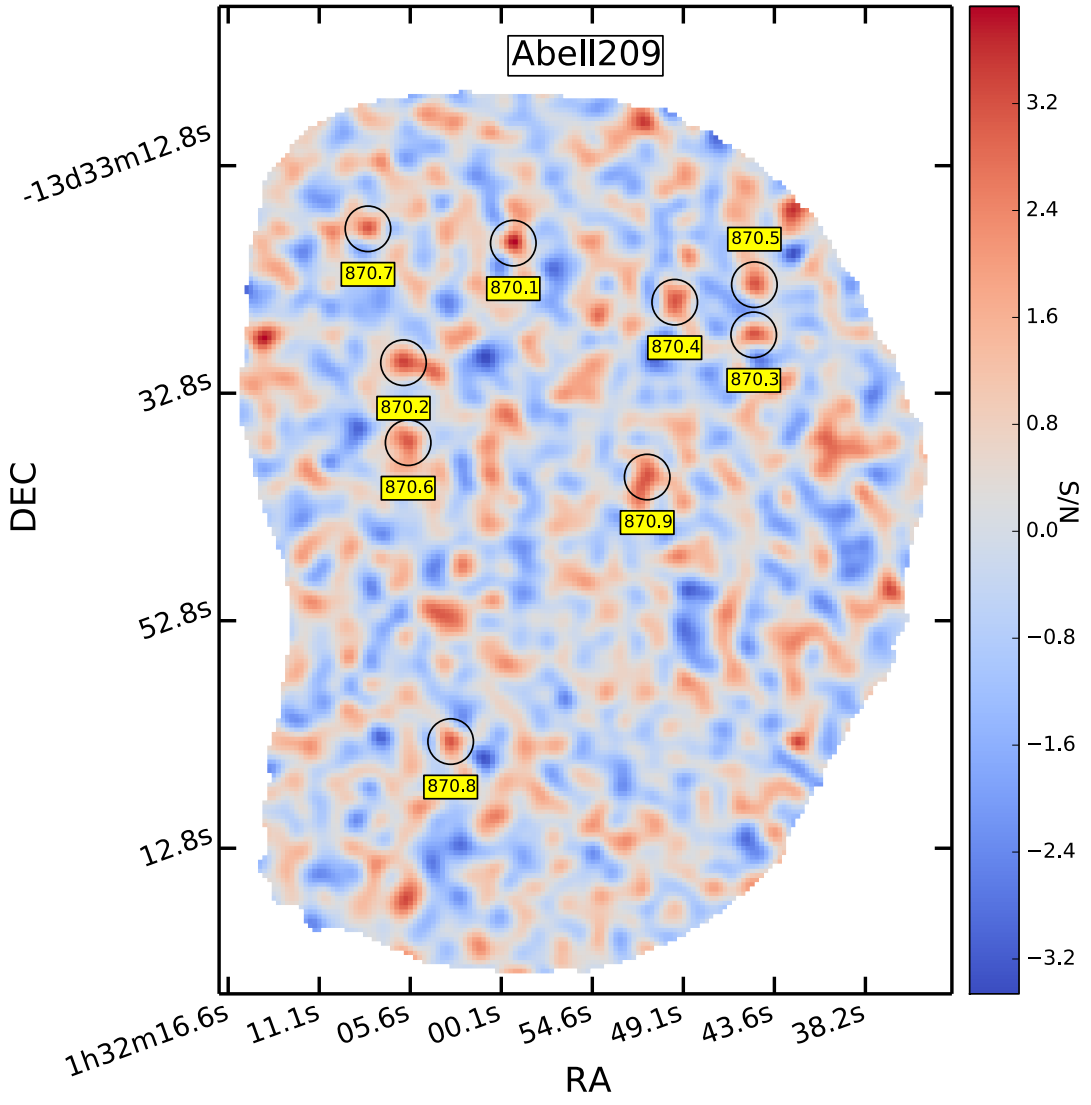

Figure 4.3 LABOCA signal-to-noise map towards the galaxy cluster Abell209. Each detected source is marked as black circle with the corresponding name.

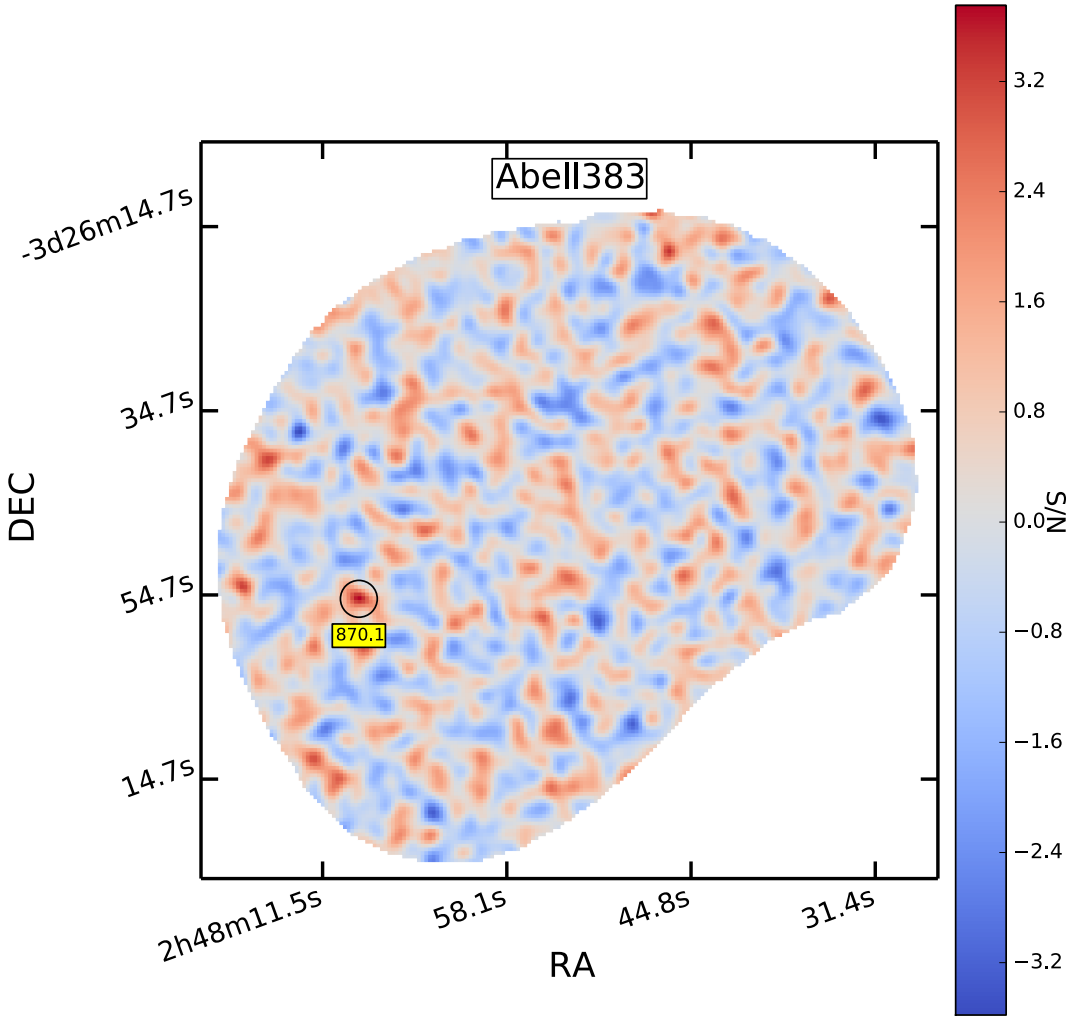

Figure 4.4 LABOCA signal-to-noise map towards the galaxy cluster Abell383. Each detected source is marked as black circle with the corresponding name.

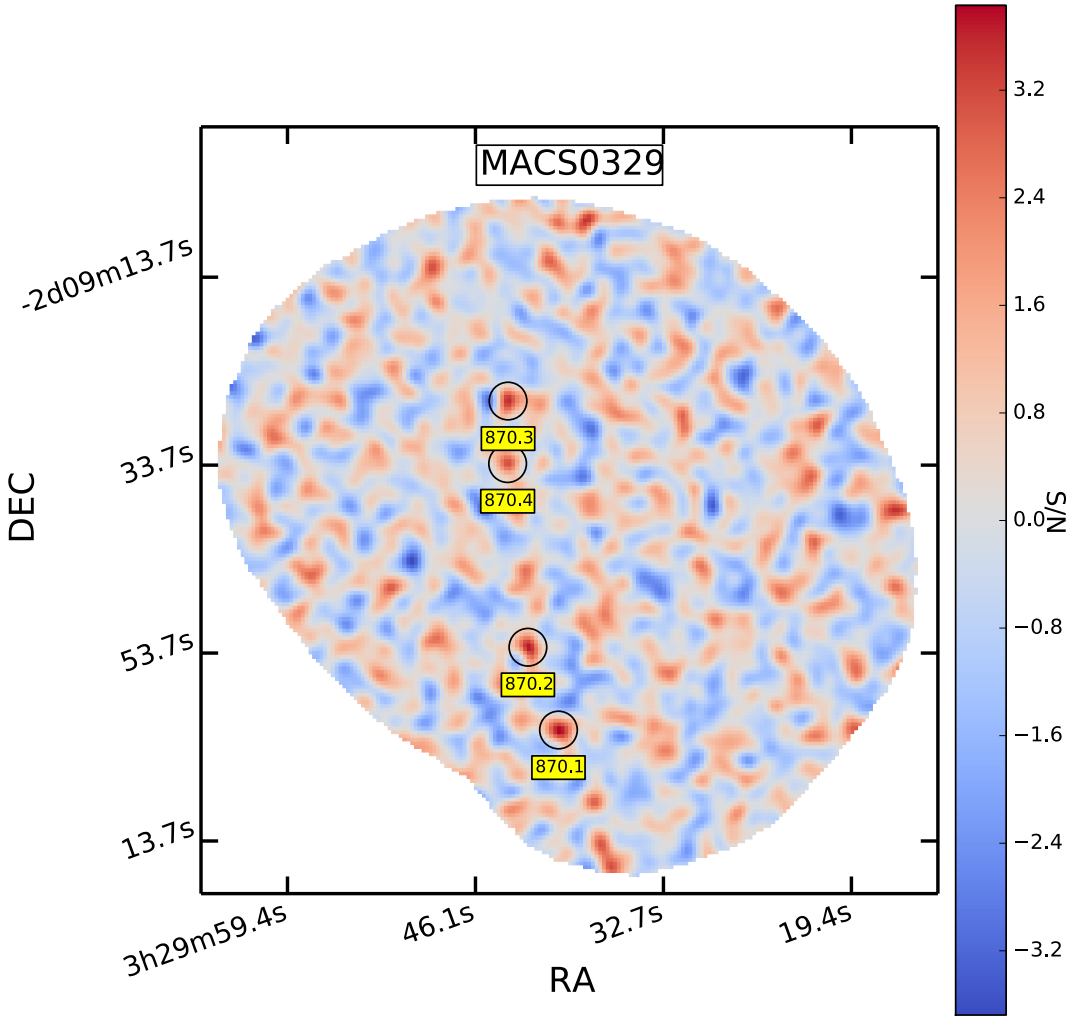

Figure 4.5 LABOCA signal-to-noise map towards the galaxy cluster MACS0329. Each detected source is marked as black circle with the corresponding name.

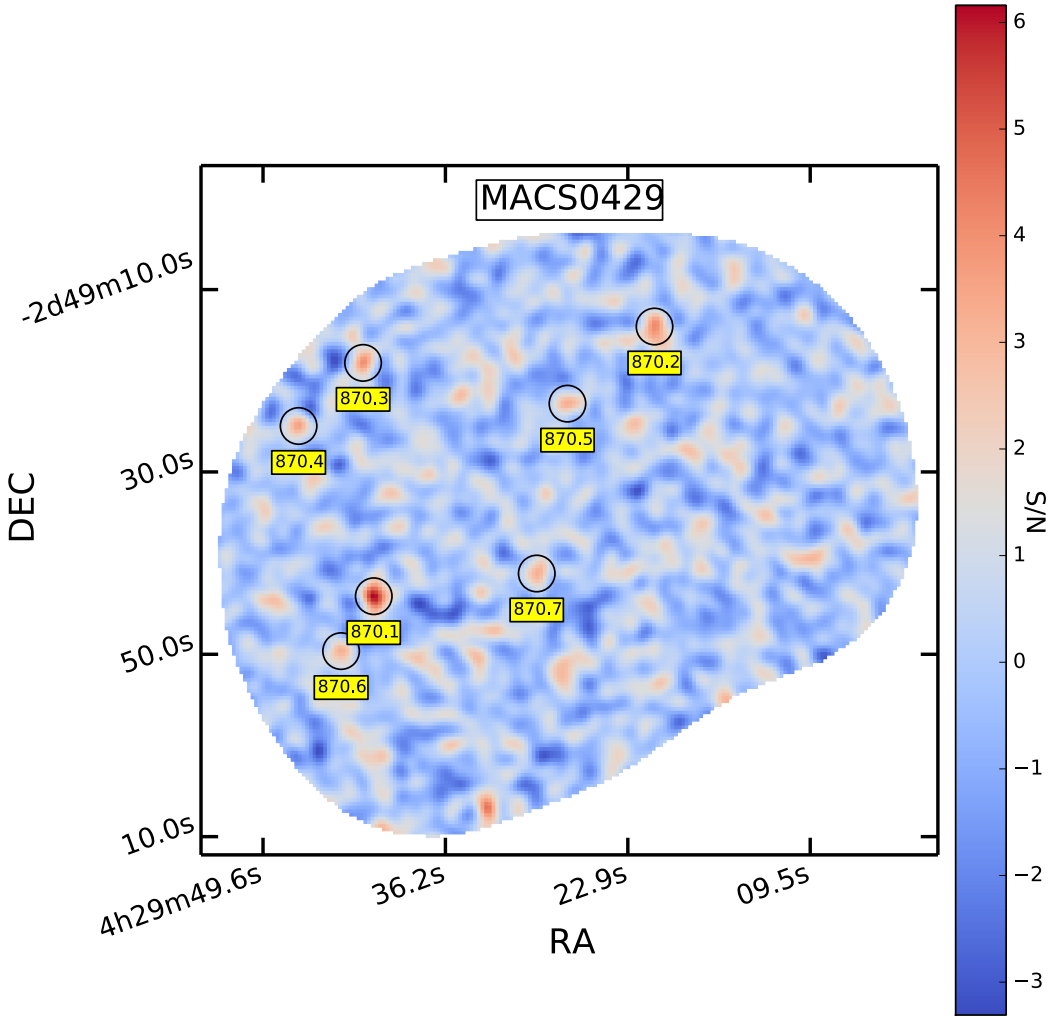

Figure 4.6 LABOCA signal-to-noise map towards the galaxy cluster MACS0429. Each detected source is marked as black circle with the corresponding name.

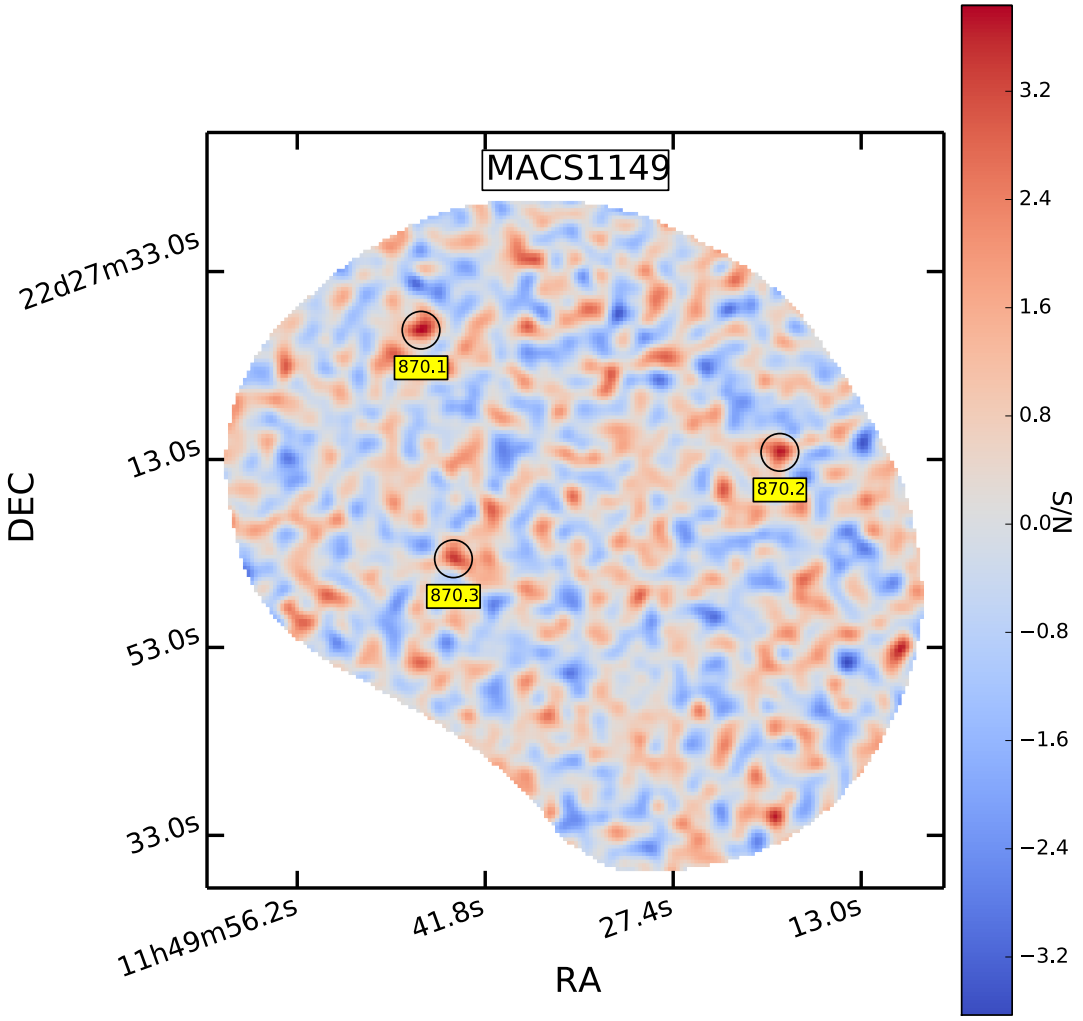

Figure 4.7 LABOCA signal-to-noise map towards the galaxy cluster MACS1149. Each detected source is marked as black circle with the corresponding name.

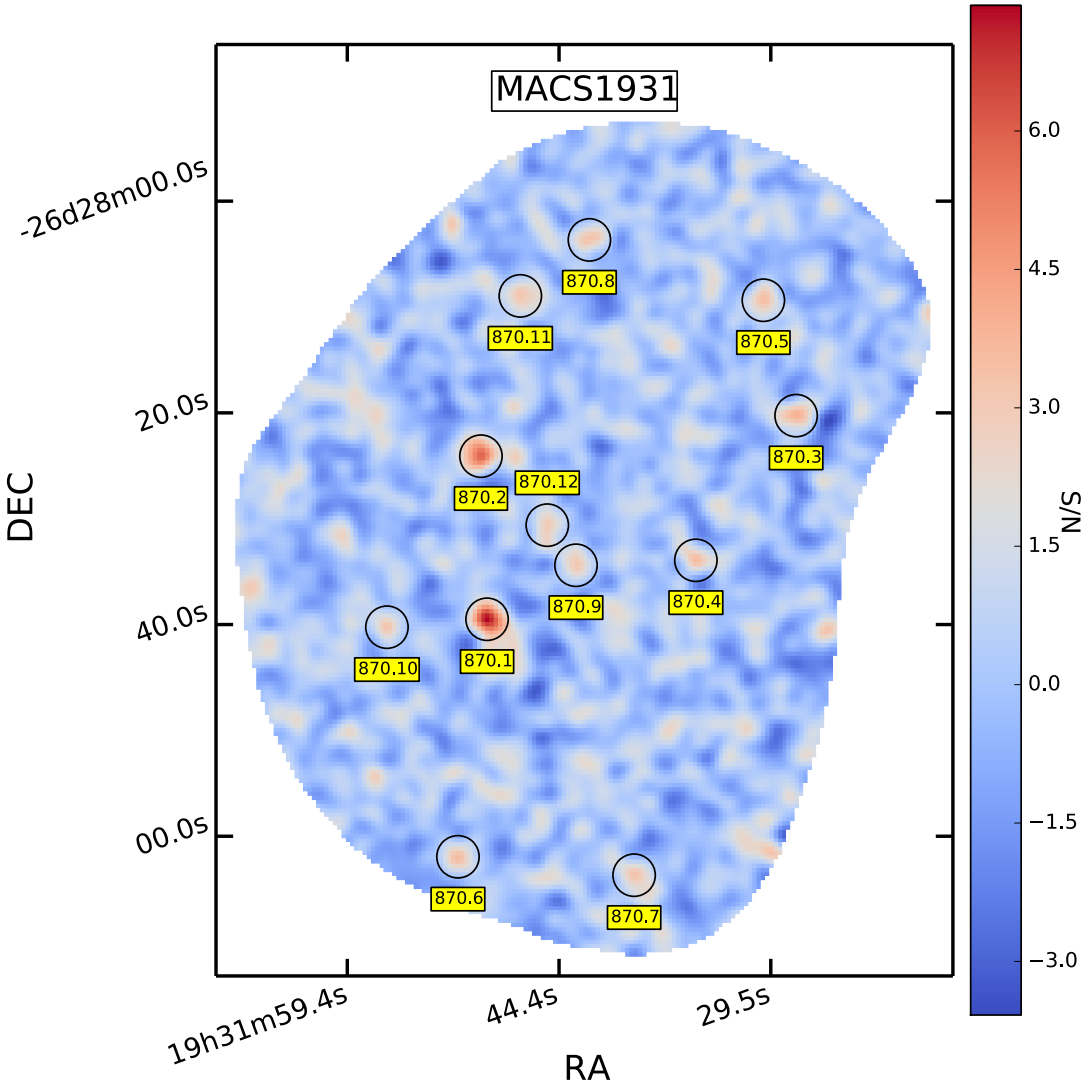

Figure 4.8 LABOCA signal-to-noise map towards the galaxy cluster MACS1931. Each detected source is marked as black circle with the corresponding name.

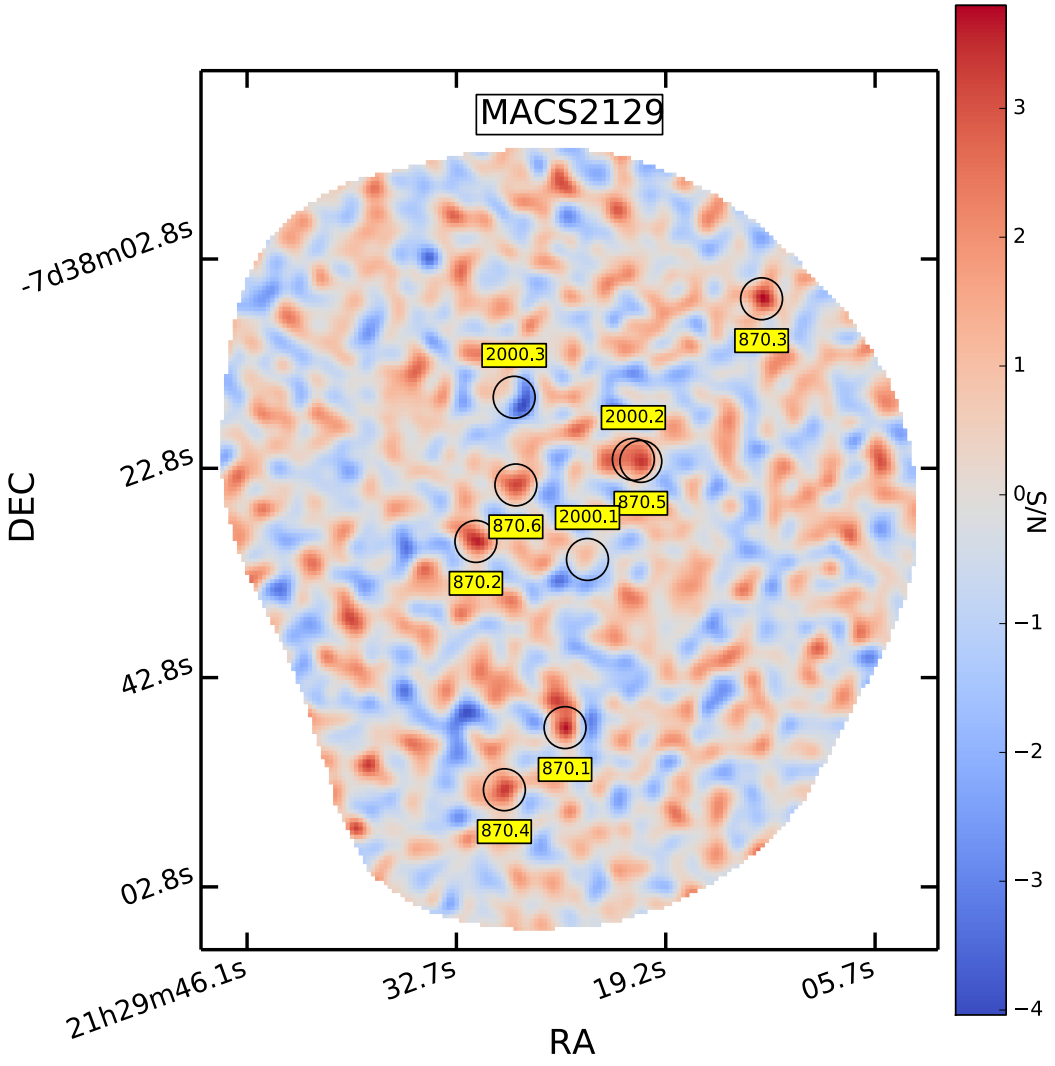

Figure 4.9 LABOCA signal-to-noise map towards the galaxy cluster MACS2129. Each detected source is marked as black circle with the corresponding name. Here are also plotted the GISMO detection.

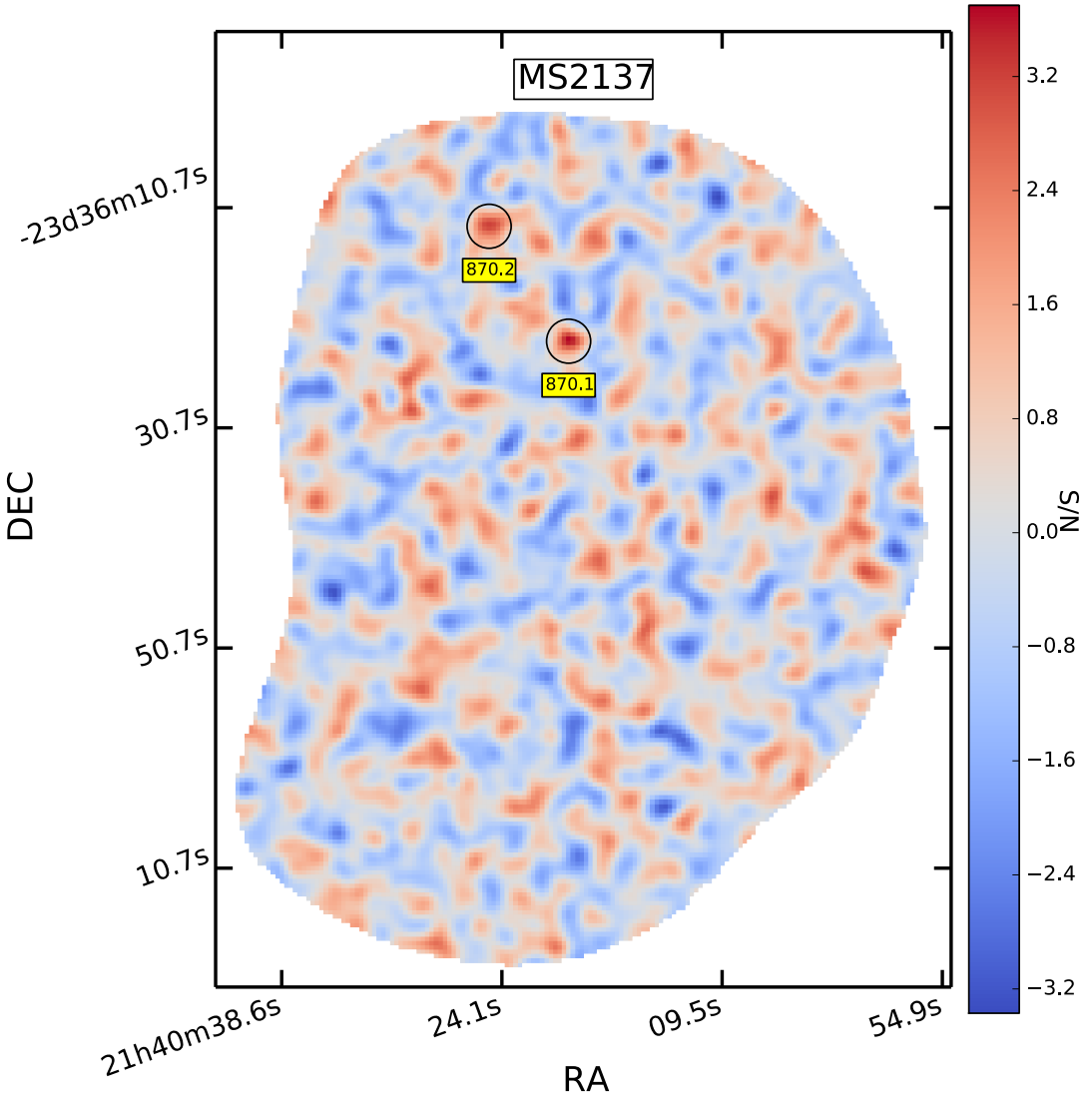

Figure 4.10 LABOCA signal-to-noise map towards the galaxy cluster MS2137. Each detected source is marked as black circle with the corresponding name.

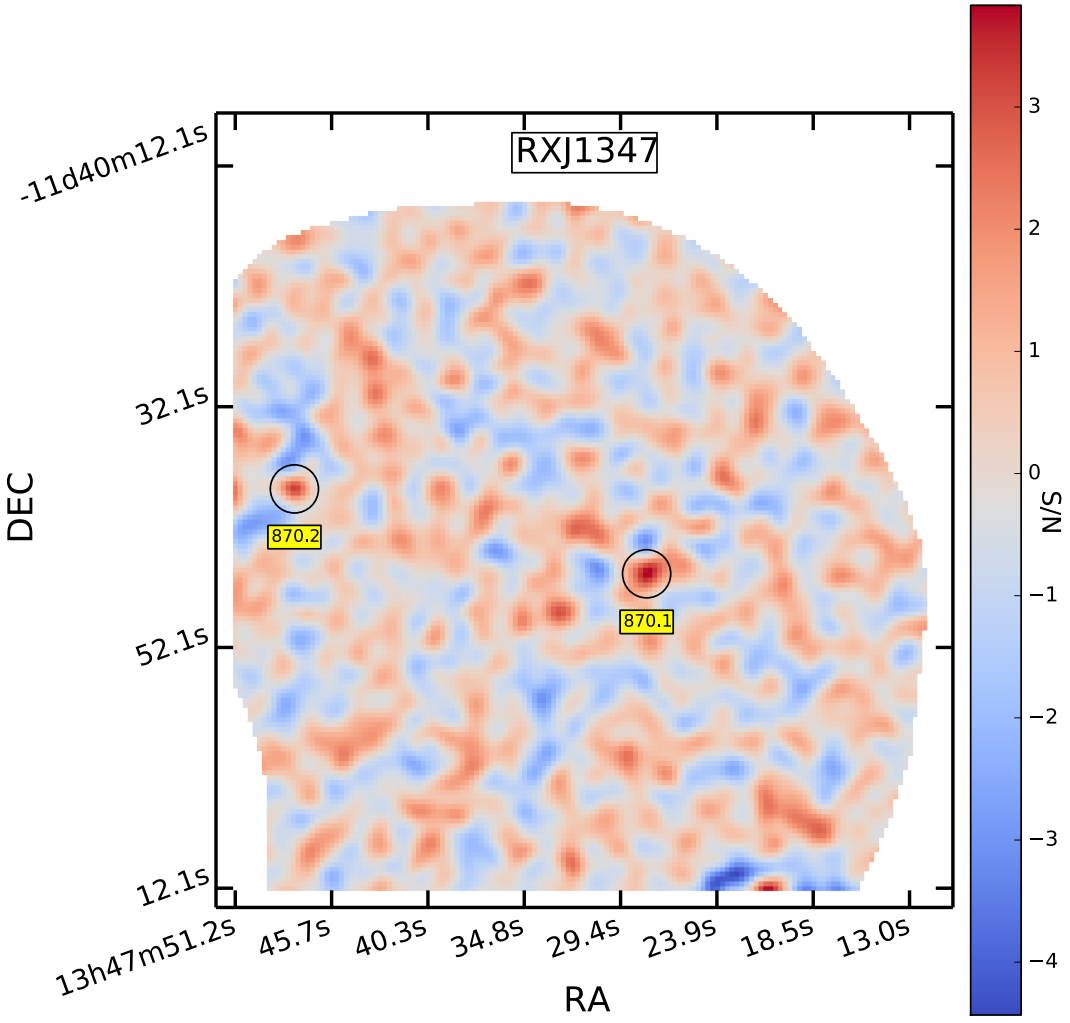

Figure 4.11 LABOCA signal-to-noise map towards the galaxy cluster RXJ1347. Each detected source is marked as black circle with the corresponding name.

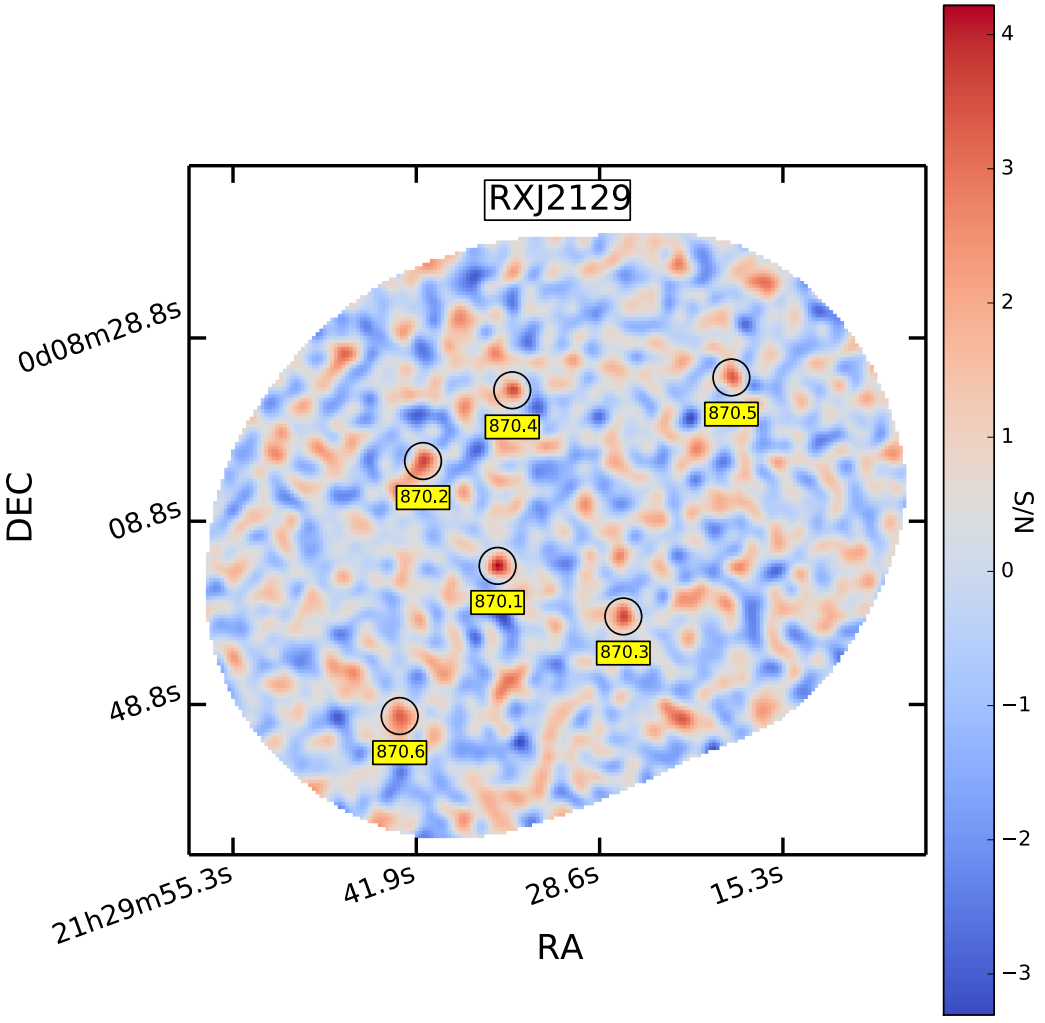

Figure 4.12 LABOCA signal-to-noise map towards the galaxy cluster RXJ2129. Each detected source is marked as black circle with the corresponding name.

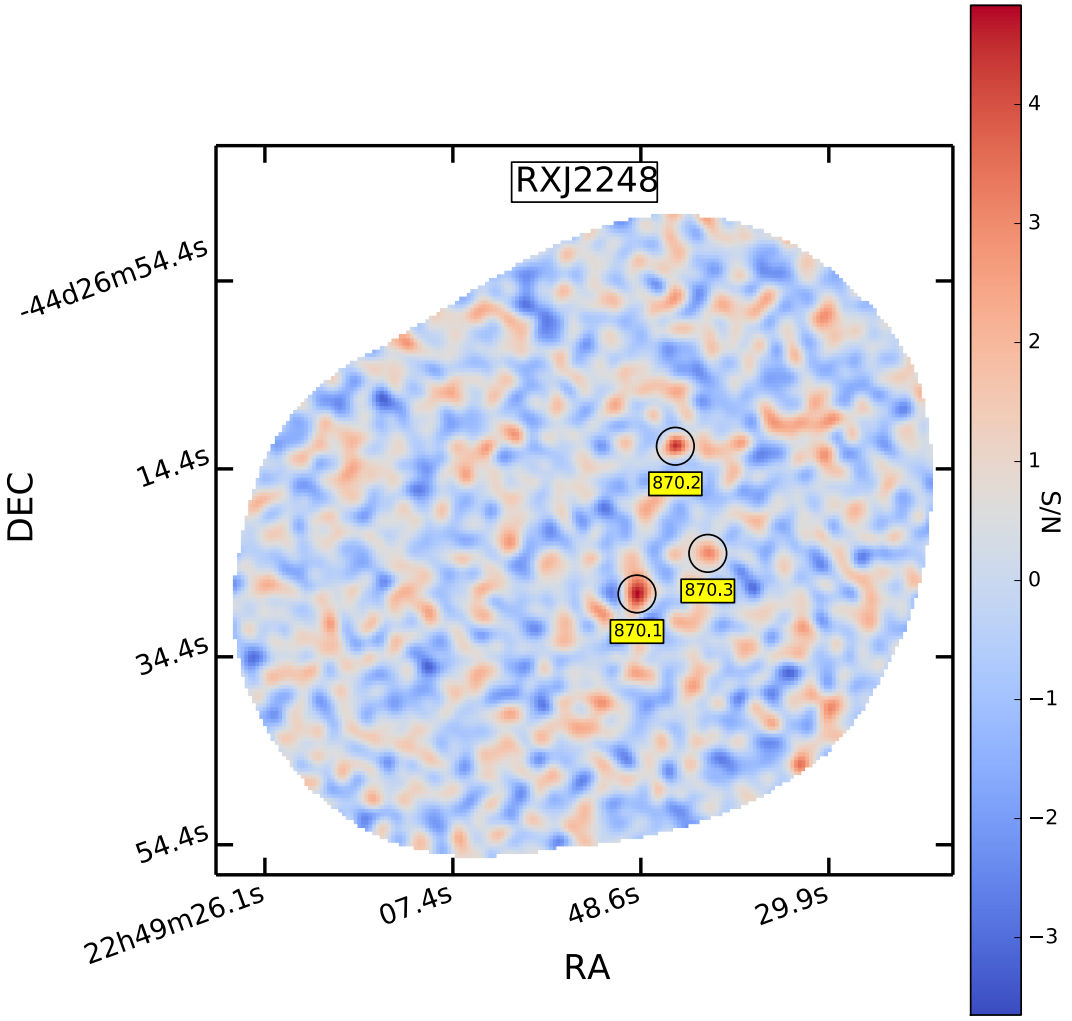

Figure 4.13 LABOCA signal-to-noise map towards the galaxy cluster RXJ2248. Each detected source is marked as black circle with the corresponding name.

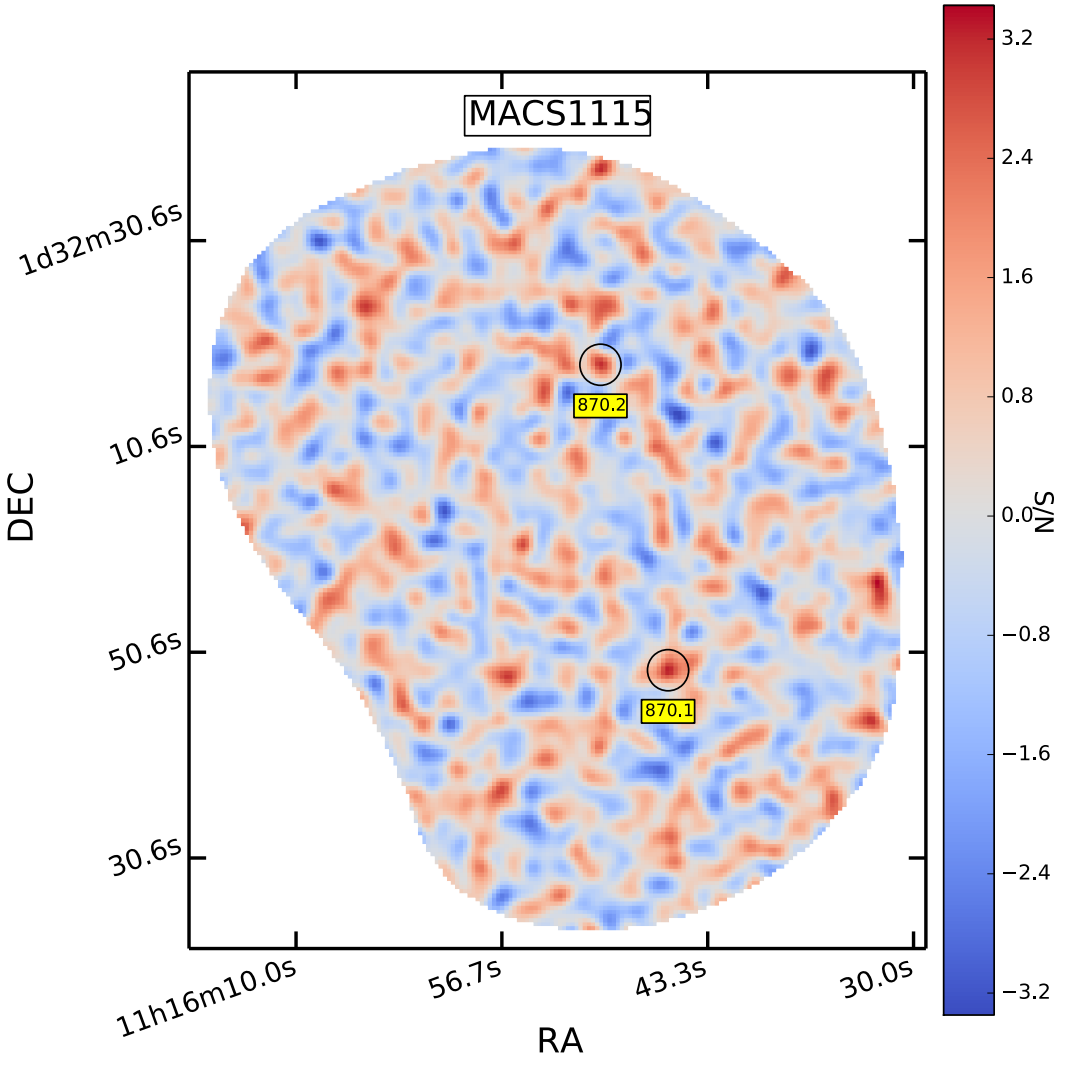

Figure 4.14 LABOCA signal-to-noise map towards the galaxy cluster MACS1115. Each detected source is marked as black circle with the corresponding name.

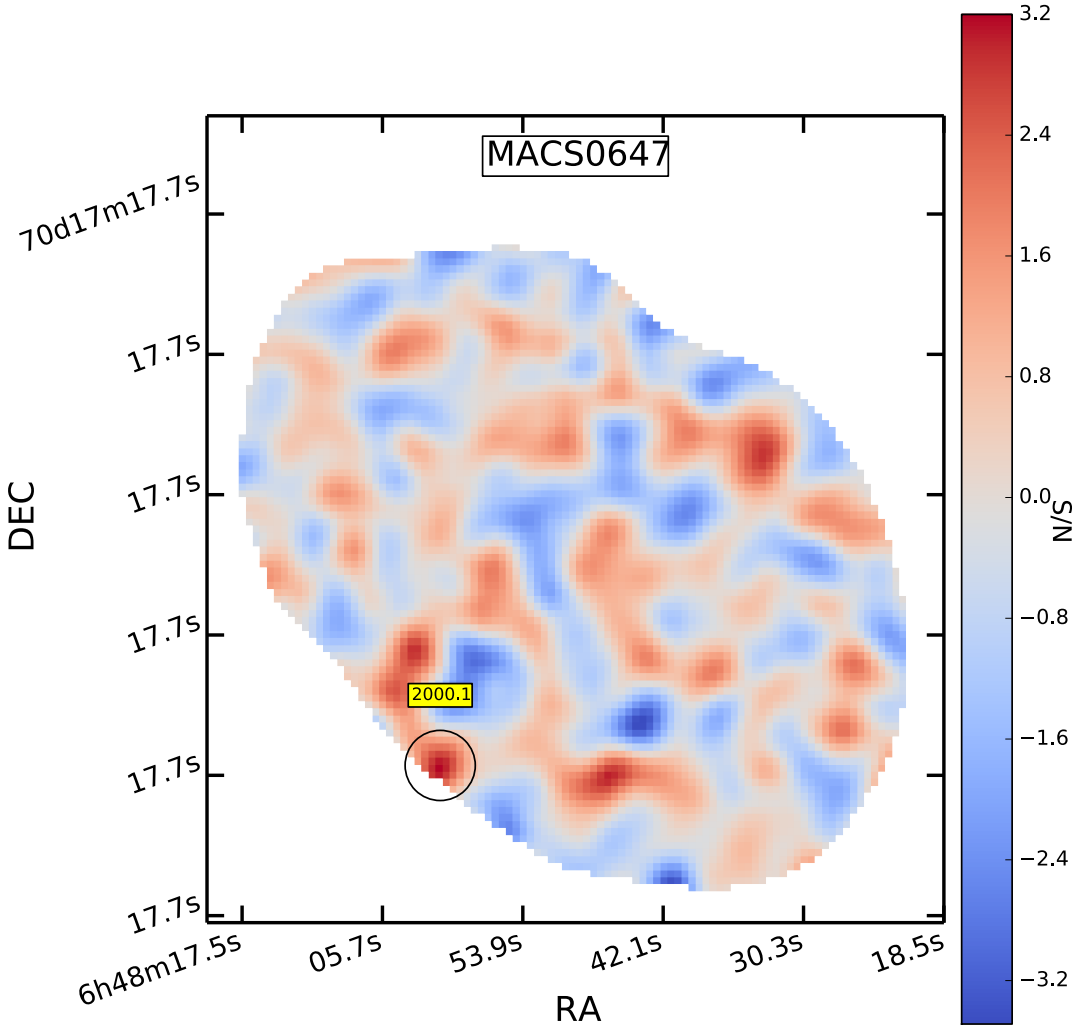

Figure 4.15 GISMO signal-to-noise map towards the galaxy cluster MACS0647. Each detected source is marked as black circle with the corresponding name.

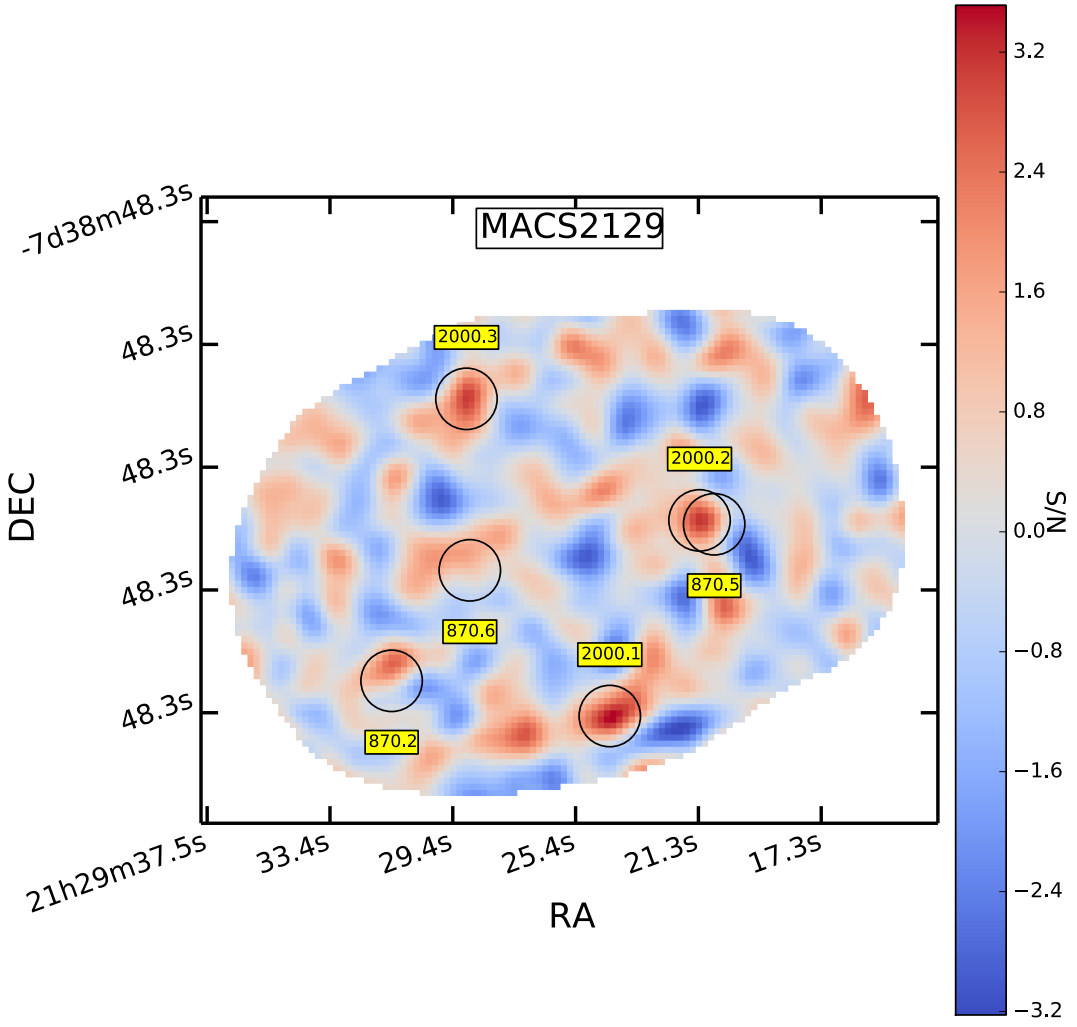

Figure 4.16 GISMO signal-to-noise map towards the galaxy cluster MACS2129. Each detected source is marked as black circle with the corresponding name. Here are also plotted the LABOCA detection.

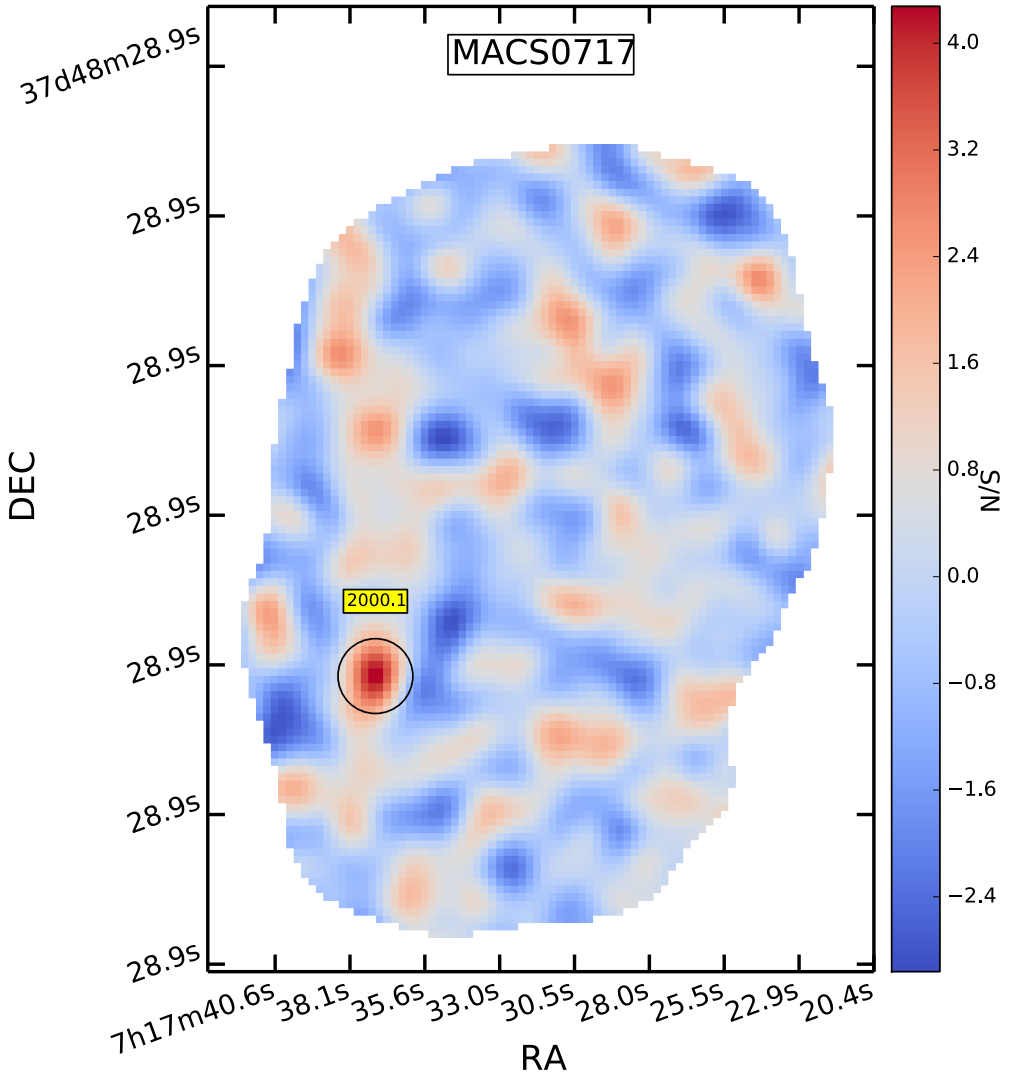

Figure 4.17 GISMO signal-to-noise map towards the galaxy cluster MACS0717. Each detected source is marked as black circle with the corresponding name.

Table 4.1. Properties of the galaxy clusters observed with LABOCA/APEX

Cluster	RA (J2000)	DEC (J2000)	$z_{\rm Cl}$	RMS [mJy b^{-1}]
Abell 209	01:31:52.57	-13:36:38.8	0.206	8.4
Abell 383	02:48:03.36	-03:31:44.7	0.187	8.4
MACS0329.7-0211	03:29:41.68	-02:11:47.7	0.450	7.5
MACS0416.1-2403	04:16:09.39	-24:04:03.9	0.42	3.1
MACS0429.6-0253	04:29:36.10	-02:53:08.0	0.399	3.0
MACS1115.9+0129	11:15:52.05	+01:29:56.6	0.352	1.9
MACS1149.6+2223	11:49:35.86	+22:23:55.0	0.544	3.0
RXJ1347.5-1145	13:47:30.59	-11:45:10.1	0.451	3.8
MACS1931.8-2635	19:31:49.66	-26:34:34.0	0.352	2.5
MACS2129.4-0741	21:29:26.06	-07:41:28.8	0.570	2.3
RXJ2129.7+0005	21:29:39.94	+00:05:18.8	0.234	3.4
MS2137-2353	21:40:15.18	-23:39:40.7	0.313	2.8
RXJ2248.7-4431 (Abell 1063S)	22:48:44.29	-44:31:48.4	0.348	2.9

Note. — The RMS correspond to the deepest region of the observations. References: Coordinates and redshift from Postman et al. 2012.

Table 4.2. Properties of the galaxy clusters observed with GISMO

Cluster	RA (J2000)	DEC (J2000)	$z_{\rm Cl}$	RMS [$\times 10^{-4}$ Jy b^{-1}]
MACS0647.8+7015	06:47:50.03	+70:14:49.7	0.584	2.2
MACS0717.5+3745	07:17:31.65	+37:45:18.5	0.548	2.4
MACS2129.4-0741	21:29:26.06	-07:41:28.8	0.570	1.7

Note. — These galaxy clusters were selected as high magnification clusters. References: Coordinates and redshift from Postman et al. 2012.

4.3.1 Source Extractor

To find the sources we used the task provided together with CRUSH, the name of the task is 'detect'. The extraction algorithm implements a false-detection rate approach, that continues until a set false detection (or detection confidence) goal is reached. Each source extracted from the maps has an assigned confidence level, based on the likelihood of being a false detection at the same significance level in the given extraction area. The task also returns a cumulative number of false detections that are expected at levels above each source. The minimum confidence level set for each detection is 0.95, the minimum signal to noise was set to 3.0, the expected number of false detection was set to 1 and the minimum integration time for a detection was set to half of the maximum integration time. In Tabs. 4.4 we present the sources found by the task in the LABOCA and GISMO observations, we present all the sources where the corresponding false detection was less than $N_{\rm f} < 2$, allowing one more possible false detection than the requested of 1.

Table 4.3. Properties of the galaxy clusters observed with PACS/Herschel and SPIRE/Herschel

Cluster	100 μm [mJy b^{-1}]	160 μm [mJy b^{-1}]	250 μm [mJy b^{-1}]	350 μm [mJy b^{-1}]	500 μm [mJy b^{-1}]
Abell 209	17.9	21.0	1.7	1.6	1.8
Abell 383	3.3	6.3	2.8	1.7	2.2
MACS0329.7-0211	1.6	1.6	2.3	2.5	2.9
MACS0416.1-2403	16.5	18.4	2.5	2.5	2.5
MACS0429.6-0253	1.8	1.9	3.0	2.1	2.6
MACS1115.9+0129	3.2	5.7	2.4	2.9	3.1
MACS1149.6+2223	3.2	6.0	1.6	1.6	1.8
RXJ1347.5-1145	3.0	5.3	4.0	3.6	3.8
MACS1931.8-2635	1.6	1.6	2.7	2.4	3.0
MACS2129.4-0741	3.3	6.1	1.9	1.5	1.9
RXJ2129.7+0005	2.8	5.7	4.9	3.9	4.4
MS2137-2353	3.4	6.4	1.9	1.7	1.8
RXJ2248.7-4431 (Abell 1063S)	3.3	6.3	1.7	1.6	1.8
MACS0647.8+7015	6.2	5.4	1.6	1.4	1.7
MACS0717.5+3745	6.2	5.4	1.8	1.5	1.9

Note. — The RMS correspond to the deepest region of the observations.

4.3.2 Flux deboosting

As explained by Scott et al. (2008) for the search of SMGs at 1.1 mm in the COSMOS field, sources with low signal-to-noise ratio are detected at fluxes systematically higher than their intrinsic flux density when the source population increases in number with decreasing flux. When there are a large number of faint sources, with fluxes below the detection limit (specially important in our observations) than are bright sources, there is a higher probability of detecting faint sources boosted by the noise than observing bright sources with fluxes decreases by noise. This effect is important when searching for SMGs because of the typical low S/N detections and because of the steep luminosity distribution known for SMGs (Scott et al., 2006).

To take this effect into account, for each source detected in our observations we need to calculate a posterior flux distribution (PFD) which describes the intrinsic flux densities of the sources in terms of probabilities. The goal is to find the probability distribution of a source having an intrinsic flux density S_i when measured a flux density of $S_m \pm \sigma_m$. This probability distribution can be express as

$$p(S_i|S_m, \sigma_m) = \frac{p(S_i)p(S_m, \sigma_m|S_i)}{p(S_m, \sigma_m)}, \tag{4.1}$$

where $p(S_i)$ is the prior distribution of flux densities, $p(S_m, \sigma_m|S_i)$ is the likelihood of observing the data and $p(S_m, \sigma_m)$ is a normalizing constant. For the likelihood of observing the data we used a Gaussian noise distribution motivated by the results observed

in Fig. 4.1, where

$$p(S_m, \sigma_m|S_i) = \frac{1}{\sqrt{2\pi\sigma_m^2}} \exp\left[\frac{-(S_m - S_i)^2}{2\sigma_m^2}\right]. \tag{4.2}$$

To simulate flux distribution $p(S_i)$ we use the Schechter function of the form

$$\frac{dN}{dS} = N'\left(\frac{S}{S'}\right)^{\alpha+1} \exp(-S/S'), \tag{4.3}$$

where we use the same parameters used by Johansson et al. (2010) for the LABOCA observations, $N' = 1703\,\mathrm{deg}^2\,\mathrm{mJy}^{-1}$, $S' = 3.1\,\mathrm{mJy}$ and $\alpha = -2.0$. These parameters were scaled from the values fitted to the SCUBA SHADES survey of Coppin et al. (2006) at 850μm to 870μm using a spectral index of 2.7. For GISMO the same procedure was made by this time scaling the values to 2 mm, resulting in $N' = 16113\,\mathrm{deg}^2\,\mathrm{mJy}^{-1}$, $S' = 0.33\,\mathrm{mJy}$ and $\alpha = -2.0$.

For the detected sources, the peak of the PFD corresponds to the deboosted flux density and the deboosted error corresponds to the σ of a gaussian function fitted to the PFD. As an example of the process, we used the the measured flux of MACS1931-870.2 of $S_m = 17.9\,\mathrm{mJy}$ with $\sigma_m = 2.8\,\mathrm{mJy}$. In Fig. 4.18 we show the PFD for the source (black solid line), the likelihood of observing the data $p(S_m, \sigma_m|S_i)$ (green dash line), the simulated flux distribution $p(S_i)$ (red blue line) together with the Schechter function (red solid line). The vertical lines show the observed flux density (vertical green dash line) and the deboosted flux density (vertical black line), in this case $S_i = 14.8 \pm 3.0\,\mathrm{mJy}$.

There are cases where the observed flux is so high and the detection is of low signal-to-noise that the PFD does not have a local maximum. This is the case for MACS0329-870.3 where $S_m = 28.4\,\mathrm{mJy}$ and $\sigma_m = 7.7\,\mathrm{mJy}$. Despite of having a $S/N \sim 3.7$, the PFD in Fig 4.19 has only a maximum at 0 mJy. This result is due to the fact that it is very unlikely to find a SMG with such high flux density at 870 μm. We could use these results as a method to estimate which of the detection are probably false, because they are not likely to have a deboosted flux different from 0.

The problem with this approach is that we are looking for lensed SMG, which will have higher fluxes than the normal population, meaning that not having a deboosted flux does not mean strictly that the source is false. Hereafter we will focus in the sources that fall within the CLASH observed region,where there is a higher probability that the SMGs are in fact lensed due to the closeness to the most magnified region of the clusters. For those sources, with the purpose of having a deboosted flux to search for possible counterparts, we will assume that the SMG is lensed with a magnification value of $\mu = 2.5$, resulting

in a lower demagnified flux density and errors. To the demagnified values we apply the same procedure to estimate the deboosted fluxes than before and then multiplying the results by μ to get a deboosted observed flux density. As an example, for MACS0329-870.3, assuming $\mu = 2.5$ we get $S_m = 11.3\,\mathrm{mJy}$ and $\sigma_m = 3.1\,\mathrm{mJy}$, which deboosted flux is $S_i = 6.9 \pm 3.4\,\mathrm{mJy}$, applying $\mu = 2.5$ again we obtain a deboosted observed flux density of $S_i = 17.2 \pm 8.5\,\mathrm{mJy}$. We apply this method to estimate a deboosted flux for all the sources that fall within the CLASH catalogs and does not have a deboosted flux in the same way as the others. In the last column of Tab. 4.4 we present the deboosted flux densities for the observed sources, in blank are the sources that do not have a deboosted flux for the reasons stated above and in some cases the estimated deboosted flux by using $\mu = 2.5$.

No deboosted fluxes were derived for the PACS and SPIRE detections. Despite of the PACS and SPIRE observations being affected in the same way as the LABOCA and GISMO observations, the smaller beam sizes of the PACS observations and the higher signal-to-noise of the PACS and SPIRE detections should make the effects less important in comparison to the LABOCA and GISMO detections.

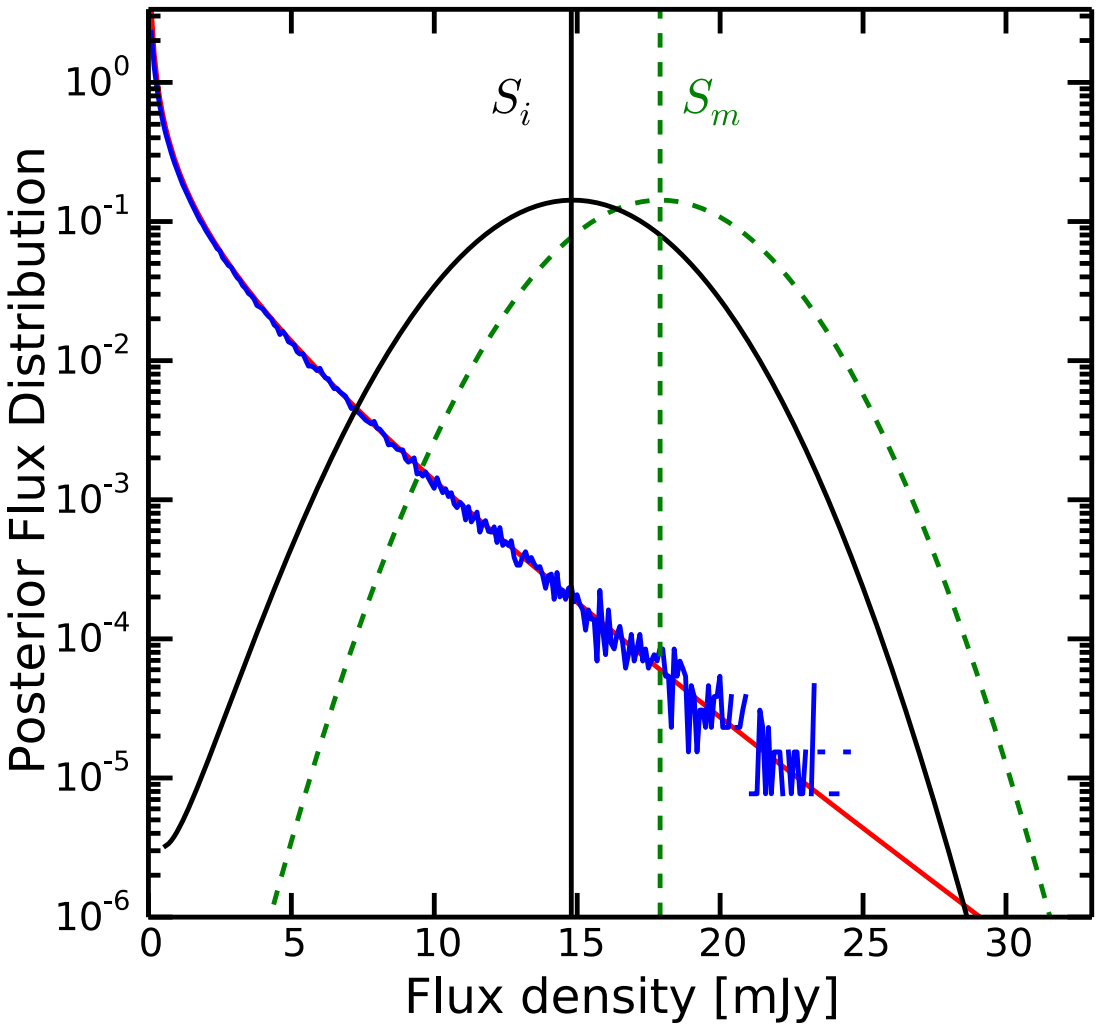

Figure 4.18 We show the PFD for MACS1931-870.2 (black solid line), the likelihood of observing the data $p(S_m, \sigma_m|S_i)$ (green dash line), the simulated flux distribution $p(S_i)$ (blue line) together with the Schechter function (red solid line). The vertical lines show the observed flux density (vertical green dash line) and the deboosted flux density (vertical black line). For this source we found a slightly lower deboosted flux density with a similar associated error.

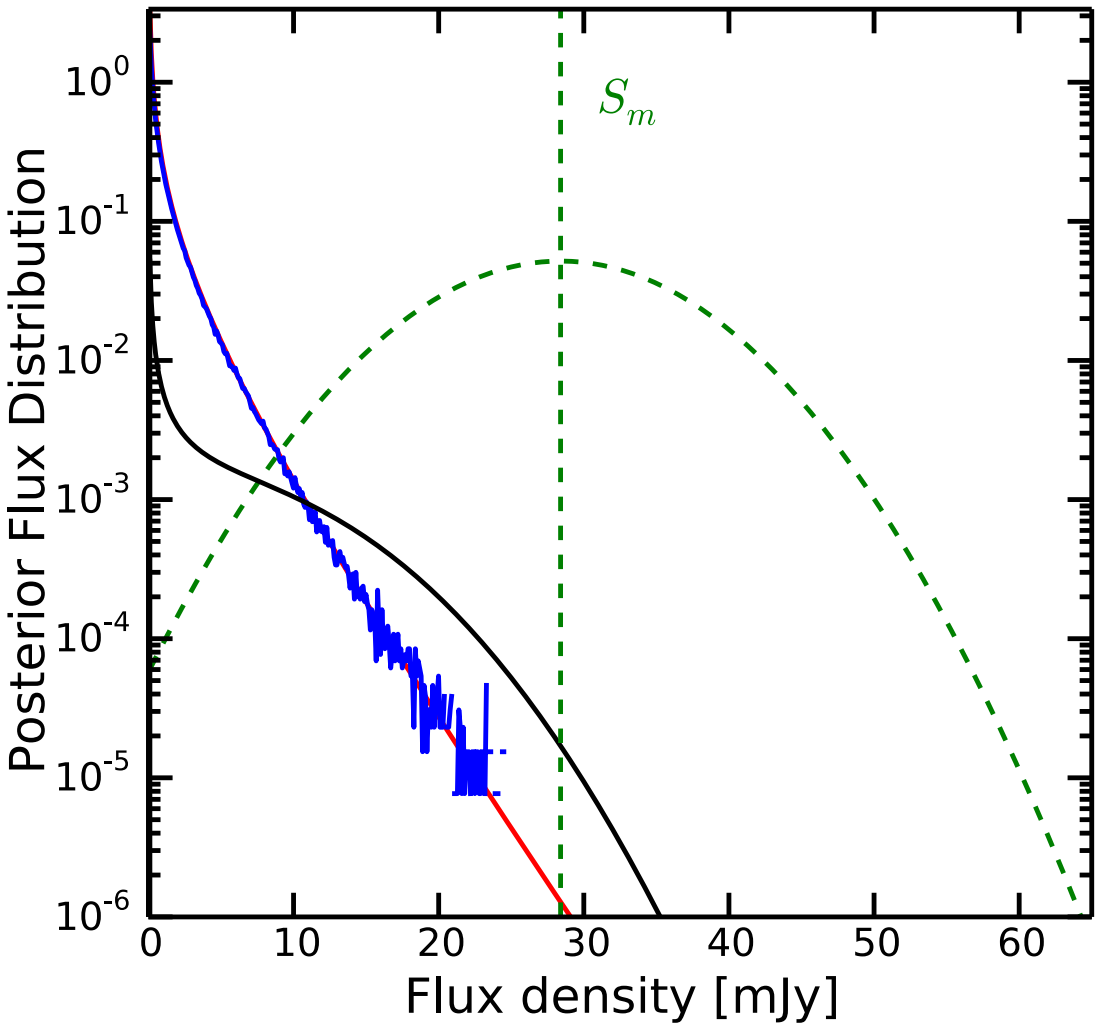

Figure 4.19 We show the PFD for MACS0329-870.3 (black solid line), the likelihood of observing the data $p(S_m, \sigma_m|S_i)$ (green dash line), the simulated flux distribution $p(S_i)$ (red blue line) together with the Schechter function (red solid line). The vertical lines show the observed flux density (vertical green dash line) and the deboosted flux density (vertical black line). Fro this source we are not able to estimate a deboosted flux density since the PFD does not have a local maximum for $S_\nu > 0$.

Table 4.4. List of sources detected in the LABOCA and GISMO observations.

ID	RA (J2000)	DEC (J2000)	S_ν[mJy]	S/N	Conf. [%]	N_f	S^d_ν [mJy]
MACS0416-870.1[a]	04:16:14.54	-24:05:10.6	11.0±3.2	3.47	46.0	0.78	6.1±3.6
Abell209-870.1	01:31:59.39	-13:34:20.9	44.6±10.8	4.13	94.0	0.06	-
Abell209-870.2	01:32:06.01	-13:36:06.0	34.7±9.3	3.74	87.0	0.28	-
Abell209-870.3[a]	01:31:44.90	-13:35:41.5	33.0±9.4	3.53	81.0	0.64	-/16.0±10.8[b]
Abell209-870.4[a]	01:31:49.66	-13:35:12.8	32.5±9.4	3.47	81.0	0.82	-/15.2±11.1[b]
Abell209-870.5	01:31:44.86	-13:34:57.4	36.6±10.6	3.46	82.0	0.83	-
Abell209-870.6	01:32:05.73	-13:37:16.3	38.0±11.3	3.35	79.0	1.25	-
Abell209-870.7	01:32:08.15	-13:34:08.3	30.9±9.3	3.33	79.0	1.35	-
Abell209-870.8	01:32:03.17	-13:41:39.0	38.8±11.7	3.31	79.0	1.45	-
Abell209-870.9[a]	01:31:51.32	-13:37:46.5	33.0±10.0	3.29	79.0	1.55	-/15.9±11.7[c]
Abell383-870.1[a]	02:48:08.88	-03:32:58.9	42.1±11.5	3.66	68.0	0.39	-/17.5±13.6[b]
MACS0329-870.1	03:29:40.19	-02:17:15.6	47.2±11.9	3.98	91.0	0.1	-
MACS0329-870.2	03:29:42.36	-02:15:47.5	36.1±9.4	3.86	92.0	0.17	-
MACS0329-870.3[a]	03:29:43.77	-02:11:25.5	28.4±7.7	3.69	89.0	0.33	-/17.2±8.5[b]
MACS0329-870.4[a]	03:29:43.80	-02:12:32.1	26.8±8.1	3.29	75.0	1.44	-/13.5±9.4[b]
MACS0429-870.1[a]	04:29:41.48	-02:54:46.3	23.4±3.6	6.46	100.0	0.0	18.5±3.7
MACS0429-870.2	04:29:20.93	-02:49:50.5	15.9±3.8	4.24	98.0	0.03	10.0±4.0
MACS0429-870.3	04:29:42.26	-02:50:30.4	15.9±3.8	4.18	99.0	0.04	9.8±4.1
MACS0429-870.4	04:29:46.98	-02:51:39.6	15.8±4.4	3.62	91.0	0.44	6.9±5.1
MACS0429-870.5	04:29:27.30	-02:51:15.1	11.0±3.3	3.36	84.0	1.18	5.6±3.8
MACS0429-870.6	04:29:43.87	-02:55:46.5	14.7±4.4	3.35	85.0	1.22	-
MACS0429-870.7[a]	04:29:29.55	-02:54:21.4	14.7±4.5	3.3	84.0	1.48	-/10±5.1[b]
MACS1149-870.1	11:49:46.70	22:26:30.6	19.8±4.8	4.08	93.0	0.07	9.8±5.4
MACS1149-870.2	11:49:19.17	22:24:20.6	19.5±5.2	3.78	88.0	0.24	7.2±6.3
MACS1149-870.3[a]	11:49:44.21	22:22:27.3	14.9±4.3	3.47	78.0	0.82	5.7±5.4
MACS1931-870.1[a]	19:31:49.51	-26:34:35.0	20.5±2.5	8.11	100.0	0.0	18.1±2.6
MACS1931-870.2	19:31:49.94	-26:32:00.9	17.9±2.8	6.34	100.0	0.0	14.8±3.0
MACS1931-870.3	19:31:27.76	-26:31:22.6	18.3±4.4	4.13	98.0	0.06	10.0±4.8
MACS1931-870.4	19:31:34.81	-26:33:39.3	15.5±4.1	3.82	95.0	0.2	8.2±4.5
MACS1931-870.5	19:31:30.07	-26:29:33.6	14.2±3.9	3.69	94.0	0.35	7.4±4.3
MACS1931-870.6	19:31:51.56	-26:38:19.4	20.5±5.8	3.54	91.0	0.62	0.1±0.2
MACS1931-870.7	19:31:39.15	-26:38:36.8	12.4±3.6	3.48	91.0	0.77	6.3±4.1
MACS1931-870.8	19:31:42.31	-26:28:36.6	11.2±3.2	3.47	91.0	0.81	6.2±3.6
MACS1931-870.9[a]	19:31:43.25	-26:33:44.0	10.5±3.1	3.4	90.0	1.05	5.8±3.5
MACS1931-870.10[a]	19:31:56.56	-26:34:42.5	8.5±2.5	3.39	90.0	1.06	5.3±2.7
MACS1931-870.11	19:31:47.17	-26:29:29.5	10.5±3.1	3.39	90.0	1.09	5.7±3.5
MACS1931-870.12[a]	19:31:45.27	-26:33:06.1	9.2±2.8	3.32	89.0	1.41	5.3±3.1
MACS2129-870.1	21:29:25.67	-07:45:30.6	12.0±3.1	3.83	82.0	0.2	7.5±3.4
MACS2129-870.2[a]	21:29:31.40	-07:42:32.7	12.1±3.3	3.69	83.0	0.34	7.1±3.7
MACS2129-870.3	21:29:13.04	-07:38:40.8	13.6±3.7	3.65	85.0	0.4	7.2±4.2
MACS2129-870.4	21:29:29.57	-07:46:30.0	13.5±4.0	3.38	75.0	1.09	5.4±4.9
MACS2129-870.5[a]	21:29:20.80	-07:41:16.2	8.7±2.6	3.37	76.0	1.15	5.3±2.9
MACS2129-870.6[a]	21:29:28.83	-07:41:38.7	9.0±2.8	3.24	72.0	1.85	4.9±3.2
MS2137-870.1[a]	21:40:19.65	-23:38:12.0	12.1±3.2	3.75	78.0	0.25	7.3±3.6
MS2137-870.2	21:40:24.90	-23:36:27.6	12.0±3.7	3.23	49.0	1.78	4.4±4.8
RXJ1347-870.1[a]	13:47:27.90	-11:45:50.9	17.4±4.4	3.93	89.0	0.11	8.9±4.9

Table 4.4 (cont'd)

ID	RA (J2000)	DEC (J2000)	S_ν[mJy]	S/N	Conf. [%]	N_f	S^d_ν [mJy]
RXJ1347-870.2	13:47:47.82	-11:44:40.4	14.4±4.4	3.28	59.0	1.36	-
RXJ2129-870.1[a]	21:29:36.03	00:04:20.1	18.1±4.2	4.3	98.0	0.03	10.7±4.6
RXJ2129-870.2[a]	21:29:41.45	00:06:14.5	13.5±3.5	3.83	91.0	0.19	7.9±3.9
RXJ2129-870.3	21:29:26.88	00:03:24.9	14.9±4.0	3.69	90.0	0.33	7.4±4.6
RXJ2129-870.4	21:29:34.96	00:07:31.7	16.3±4.4	3.67	91.0	0.35	7.2±5.2
RXJ2129-870.5	21:29:19.02	00:07:45.7	18.3±5.4	3.41	84.0	0.95	0.1±0.2
RXJ2129-870.6	21:29:43.15	00:01:36.2	13.0±3.9	3.31	82.0	1.36	4.9±4.9
RXJ2248-870.1[a]	22:48:48.98	-44:32:27.5	15.5±3.2	4.89	100.0	0.0	11.4±3.3
RXJ2248-870.2[a]	22:48:45.16	-44:29:50.3	15.7±3.4	4.54	100.0	0.01	10.7±3.7
RXJ2248-870.3[a]	22:48:41.93	-44:31:44.3	9.5±3.0	3.21	72.0	1.85	4.9±3.5
MACS1115-870.1	11:15:45.90	01:25:33.1	7.7±2.3	3.41	38.0	0.98	5.0±2.6
MACS1115-870.2[a]	11:15:50.28	01:30:30.0	6.1±1.9	3.23	32.0	1.85	4.1±2.0
MACS0647-2000.1[a]	06:48:00.83	70:13:22.4	1.48±0.49	3.0	37.0	0.98	-/0.93±0.57[b]
MACS0717-2000.1[a]	07:17:37.24	37:44:24.5	1.32±0.31	4.28	99.0	0.00	0.93±0.31
MACS2129-2000.1[a]	21:29:24.23	-07:42:49.9	0.83±0.23	3.59	87.0	0.13	0.58±0.24
MACS2129-2000.2[a]	21:29:21.28	-07:41:14.3	0.70±0.22	3.20	76.0	0.56	0.44±0.24
MACS2129-2000.3[a]	21:29:28.94	-07:40:14.9	0.80±0.26	3.09	75.0	0.81	0.44±0.30

Note. — Sources found by the detect task. In the first column, the ID corresponds to -870 when the detection was made in the LABOCA observations and -2000 when the detection was made in the GISMO observations. The fourth column shows the flux densities extracted and in the fifth column the signal-to-noise. The sixth column corresponds to a probability assign to each detection of being real, based in the sources and noise distribution of each observations. The seventh column corresponds to the expected number of false detection whit a signal-to-noise equal or higher than the detected source. The last columns shows the deboosted flux densities for each source, when no deboosted flux is estimated a magnification is assumed and a estimation of the deboosted flux is used.

[a]Detection that is within the fields of the CLASH observations.

[b]Deboosted flux density estimated by assuming a magnification of $\mu = 2.5$.

[c]Deboosted flux density estimated by assuming a magnification of $\mu = 3.0$.

4.4 Counterparts

One of the challenges of studying SMGs discovered by bolometer observations is finding and identifying the counterparts to the emission. In the past, the most used method was to use radio interferometers to pin point the emission of these bright sources thanks to its higher angular resolution. The problems with this method is that it assumes that a SMG is going to be bright in radio wavelengths, which is not intrinsically true. The second problem is that there is a bias to detect object with $z < 4$ when using radio observations, this is because the K correction is not the same in the sub-mm as in cm wavelengths.

As presented by several studies, the best way to truly confirm the counterparts to bolometers detected SMGs is by using interferometers in the sub-mm, since it is possible that one bolometer detected source can be the combination of the emission of several sources (Hodge et al., 2013).

For each LABOCA and GISMO sources, we look for sources in the Herschel SPIRE and PACS images that could belong to the same galaxy. After having the sub-mm fluxes we

combine those to the optical and near-IR photometry provided by CLASH and explore if any of the galaxies could account to the observe LABOCA and GISMO fluxes.

4.4.1 MAGPHYS

We use Multi-wavelength Analysis of Galaxy Physical Properties (MAGPHYS) to find the best candidate for the counterpart of the LABOCA and GISMO emission. We use all the galaxies within a radius of 14 arcseconds around the position of the LABOCA detection as possible counterparts, this value is based in the results from Hodge et al. (2013). We fit the photometry with MAGPHYS and find the best fit according to the sub-mm fluxes and the optical fluxes. MAGPHYS is a self-contained, user-friendly model package that interprets observed spectral energy distributions of galaxies in terms of galaxy-wide physical parameters pertaining to the stars and the interstellar medium. MAGPHYS returns a chi-squared of the best fit to the data, we used that value to estimate which of the galaxies could be associated to the sub-mm detection.

4.4.2 Counterpart candidates.

The criteria to determine if one galaxy can be the counterpart to the bolometer emission is that the model expected flux density has to fall within 1σ of the submm deboosted flux. If multiple galaxies have models that can account for the detected sub-mm and mm fluxes, in the cases of PACS or SPIRE detection, we use those detection as prior to estimate which are the correct counterparts, since the resolution of that instruments are higher. The galaxies with lower χ^2 values and that are closer to the PACS and SPIRE detection are selected as candidate to counterparts. In the case of only detection in LABOCA or GISMO, the galaxies with lower χ^2 values and closer to the center of the corresponding detection is favored as candidate to counterpart. The search for counterparts was made just in the region covered by the HST CLASH observations.

In Fig. 4.20, 4.21, 4.22, 4.23 and 4.24 we show false color images of the positions where the counterpart candidates are. Below we present the search for counterparts for each of the detected sources.

MACS0416-870.1: There is one galaxy that has the photometric properties to be a counterpart to the LABOCA emission. The photometric redshift of the galaxy is $z_{\rm ph} = 2.628$.

Abell209-870.3: No galaxies have the properties to account for the observed emission. Meaning that there is a high chance that this source is a false detection.

Abell209-870.4: No galaxies have the properties to account for the observed emission. Meaning that there is a high chance that this source is a false detection.

Abell209-870.9: There is one galaxy that has the photometric properties to be a counterpart to the LABOCA emission. The photometric redshift of the galaxy is $z_{\rm ph} = 1.129$.

Abell383-870.1: There are three possible candidates to be the counterpart to the LABOCA emission. The one at the center is favored by the higher resolution detection in SPIRE and PACS and we will select it as the counterpart galaxy. The The photometric redshift of the galaxy is $z_{\rm ph} = 0.438$.

MACS0329-870.3: No single galaxies have the properties to account for the observed emission. This could a case where the emission is produced by the combination of multiple sources, since some galaxies are expected to have similar flux densities in the FIR.

MACS0329-870.4: There are two galaxies that have the photometric properties to be a counterpart to the LABOCA emission. The galaxy at $z_{\rm ph} = 1.955$ is closer to the PACS/SPIRE detection, meaning that is favored by them. The other galaxy at $z_{\rm ph} = 1.061$ best fit the photometry. We will treat both as possible candidates.

MACS0429-870.1: No galaxies have the properties to account for the observed emission. The source is detected in SPIRE and PACS. The center of the detections falls in the border of the HST images, having a large part of the LABOCA beam outside the ACS field. There is a high probability that the counterpart is not in the catalog.

MACS0429-870.7: No galaxies have the properties to account for the observed emission. Meaning that there is a high chance that this source is a false detection.

MACS1149-870.3: The detection falls in the border of the ACS field and no galaxy has the photometric properties to account for the LABOCA emission.

MACS1931-870.1: Corresponds to the brightest cluster galaxy (BCG) of the galaxy cluster. It has been detected in other wavelengths, from FIR to radio.

MACS1931-870.9: The three closest galaxies to the center could account for the LABOCA emission. At this points it is impossible to disentangle if there is only one counterpart or is the combination of the emission from several sources.

MACS1931-870.10: There are several galaxies that can account for the LABOCA emission. We select the galaxy closest to the PACS detection at 125 micron as the counterpart to the LABOCA emission.

MACS1931-870.12: Two galaxies can account for the LABOCA emission. The one at $z_{\rm ph} = 5.355$ better fit the observed fluxes but is farther from the center of the LABOCA detection. We will select both as possible counterparts.

MACS2129-870.2: There are several galaxies that can account for the LABOCA emission. We select two galaxies as the possible counterparts. The first the one at $z_{\rm ph} = 0.675$ because it better fit the photometry and is closest to the center of the LABOCA detection. The second galaxy is the one at $z_{\rm ph} = 1.302$, which is closest to the PACS detection at 160 microns.

MACS2129-870.5/MACS2129-2000.2: This source is detected in LABOCA and in GISMO. There are many options as possible counterparts, the best candidate is the one $z_{\rm ph} = 2.282$ because it at the center of the emission in SPIRE at 250 microns.

MACS2129-870.6: No galaxies have the properties to account for the observed emission. Meaning that there is a high chance that this source is a false detection.

MS2137-870.1: Several galaxies can account for the LABOCA emission. We select the one at $z_{\rm ph} = 0.938$ because of the detection in SPIRE at 250 microns.

RXJ1347-870.1: Several galaxies can account for the LABOCA emission but the high resolution detection only allows the galaxy behind the cluster member at $z_{\rm ph} = 1.431$, which photometry is only partial, due to the galaxy member superposition.

RXJ2129-870.1: As in the other cases, several galaxies could account for the LABOCA emission but the high resolution detection only allows the one at the center, close to the center of the detection. The redshift of the galaxy is $z_{\rm ph} = 1.932$.

RXJ2129-870.2: From the sed fit and the high resolution detections we select the two central galaxies as possible counterparts. The first one is separated in two detections at $z_{\rm ph} = 0.628$ and the second one is the larger galaxy that has a better sed fit at $z_{\rm ph} = 0.728$, being the latter the one favored.

RXJ2248-870.1: There is only one detection that can account for the LABOCA emission and is also favored by the SPIRE detection at 250 microns. The galaxy is mainly detected in the near-IR HST filters. The redshift of the sources is estimated in $z_{\rm ph} = 1.938$.

RXJ2248-870.2: The detection is in the edge of the ACS observations, meaning that we are not able to estimate a possible counterpart for the emission.

RXJ2248-870.3: There are three galaxies that pass the MAGPHYS fit to be possible counterpart to the emission. The three galaxies are well spread over the LABOCA beam and the SPIRE and PACS detection clearly favored the one in bottom at $z_{\rm ph} = 0.569$. This galaxy has a measured spectroscopic redshift of $z = 0.607$ (Karman et al., 2014).

MACS1115-870.2: Three galaxies could account for the LABOCA emission. Although the high resolution detection clearly favored the one at $z_{\rm ph} = 1.165$.

MACS0647-2000.1: In the edge of the ACS field. No galaxies can account for the GISMO emission.

MACS0717-2000.1 This detection corresponds to a known radio galaxy previously detected at 1.425 GHz with the Very Large Array (VLA). The galaxy has been identified as a foreground galaxy at $z = 0.1546$ (Bonafede et al., 2009) and is not detected in any of our submm observations.

MACS2129-2000.1: There are four galaxies that could account for the GISMO emission. Of the galaxies, the one at $z_{\rm ph} = 3.193$ has the lower value for chi square and therefore is our candidate to be the counterpart of the GISMO emission.

MACS2129-2000.3: For this source we have two possible counterparts to the GISMO emission. The galaxy at $z_{\rm ph} = 3.967$ is at the edge of the GISMO beam, reason why we will use the other galaxy closer to the center of the GISMO detection as the counterpart. The redshift of the galaxy is $z_{\rm ph} = 3.798$

In Tab. 4.5 we present the list of the galaxies that are candidates to be the counterpart to the LABOCA and GISMO detections. For the cases where there are more than 1 candidate for a counterpart, we name each candidate to counterpart with a letter, being A the one with the highest priority, B the second in priority and C the last in priority. Each candidate assumes that the FIR emission correspond to that particular galaxy. This is because we can not estimate which fraction of the FIR emission belong to each possible counterpart, this assumption could overestimate the dust emission properties.

4.5 Discussion

4.5.1 MACS1931 BCG

The source MACS1931-870.1 corresponds to the BCG of the galaxy cluster MACS1931. A extended radio emission is observed surrounding the central AGN and also surrounding the observed X-ray cavities (Ehlert et al., 2011). The power estimates for the jets in the BCG are among the most powerful observed jets ever. In Fig. 4.29 we show the LABOCA emission toward the BCG. The emission is clearly extended in a direction close to the direction of the jets which are causing the radio cavities (red circles). The

Table 4.5. List of candidates to be the counterpart of the LABOCA and GISMO detections.

ID	RA (J2000)	DEC (J2000)	$z_{\rm ph}$
MACS0416-870.1A	4:16:13.96	-24:05:13.49	2.628
Abell209-870.9A	1:31:51.54	-13:37:52.99	1.129
Abell383-870.1A	2:48:08.94	-3:32:58.92	0.438
MACS0329-870.4A	3:29:43.99	-2:12:27.76	1.061
MACS0329-870.4B	3:29:44.14	-2:12:31.70	1.955
MACS0429-870.7A	4:29:29.25	-2:54:26.65	3.254
MACS1115-870.2A	11:15:50.68	1:30:35.62	1.165
RXJ1347-870.1A	13:47:27.62	-11:45:50.67	1.431
MACS1931-870.9A	19:31:43.46	-26:33:50.92	3.639
MACS1931-870.9B	19:31:43.80	-26:33:40.89	2.81
MACS1931-870.9C	19:31:43.78	-26:33:39.78	2.566
MACS1931-870.10A	19:31:56.22	-26:34:47.44	1.263
MACS1931-870.12A	19:31:44.77	-26:33:09.08	2.468
MACS1931-870.12B	19:31:44.69	-26:33:13.32	5.355
MACS2129-870.2A	21:29:31.45	-7:42:31.63	0.675
MACS2129-870.2B	21:29:31.54	-7:42:24.46	1.302
MS2137-870.1A	21:40:19.82	-23:38:07.75	0.983
RXJ2129-870.1A	21:29:35.93	0:04:19.54	1.932
RXJ2129-870.2A	21:29:41.36	0:06:12.62	0.628
RXJ2129-870.2B	21:29:41.59	0:06:06.80	0.728
RXJ2248-870.1A	22:48:49.06	-44:32:25.05	1.938
RXJ2248-870.3A	22:48:41.77	-44:31:56.84	0.607
MACS2129-2000.1A	21:29:23.66	-7:42:41.52	3.193
MACS2129-2000.2A	21:29:21.28	-7:41:17.74	2.282
MACS2129-2000.3A	21:29:29.09	-7:40:17.60	3.798

Note. — List of possible galaxy counterparts to the LABOCA and GISMO detections. For al the sources, the letter in the ID corresponds to the priority of being the only counterpart to the emission. In the case where more than 1 letter is assign to a LABOCA or GISMO detection, the order of the letters means the order of priorities. The Last column corresponds to the photometric redshift assigned to each galaxy in the CLASH catalogs.

LABOCA emission extends farther than the radio emission, showing that the emission could come from the ejected material. The spectral energy distribution of the BCG shows that the LABOCA emission at 870 μm is mainly non-thermal (the expected flux density at 870 μm is several times lower than observed). The emission at 500 μm observed in SPIRE may also be non-thermal, but in less fraction. The SFR estimated from the sed fit is $98.2^{+21.2}_{-17.5}$ $M_\odot$ yr^{-1}, lower than the $\sim$ 170 $M_\odot$ yr^{-1} estimated from the Hα emission (Ehlert et al., 2011). This could indicate that part of the Hα emission is powered by the AGN instead of star formation.

4.5.2 Lensed SMGs

For each of the candidates presented in Tab 4.5 we estimated the magnification values using the mass model provided by the CLASH team for the observed galaxy clusters (Postman et al., 2012) (The magnification values were estimated by Mauricio Carrasco,

Table 4.6. FIR photometry of the candidates to counterparts of LABOCA.

ID	PACS 100μm	PACS 160μm	SPIRE 250μm	SPIRE 350μm	SPIRE 500μm	LABOCA 870μm
MACS0416-870.1A	< 49.4	< 55.2	< 11.2	< 7.6	< 7.8	6.1 ± 3.6
Abell209-870.9A	< 53.8	< 63.0	23.2 ± 2.0	24.7 ± 1.9	21.4 ± 2.0	15.9 ± 11.7
Abell383-870.1A	< 10.0	< 18.8	33.0 ± 2.8	28.7 ± 1.7	18.1 ± 2.2	17.5 ± 13.6
MACS0329-870.4A	< 5.4	< 7.0	19.5 ± 2.3	29.9 ± 2.7	21.0 ± 3.6	13.5 ± 9.4
MACS0329-870.4B	< 5.4	< 7.0	19.5 ± 2.3	29.9 ± 2.7	21.0 ± 3.6	13.5 ± 9.4
MACS1115-870.2A	49.1 ± 3.2	61.0 ± 5.7	77.0 ± 2.4	74.3 ± 2.9	22.0 ± 3.1	4.1 ± 2.0
RXJ1347-870.1A	14.6 ± 3.0	41.3 ± 5.3	99.0 ± 4.0	97.8 ± 4.5	37.4 ± 3.8	8.9 ± 4.9
MACS1931-870.9A	< 5.0	< 5.5	< 8.2	< 8.0	< 10.3	5.8 ± 3.5
MACS1931-870.9B	< 5.0	< 5.5	< 8.2	< 8.0	< 10.3	5.8 ± 3.5
MACS1931-870.9C	< 5.0	< 5.5	< 8.2	< 8.0	< 10.3	5.8 ± 3.5
MACS1931-870.10A	5.5 ± 1.6	14.4 ± 1.6	30.2 ± 3.1	19.3 ± 2.5	13.1 ± 6.1	5.3 ± 2.7
MACS1931-870.12A	< 5.4	< 4.9	< 10.2	< 7.3	< 9.1	5.3 ± 3.1
MACS1931-870.12B	< 5.4	< 4.9	< 10.2	< 7.3	< 9.1	5.3 ± 3.1
MACS2129-870.2A	< 9.9	10.8 ± 2.0	15.4 ± 2.7	21.4 ± 1.8	8.6 ± 2.0	7.1 ± 3.7
MACS2129-870.2B	< 9.9	10.8 ± 2.0	15.4 ± 2.7	21.4 ± 1.8	8.6 ± 2.0	7.1 ± 3.7
MS2137-870.1A	$\cdots$	$\cdots$	34.8 ± 2.1	29.2 ± 1.9	24.7 ± 2.1	7.3 ± 3.6
RXJ2129-870.1A	5.2 ± 1.0	20.8 ± 5.7	60.9 ± 6.2	59.0 ± 5.7	46.3 ± 6.2	10.7 ± 4.6
RXJ2129-870.2A	9.3 ± 2.8	28.3 ± 5.7	55.2 ± 5.6	39.8 ± 4.7	23.3 ± 6.5	7.9 ± 3.9
RXJ2129-870.2B	9.3 ± 2.8	28.3 ± 5.7	55.2 ± 5.6	39.8 ± 4.7	23.3 ± 6.5	7.9 ± 3.9
RXJ2248-870.1A	< 10.0	< 19.0	14.6 ± 2.7	22.9 ± 1.6	21.5 ± 1.8	11.4 ± 3.3
RXJ2248-870.3A	42.0 ± 3.3	67.5 ± 6.3	75.0 ± 2.0	32.9 ± 1.8	11.0 ± 2.0	4.9 ± 3.5

Note. — FIR observations of the candidates to be the counterparts to the LABOCA emission. The units of the flux densities are mJy b^{-1}. The upper limits correspond to 3σ.

Table 4.7. FIR photometry of the candidates to counterparts of GISMO.

ID	PACS 100μm	PACS 160μm	SPIRE 250μm	SPIRE 350μm	SPIRE 500μm	LABOCA 870μm	GISMO 2000μm
MACS2129-2000.1A	< 8.3	< 15.5	< 6.1	< 5.6	< 5.7	< 8.1	0.6 ± 0.2
MACS2129-2000.2A	< 9.9	7.9 ± 1.8	10.2 ± 2.7	20.5 ± 1.9	8.9 ± 2.2	5.3 ± 2.9	0.4 ± 0.2
MACS2129-2000.3A	< 8.3	< 15.5	< 6.1	< 4.8	< 6.3	< 7.2	0.4 ± 0.3

Note. — FIR observations of the candidates to be the counterparts to the GISMO emission. The units of the flux densities are mJy b^{-1}. The upper limits correspond to 3σ.

Table 4.8. Properties estimated using the SED fit for the the candidates to counterparts.

ID	$z_{\rm ph}$	μ	$M_*[\times 10^9\ M_\odot]$	$M_d[\times 10^8\ M_\odot]$	$L_d[\times 10^{11}\ L_\odot]$	SFR $[M_\odot\ yr^{-1}]$
MACS0416-870.1A	2.628	1.2	60.4(–36.3,+49.5)	8.7(–5.7,+16.9)	6.8(–2.4,+3.2)	57.3(–16.7,+25.5)
Abell209-870.9A	1.129	1.2	76.0(–19.7,+19.7)	26.5(–7.1,+8.4)	6.5(–0.8,+2.5)	45.5(–10.6,+17.3)
Abell383-870.1A	0.438	1.0	20.0(–4.5,+7.0)	10.3(–1.7,+1.1)	1.5(–0.3,+0.4)	9.7(–2.4,+3.7)
MACS0329-870.4A	1.061	1.8	2.9(–1.1,+0.0)	14.7(–3.3,+1.2)	2.7(–0.6,+0.0)	21.2(–1.9,+0.0)
MACS0329-870.4B	1.955	2.1	5.6(–0.0,+0.0)	6.0(–0.6,+3.0)	7.4(–0.0,+0.0)	23.2(–0.0,+0.0)
MACS1115-870.2A	1.165	3.0	13.6(–0.0,+0.0)	6.0(–0.7,+1.1)	19.6(–0.0,+0.0)	108.4(–1.2,+0.0)
RXJ1347-870.1A	1.431	2.8	41.0(–11.3,+0.0)	11.3(–1.0,+1.1)	17.1(–0.0,+1.6)	136.4(–1.6,+1.6)
MACS1931-870.9A	3.639	1.2	41.8(–22.2,+36.0)	4.5(–3.2,+11.8)	5.1(–2.3,+4.4)	57.3(–17.6,+30.4)
MACS1931-870.9B	2.81	1.2	408.1(–238.0,+317.7)	16.1(–9.7,+25.3)	27.0(–7.9,+7.0)	439.4(–155.7,+107.4)
MACS1931-870.9C	2.566	1.2	1150.3(–826.1,+0.0)	17.5(–10.4,+25.9)	14.8(–0.0,+2.6)	233.2(–0.0,+717.0)
MACS1931-870.10A	1.263	1.1	4.9(–0.1,+0.0)	7.0(–1.8,+3.7)	7.4(–0.0,+0.2)	41.7(–0.5,+0.0)
MACS1931-870.12A	2.468	1.2	11.8(–7.2,+15.2)	0.3(–0.2,+1.0)	0.6(–0.3,+1.2)	16.7(–1.8,+8.3)
MACS1931-870.12B	5.355	1.2	263.5(–165.6,+205.1)	26.8(–20.9,+66.1)	45.8(–41.3,+30.2)	493.0(–327.8,+353.9)
MACS2129-870.2A	0.675	1.0	4.0(–0.5,+0.8)	11.9(–2.5,+2.6)	2.8(–0.6,+0.4)	24.4(–4.3,+5.6)
MACS2129-870.2B	1.302	1.2	3.8(–0.0,+7.0)	10.7(–3.9,+5.9)	5.8(–0.0,+2.8)	32.2(–0.4,+12.8)
MS2137-870.1A	0.983	1.1	15.4(–7.6,+25.2)	26.6(–6.7,+6.9)	9.7(–2.2,+2.5)	70.9(–15.9,+24.7)
RXJ2129-870.1A	1.932	1.2	66.2(–3.0,+25.2)	30.0(–5.9,+11.0)	50.2(–3.4,+8.8)	476.2(–311.1,+58.1)
RXJ2129-870.2A	0.628	1.2	15.5(–8.9,+0.0)	17.3(–4.5,+4.7)	3.3(–0.1,+0.3)	26.5(–2.0,+3.6)
RXJ2129-870.2B	0.728	1.5	65.1(–13.4,+7.9)	14.3(–4.3,+5.2)	3.9(–0.3,+0.7)	39.0(–2.6,+11.2)
RXJ2248-870.1A	1.938	1.4	13.0(–2.9,+0.3)	36.0(–11.6,+17.8)	13.9(–1.5,+0.3)	89.3(–3.0,+38.3)
RXJ2248-870.3A	0.607	4.0	26.2(–1.7,+3.2)	1.1(–0.1,+0.1)	2.1(–0.2,+0.2)	18.8(–1.7,+2.8)
MACS2129-2000.1A	3.193	1.3	6.4(–3.7,+6.6)	0.6(–0.4,+1.8)	0.9(–0.3,+0.6)	11.7(–3.0,+4.6)
MACS2129-2000.2A	2.282	2.3	8.9(–0.0,+0.2)	4.7(–1.2,+1.8)	9.7(–0.2,+0.0)	17.0(–0.4,+0.2)
MACS2129-2000.3A	3.798	1.3	216.8(–63.3,+168.7)	10.3(–4.3,+7.8)	16.4(–8.9,+2.0)	82.8(–42.7,+14.5)

Note. — List of properties estimated using MAGPHYS for the galaxies identified as possible candidates to the LABOCA and GISMO emission listed in Tab. 5. The magnification in the third column was estimated using the photometric redshift and the mass model published by the CLASH team. The stellar mass, dust mass, IR luminosity (dust luminosity) and star formation rate are presented, being all the quantities corrected by the magnification value in the third column. The errors for that quantities correspond to the 1 σ in the probability distribution of the best bit parameters. When the probability distribution is not 'well behave' and just singular parameters can account for the observed photometry the errors are around the minimum of the flux density.

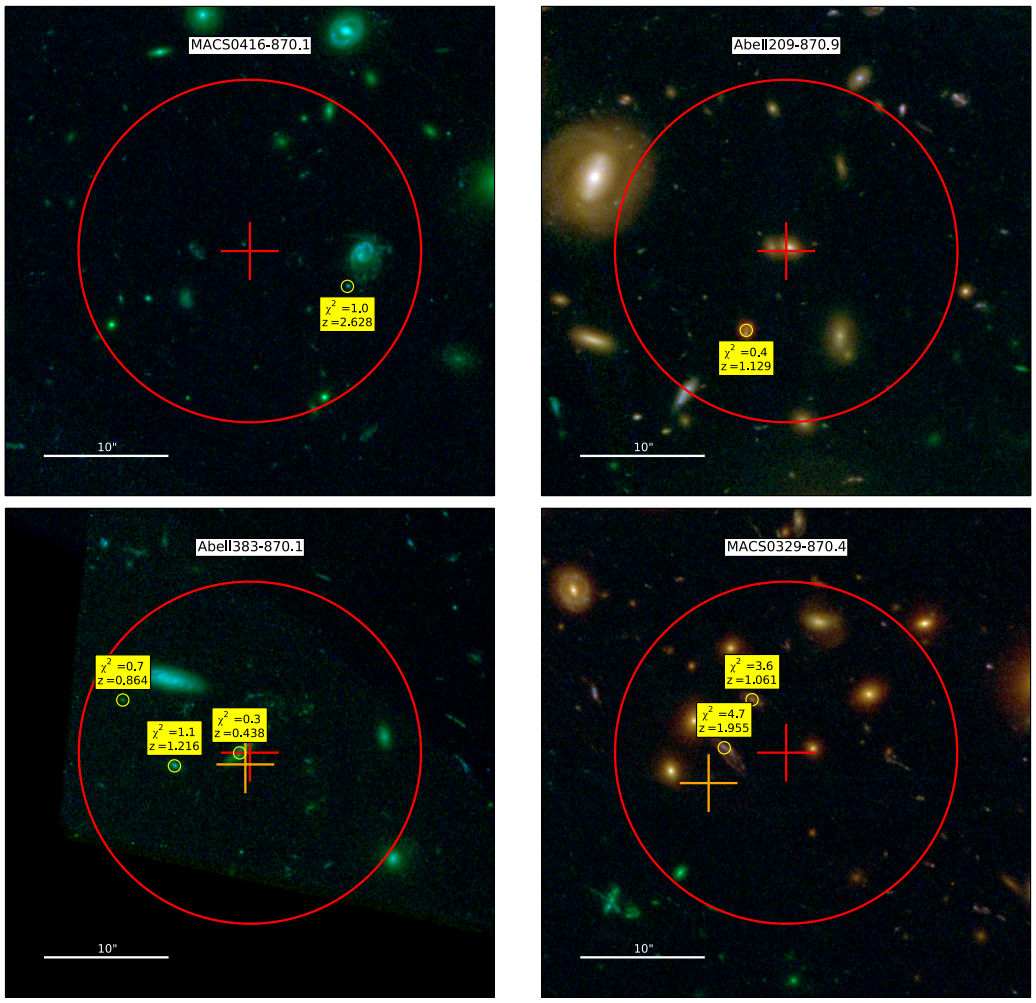

Figure 4.20 False color image of the CLASH galaxy clusters at the position of LABOCA and GISMO detections. The central red cross represent the position of the LABOCA/GISMO detection and the red circle is the 14" radius allowed for the search for counterparts (16.7" in the case of the GISMO detections). The yellow circles show the galaxies that were selected as possible counterparts. For each galaxy is also presented the value of ξ^2 from the MAGPHYS fit and the photometric redshift estimated from the CLASH observations. The orange cross shows the center of the lower wavelength detection of the source in either PACS or SPIRE instruments in Herschel shown in Figs. 4.25-4.28.

member of the CLASH team). Once we have the magnification values and the best fit from MAGPHYS, which are presented in Fig 4.25, 4.26, 4.27 and 4.28 we are able to estimate some physical properties of the lensed galaxies. In Tab. 4.8 we present the candidates, the magnification values, the stellar and dust masses, dust luminosity and the star formation rate estimated from MAGPHYS. The FIR flux densities for the candidates are presented in Tab. 4.6 and 4.7. Below we compare the intrinsic properties with other non and lensed galaxies.

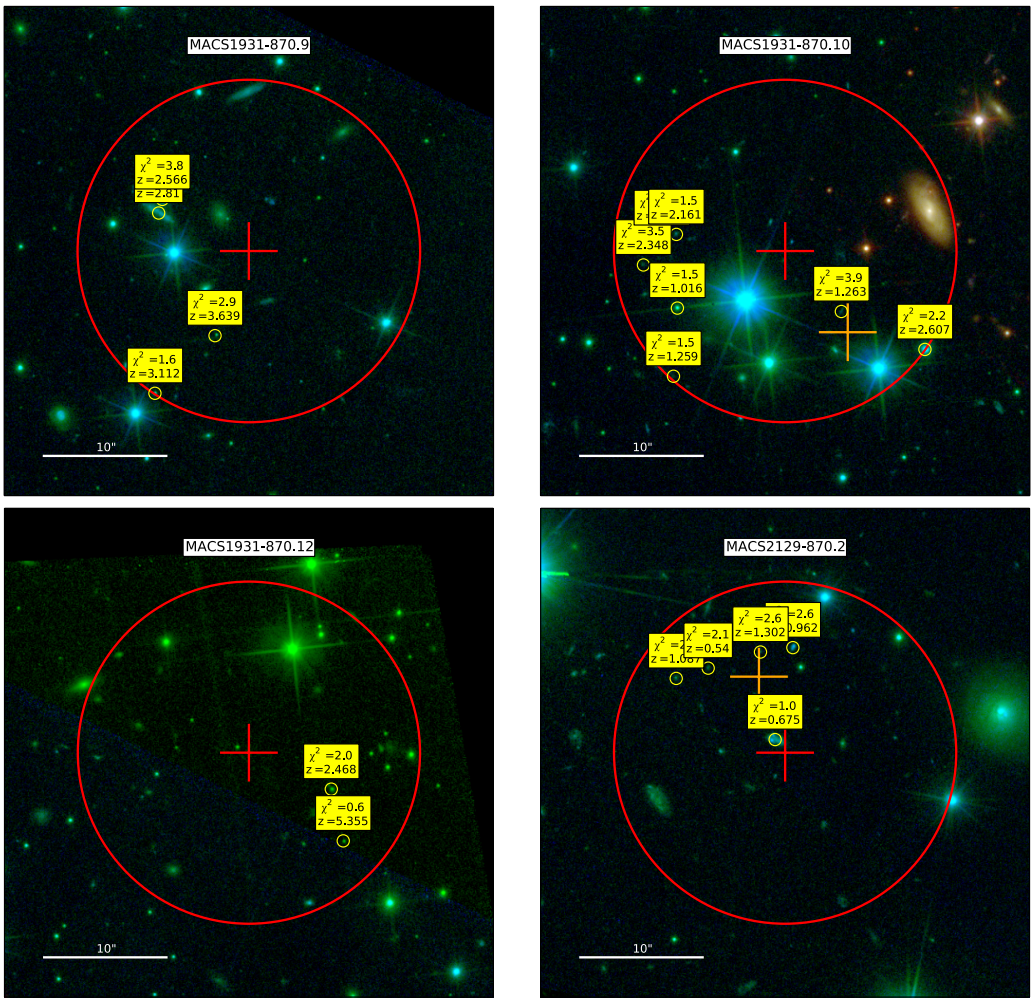

Figure 4.21 Continuation of Fig. 4.20.

4.5.2.1 Infrared Luminosity.

The IR luminosity (8 to 1000 μm restframe) is usually used as an estimator of star formation activity (Kennicutt, 1998). We compare the intrinsic IR luminosity our sample of lensed SMGs with other studies at different redshifts in Fig. 4.31. Most of the SMGs studied follow a clear relation between the observed L_{IR} and redshift, which is determined by the depth of the observations (Combes et al., 2012; Elbaz et al., 2011; Magdis et al., 2010; Magnelli et al., 2012; Symeonidis et al., 2013). Our targets at $z < 2$ are in the same region as those from other studies. Since the magnification is higher for the galaxies at $z > 2$, our sample is below the previous studies and even below other sample of lensed galaxies (Johansson et al., 2010; Sklias et al., 2014).

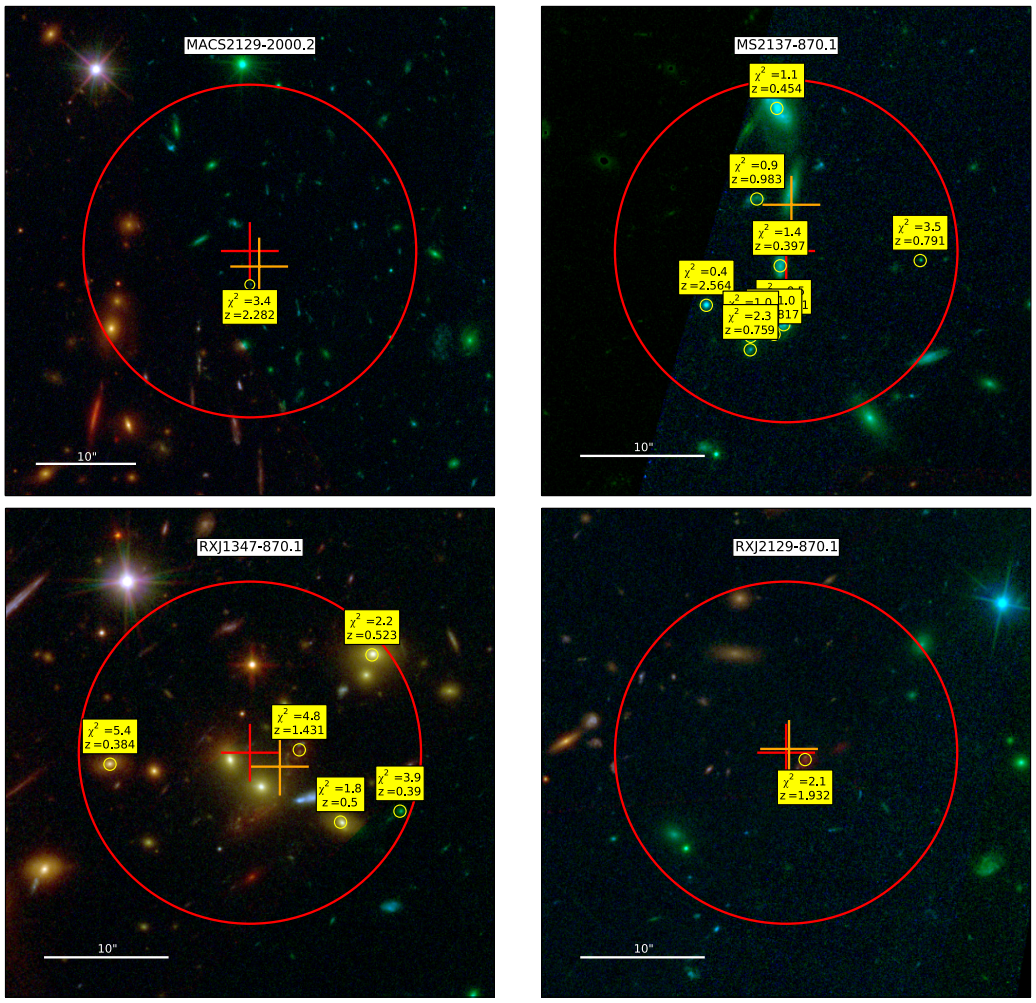

Figure 4.22 Continuation of Fig. 4.20.

4.5.2.2 Star Formation Rate and Stellar mass

In the star-forming galaxies population, there are two proposed categories defined by the process that they are enduring during the star formation. Most galaxies follow a relation between the amount of star formation for a given amount of stellar mass, this population is called the 'normal' star-forming galaxies. Galaxies that have a higher star formation rate for a given stellar mass are called 'starburts' galaxies, population where the star formation process has been enhanced by other processes as mergers or cold gas accretion. When we compare our observed lensed galaxies we see that most of them, if not all of them, follow the relation between stellar mass and SFR found for normal star-forming galaxies. It is important to note that our sample is in the lower part of the range of SFR and stellar mass. In the same range of stellar masses is located the SMGs discovered behind the Bullet Cluster (Johansson et al., 2012, 2010), the SFR for that galaxy is considerably higher than the values of our sample, being an example of the starbursting nature of that lensed SMG.

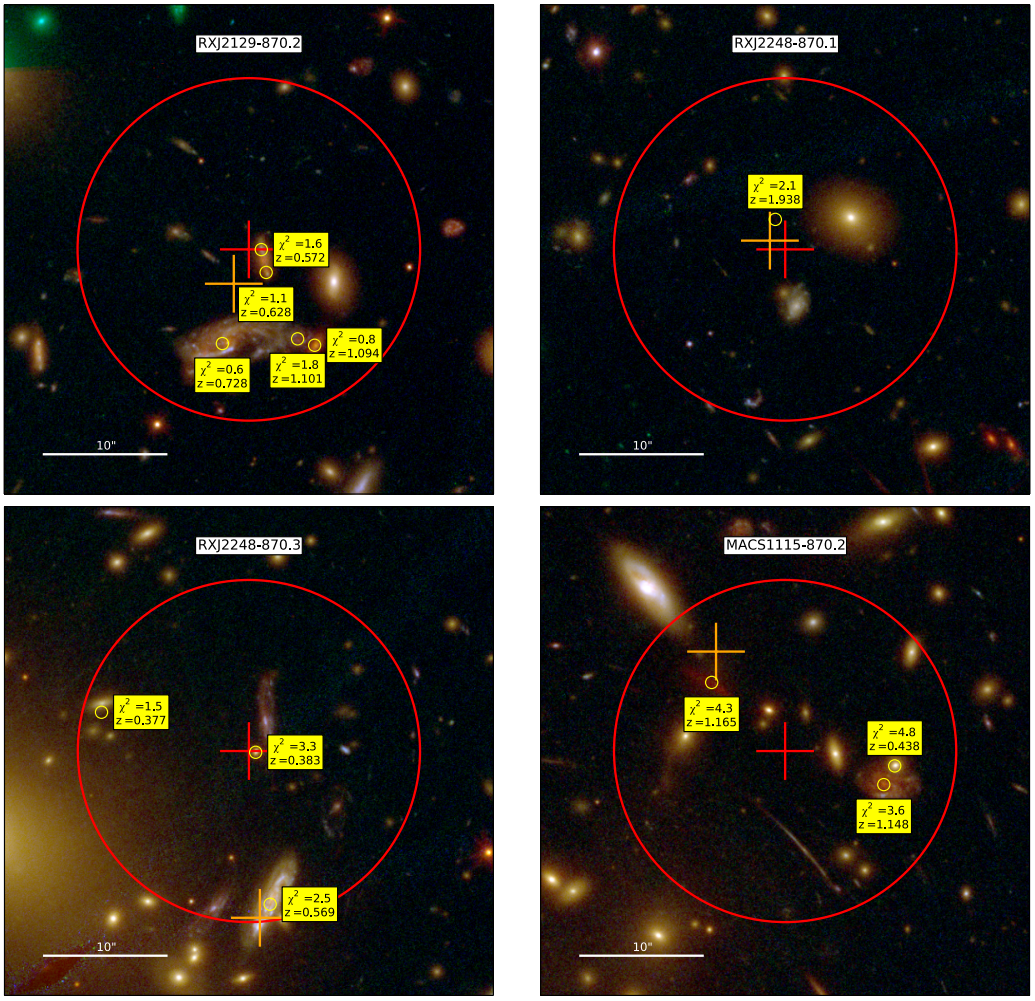

Figure 4.23 Continuation of Fig. 4.20.

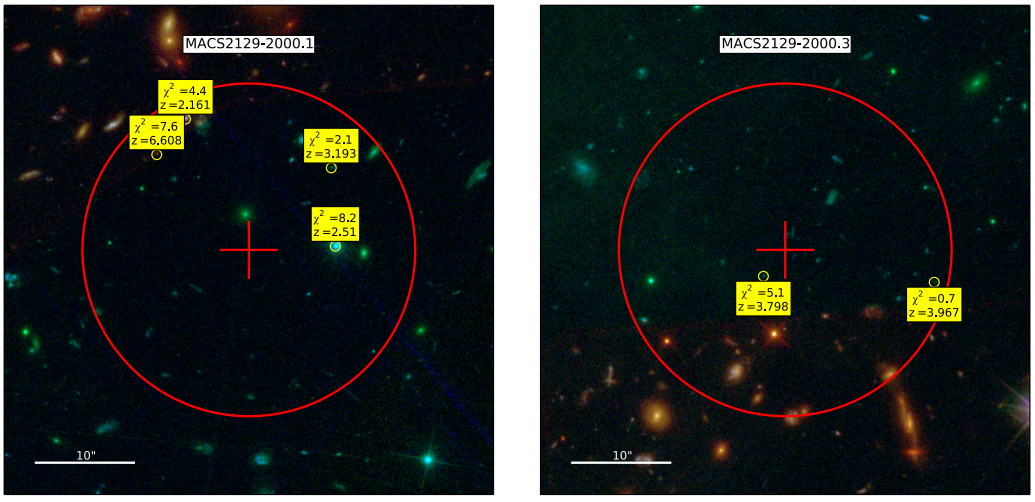

Figure 4.24 Continuation of Fig. 4.20.

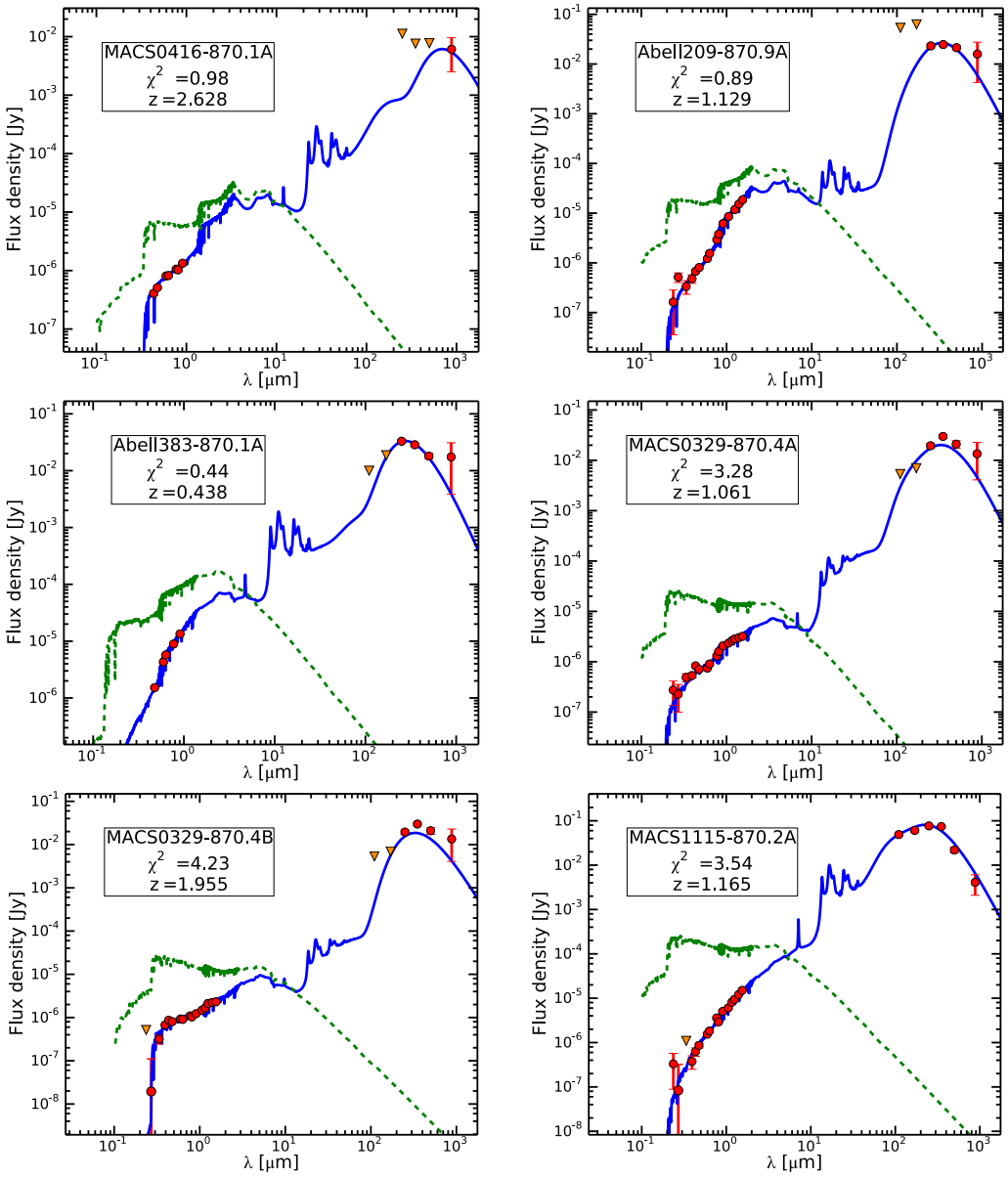

Figure 4.25 Spectral energy distribution of the best fit model made with MAGPHYS for the candidates to counterparts of the LABOCA and GISMO detections. The red points correspond to the observed photometry from the CLASH catalogs and from the archive images of PACS/SPIRE in Herschel and in the LABOCA/GISMO observations, the orange triangles show the upper limits of the observations. The green lines corresponds to the stellar un-attenuated emission and the blue line corresponds to the observed emission after the stellar emission is attenuated by the dust and re-emitted in the FIR. In the box we show the ID of the candidate, the χ^2 value for the fit and the assumed redshift.

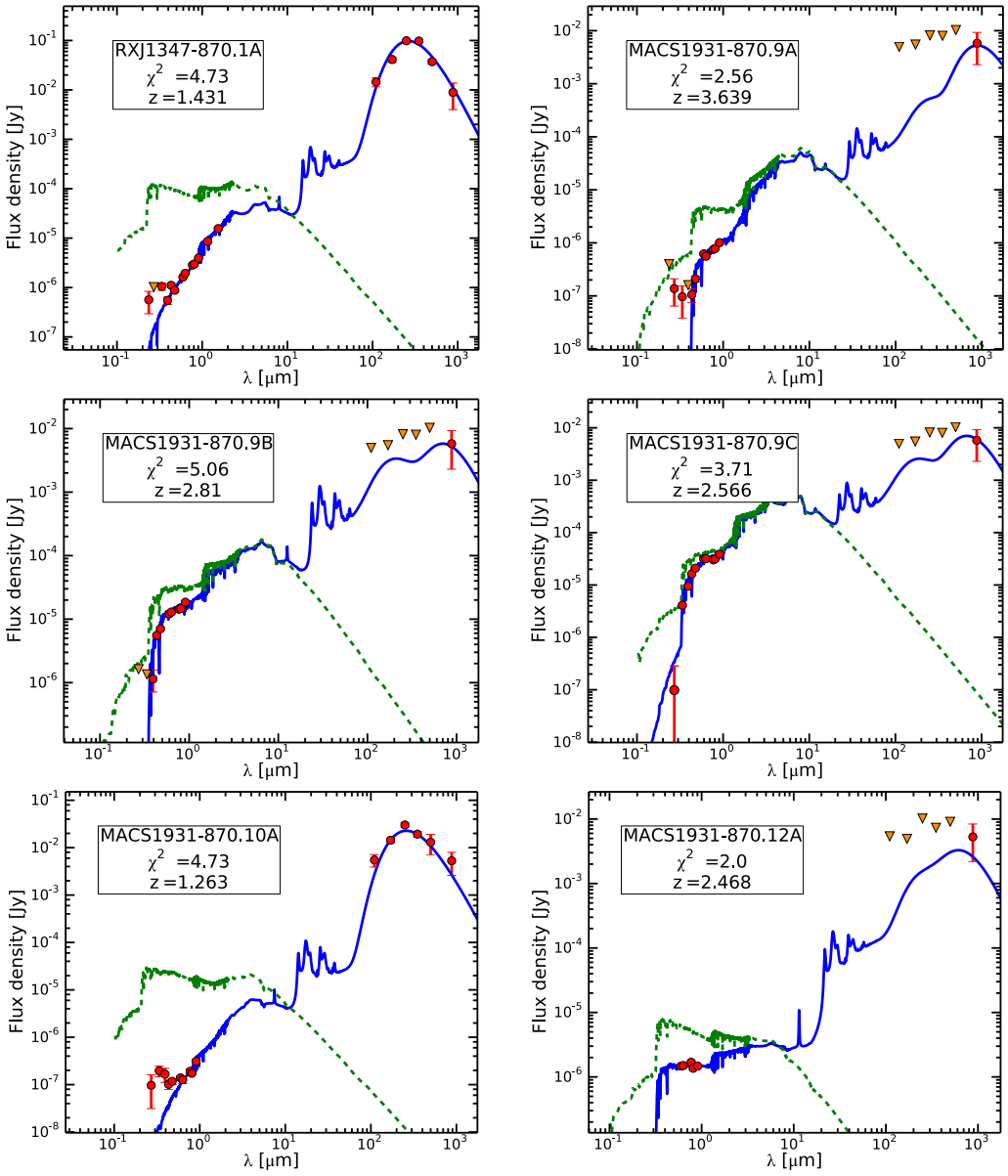

Figure 4.26 Continuation of Fig. 4.25.

The red line represents the Main-Sequence (MS) of star-forming galaxies in a redshift range of $1.5 < z < 2.5$ observed in the COSMOS and GOODS-South fields (Rodighiero et al., 2011). The green line is the same relation but amplified by a factor of 4, it represents where the starbursting population begins to separate from the MS population. In purple is shown the MS estimated for star-forming galaxies at $z \sim 2$ by Daddi et al. (2007), which is slightly steeper than the one estimated by (Rodighiero et al., 2011). It has been observed that the fraction of SMGs in outburst phase increases with the star formation rate, being $\sim 50\%$ for SMGs with $SFR > 1000$ $M_\odot$ yr^{-1}. This fraction decreases for lower values of SFR. A sample of lensed SMGs with intrinsic lower SFRs values should be dominated by MS galaxies, just as observed in our case.

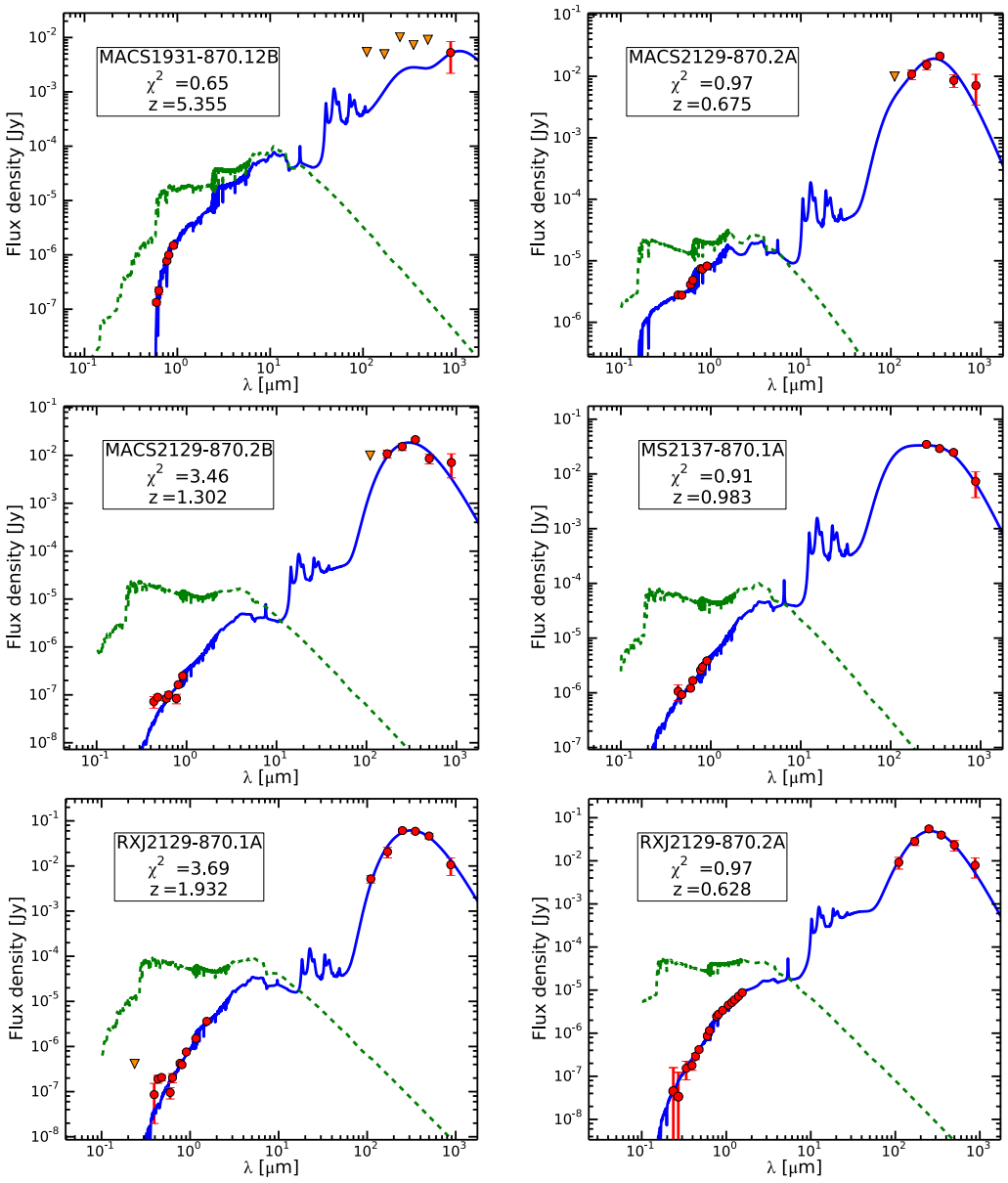

Figure 4.27 Continuation of Fig. 4.25.

4.5.2.3 Dust Mass and Stellar mass

One of the main properties of the SMG population is the presence of large amount of dust, therefore they are good laboratories to study the dust formation at different redshift. The dust mass is related to the SFR as a consequence of the SFR being correlated with the gas mass and the latter being roughly proportional to the dust mass. Galaxies with higher SFR show a higher amount of gas, and the amount of gas is correlated with the amount of dust. The relation between SFR and dust mass has been observed for a large sample of galaxies. When we combine that relation with the fact of the existence of the MS observed in Fig. 4.32 between stellar mass and SFR. A correlation between stellar mass and dust mass is a reasonable conclusion.

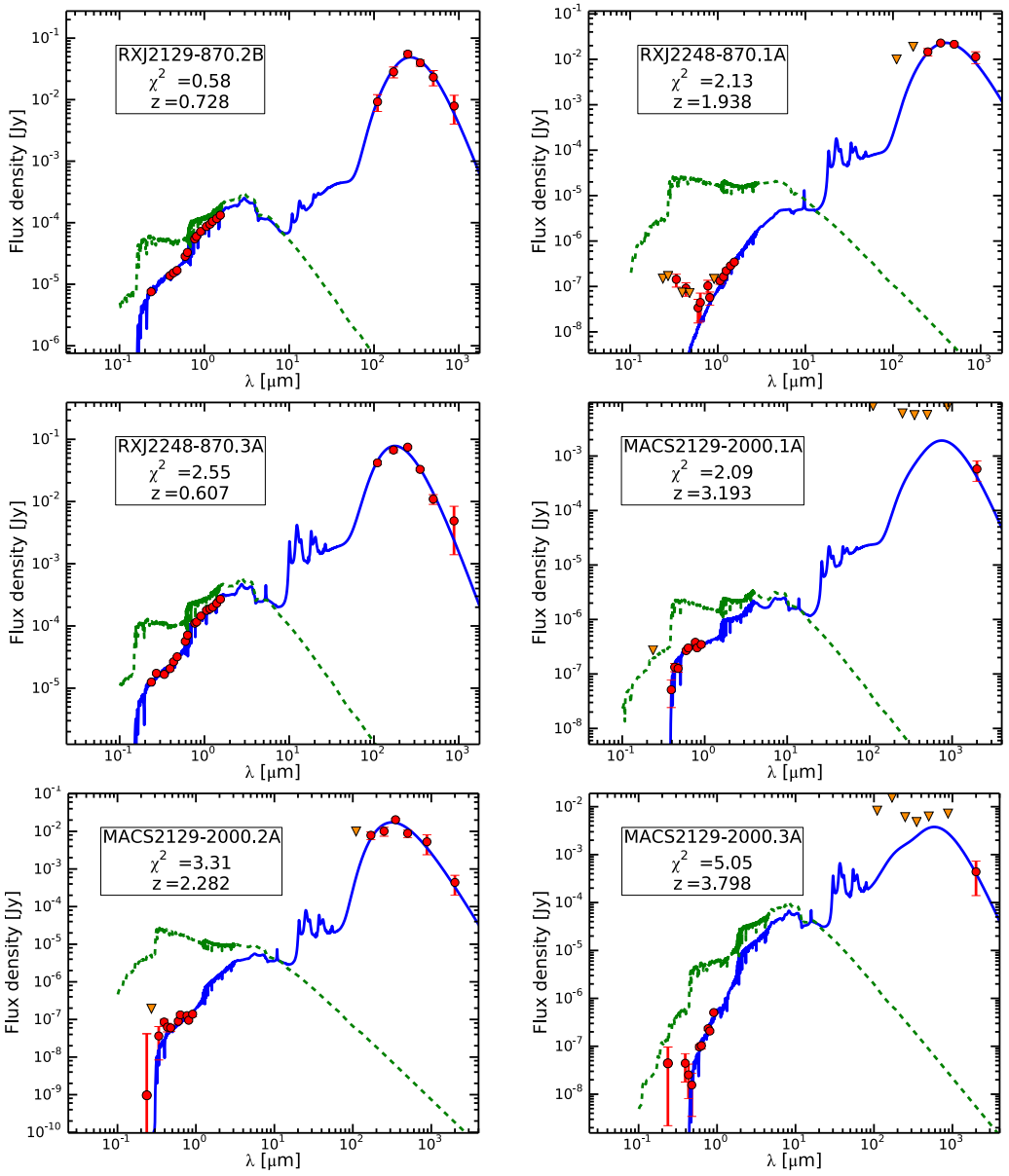

Figure 4.28 Continuation of Fig. 4.25.

In Fig. 4.33 we show the result of our observations together with a sample of local spiral galaxies, ULIRGS, SMGs and lensed SMGs (Johansson et al., 2010; Michałowski et al., 2010; Santini et al., 2010; Sklias et al., 2014). The green line corresponds to the relation found dust mass and stellar by Smith et al. (2012) for the Herschel-ATLAS sample of galaxies at $z < 0.5$. The green dashed line corresponds to the fit to the local galaxies observed as part of the KINGFISH survey (Skibba et al., 2011). The red line corresponds to the maximum amount of dust allowed for a given amount of stellar mass in the case of a closed box scenario (Rowlands et al., 2014). Several galaxies, from our and other samples, fall above the red line, meaning that they have more dust that they should,according to the current understanding of dust production in galaxies. The lack

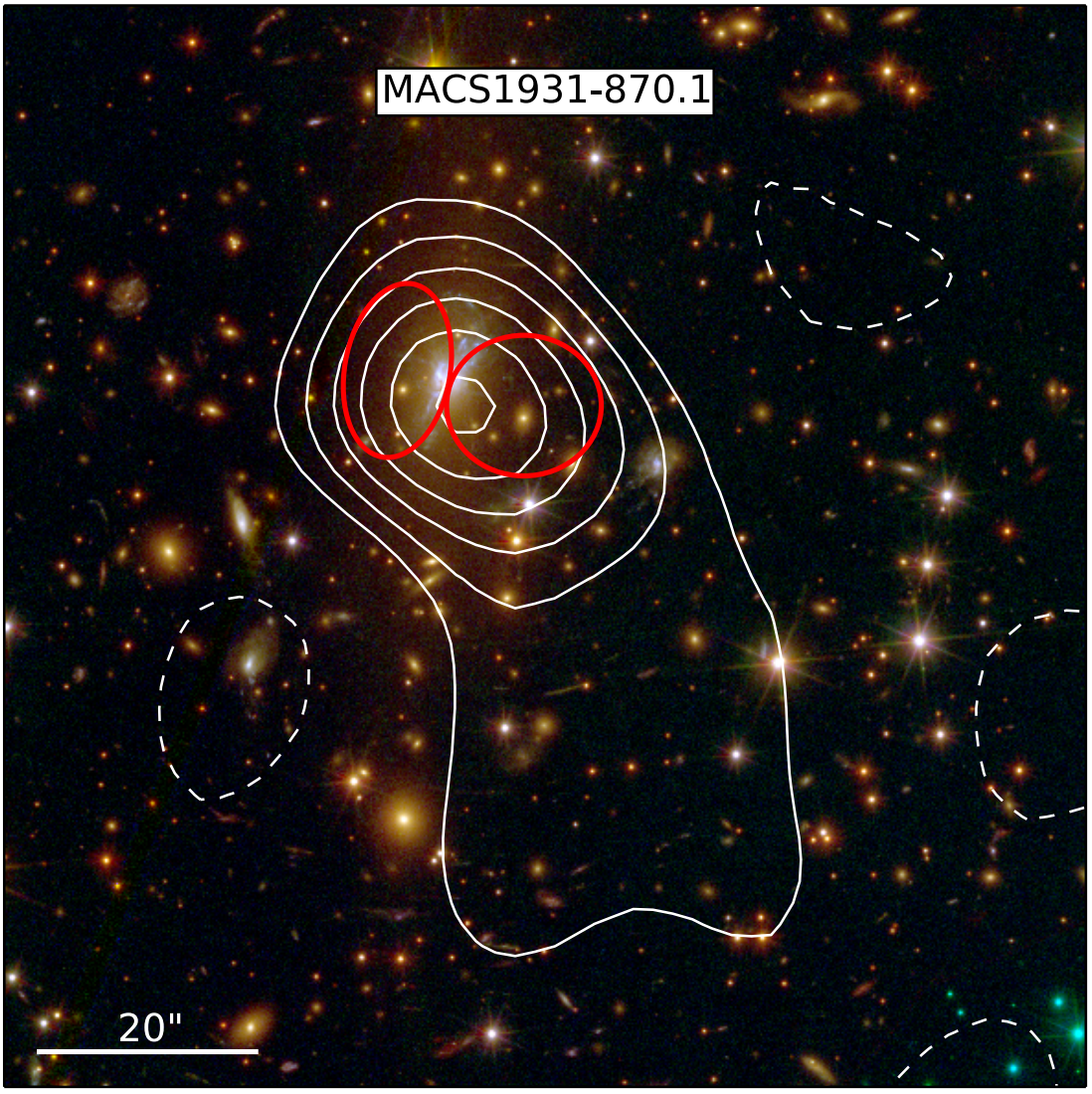

Figure 4.29 False color image of the galaxy cluster MACS1931 in the position of the detected LABOCA source MACS01931-870.1. Each white line corresponds to a 1σ emission starting at $\pm 2\sigma$ with $\sigma = 2.7$ mJy b^{-1}. The LABOCA detection is clearly over the BCG of the galaxy cluster, being this known by hosting a powerful AGN. The red ellipses corresponds to the radio cavities identified by Ehlert et al. (2011). This cavities are aligned with the X-ray cavities, being the latter of smaller size than the ones shown in the image. The BCG is known by having powerful jets, which push the cavities in each directions. The extension of the LABOCA emission could be an indication of the emitting dust following the direction of the jets, more observations are needed to confirm this relation. The extended emission could also be a residual of the Sunyaev-Zel'dovich effect, although the extended emission should be filtered out by the mapping algorithm.

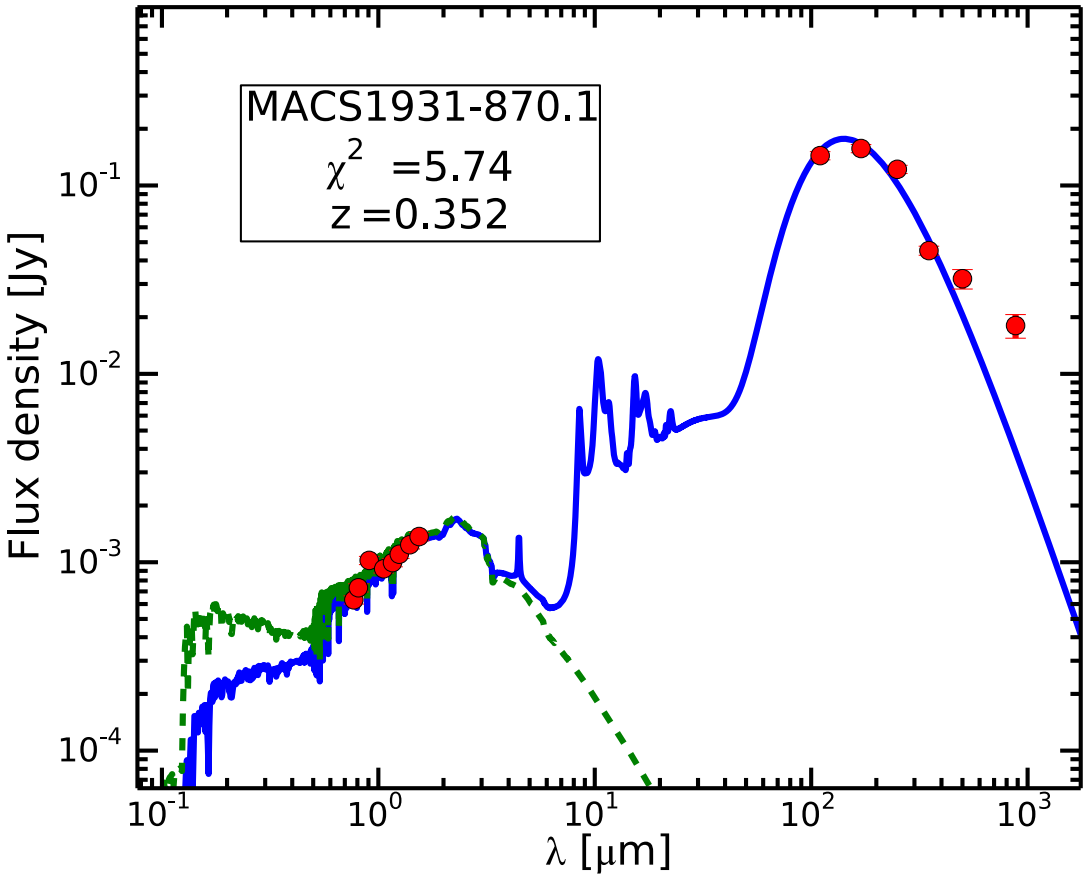

Figure 4.30 Spectral energy distribution of the best fit model made with MAGPHYS. The red points correspond to the observed photometry from the CLASH catalogs and from the archive images of PACS/SPIRE in Herschel and in the LABOCA observations. The green lines corresponds to the stellar un-attenuated emission the blue line corresponds to observed emission, after the stellar emission is attenuated by the dust and re-emitted in the FIR. In the box we shoes the χ^2 value for the fist and the assumed redshift, being this the redshift of the galaxy cluster MACS1931.

of explanation for the amount of dust in these galaxies is well-known as the 'dust-budget crisis'.

In our case, a possible explanation of these results is the miss-identification of the counterparts. We could be assigning the wrong galaxy to the submm and mm emission, meaning that it is possible to be selecting galaxies with lower stellar masses than the proper ones. This explanation is a possibility, and it has been commented in Santini et al. (2014) as an explanation to the 'dust-budget crisis' at lower stellar massesm because of the difficulties of assigning counterparts to the SMGs with lower luminosities. The fact that other galaxies from other surveys also show that amount of dust for such lower stellar masses reflect the possibility of our resulting being true. It is important to note that half of our sample follow the relation found for the galaxies between stellar and dust mass, while the other half have a higher amount of dust.

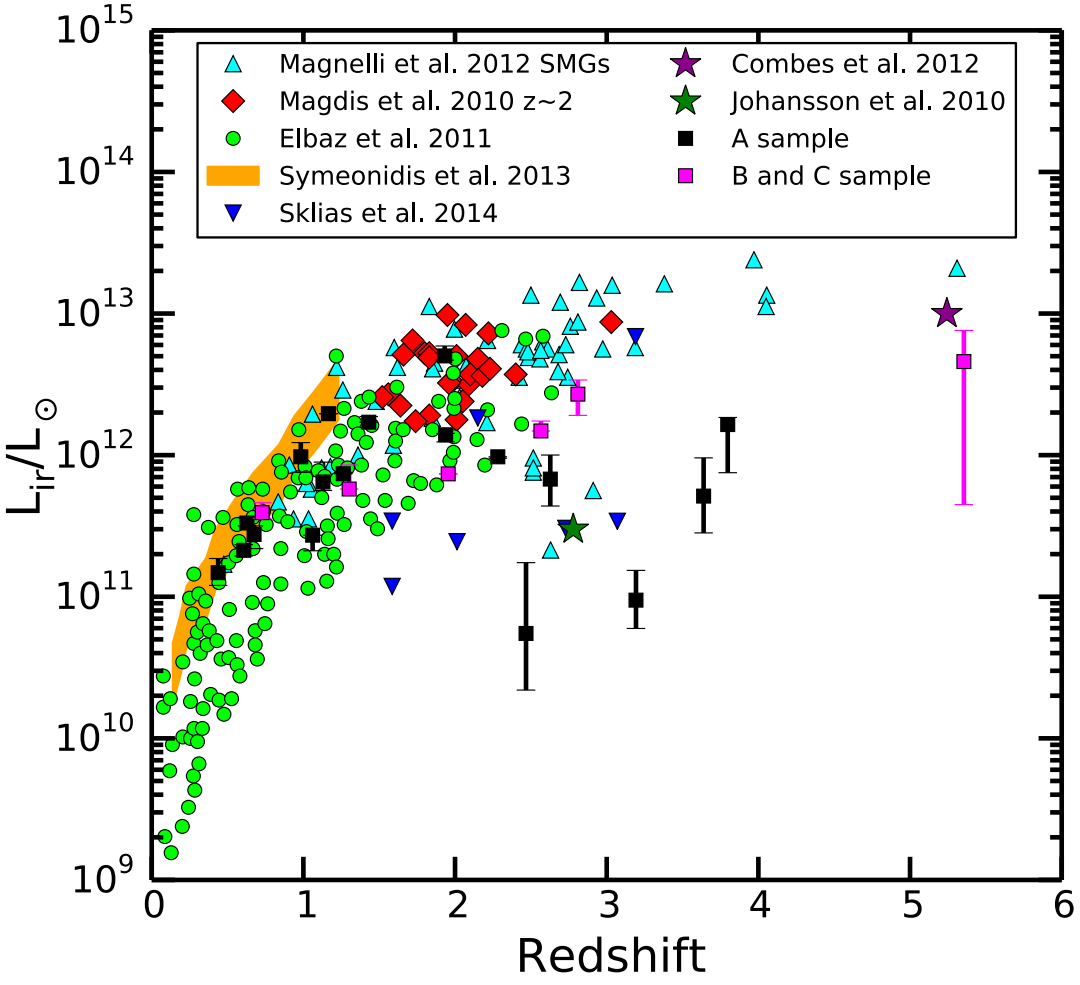

Figure 4.31 IR luminosities estimates for the list our list of candidates given by MAGPHYS and their photometric redshift. As comparison to our sample we also plot a number of SMGs detected in previous surveys in different colors. The black squares correspond to our sample candidates that are first priority to be the unique counterpart to the LABOCA and GISMO emission, the magenta sample correspond to the B and C priorities. For the Symeonidis et al. (2013) sample we present the region with a 1σ dispersion (yellow regions). It is important to note that the purple and green stars correspond to the lensed SMGs studied in Combes et al. (2012) and in Johansson et al. (2010). The down blue triangles correspond to a sample of lensed SMGs studied with Herschel. The other points correspond to the references: Sklias et al. (2014). (Elbaz et al., 2011; Magdis et al., 2010; Magnelli et al., 2012). Our sample of galaxies at $z < 2$ is located in the same region as other surveys. For the galaxies at $z > 2$ of our sample, they have very low IR luminosities in comparison to other observed SMGs showing that despite of our galaxies with low magnification they are still intrinsically fainter than previous studies.

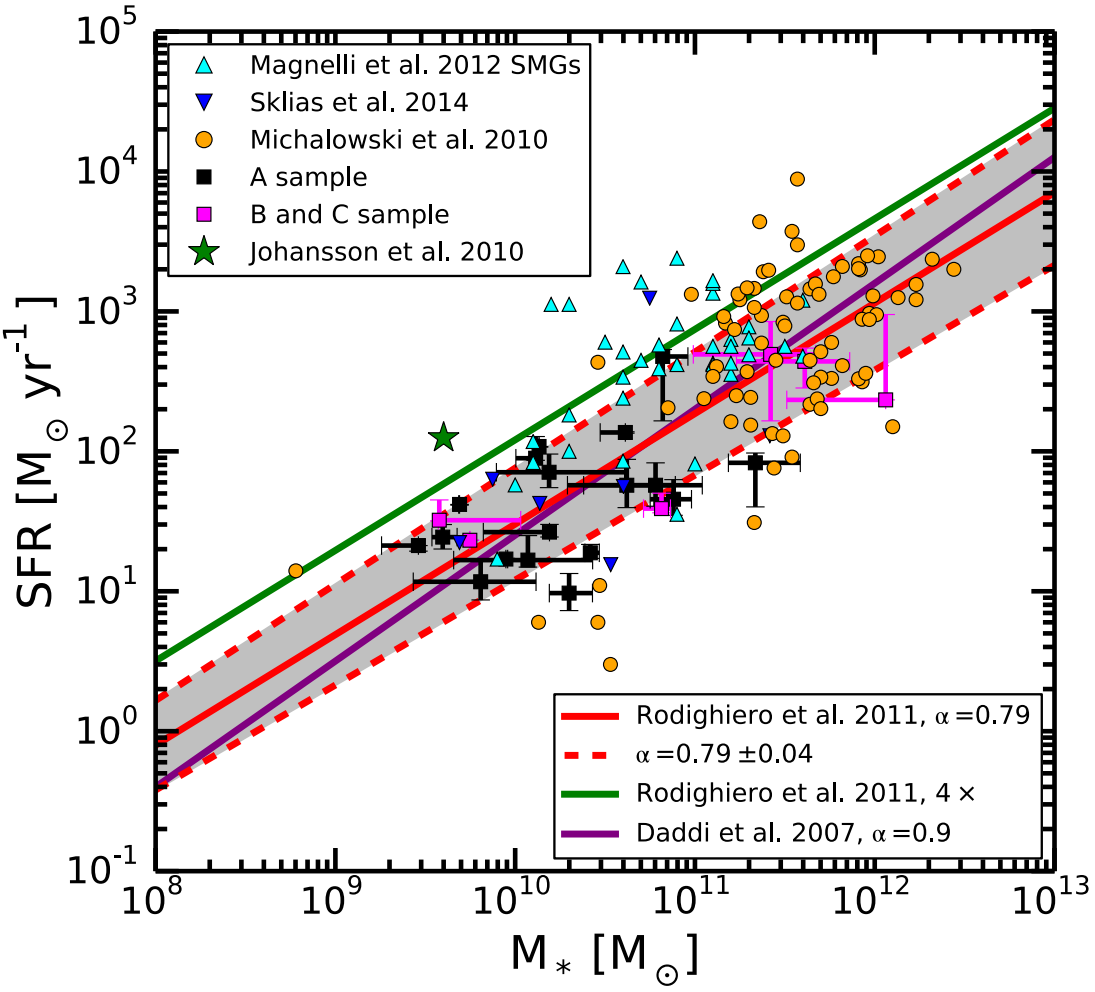

Figure 4.32 Comparison of the SED fit derived SFR and stellar mass of our candidates with a sample of other SMGs. The solid red line corresponds to the fit to the main sequence of galaxies at $z \sim 2$ done by Rodighiero et al. (2011), the dashed red lines corresponds to 1σ range in the α index from the red line. The purple line corresponds to the MS estimated by Daddi et al. (2007). The green line corresponds to the multiplication of the red line by $\times 4$ and it represents a separation between the MS and the starburst galaxies. The black squares correspond to our sample candidates that are first priority to be the unique counterpart to the LABOCA and GISMO emission, the magenta sample correspond to the B and C priorities. Most of our sample galaxies fall well within the 1σ range of the MS sequence, showing that the nature of these galaxies appears to be that of the main-sequence normal star-forming phase. These results are different as some of the SMGs in other surveys have SFR above the MS line, showing how some SMGs are better represented as galaxies in starburst phase. Reference of the SMGs are Johansson et al. (2010); Magnelli et al. (2012); Michałowski et al. (2010); Sklias et al. (2014).

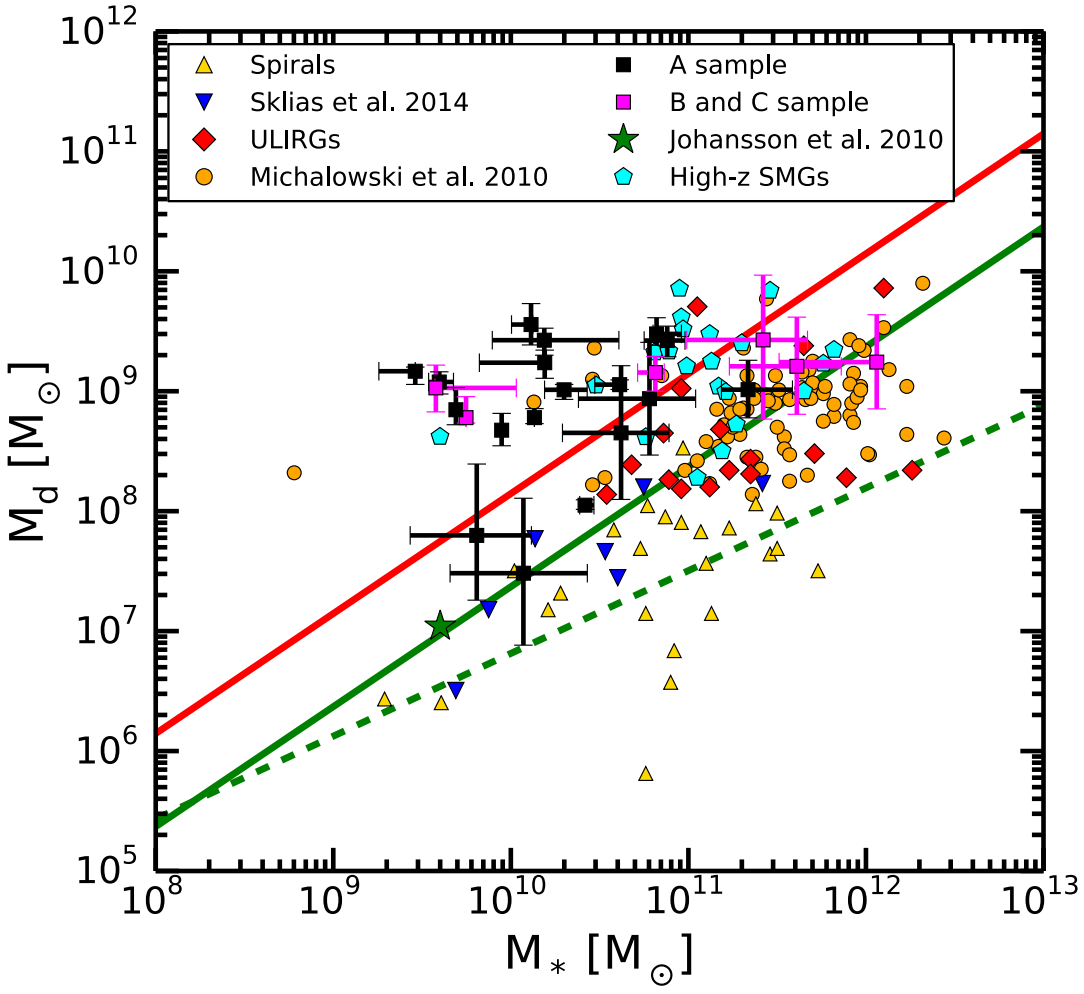

Figure 4.33 Comparison of the SED fit derived dust and stellar masses of our candidates with a sample of other SMGs. The solid green line corresponds to the fit to a sample of galaxies at $z < 0.5$ done by Smith et al. (2012). The dashed red lines corresponds to the KINGFISH survey of nearby galaxies (Skibba et al., 2011). The red continuum line corresponds to the maximum amount of dust estimated for a given value of stellar mass assuming the highest efficiency in the production of dust by stars in a 'closed box' scenario (Santini et al., 2014). The black squares correspond to our sample candidates that are first priority to be the unique counterpart to the LABOCA and GISMO emission, the magenta sample correspond to the B and C priorities. The spirals, ULIRGs and high-z SMGs sample were taken from Santini et al. (2010). Here we see that a big part of the SMGs fall in the regions around the solid green line, showing similarities with the $z < 0.5$ population of galaxies. A second part of the SMGs in our sample and in the other surveys fall well above the red line, showing a large amount of dust in comparison to their stellar mass. We see that at the lower values of stellar masses higher is the difference between the local relation (green lines) and the estimated dust masses for our and other samples. Reference of the SMGs are Johansson et al. (2010); Magnelli et al. (2012); Michałowski et al. (2010); Sklias et al. (2014).

This duality makes harder to have a simple explanation of the results. Bourne et al. (2012) showed an anti-correlation between the dust-to-stellar ratio and the stellar mass, meaning that galaxies with lower stellar masses have a higher fraction of dust than the galaxies with higher stellar masses. This could be the explanation for our case, where the magnification is allowing to study galaxies with intrinsically lower stellar masses.

Different theories have arise to explain the budget crisis, from the supernovae efficiency to intersterllar medium (ISM) dust grains productions(Rowlands et al., 2014). The study of lensed galaxies could add very interesting information the study of the 'dust-budget crisis'.

Chapter 5

Summary and Future Work

5.1 Summary.

5.1.1 Search for [CII] emission in $z = 6.5 - 11$ star-forming galaxies.

We have presented a search for [C II] emission in three LAEs at $z \sim 7$ and in a LBG at $z \sim 11$ using CARMA and the PdBI. We summarize our results and conclusions as follows:

1. We have not detected [C II] emission line any of our targets. Given the recent observational results and simulations of the [C II] emission in high redshift LAE, we adopt a line width of 50 $\mathrm{km\,s^{-1}}$ for the [C II] emission. We put constrains on the luminosity of the line for the targets. For the LAEs the 3σ $L_{[CII]}$ upper limit are < 2.05, < 4.52 and $< 10.56 \times 10^8 L_\odot$ for IOK-1, SDF J132415.7+273058 and SDF J132408.3+271543 respectively. Our [C II] upper limits are consistent with the relation of SFR-$L_{[CII]}$ found by de Looze et al. (2011). The 3σ upper limit in the [C II] luminosity of MACS0647-JD is $< 5.27 \times 10^7 \times (\mu/15)^{-1} L_\odot$ (Assuming that the redshift of the galaxy is within the most sensitive setup).

2. No detection of the FIR continuum is found at a wavelength of 158 μm rest frame for any of the 4 targets. Assuming a spectral energy distribution template for the local galaxy NGC 6946 as a template for the high redshift galaxies observed here, we present conservatives upper limits for the FIR luminosity. We find < 2.33, 3.79 and $7.72 \times 10^{11} L_\odot$ as upper limits for IOK-1, SDF J132415.7+273058 and SDF J132408.3+271543 respectively, these values account for the effect of the CMB on the observations. For MACS0647-JD, the upper limit in the FIR luminosity is $< 6.1 \times 10^{10} \times (\mu/15)^{-1} L_\odot$, after correcting for the CMB and the lensing magnification.

3. We present the results of simulations supporting the brightest component of the [C II] line having a width of the order of 50 $\mathrm{km\,s^{-1}}$. Here we want to emphasize the necessity of resolving such emission lines in future ALMA observations, to not loose signal-to-noise ratio, by selecting a channel resolution that is too low.

4. The effect of the CMB must to be taken into account in attempts to detect the FIR continuum in galaxies at high redshift. The heating of cold dust by CMB photons can shift the peak of the FIR continuum to values up to a $\sim$ 400 microns for galaxies with temperature of $\sim$ 25 K and redshift of $z \sim 11$. We emphasize that not including the effects of the CMB on the observations results in an underestimation of the FIR luminosities for the targets. The CMB corrected FIR luminosity limits are 35% higher than those without CMB correction at $z \sim 6.6$, 50% higher at $z \sim 7$, and 350% higher at $z \sim 11$ for a T= 26 K.

5. Simulations are already showing us that the task of detecting [C II] in high redshift galaxies is going to be difficult even with ALMA, as confirmed by the recent sensitive non-detection of Himiko by Ouchi et al. (2013). Accordingly to our IOK-1 simulations, a key parameter for the [C II] emission in LAEs is the metallicity, as we discussed in Sect. 2.4.6. If these simulations were applicable to all high redshift LAEs, we should first try to detect [C II] in the LAEs with the highest metallicity. Estimating the metallicity of LAEs at high redshift is not an easy task, however, Cowie et al. (2011) found that for the sample of LAEs discovered by the Galaxy Evolution Explorer (GALEX) grism in the redshift range of $z = 0.195 - 0.44$, there is an anti-correlation of the equivalent width of the Hα emission line with metallicity. Higher EW(Hα) sources all have lower metallicities, bluer colors, smaller sizes, and less extinction. Cowie et al. (2011) also found a broad general trend that for higher EW(Hα), the EW(lyα) is also higher. If we assume that these relations are valid for the LAEs at high redshift, and that the goal is to observe the LAE with the highest metallicity possible, it may be best to target the brightest LAE in the UV but with the lowest Lyα equivalent width. Lyman-break galaxies with Lyα detection may thus be ideal targets for [C II] searches at high redshift.

5.1.2 Search for [C II] emission in a normal star-forming lensed galaxy at the end of the reionization epoch.

We have presented the search for the [C II] emission line in a multiple-imaged lensed galaxy at the end of the reionization epoch using ALMA. We have used the data cube to also search for continuum and line emissions in the galaxies within the ALMA pointing. We summarize our results and conclusions as follows:

1. We have not detected a robust signal of [C II] emission line in the lensed galaxy but we do find a tentative detection. We explore the possibility of the non detection and of the tentative detection being real. In the case of the non detection, we put a 3σ upper limit of $L_{[CII]} < 3.0 \times 10^7 \times (\mu/29.2)^{-1} L_\odot$ for the [C II] luminosity, being $\mu = 29.2$ the estimated magnification for the two brightest lensed images D1 and D2 (Zitrin et al., 2012) (assuming that the line falls within the range of frequencies observed). For the tentative detection of [C II], we observed a [C II] luminosity of $L_{[CII]} = (3.7 \pm 1.0) \times 10^7 \times (\mu/29.2)^{-1} L_\odot$. The gaussian function fit to the tentative line results in a FWHM$= 14.6 \pm 4.9$ km s^{-1} an amplitude of 55.4 ± 17.4 mJy and a central frequency of 264.8012 ± 0.0023 GHz resulting in a possible z $= 6.17722 \pm 0.00005$. This line, if real, would be one of the faintest [C II] emission lines detected at high redshift. The amplitude and the frequency agree with what is expected for a [C II] emission line in a galaxy at this redshift. The possible measured redshift from the [C II] line is at less than 0.1σ from the photometric estimates. The low signal-to-noise (sn=3.7) and the narrowness of the tentative line do not allow us to claim it as a detection of [C II], just as a tentative line.

2. We find that MACS0329-iD is in agreement, within the errors, with the SFR-$L_{[CII]}$ found by de Looze et al. (2011), for the two cases, of a non detection and of the tentative detection. For the tentative detection, we observed that it would locate MACS0329-iD slightly lower than the other two detection at similar redshift (LAE-1 and LBG-1).

3. No detection of the FIR continuum is found at a wavelength of 158 μm rest frame for MACS0329-iD. Our 3σ upper limit of 1.8 mJy put an upper limit to the FIR luminosity of $< 5.7 \times 10^{10}$ L$_\odot$ (using the SED of NGC6946), resulting in a SFR$_{\rm dust} < 26.9$ M$_\odot$yr^{-1}. The ratio $L_{[CII]}/L_{\rm FIR} > 5 \times 10^{-4}$ (using the tentative detection) is low in comparison to local star-forming galaxies but it can be explained because of the continuum observation being not deep enough. Similar result is observed for LAE-1 at z=4.7.

4. This detection, of being real, confirm the possibility of using the [C II] emission line as a way to measure spectroscopic redshifts for high redshift galaxies and as an complementary way to study them.

5. We detected one continuum emission from a galaxy at $z_{\rm photo} = \approx 3.5$ that according to the sed fitting and the mass distribution model of the galaxy cluster we find that the galaxy corresponds to a high redshift dwarf galaxy. With a magnification of $\mu \sim 21$ we find the intrinsic value of star formation rate, dust mass and stellar mass for the galaxy. When we compare the galaxy with the local population studied in the KINGFISH survey, we see that the galaxy agrees well in the SFR-dust

mass relation, but it fall higher than the local population in the stellar-dust mass relation. We conclude that this is one of the first detections of a dusty dwarf galaxy at high redshift that roughly follows the characteristic of local dwarf galaxies. More observations at shorter wavelength are needed to explore the possibility of this galaxy being dustier than the local counterparts.

6. We have done a stacking of the continuum emission of the galaxies inside the HPBW of ALMA. Using the photometric redshift estimator BPZ we have found 5 different group of galaxies separated in redshift. We have calculated 3σ upper limits to the emission at 1.1 mm for the galaxies. The lowest upper limit corresponds to the galaxies being at the redshift of the galaxy cluster, with $F_\nu < 182$ μJy b^{-1} using the nominal resolution.

7. We have performed a search for emission lines in the data cube of the ALMA observations. Using a simple approach for looking for gaussian-like emission like we have found 4 candidate to emission lines. For the first line, L1, the line frequency agrees with the photometric redshift of a galaxy near the peak of the emission if the line is CI(1-0). Although, the sed fitting parameters of the galaxy does not account for the observed luminosity of the line. The faintness of the galaxy, even for HST, makes the photometry and therefore the photometric redshift distribution not reliable. We do not confirm this emission lines as CI(1-0).

   For the second line, L2, the frequency of the line agrees with being CO(7-6) for the redshift distribution of the galaxy in the peak of the emission. The galaxy is faint as the galaxy in L1, making the photometric redshift not reliable. It is difficult to estimate the emission of CO(7-6) for galaxy without knowing the emission of others CO lines, therefore, we do not confirm this emission line as CO(7-6).

   The third line, L3, agrees well with being [N II] in a galaxy at $z_{\rm phot} = 4.4^{+0.2}_{-0.3}$. Resulting in a spectroscopic redshift of $z = 4.4965 \pm 0.0001$. The star formation rate and the observed [N II] luminosity agree very well with the previous detection of [N II] in a LAE at $z = 4.7$, supporting the fact that this emission line is actually [N II] . This is the faintest [N II] emission line observed at high redshift and it is also the first time that a photometric redshift is confirmed by using this line.

   The emission line L4, it is related to a galaxy that has a photometric redshift not well constrained. The redshift probability distribution of the galaxy has two peak with similar values, one at $z \sim 0.4$ and the other at $z \sim 3.6$. For the peak at high redshift the none emission lines agree well with the redshift, for the one at low redshift, the possible lines are HCO(4-3) and HCN(4-3). These emission lines should be fainter than the line observed, so we do not suggest those as possible

counterpart. We are not able to find possible counterpart to the observed emission line.

We have used the light magnification by the galaxy cluster to explore the faint population at high redshift. With just 1 short observation, we have been able to find the continuum emission of a dwarf galaxy and the very secure detection of [N II] in a normal star-forming galaxy at $z = 4.5$. These results have been only possible by the extended studied made of the galaxy cluster by the CLASH survey. In the future we expect to confirm our results by observing the same galaxies at shorter wavelength and in other emission lines, such as [C II] or [O III] .

5.1.3 Submillimeter Galaxies behind the CLASH galaxy clusters.

We have presented the search for strongly lensed SMGs behind 15 CLASH galaxy clusters using the bolometers LABOCA and GISMO. For the 15 galaxy clusters observed, we have created a catalog of 62 unique detection at 870 μm or at 2 mm. For the sample of LABOCA and GISMO detections that fall inside the observed regions by CLASH we have presented the deboosted flux densities estimated for the flux densities measured. Using the deboosted fluxes, the HST observations from CLASH and the archive images of PACS and SPIRE in Herschel we did a search for the possible counterparts to the submm and mm detections. Using MAGPHYS to do SED fitting of the galaxies around the detections we searched for the possible galaxies that have been detected in the optical and NIR by HST and could account for the FIR observed flux densities. For the galaxies that could account for the FIR emission, we use the higher resolution detection with SPIRE or PACS when available to estimate which of the galaxies are the counterparts to the observed LABOCA and GISMO emissions.

At this point we identified two sources that where at redshifts lower or equal of the corresponding observed galaxy clusters. One of the sources is a radio galaxy in the foreground of the galaxy cluster MACS0717 with a $z = 0.1546$ that has been studied in the past. The emission for this source is clearly not related with thermal emission because of the non detection at shorter wavelength (Bonafede et al., 2009). The second source corresponds to the BCG of the galaxy cluster MACS1931, being this one of the brightest AGN detected in X-ray and radio. The LABOCA emission is extended in a direction that could be aligned to the observed jets cavities observed in radio and X-ray, meaning that some of the ejected material could be emitting at 870 μm. When we do a SED fitting of the galaxy we recover a SFR$\sim$ 100 $M_\odot$ yr^{-1} which is lower than the previously estimated from Hα observations of $\sim$ 170 $M_\odot$ yr^{-1} (Ehlert et al., 2011). From

the SED fitting we see that part of the emission at 500 and 870 μm does not correspond to a thermal emission, being powered by the AGN undergoing in the galaxy.

For the galaxies selected as possible counterparts to the submm/mm emissions we estimated the magnification produced by the galaxy clusters using the mass models published by the CLASH team and assuming that the photometric redshifts are correct. Once we had the magnification values we used the MAGPHYS results to estimate the intrinsic stellar and dust masses, IR luminosities and SFR values for the galaxies. The first that we noted is that the magnification values are not so high, being the maximum of $\mu \sim 4$, showing that no bright strongly lensed SMGs are detected behind any of the galaxy clusters. This could indicate that galaxy clusters as a whole, are not the best candidates to study bright strongly lensed SMGs. Despite of the low magnification observed for the counterparts, we still measured a lower IR luminosity than the SMGs observed at black fields at $z > 2$.

When comparing the estimated stellar masses and star formation rate with other samples of SMG we note that most of our sample of galaxies follow the main sequence relation at $z \sim 2$, showing that non of these galaxies are in a starbursting phase of star formation. When we compare the dust and stellar masses of our sample with other surveys, we note that a large fraction of the galaxies have higher amount of dust mass for the corresponding stellar masses. This fact has been observed in other samples of SMGs at high redshift but is important to note that the higher ratio of dust-to-stellar are present mainly in the galaxies with the lower values of stellar masses, which could be an indication that we are not finding the correct counterparts to the emissions or that there are more than 1 galaxy associated to each LABOCA or GISMO detections. Observations with higher resolution could help disentangle if these galaxies are actually as dusty as estimated by our results. ALMA is the perfect instrument to do these kind of studies in the future.

5.2 Future Work.

In my future research, I want to follow and expand my current research. A project accepted for ALMA cycle 1 to search for [C II] in a lensed galaxy at $z = 6.027$ behind the galaxy cluster Abell 383 is currently being observed. I will do an analysis similar to the one made for the lensed galaxy behind MACS0329 presented in this thesis. With the purpose of understanding the [CII] emission at high redshift, I have a project accepted for ALMA cycle 2. The z=4.4 quasar BRI 1335-0417 provides the unique opportunity to study the ISM of a quasar host galaxy in unprecedented detail. The high-quality, 0.2" (∼1kpc) resolution imaging of the CO(2-1) emission (using the VLA)

demonstrates that the molecular gas in the host galaxy is distributed over 10 kpc, and is dynamically complex, hinting at an ongoing gas-rich ("wet") merger. This is the highest-quality/resolution CO dataset available for any unlensed high-redshift source accessible with ALMA. We will complement this dataset with spatially-matched [CII] (and underlying continuum) emission. This is possible given the recent detection of strong [CII] emission in the source using APEX. We will map the [CII] and underlying continuum at kpc resolution and unprecedented sensitivity. Together with the CO imaging, this will provide the first beam-matched dataset of a high-z galaxy to study the interplay of star formation (as traced through [CII] and FIR emission), central black hole accretion (through unresolved FIR emission) and the molecular gas reservoir (CO).

In complement to this future ALMA observations, with my collaborators we have CO(4-3) observations with CARMA, and high-resolution imaging of the [CI] and CO(7-6) lines and 1.2 mm continuum with the PdBI. The analysis of this galaxy in such a detail will help us understanding galaxy formation and the processes of emission of [CII] at high redshift.

In parallel, I am part of three projects that will use ALMA cycle 2 observations. Two of the projects will do a spectroscopic survey in the Hubble Ultra Deep Field at 1 and 3 mm. The survey at 1.3 mm should detect [CII] emission at $z \sim 6$. The third project is survey for imaging the first 3 massive strong-lensing clusters in the HST Frontier Fields, which will reveal the faint mm emission of lensed galaxies, and it is a perfect continuation to our LABOCA and GISMO campaign.

The long term goal of my research is to use the FIR emission lines to characterize the normal star-forming galaxies at high redshift and check how the ISM properties such as density, temperature, radiation field and dynamics complexity evolve with redshift. To fulfill this goal I plan to use EVLA and ALMA to observe the molecular and fine structure emission lines on a sample of strongly lensed galaxies. The plan is to use EVLA to observe low-J CO lines and ALMA to observe the fine structure lines. The first step is to detect the different emission lines and use that information to study galaxies at the higher redshift. The sample that I will use corresponds to the 50-100 $z > 1$ strongly lensed galaxies detected as part of CLASH. These galaxies have publish redshifts and magnification values, which are key factors to search for FIR lines and properly analyze the observed emissions.

Once the lines are detected, the next step will be to resolve the emission of each line to study the ISM in detail. As part of this project, I want to develop tools to reconstruct high resolution maps of lensed galaxies taken with EVLA and ALMA. I want to combine the magnification maps provided by CLASH with UV-plane modeling (EVLA and ALMA) to reconstruct the source images of interferometric data.

Bibliography

Alexander, D. M., Bauer, F. E., Chapman, S. C., Smail, I., Blain, A. W., Brandt, W. N., and Ivison, R. J. (2005). The X-Ray Spectral Properties of SCUBA Galaxies. *ApJ*, 632:736–750.

Baker, A. J., Lutz, D., Genzel, R., Tacconi, L. J., and Lehnert, M. D. (2001). Dust emission from the lensed Lyman break galaxy ¡ASTROBJ¿cB58¡/ASTROBJ¿. *A&A*, 372:L37–L40.

Baker, A. J., Tacconi, L. J., Genzel, R., Lehnert, M. D., and Lutz, D. (2004). Molecular Gas in the Lensed Lyman Break Galaxy cB58. *ApJ*, 604:125–140.

Bianchi, S. (2013). Vindicating single-T modified blackbody fits to Herschel SEDs. *A&A*, 552:A89.

Blain, A. W., Smail, I., Ivison, R. J., Kneib, J.-P., and Frayer, D. T. (2002). Submillimeter galaxies. *Phys. Rep.*, 369:111–176.

Bonafede, A., Feretti, L., Giovannini, G., Govoni, F., Murgia, M., Taylor, G. B., Ebeling, H., Allen, S., Gentile, G., and Pihlström, Y. (2009). Revealing the magnetic field in a distant galaxy cluster: discovery of the complex radio emission from MACS J0717.5 +3745. *A&A*, 503:707–720.

Boone, F., Clément, B., Richard, J., Schaerer, D., Lutz, D., Weiß, A., Zemcov, M., Egami, E., Rawle, T. D., Walth, G. L., Kneib, J.-P., Combes, F., Smail, I., Swinbank, A. M., Altieri, B., Blain, A. W., Chapman, S., Dessauges-Zavadsky, M., Ivison, R. J., Knudsen, K. K., Omont, A., Pelló, R., Pérez-González, P. G., Valtchanov, I., van der Werf, P., and Zamojski, M. (2013). An extended Herschel drop-out source in the center of AS1063: a normal dusty galaxy at z = 6.1 or SZ substructures? *A&A*, 559:L1.

Bourne, N., Maddox, S. J., Dunne, L., Auld, R., Baes, M., Baldry, I. K., Bonfield, D. G., Cooray, A., Croom, S. M., Dariush, A., de Zotti, G., Driver, S. P., Dye, S., Eales, S., Gomez, H. L., González-Nuevo, J., Hopkins, A. M., Ibar, E., Jarvis, M. J., Lapi, A., Madore, B., Michałowski, M. J., Pohlen, M., Popescu, C. C., Rigby, E. E., Seibert,

M., Smith, D. J. B., Tuffs, R. J., Werf, P. v. d., Brough, S., Buttiglione, S., Cava, A., Clements, D. L., Conselice, C. J., Fritz, J., Hopwood, R., Ivison, R. J., Jones, D. H., Kelvin, L. S., Liske, J., Loveday, J., Norberg, P., Robotham, A. S. G., Rodighiero, G., and Temi, P. (2012). Herschel-ATLAS/GAMA: a census of dust in optically selected galaxies from stacking at submillimetre wavelengths. *MNRAS*, 421:3027–3059.

Bouwens, R. J., Bradley, L., Zitrin, A., Coe, D., Franx, M., Zheng, W., Smit, R., Host, O., Postman, M., Moustakas, L., Labbé, I., Carrasco, M., Molino, A., Donahue, M., Kelson, D. D., Meneghetti, M., Benítez, N., Lemze, D., Umetsu, K., Broadhurst, T., Moustakas, J., Rosati, P., Jouvel, S., Bartelmann, M., Ford, H., Graves, G., Grillo, C., Infante, L., Jimenez-Teja, Y., Lahav, O., Maoz, D., Medezinski, E., Melchior, P., Merten, J., Nonino, M., Ogaz, S., and Seitz, S. (2014). A Census of Star-forming Galaxies in the Z ˜ 9-10 Universe based on HST+Spitzer Observations over 19 Clash Clusters: Three Candidate Z ˜ 9-10 Galaxies and Improved Constraints on the Star Formation Rate Density at Z ˜ 9.2. *ApJ*, 795:126.

Bouwens, R. J., Illingworth, G. D., Franx, M., and Ford, H. (2007). UV Luminosity Functions at z˜4, 5, and 6 from the Hubble Ultra Deep Field and Other Deep Hubble Space Telescope ACS Fields: Evolution and Star Formation History. *ApJ*, 670:928–958.

Bouwens, R. J., Illingworth, G. D., Labbe, I., Oesch, P. A., Trenti, M., Carollo, C. M., van Dokkum, P. G., Franx, M., Stiavelli, M., González, V., Magee, D., and Bradley, L. (2011a). A candidate redshift z˜10 galaxy and rapid changes in that population at an age of 500Myr. *Nature*, 469:504–507.

Bouwens, R. J., Illingworth, G. D., Oesch, P. A., Labbé, I., Trenti, M., van Dokkum, P., Franx, M., Stiavelli, M., Carollo, C. M., Magee, D., and Gonzalez, V. (2011b). Ultraviolet Luminosity Functions from 132 z ˜ 7 and z ˜ 8 Lyman-break Galaxies in the Ultra-deep HUDF09 and Wide-area Early Release Science WFC3/IR Observations. *ApJ*, 737:90.

Bradford, C. M., Bolatto, A. D., Maloney, P. R., Aguirre, J. E., Bock, J. J., Glenn, J., Kamenetzky, J., Lupu, R., Matsuhara, H., Murphy, E. J., Naylor, B. J., Nguyen, H. T., Scott, K., and Zmuidzinas, J. (2011). The Water Vapor Spectrum of APM 08279+5255: X-Ray Heating and Infrared Pumping over Hundreds of Parsecs. *ApJ*, 741:L37.

Brammer, G. B., van Dokkum, P. G., Illingworth, G. D., Bouwens, R. J., Labbé, I., Franx, M., Momcheva, I., and Oesch, P. A. (2013). A Tentative Detection of an Emission Line at 1.6 μm for the z ˜ 12 Candidate UDFj-39546284. *ApJ*, 765:L2.

Cai, Z., Fan, X., Jiang, L., Bian, F., McGreer, I., Davé, R., Egami, E., Zabludoff, A., Yang, Y., and Oh, S. P. (2011). Probing Population III Stars in Galaxy IOK-1 at z = 6.96 Through He II Emission. *ApJ*, 736:L28.

Capak, P., Faisst, A., Vieira, J. D., Tacchella, S., Carollo, M., and Scoville, N. Z. (2013). Keck-I MOSFIRE Spectroscopy of the z ˜ 12 Candidate Galaxy UDFj-39546284. *ApJ*, 773:L14.

Carilli, C. L., Murayama, T., Wang, R., Schinnerer, E., Taniguchi, Y., Smolčić, V., Bertoldi, F., Ajiki, M., Nagao, T., Sasaki, S. S., Shioya, Y., Aguirre, J. E., Blain, A. W., Scoville, N., and Sanders, D. B. (2007). Radio and Millimeter Properties of z˜5.7 Lyα Emitters in the COSMOS Field: Limits on Radio AGNs, Submillimeter Galaxies, and Dust Obscuration. *ApJS*, 172:518–522.

Carilli, C. L., Riechers, D., Walter, F., Maiolino, R., Wagg, J., Lentati, L., McMahon, R., and Wolfe, A. (2013). The Anatomy of an Extreme Starburst within 1.3 Gyr of the Big Bang Revealed by ALMA. *ApJ*, 763:120.

Carilli, C. L. and Walter, F. (2013). Cool Gas in High-Redshift Galaxies. *ARA&A*, 51:105–161.

Carral, P., Hollenbach, D. J., Lord, S. D., Colgan, S. W. J., Haas, M. R., Rubin, R. H., and Erickson, E. F. (1994). The interstellar medium in the starburst regions of NGC 253 and NGC 3256. *ApJ*, 423:223–236.

Chapman, S. C., Lewis, G. F., Scott, D., Richards, E., Borys, C., Steidel, C. C., Adelberger, K. L., and Shapley, A. E. (2001). Submillimeter Imaging of a Protocluster Region at Z=3.09. *ApJ*, 548:L17–L21.

Chapman, S. C., Scott, D., Borys, C., and Fahlman, G. G. (2002). Submillimetre sources in rich cluster fields: source counts, redshift estimates and cooling flow limits. *MNRAS*, 330:92–104.

Chapman, S. C., Scott, D., Steidel, C. C., Borys, C., Halpern, M., Morris, S. L., Adelberger, K. L., Dickinson, M., Giavalisco, M., and Pettini, M. (2000). A search for the submillimetre counterparts to Lyman break galaxies. *MNRAS*, 319:318–330.

Coe, D., Zitrin, A., Carrasco, M., Shu, X., Zheng, W., Postman, M., Bradley, L., Koekemoer, A., Bouwens, R., Broadhurst, T., Monna, A., Host, O., Moustakas, L. A., Ford, H., Moustakas, J., van der Wel, A., Donahue, M., Rodney, S. A., Benítez, N., Jouvel, S., Seitz, S., Kelson, D. D., and Rosati, P. (2013). CLASH: Three Strongly Lensed Images of a Candidate z $\sim$ 11 Galaxy. *ApJ*, 762:32.

Colbert, J. W., Malkan, M. A., Clegg, P. E., Cox, P., Fischer, J., Lord, S. D., Luhman, M., Satyapal, S., Smith, H. A., Spinoglio, L., Stacey, G., and Unger, S. J. (1999). ISO LWS Spectroscopy of M82: A Unified Evolutionary Model. *ApJ*, 511:721–729.

Combes, F., Rex, M., Rawle, T. D., Egami, E., Boone, F., Smail, I., Richard, J., Ivison, R. J., Gurwell, M., Casey, C. M., Omont, A., Berciano Alba, A., Dessauges-Zavadsky, M., Edge, A. C., Fazio, G. G., Kneib, J.-P., Okabe, N., Pelló, R., Pérez-González, P. G., Schaerer, D., Smith, G. P., Swinbank, A. M., and van der Werf, P. (2012). A bright z = 5.2 lensed submillimeter galaxy in the field of Abell 773. HLSJ091828.6+514223. *A&A*, 538:L4.

Coppin, K., Chapin, E. L., Mortier, A. M. J., Scott, S. E., Borys, C., Dunlop, J. S., Halpern, M., Hughes, D. H., Pope, A., Scott, D., Serjeant, S., Wagg, J., Alexander, D. M., Almaini, O., Aretxaga, I., Babbedge, T., Best, P. N., Blain, A., Chapman, S., Clements, D. L., Crawford, M., Dunne, L., Eales, S. A., Edge, A. C., Farrah, D., Gaztañaga, E., Gear, W. K., Granato, G. L., Greve, T. R., Fox, M., Ivison, R. J., Jarvis, M. J., Jenness, T., Lacey, C., Lepage, K., Mann, R. G., Marsden, G., Martinez-Sansigre, A., Oliver, S., Page, M. J., Peacock, J. A., Pearson, C. P., Percival, W. J., Priddey, R. S., Rawlings, S., Rowan-Robinson, M., Savage, R. S., Seigar, M., Sekiguchi, K., Silva, L., Simpson, C., Smail, I., Stevens, J. A., Takagi, T., Vaccari, M., van Kampen, E., and Willott, C. J. (2006). The SCUBA Half-Degree Extragalactic Survey - II. Submillimetre maps, catalogue and number counts. *MNRAS*, 372:1621–1652.

Coppin, K. E. K., Swinbank, A. M., Neri, R., Cox, P., Smail, I., Ellis, R. S., Geach, J. E., Siana, B., Teplitz, H., Dye, S., Kneib, J.-P., Edge, A. C., and Richard, J. (2007). A Detailed Study of Gas and Star Formation in a Highly Magnified Lyman Break Galaxy at z = 3.07. *ApJ*, 665:936–943.

Cormier, D., Lebouteiller, V., Madden, S. C., Abel, N., Hony, S., Galliano, F., Baes, M., Barlow, M. J., Cooray, A., De Looze, I., Galametz, M., Karczewski, O. Ł., Parkin, T. J., Rémy, A., Sauvage, M., Spinoglio, L., Wilson, C. D., and Wu, R. (2012). The nature of the interstellar medium of the starburst low-metallicity galaxy Haro 11: a multi-phase model of the infrared emission. *A&A*, 548:A20.

Cowie, L. L., Barger, A. J., and Hu, E. M. (2011). Lyα Emitting Galaxies as Early Stages in Galaxy Formation. *ApJ*, 738:136.

Cox, P., Krips, M., Neri, R., Omont, A., Güsten, R., Menten, K. M., Wyrowski, F., Weiß, A., Beelen, A., Gurwell, M. A., Dannerbauer, H., Ivison, R. J., Negrello, M., Aretxaga, I., Hughes, D. H., Auld, R., Baes, M., Blundell, R., Buttiglione, S., Cava, A., Cooray, A., Dariush, A., Dunne, L., Dye, S., Eales, S. A., Frayer, D., Fritz, J.,

Gavazzi, R., Hopwood, R., Ibar, E., Jarvis, M., Maddox, S., Michałowski, M., Pascale, E., Pohlen, M., Rigby, E., Smith, D. J. B., Swinbank, A. M., Temi, P., Valtchanov, I., van der Werf, P., and de Zotti, G. (2011). Gas and Dust in a Submillimeter Galaxy at z = 4.24 from the Herschel Atlas. *ApJ*, 740:63.

Crawford, M. K., Genzel, R., Townes, C. H., and Watson, D. M. (1985). Far-infrared spectroscopy of galaxies - The 158 micron C(+) line and the energy balance of molecular clouds. *ApJ*, 291:755–771.

da Cunha, E., Charlot, S., and Elbaz, D. (2008). A simple model to interpret the ultraviolet, optical and infrared emission from galaxies. *MNRAS*, 388:1595–1617.

da Cunha, E., Groves, B., Walter, F., Decarli, R., Weiss, A., Bertoldi, F., Carilli, C., Daddi, E., Elbaz, D., Ivison, R., Maiolino, R., Riechers, D., Rix, H.-W., Sargent, M., and Smail, I. (2013). On the Effect of the Cosmic Microwave Background in High-redshift (Sub-)millimeter Observations. *ApJ*, 766:13.

Daddi, E., Bournaud, F., Walter, F., Dannerbauer, H., Carilli, C. L., Dickinson, M., Elbaz, D., Morrison, G. E., Riechers, D., Onodera, M., Salmi, F., Krips, M., and Stern, D. (2010). Very High Gas Fractions and Extended Gas Reservoirs in z = 1.5 Disk Galaxies. *ApJ*, 713:686–707.

Daddi, E., Dickinson, M., Morrison, G., Chary, R., Cimatti, A., Elbaz, D., Frayer, D., Renzini, A., Pope, A., Alexander, D. M., Bauer, F. E., Giavalisco, M., Huynh, M., Kurk, J., and Mignoli, M. (2007). Multiwavelength Study of Massive Galaxies at z˜2. I. Star Formation and Galaxy Growth. *ApJ*, 670:156–172.

Dale, D. A., Gil de Paz, A., Gordon, K. D., Hanson, H. M., Armus, L., Bendo, G. J., Bianchi, L., Block, M., Boissier, S., Boselli, A., Buckalew, B. A., Buat, V., Burgarella, D., Calzetti, D., Cannon, J. M., Engelbracht, C. W., Helou, G., Hollenbach, D. J., Jarrett, T. H., Kennicutt, R. C., Leitherer, C., Li, A., Madore, B. F., Martin, D. C., Meyer, M. J., Murphy, E. J., Regan, M. W., Roussel, H., Smith, J. D. T., Sosey, M. L., Thilker, D. A., and Walter, F. (2007). An Ultraviolet-to-Radio Broadband Spectral Atlas of Nearby Galaxies. *ApJ*, 655:863–884.

Davé, R., Finlator, K., Oppenheimer, B. D., Fardal, M., Katz, N., Kereš, D., and Weinberg, D. H. (2010). The nature of submillimetre galaxies in cosmological hydrodynamic simulations. *MNRAS*, 404:1355–1368.

Davies, L. J. M., Bremer, M. N., Stanway, E. R., and Lehnert, M. D. (2013). The detection of FIR emission from high-redshift star-forming galaxies in the ECDF-S. *MNRAS*, 433:2588–2603.

Davies, L. J. M., Bremer, M. N., Stanway, E. R., Mannering, E., Lehnert, M. D., and Omont, A. (2012). Limits on dust emission from z $\sim$ 5 LBGs and their local environments. *MNRAS*, 425:153–161.

Dayal, P. and Ferrara, A. (2012). Lyα emitters and Lyman-break galaxies: dichotomous twins. *MNRAS*, 421:2568–2579.

De Breuck, C., Maiolino, R., Caselli, P., Coppin, K., Hailey-Dunsheath, S., and Nagao, T. (2011). Enhanced [CII] emission in a z = 4.76 submillimetre galaxy. *A&A*, 530:L8.

de Looze, I., Baes, M., Bendo, G. J., Cortese, L., and Fritz, J. (2011). The reliability of [C II] as an indicator of the star formation rate. *MNRAS*, 416:2712–2724.

Decarli, R., Walter, F., Carilli, C., Bertoldi, F., Cox, P., Ferkinhoff, C., Groves, B., Maiolino, R., Neri, R., Riechers, D., and Weiss, A. (2014). Varying [C II]/[N II] Line Ratios in the Interacting System BR1202-0725 at z = 4.7. *ApJ*, 782:L17.

Decarli, R., Walter, F., Neri, R., Bertoldi, F., Carilli, C., Cox, P., Kneib, J. P., Lestrade, J. F., Maiolino, R., Omont, A., Richard, J., Riechers, D., Thanjavur, K., and Weiss, A. (2012). Ionized Nitrogen at High Redshift. *ApJ*, 752:2.

Dekel, A., Birnboim, Y., Engel, G., Freundlich, J., Goerdt, T., Mumcuoglu, M., Neistein, E., Pichon, C., Teyssier, R., and Zinger, E. (2009). Cold streams in early massive hot haloes as the main mode of galaxy formation. *Nature*, 457:451–454.

Díaz-Santos, T., Armus, L., Charmandaris, V., Stierwalt, S., Murphy, E. J., Haan, S., Inami, H., Malhotra, S., Meijerink, R., Stacey, G., Petric, A. O., Evans, A. S., Veilleux, S., van der Werf, P. P., Lord, S., Lu, N., Howell, J. H., Appleton, P., Mazzarella, J. M., Surace, J. A., Xu, C. K., Schulz, B., Sanders, D. B., Bridge, C., Chan, B. H. P., Frayer, D. T., Iwasawa, K., Melbourne, J., and Sturm, E. (2013). Explaining the [C II]157.7 μm Deficit in Luminous Infrared Galaxies—First Results from a Herschel/PACS Study of the GOALS Sample. *ApJ*, 774:68.

Eales, S., Lilly, S., Gear, W., Dunne, L., Bond, J. R., Hammer, F., Le Fèvre, O., and Crampton, D. (1999). The Canada-UK Deep Submillimeter Survey: First Submillimeter Images, the Source Counts, and Resolution of the Background. *ApJ*, 515:518–524.

Egami, E., Rex, M., Rawle, T. D., Pérez-González, P. G., Richard, J., Kneib, J.-P., Schaerer, D., Altieri, B., Valtchanov, I., Blain, A. W., Fadda, D., Zemcov, M., Bock, J. J., Boone, F., Bridge, C. R., Clement, B., Combes, F., Dessauges-Zavadsky, M., Dowell, C. D., Ilbert, O., Ivison, R. J., Jauzac, M., Lutz, D., Metcalfe, L., Omont, A., Pelló, R., Pereira, M. J., Rieke, G. H., Rodighiero, G., Smail, I., Smith, G. P., Tramoy, G., Walth, G. L., van der Werf, P., and Werner, M. W. (2010). The Herschel Lensing Survey (HLS): Overview. *A&A*, 518:L12.

Ehlert, S., Allen, S. W., von der Linden, A., Simionescu, A., Werner, N., Taylor, G. B., Gentile, G., Ebeling, H., Allen, M. T., Applegate, D., Dunn, R. J. H., Fabian, A. C., Kelly, P., Million, E. T., Morris, R. G., Sanders, J. S., and Schmidt, R. W. (2011). Extreme active galactic nucleus feedback and cool-core destruction in the X-ray luminous galaxy cluster MACS J1931.8-2634. *MNRAS*, 411:1641–1658.

Elbaz, D., Daddi, E., Le Borgne, D., Dickinson, M., Alexander, D. M., Chary, R.-R., Starck, J.-L., Brandt, W. N., Kitzbichler, M., MacDonald, E., Nonino, M., Popesso, P., Stern, D., and Vanzella, E. (2007). The reversal of the star formation-density relation in the distant universe. *A&A*, 468:33–48.

Elbaz, D., Dickinson, M., Hwang, H. S., Díaz-Santos, T., Magdis, G., Magnelli, B., Le Borgne, D., Galliano, F., Pannella, M., Chanial, P., Armus, L., Charmandaris, V., Daddi, E., Aussel, H., Popesso, P., Kartaltepe, J., Altieri, B., Valtchanov, I., Coia, D., Dannerbauer, H., Dasyra, K., Leiton, R., Mazzarella, J., Alexander, D. M., Buat, V., Burgarella, D., Chary, R.-R., Gilli, R., Ivison, R. J., Juneau, S., Le Floc'h, E., Lutz, D., Morrison, G. E., Mullaney, J. R., Murphy, E., Pope, A., Scott, D., Brodwin, M., Calzetti, D., Cesarsky, C., Charlot, S., Dole, H., Eisenhardt, P., Ferguson, H. C., Förster Schreiber, N., Frayer, D., Giavalisco, M., Huynh, M., Koekemoer, A. M., Papovich, C., Reddy, N., Surace, C., Teplitz, H., Yun, M. S., and Wilson, G. (2011). GOODS-Herschel: an infrared main sequence for star-forming galaxies. *A&A*, 533:A119.

Ellis, R. S., McLure, R. J., Dunlop, J. S., Robertson, B. E., Ono, Y., Schenker, M. A., Koekemoer, A., Bowler, R. A. A., Ouchi, M., Rogers, A. B., Curtis-Lake, E., Schneider, E., Charlot, S., Stark, D. P., Furlanetto, S. R., and Cirasuolo, M. (2013). The Abundance of Star-forming Galaxies in the Redshift Range 8.5-12: New Results from the 2012 Hubble Ultra Deep Field Campaign. *ApJ*, 763:L7.

Engel, H., Tacconi, L. J., Davies, R. I., Neri, R., Smail, I., Chapman, S. C., Genzel, R., Cox, P., Greve, T. R., Ivison, R. J., Blain, A., Bertoldi, F., and Omont, A. (2010). Most Submillimeter Galaxies are Major Mergers. *ApJ*, 724:233–243.

Ferkinhoff, C., Brisbin, D., Nikola, T., Parshley, S. C., Stacey, G. J., Phillips, T. G., Falgarone, E., Benford, D. J., Staguhn, J. G., and Tucker, C. E. (2011). First Detections of the [N II] 122 μm Line at High Redshift: Demonstrating the Utility of the Line for Studying Galaxies in the Early Universe. *ApJ*, 740:L29.

Ferkinhoff, C., Hailey-Dunsheath, S., Nikola, T., Parshley, S. C., Stacey, G. J., Benford, D. J., and Staguhn, J. G. (2010). First Detection of the [O III] 88 μm Line at High Redshifts: Characterizing the Starburst and Narrow-line Regions in Extreme Luminosity Systems. *ApJ*, 714:L147–L151.

Finkelstein, S. L., Rhoads, J. E., Malhotra, S., and Grogin, N. (2009). Lyman Alpha Galaxies: Primitive, Dusty, or Evolved? *ApJ*, 691:465–481.

Finkelstein, S. L., Rhoads, J. E., Malhotra, S., Pirzkal, N., and Wang, J. (2007). The Ages and Masses of Lyα Galaxies at z ˜ 4.5. *ApJ*, 660:1023–1029.

Fontana, A., Vanzella, E., Pentericci, L., Castellano, M., Giavalisco, M., Grazian, A., Boutsia, K., Cristiani, S., Dickinson, M., Giallongo, E., Maiolino, R., Moorwood, A., and Santini, P. (2010). The Lack of Intense Lyα in Ultradeep Spectra of z = 7 Candidates in GOODS-S: Imprint of Reionization? *ApJ*, 725:L205–L209.

Gallerani, S., Neri, R., Maiolino, R., Martín, S., De Breuck, C., Walter, F., Caselli, P., Krips, M., Meneghetti, M., Nagao, T., Wagg, J., and Walmsley, M. (2012). Resolved [CII] emission in a lensed quasar at z = 4.4. *A&A*, 543:A114.

Gawiser, E., van Dokkum, P. G., Gronwall, C., Ciardullo, R., Blanc, G. A., Castander, F. J., Feldmeier, J., Francke, H., Franx, M., Haberzettl, L., Herrera, D., Hickey, T., Infante, L., Lira, P., Maza, J., Quadri, R., Richardson, A., Schawinski, K., Schirmer, M., Taylor, E. N., Treister, E., Urry, C. M., and Virani, S. N. (2006). The Physical Nature of Lyα-emitting Galaxies at z=3.1. *ApJ*, 642:L13–L16.

Gonzalez, A. H., Papovich, C., Bradač, M., and Jones, C. (2010). Spectroscopic Confirmation of a z = 2.79 Multiply Imaged Luminous Infrared Galaxy Behind the Bullet Cluster. *ApJ*, 720:245–251.

González, J. E., Lacey, C. G., Baugh, C. M., Frenk, C. S., and Benson, A. J. (2012). The nature and descendants of Lyman-break galaxies in the Λ cold dark matter cosmology. *MNRAS*, 423:3709–3726.

González-López, J., Riechers, D. A., Decarli, R., Walter, F., Vallini, L., Neri, R., Bertoldi, F., Bolatto, A. D., Carilli, C. L., Cox, P., da Cunha, E., Ferrara, A., Gallerani, S., and Infante, L. (2014). Search for [C II] Emission in z = 6.5-11 Star-forming Galaxies. *ApJ*, 784:99.

Griffin, M. J., Abergel, A., Abreu, A., Ade, P. A. R., André, P., Augueres, J.-L., Babbedge, T., Bae, Y., Baillie, T., Baluteau, J.-P., Barlow, M. J., Bendo, G., Benielli, D., Bock, J. J., Bonhomme, P., Brisbin, D., Brockley-Blatt, C., Caldwell, M., Cara, C., Castro-Rodriguez, N., Cerulli, R., Chanial, P., Chen, S., Clark, E., Clements, D. L., Clerc, L., Coker, J., Communal, D., Conversi, L., Cox, P., Crumb, D., Cunningham, C., Daly, F., Davis, G. R., de Antoni, P., Delderfield, J., Devin, N., di Giorgio, A., Didschuns, I., Dohlen, K., Donati, M., Dowell, A., Dowell, C. D., Duband, L., Dumaye, L., Emery, R. J., Ferlet, M., Ferrand, D., Fontignie, J., Fox, M., Franceschini, A., Frerking, M., Fulton, T., Garcia, J., Gastaud, R., Gear, W. K., Glenn, J., Goizel,

A., Griffin, D. K., Grundy, T., Guest, S., Guillemet, L., Hargrave, P. C., Harwit, M., Hastings, P., Hatziminaoglou, E., Herman, M., Hinde, B., Hristov, V., Huang, M., Imhof, P., Isaak, K. J., Israelsson, U., Ivison, R. J., Jennings, D., Kiernan, B., King, K. J., Lange, A. E., Latter, W., Laurent, G., Laurent, P., Leeks, S. J., Lellouch, E., Levenson, L., Li, B., Li, J., Lilienthal, J., Lim, T., Liu, S. J., Lu, N., Madden, S., Mainetti, G., Marliani, P., McKay, D., Mercier, K., Molinari, S., Morris, H., Moseley, H., Mulder, J., Mur, M., Naylor, D. A., Nguyen, H., O'Halloran, B., Oliver, S., Olofsson, G., Olofsson, H.-G., Orfei, R., Page, M. J., Pain, I., Panuzzo, P., Papageorgiou, A., Parks, G., Parr-Burman, P., Pearce, A., Pearson, C., Pérez-Fournon, I., Pinsard, F., Pisano, G., Podosek, J., Pohlen, M., Polehampton, E. T., Pouliquen, D., Rigopoulou, D., Rizzo, D., Roseboom, I. G., Roussel, H., Rowan-Robinson, M., Rownd, B., Saraceno, P., Sauvage, M., Savage, R., Savini, G., Sawyer, E., Scharmberg, C., Schmitt, D., Schneider, N., Schulz, B., Schwartz, A., Shafer, R., Shupe, D. L., Sibthorpe, B., Sidher, S., Smith, A., Smith, A. J., Smith, D., Spencer, L., Stobie, B., Sudiwala, R., Sukhatme, K., Surace, C., Stevens, J. A., Swinyard, B. M., Trichas, M., Tourette, T., Triou, H., Tseng, S., Tucker, C., Turner, A., Vaccari, M., Valtchanov, I., Vigroux, L., Virique, E., Voellmer, G., Walker, H., Ward, R., Waskett, T., Weilert, M., Wesson, R., White, G. J., Whitehouse, N., Wilson, C. D., Winter, B., Woodcraft, A. L., Wright, G. S., Xu, C. K., Zavagno, A., Zemcov, M., Zhang, L., and Zonca, E. (2010). The Herschel-SPIRE instrument and its in-flight performance. *A&A*, 518:L3.

Hailey-Dunsheath, S., Nikola, T., Stacey, G. J., Oberst, T. E., Parshley, S. C., Benford, D. J., Staguhn, J. G., and Tucker, C. E. (2010). Detection of the 158 μm [C II] Transition at z = 1.3: Evidence for a Galaxy-wide Starburst. *ApJ*, 714:L162–L166.

Hainline, L. J., Blain, A. W., Smail, I., Alexander, D. M., Armus, L., Chapman, S. C., and Ivison, R. J. (2011). The Stellar Mass Content of Submillimeter-selected Galaxies. *ApJ*, 740:96.

Hodge, J. A., Karim, A., Smail, I., Swinbank, A. M., Walter, F., Biggs, A. D., Ivison, R. J., Weiss, A., Alexander, D. M., Bertoldi, F., Brandt, W. N., Chapman, S. C., Coppin, K. E. K., Cox, P., Danielson, A. L. R., Dannerbauer, H., De Breuck, C., Decarli, R., Edge, A. C., Greve, T. R., Knudsen, K. K., Menten, K. M., Rix, H.-W., Schinnerer, E., Simpson, J. M., Wardlow, J. L., and van der Werf, P. (2013). An ALMA Survey of Submillimeter Galaxies in the Extended Chandra Deep Field South: Source Catalog and Multiplicity. *ApJ*, 768:91.

Hughes, D. H., Serjeant, S., Dunlop, J., Rowan-Robinson, M., Blain, A., Mann, R. G., Ivison, R., Peacock, J., Efstathiou, A., Gear, W., Oliver, S., Lawrence, A., Longair, M., Goldschmidt, P., and Jenness, T. (1998). High-redshift star formation in the

Hubble Deep Field revealed by a submillimetre-wavelength survey. *Nature*, 394:241–247.

Hunt, L., Bianchi, S., and Maiolino, R. (2005). The optical-to-radio spectral energy distributions of low-metallicity blue compact dwarf galaxies. *A&A*, 434:849–866.

Iono, D., Wilson, C. D., Yun, M. S., Baker, A. J., Petitpas, G. R., Peck, A. B., Krips, M., Cox, T. J., Matsushita, S., Mihos, J. C., and Pihlstrom, Y. (2009). Luminous Infrared Galaxies with the Submillimeter Array. II. Comparing the CO (3-2) Sizes and Luminosities of Local and High-Redshift Luminous Infrared Galaxies. *ApJ*, 695:1537–1549.

Iono, D., Yun, M. S., Elvis, M., Peck, A. B., Ho, P. T. P., Wilner, D. J., Hunter, T. R., Matsushita, S., and Muller, S. (2006). A Detection of [C II] Line Emission in the z = 4.7 QSO BR 1202-0725. *ApJ*, 645:L97–L100.

Israel, F. P., Maloney, P. R., Geis, N., Herrmann, F., Madden, S. C., Poglitsch, A., and Stacey, G. J. (1996). C + Emission from the Magellanic Clouds. I. The Bright H II Region Complexes N159 and N160. *ApJ*, 465:738.

Ivison, R. J., Swinbank, A. M., Swinyard, B., Smail, I., Pearson, C. P., Rigopoulou, D., Polehampton, E., Baluteau, J.-P., Barlow, M. J., Blain, A. W., Bock, J., Clements, D. L., Coppin, K., Cooray, A., Danielson, A., Dwek, E., Edge, A. C., Franceschini, A., Fulton, T., Glenn, J., Griffin, M., Isaak, K., Leeks, S., Lim, T., Naylor, D., Oliver, S. J., Page, M. J., Pérez Fournon, I., Rowan-Robinson, M., Savini, G., Scott, D., Spencer, L., Valtchanov, I., Vigroux, L., and Wright, G. S. (2010). Herschel and SCUBA-2 imaging and spectroscopy of a bright, lensed submillimetre galaxy at z = 2.3. *A&A*, 518:L35.

Iye, M., Ota, K., Kashikawa, N., Furusawa, H., Hashimoto, T., Hattori, T., Matsuda, Y., Morokuma, T., Ouchi, M., and Shimasaku, K. (2006). A galaxy at a redshift z = 6.96. *Nature*, 443:186–188.

Jiang, L., Egami, E., Mechtley, M., Fan, X., Cohen, S. H., Windhorst, R. A., Davé, R., Finlator, K., Kashikawa, N., Ouchi, M., and Shimasaku, K. (2013). Physical Properties of Spectroscopically Confirmed Galaxies at z >= 6. I. Basic Characteristics of the Rest-frame UV Continuum and Lyα Emission. *ApJ*, 772:99.

Johansson, D., Horellou, C., Lopez-Cruz, O., Muller, S., Birkinshaw, M., Black, J. H., Bremer, M. N., Wall, W. F., Bertoldi, F., Castillo, E., and Ibarra-Medel, H. J. (2012). Molecular gas and dust in the highly magnified z ˜ 2.8 galaxy behind the Bullet Cluster. *A&A*, 543:A62.

Johansson, D., Horellou, C., Sommer, M. W., Basu, K., Bertoldi, F., Birkinshaw, M., Lancaster, K., Lopez-Cruz, O., and Quintana, H. (2010). Submillimeter galaxies behind the Bullet cluster (1E 0657-56). *A&A*, 514:A77.

Johansson, D., Sigurdarson, H., and Horellou, C. (2011). A LABOCA survey of submillimeter galaxies behind galaxy clusters. *A&A*, 527:A117.

Kanekar, N., Wagg, J., Ram Chary, R., and Carilli, C. L. (2013). A Search for C II 158 μm Line Emission in HCM 6A, a Lyα Emitter at z = 6.56. *ApJ*, 771:L20.

Karman, W., Caputi, K. I., Grillo, C., Balestra, I., Rosati, P., Vanzella, E., Coe, D., Christensen, L., Koekemoer, A. M., Kruehler, T., Lombardi, M., Mercurio, A., Nonino, M., and van der Wel, A. (2014). MUSE integral-field spectroscopy towards the Frontier Fields Cluster Abell S1063: I. Data products and redshift identifications. *ArXiv e-prints*.

Kennicutt, Jr., R. C. (1998). Star Formation in Galaxies Along the Hubble Sequence. *ARA&A*, 36:189–232.

Knudsen, K. K., Barnard, V. E., van der Werf, P. P., Vielva, P., Kneib, J.-P., Blain, A. W., Barreiro, R. B., Ivison, R. J., Smail, I., and Peacock, J. A. (2006). An ultradeep submillimetre map: beneath the SCUBA confusion limit with lensing and robust source extraction. *MNRAS*, 368:487–496.

Knudsen, K. K., van der Werf, P., Franx, M., Förster Schreiber, N. M., van Dokkum, P. G., Illingworth, G. D., Labbé, I., Moorwood, A., Rix, H.-W., and Rudnick, G. (2005). Submillimeter Observations of Distant Red Galaxies: Uncovering the 1 mJy 850 μm Population. *ApJ*, 632:L9–L12.

Knudsen, K. K., van der Werf, P. P., and Kneib, J.-P. (2008). Probing the submillimetre number counts at $f_{850\mu m} < 2$mJy. *MNRAS*, 384:1611–1626.

Lai, K., Huang, J.-S., Fazio, G., Gawiser, E., Ciardullo, R., Damen, M., Franx, M., Gronwall, C., Labbe, I., Magdis, G., and van Dokkum, P. (2008). Spitzer Constraints on the Stellar Populations of Lyα-Emitting Galaxies at z = 3.1. *ApJ*, 674:70–74.

Le Floc'h, E., Papovich, C., Dole, H., Bell, E. F., Lagache, G., Rieke, G. H., Egami, E., Pérez-González, P. G., Alonso-Herrero, A., Rieke, M. J., Blaylock, M., Engelbracht, C. W., Gordon, K. D., Hines, D. C., Misselt, K. A., Morrison, J. E., and Mould, J. (2005). Infrared Luminosity Functions from the Chandra Deep Field-South: The Spitzer View on the History of Dusty Star Formation at $0 <\tilde{} z <\tilde{} 1$. *ApJ*, 632:169–190.

Livermore, R. C., Swinbank, A. M., Smail, I., Bower, R. G., Coppin, K. E. K., Crain, R. A., Edge, A. C., Geach, J. E., and Richard, J. (2012). Observational Limits on the Gas Mass of a z = 4.9 Galaxy. *ApJ*, 758:L35.

Lord, S. D., Hollenbach, D. J., Haas, M. R., Rubin, R. H., Colgan, S. W. J., and Erickson, E. F. (1996). Interstellar Properties of a Dual Nuclear Starburst: Far-Infrared Spectroscopy of M82. *ApJ*, 465:703.

Luhman, M. L., Satyapal, S., Fischer, J., Wolfire, M. G., Sturm, E., Dudley, C. C., Lutz, D., and Genzel, R. (2003). The [C II] 158 Micron Line Deficit in Ultraluminous Infrared Galaxies Revisited. *ApJ*, 594:758–775.

Madden, S. C., Poglitsch, A., Geis, N., Stacey, G. J., and Townes, C. H. (1997). [C II] 158 Micron Observations of IC 10: Evidence for Hidden Molecular Hydrogen in Irregular Galaxies. *ApJ*, 483:200–209.

Magdis, G. E., Daddi, E., Béthermin, M., Sargent, M., Elbaz, D., Pannella, M., Dickinson, M., Dannerbauer, H., da Cunha, E., Walter, F., Rigopoulou, D., Charmandaris, V., Hwang, H. S., and Kartaltepe, J. (2012). The Evolving Interstellar Medium of Star-forming Galaxies since z = 2 as Probed by Their Infrared Spectral Energy Distributions. *ApJ*, 760:6.

Magdis, G. E., Elbaz, D., Hwang, H. S., Amblard, A., Arumugam, V., Aussel, H., Blain, A., Bock, J., Boselli, A., Buat, V., Castro-Rodríguez, N., Cava, A., Chanial, P., Clements, D. L., Conley, A., Conversi, L., Cooray, A., Dowell, C. D., Dwek, E., Eales, S., Farrah, D., Franceschini, A., Glenn, J., Griffin, M., Halpern, M., Hatziminaoglou, E., Huang, J., Ibar, E., Isaak, K., Le Floc'h, E., Lagache, G., Levenson, L., Lonsdale, C. J., Lu, N., Madden, S., Maffei, B., Mainetti, G., Marchetti, L., Morrison, G. E., Nguyen, H. T., O'Halloran, B., Oliver, S. J., Omont, A., Owen, F. N., Page, M. J., Pannella, M., Panuzzo, P., Papageorgiou, A., Pearson, C. P., Pérez-Fournon, I., Pohlen, M., Rigopoulou, D., Rizzo, D., Roseboom, I. G., Rowan-Robinson, M., Schulz, B., Scott, D., Seymour, N., Shupe, D. L., Smith, A. J., Stevens, J. A., Strazzullo, V., Symeonidis, M., Trichas, M., Tugwell, K. E., Vaccari, M., Valtchanov, I., Vigroux, L., Wang, L., Wright, G., Xu, C. K., and Zemcov, M. (2010). Herschel reveals a T_{dust}-unbiased selection of z ˜ 2 ultraluminous infrared galaxies. *MNRAS*, 409:22–28.

Magnelli, B., Lutz, D., Santini, P., Saintonge, A., Berta, S., Albrecht, M., Altieri, B., Andreani, P., Aussel, H., Bertoldi, F., Béthermin, M., Bongiovanni, A., Capak, P., Chapman, S., Cepa, J., Cimatti, A., Cooray, A., Daddi, E., Danielson, A. L. R., Dannerbauer, H., Dunlop, J. S., Elbaz, D., Farrah, D., Förster Schreiber, N. M., Genzel, R., Hwang, H. S., Ibar, E., Ivison, R. J., Le Floc'h, E., Magdis, G., Maiolino,

R., Nordon, R., Oliver, S. J., Pérez García, A., Poglitsch, A., Popesso, P., Pozzi, F., Riguccini, L., Rodighiero, G., Rosario, D., Roseboom, I., Salvato, M., Sanchez-Portal, M., Scott, D., Smail, I., Sturm, E., Swinbank, A. M., Tacconi, L. J., Valtchanov, I., Wang, L., and Wuyts, S. (2012). A Herschel view of the far-infrared properties of submillimetre galaxies. *A&A*, 539:A155.

Maiolino, R., Caselli, P., Nagao, T., Walmsley, M., De Breuck, C., and Meneghetti, M. (2009). Strong [CII] emission at high redshift. *A&A*, 500:L1–L4.

Maiolino, R., Cox, P., Caselli, P., Beelen, A., Bertoldi, F., Carilli, C. L., Kaufman, M. J., Menten, K. M., Nagao, T., Omont, A., Weiß, A., Walmsley, C. M., and Walter, F. (2005). First detection of [CII]158 μm at high redshift: vigorous star formation in the early universe. *A&A*, 440:L51–L54.

Malhotra, S., Kaufman, M. J., Hollenbach, D., Helou, G., Rubin, R. H., Brauher, J., Dale, D., Lu, N. Y., Lord, S., Stacey, G., Contursi, A., Hunter, D. A., and Dinerstein, H. (2001). Far-Infrared Spectroscopy of Normal Galaxies: Physical Conditions in the Interstellar Medium. *ApJ*, 561:766–786.

Mentuch Cooper, E., Wilson, C. D., Foyle, K., Bendo, G., Koda, J., Baes, M., Boquien, M., Boselli, A., Ciesla, L., Cooray, A., Eales, S., Galametz, M., Lebouteiller, V., Parkin, T., Roussel, H., Sauvage, M., Spinoglio, L., and Smith, M. W. L. (2012). Spatially Resolved Stellar, Dust, and Gas Properties of the Post-interacting Whirlpool Galaxy System. *ApJ*, 755:165.

Michałowski, M., Hjorth, J., and Watson, D. (2010). Cosmic evolution of submillimeter galaxies and their contribution to stellar mass assembly. *A&A*, 514:A67.

Michałowski, M. J., Hjorth, J., Malesani, D., Michałowski, T., Castro Cerón, J. M., Reinfrank, R. F., Garrett, M. A., Fynbo, J. P. U., Watson, D. J., and Jørgensen, U. G. (2009). The Properties of the Host Galaxy and the Immediate Environment of GRB 980425/SN 1998bw from the Multiwavelength Spectral Energy Distribution. *ApJ*, 693:347–354.

Mihos, J. C. and Hernquist, L. (1996). Gasdynamics and Starbursts in Major Mergers. *ApJ*, 464:641.

Nagao, T., Maiolino, R., De Breuck, C., Caselli, P., Hatsukade, B., and Saigo, K. (2012). ALMA reveals a chemically evolved submillimeter galaxy at z = 4.76. *A&A*, 542:L34.

Negishi, T., Onaka, T., Chan, K.-W., and Roellig, T. L. (2001). Global physical conditions of the interstellar medium in nearby galaxies. *A&A*, 375:566–578.

Noeske, K. G., Weiner, B. J., Faber, S. M., Papovich, C., Koo, D. C., Somerville, R. S., Bundy, K., Conselice, C. J., Newman, J. A., Schiminovich, D., Le Floc'h, E., Coil, A. L., Rieke, G. H., Lotz, J. M., Primack, J. R., Barmby, P., Cooper, M. C., Davis, M., Ellis, R. S., Fazio, G. G., Guhathakurta, P., Huang, J., Kassin, S. A., Martin, D. C., Phillips, A. C., Rich, R. M., Small, T. A., Willmer, C. N. A., and Wilson, G. (2007). Star Formation in AEGIS Field Galaxies since z=1.1: The Dominance of Gradually Declining Star Formation, and the Main Sequence of Star-forming Galaxies. *ApJ*, 660:L43–L46.

Oesch, P. A., Bouwens, R. J., Illingworth, G. D., Gonzalez, V., Trenti, M., van Dokkum, P. G., Franx, M., Labbé, I., Carollo, C. M., and Magee, D. (2012). The Bright End of the Ultraviolet Luminosity Function at z ˜ 8: New Constraints from CANDELS Data in GOODS-South. *ApJ*, 759:135.

Oesch, P. A., Bouwens, R. J., Illingworth, G. D., Labbé, I., Franx, M., van Dokkum, P. G., Trenti, M., Stiavelli, M., Gonzalez, V., and Magee, D. (2013). Probing the Dawn of Galaxies at z ˜ 9-12: New Constraints from HUDF12/XDF and CANDELS data. *ApJ*, 773:75.

Oesch, P. A., Bouwens, R. J., Illingworth, G. D., Labbé, I., Smit, R., Franx, M., van Dokkum, P. G., Momcheva, I., Ashby, M. L. N., Fazio, G. G., Huang, J.-S., Willner, S. P., Gonzalez, V., Magee, D., Trenti, M., Brammer, G. B., Skelton, R. E., and Spitler, L. R. (2014). The Most Luminous z ˜ 9-10 Galaxy Candidates Yet Found: The Luminosity Function, Cosmic Star-formation Rate, and the First Mass Density Estimate at 500 Myr. *ApJ*, 786:108.

Ohyama, Y., Taniguchi, Y., and Shioya, Y. (2004). Subaru Deep Spectroscopy of a Star-forming Companion Galaxy of BR 1202-0725 at z=4.7. *AJ*, 128:2704–2711.

Ono, Y., Ouchi, M., Mobasher, B., Dickinson, M., Penner, K., Shimasaku, K., Weiner, B. J., Kartaltepe, J. S., Nakajima, K., Nayyeri, H., Stern, D., Kashikawa, N., and Spinrad, H. (2012). Spectroscopic Confirmation of Three z-dropout Galaxies at z = 6.844-7.213: Demographics of Lyα Emission in z ˜ 7 Galaxies. *ApJ*, 744:83.

Ota, K., Iye, M., Kashikawa, N., Shimasaku, K., Kobayashi, M., Totani, T., Nagashima, M., Morokuma, T., Furusawa, H., Hattori, T., Matsuda, Y., Hashimoto, T., and Ouchi, M. (2008). Reionization and Galaxy Evolution Probed by z = 7 Lyα Emitters. *ApJ*, 677:12–26.

Ota, K., Ly, C., Malkan, M. A., Motohara, K., Hayashi, M., Shimasaku, K., Morokuma, T., Iye, M., Kashikawa, N., and Hattori, T. (2010). Spitzer Space Telescope Constraint on the Stellar Mass of a z = 6.96 Lyα Emitter. *PASJ*, 62:1167–1175.

Ota, K., Walter, F., Ohta, K., Hatsukade, B., Carilli, C. L., da Cunha, E., González-López, J., Decarli, R., Hodge, J. A., Nagai, H., Egami, E., Jiang, L., Iye, M., Kashikawa, N., Riechers, D. A., Bertoldi, F., Cox, P., Neri, R., and Weiss, A. (2014). ALMA Observation of 158 μm [C II] Line and Dust Continuum of a z = 7 Normally Star-forming Galaxy in the Epoch of Reionization. *ApJ*, 792:34.

Oteo, I., Bongiovanni, A., Pérez García, A. M., Cepa, J., Ederoclite, A., Sánchez-Portal, M., Pintos-Castro, I., Pérez-Martínez, R., Berta, S., Magnelli, B., Popesso, P., Pozzi, F., Poglitsch, A., Lutz, D., Genzel, R., Tacconi, L., Förster Schreiber, N., Sturm, E., Elbaz, D., Aussel, H., Daddi, E., Andreani, P., Cimatti, A., Maiolino, R., Altieri, B., and Valtchanov, I. (2012a). Herschel-PACS far-infrared detections of Lyman-α emitters at $2.0 \lesssim z \lesssim 3.5$. *A&A*, 541:A65.

Oteo, I., Bongiovanni, A., Pérez García, A. M., Cepa, J., Ederoclite, A., Sánchez-Portal, M., Pintos-Castro, I., Pérez-Martínez, R., Lutz, D., Altieri, B., Andreani, P., Aussel, H., Berta, S., Cimatti, A., Daddi, E., Elbaz, D., Förster Schreiber, N., Genzel, R., Le Floc'h, E., Magnelli, B., Maiolino, R., Poglitsch, A., Popesso, P., Pozzi, F., Riguccini, L., Sturm, E., Tacconi, L., and Valtchanov, I. (2012b). Physical Properties of Lyα Emitters at z ˜ 0.3 from UV-to-FIR Measurements. *ApJ*, 751:139.

Ouchi, M., Ellis, R., Ono, Y., Nakanishi, K., Kohno, K., Momose, R., Kurono, Y., Ashby, M. L. N., Shimasaku, K., Willner, S. P., Fazio, G. G., Tamura, Y., and Iono, D. (2013). An Intensely Star-forming Galaxy at z ˜ 7 with Low Dust and Metal Content Revealed by Deep ALMA and HST Observations. *ApJ*, 778:102.

Peacock, J. A., Rowan-Robinson, M., Blain, A. W., Dunlop, J. S., Efstathiou, A., Hughes, D. H., Jenness, T., Ivison, R. J., Lawrence, A., Longair, M. S., Mann, R. G., Oliver, S. J., and Serjeant, S. (2000). Starburst galaxies and structure in the submillimetre background towards the Hubble Deep Field. *MNRAS*, 318:535–546.

Pentericci, L., Fontana, A., Vanzella, E., Castellano, M., Grazian, A., Dijkstra, M., Boutsia, K., Cristiani, S., Dickinson, M., Giallongo, E., Giavalisco, M., Maiolino, R., Moorwood, A., Paris, D., and Santini, P. (2011). Spectroscopic Confirmation of z ˜ 7 Lyman Break Galaxies: Probing the Earliest Galaxies and the Epoch of Reionization. *ApJ*, 743:132.

Petitjean, P., Pécontal, E., Valls-Gabaud, D., and Chariot, S. (1996). A companion to a quasar at redshift z = 4.7. *Nature*, 380:411–413.

Poglitsch, A., Waelkens, C., Geis, N., Feuchtgruber, H., Vandenbussche, B., Rodriguez, L., Krause, O., Renotte, E., van Hoof, C., Saraceno, P., Cepa, J., Kerschbaum, F., Agnèse, P., Ali, B., Altieri, B., Andreani, P., Augueres, J.-L., Balog, Z., Barl, L.,

Bauer, O. H., Belbachir, N., Benedettini, M., Billot, N., Boulade, O., Bischof, H., Blommaert, J., Callut, E., Cara, C., Cerulli, R., Cesarsky, D., Contursi, A., Creten, Y., De Meester, W., Doublier, V., Doumayrou, E., Duband, L., Exter, K., Genzel, R., Gillis, J.-M., Grözinger, U., Henning, T., Herreros, J., Huygen, R., Inguscio, M., Jakob, G., Jamar, C., Jean, C., de Jong, J., Katterloher, R., Kiss, C., Klaas, U., Lemke, D., Lutz, D., Madden, S., Marquet, B., Martignac, J., Mazy, A., Merken, P., Montfort, F., Morbidelli, L., Müller, T., Nielbock, M., Okumura, K., Orfei, R., Ottensamer, R., Pezzuto, S., Popesso, P., Putzeys, J., Regibo, S., Reveret, V., Royer, P., Sauvage, M., Schreiber, J., Stegmaier, J., Schmitt, D., Schubert, J., Sturm, E., Thiel, M., Tofani, G., Vavrek, R., Wetzstein, M., Wieprecht, E., and Wiezorrek, E. (2010). The Photodetector Array Camera and Spectrometer (PACS) on the Herschel Space Observatory. *A&A*, 518:L2.

Postman, M., Coe, D., Benítez, N., Bradley, L., Broadhurst, T., Donahue, M., Ford, H., Graur, O., Graves, G., Jouvel, S., Koekemoer, A., Lemze, D., Medezinski, E., Molino, A., Moustakas, L., Ogaz, S., Riess, A., Rodney, S., Rosati, P., Umetsu, K., Zheng, W., Zitrin, A., Bartelmann, M., Bouwens, R., Czakon, N., Golwala, S., Host, O., Infante, L., Jha, S., Jimenez-Teja, Y., Kelson, D., Lahav, O., Lazkoz, R., Maoz, D., McCully, C., Melchior, P., Meneghetti, M., Merten, J., Moustakas, J., Nonino, M., Patel, B., Regös, E., Sayers, J., Seitz, S., and Van der Wel, A. (2012). The Cluster Lensing and Supernova Survey with Hubble: An Overview. *ApJS*, 199:25.

Rangwala, N., Maloney, P. R., Glenn, J., Wilson, C. D., Rykala, A., Isaak, K., Baes, M., Bendo, G. J., Boselli, A., Bradford, C. M., Clements, D. L., Cooray, A., Fulton, T., Imhof, P., Kamenetzky, J., Madden, S. C., Mentuch, E., Sacchi, N., Sauvage, M., Schirm, M. R. P., Smith, M. W. L., Spinoglio, L., and Wolfire, M. (2011). Observations of Arp 220 Using Herschel-SPIRE: An Unprecedented View of the Molecular Gas in an Extreme Star Formation Environment. *ApJ*, 743:94.

Reddy, N. A. and Steidel, C. C. (2009). A Steep Faint-End Slope of the UV Luminosity Function at z ˜ 2-3: Implications for the Global Stellar Mass Density and Star Formation in Low-Mass Halos. *ApJ*, 692:778–803.

Rex, M., Ade, P. A. R., Aretxaga, I., Bock, J. J., Chapin, E. L., Devlin, M. J., Dicker, S. R., Griffin, M., Gundersen, J. O., Halpern, M., Hargrave, P. C., Hughes, D. H., Klein, J., Marsden, G., Martin, P. G., Mauskopf, P., Montaña, A., Netterfield, C. B., Olmi, L., Pascale, E., Patanchon, G., Scott, D., Semisch, C., Thomas, N., Truch, M. D. P., Tucker, C., Tucker, G. S., Viero, M. P., and Wiebe, D. V. (2009). A Bright Submillimeter Source in the Bullet Cluster (1E0657-56) Field Detected with Blast. *ApJ*, 703:348–353.

Rhoads, J. E., Hibon, P., Malhotra, S., Cooper, M., and Weiner, B. (2012). A Lyα Galaxy at Redshift z = 6.944 in the COSMOS Field. *ApJ*, 752:L28.

Riechers, D. A., Bradford, C. M., Clements, D. L., Dowell, C. D., Pérez-Fournon, I., Ivison, R. J., Bridge, C., Conley, A., Fu, H., Vieira, J. D., Wardlow, J., Calanog, J., Cooray, A., Hurley, P., Neri, R., Kamenetzky, J., Aguirre, J. E., Altieri, B., Arumugam, V., Benford, D. J., Béthermin, M., Bock, J., Burgarella, D., Cabrera-Lavers, A., Chapman, S. C., Cox, P., Dunlop, J. S., Earle, L., Farrah, D., Ferrero, P., Franceschini, A., Gavazzi, R., Glenn, J., Solares, E. A. G., Gurwell, M. A., Halpern, M., Hatziminaoglou, E., Hyde, A., Ibar, E., Kovács, A., Krips, M., Lupu, R. E., Maloney, P. R., Martinez-Navajas, P., Matsuhara, H., Murphy, E. J., Naylor, B. J., Nguyen, H. T., Oliver, S. J., Omont, A., Page, M. J., Petitpas, G., Rangwala, N., Roseboom, I. G., Scott, D., Smith, A. J., Staguhn, J. G., Streblyanska, A., Thomson, A. P., Valtchanov, I., Viero, M., Wang, L., Zemcov, M., and Zmuidzinas, J. (2013). A dust-obscured massive maximum-starburst galaxy at a redshift of 6.34. *Nature*, 496:329–333.

Riechers, D. A., Carilli, C. L., Capak, P. L., Scoville, N. Z., Smolcic, V., Schinnerer, E., Yun, M., Cox, P., Bertoldi, F., Karim, A., and Yan, L. (2014). ALMA Imaging of Gas and Dust in a Galaxy Protocluster at Redshift 5.3. *ArXiv e-prints*.

Riechers, D. A., Carilli, C. L., Walter, F., and Momjian, E. (2010). Total Molecular Gas Masses of z ˜ 3 Lyman- break Galaxies: CO(J = 1 $\rightarrow$ 0) Emission in MS 1512-cB58 and the Cosmic Eye. *ApJ*, 724:L153–L157.

Riechers, D. A., Carilli, L. C., Walter, F., Weiss, A., Wagg, J., Bertoldi, F., Downes, D., Henkel, C., and Hodge, J. (2011). Imaging the Molecular Gas Properties of a Major Merger Driving the Evolution of a z = 2.5 Submillimeter Galaxy. *ApJ*, 733:L11.

Rodighiero, G., Daddi, E., Baronchelli, I., Cimatti, A., Renzini, A., Aussel, H., Popesso, P., Lutz, D., Andreani, P., Berta, S., Cava, A., Elbaz, D., Feltre, A., Fontana, A., Förster Schreiber, N. M., Franceschini, A., Genzel, R., Grazian, A., Gruppioni, C., Ilbert, O., Le Floch, E., Magdis, G., Magliocchetti, M., Magnelli, B., Maiolino, R., McCracken, H., Nordon, R., Poglitsch, A., Santini, P., Pozzi, F., Riguccini, L., Tacconi, L. J., Wuyts, S., and Zamorani, G. (2011). The Lesser Role of Starbursts in Star Formation at z = 2. *ApJ*, 739:L40.

Rowlands, K., Gomez, H. L., Dunne, L., Aragón-Salamanca, A., Dye, S., Maddox, S., da Cunha, E., and Werf, P. v. d. (2014). The dust budget crisis in high-redshift submillimetre galaxies. *MNRAS*, 441:1040–1058.

Saintonge, A., Lutz, D., Genzel, R., Magnelli, B., Nordon, R., Tacconi, L. J., Baker, A. J., Bandara, K., Berta, S., Förster Schreiber, N. M., Poglitsch, A., Sturm, E.,

Wuyts, E., and Wuyts, S. (2013). Validation of the Equilibrium Model for Galaxy Evolution to z ˜ 3 through Molecular Gas and Dust Observations of Lensed Star-forming Galaxies. *ApJ*, 778:2.

Santini, P., Maiolino, R., Magnelli, B., Lutz, D., Lamastra, A., Li Causi, G., Eales, S., Andreani, P., Berta, S., Buat, V., Cooray, A., Cresci, G., Daddi, E., Farrah, D., Fontana, A., Franceschini, A., Genzel, R., Granato, G., Grazian, A., Le Floc'h, E., Magdis, G., Magliocchetti, M., Mannucci, F., Menci, N., Nordon, R., Oliver, S., Popesso, P., Pozzi, F., Riguccini, L., Rodighiero, G., Rosario, D. J., Salvato, M., Scott, D., Silva, L., Tacconi, L., Viero, M., Wang, L., Wuyts, S., and Xu, K. (2014). The evolution of the dust and gas content in galaxies. *A&A*, 562:A30.

Santini, P., Maiolino, R., Magnelli, B., Silva, L., Grazian, A., Altieri, B., Andreani, P., Aussel, H., Berta, S., Bongiovanni, A., Brisbin, D., Calura, F., Cava, A., Cepa, J., Cimatti, A., Daddi, E., Dannerbauer, H., Dominguez-Sanchez, H., Elbaz, D., Fontana, A., Förster Schreiber, N., Genzel, R., Granato, G. L., Gruppioni, C., Lutz, D., Magdis, G., Magliocchetti, M., Matteucci, F., Nordon, R., Pérez Garcia, I., Poglitsch, A., Popesso, P., Pozzi, F., Riguccini, L., Rodighiero, G., Saintonge, A., Sanchez-Portal, M., Shao, L., Sturm, E., Tacconi, L., and Valtchanov, I. (2010). The dust content of high-z submillimeter galaxies revealed by Herschel. *A&A*, 518:L154.

Sault, R. J., Teuben, P. J., and Wright, M. C. H. (1995). A Retrospective View of MIRIAD. In Shaw, R. A., Payne, H. E., and Hayes, J. J. E., editors, *Astronomical Data Analysis Software and Systems IV*, volume 77 of *Astronomical Society of the Pacific Conference Series*, page 433.

Schaerer, D., Boone, F., Zamojski, M., Staguhn, J., Dessauges-Zavadsky, M., Finkelstein, S., Combes, F., and Richard, J. (2014). New constraints on dust emission and UV attenuation of z=6.5-7.5 galaxies from IRAM and ALMA observations. *ArXiv e-prints*.

Schenker, M. A., Stark, D. P., Ellis, R. S., Robertson, B. E., Dunlop, J. S., McLure, R. J., Kneib, J.-P., and Richard, J. (2012). Keck Spectroscopy of Faint $3 < z < 8$ Lyman Break Galaxies: Evidence for a Declining Fraction of Emission Line Sources in the Redshift Range $6 < z < 8$. *ApJ*, 744:179.

Schiminovich, D., Ilbert, O., Arnouts, S., Milliard, B., Tresse, L., Le Fèvre, O., Treyer, M., Wyder, T. K., Budavári, T., Zucca, E., Zamorani, G., Martin, D. C., Adami, C., Arnaboldi, M., Bardelli, S., Barlow, T., Bianchi, L., Bolzonella, M., Bottini, D., Byun, Y.-I., Cappi, A., Contini, T., Charlot, S., Donas, J., Forster, K., Foucaud, S., Franzetti, P., Friedman, P. G., Garilli, B., Gavignaud, I., Guzzo, L., Heckman, T. M., Hoopes, C., Iovino, A., Jelinsky, P., Le Brun, V., Lee, Y.-W., Maccagni, D., Madore,

B. F., Malina, R., Marano, B., Marinoni, C., McCracken, H. J., Mazure, A., Meneux, B., Morrissey, P., Neff, S., Paltani, S., Pellò, R., Picat, J. P., Pollo, A., Pozzetti, L., Radovich, M., Rich, R. M., Scaramella, R., Scodeggio, M., Seibert, M., Siegmund, O., Small, T., Szalay, A. S., Vettolani, G., Welsh, B., Xu, C. K., and Zanichelli, A. (2005). The GALEX-VVDS Measurement of the Evolution of the Far-Ultraviolet Luminosity Density and the Cosmic Star Formation Rate. *ApJ*, 619:L47–L50.

Scott, K. S., Austermann, J. E., Perera, T. A., Wilson, G. W., Aretxaga, I., Bock, J. J., Hughes, D. H., Kang, Y., Kim, S., Mauskopf, P. D., Sanders, D. B., Scoville, N., and Yun, M. S. (2008). AzTEC millimetre survey of the COSMOS field - I. Data reduction and source catalogue. *MNRAS*, 385:2225–2238.

Scott, S. E., Dunlop, J. S., and Serjeant, S. (2006). A combined re-analysis of existing blank-field SCUBA surveys: comparative 850-μm source lists, combined number counts, and evidence for strong clustering of the bright submillimetre galaxy population on arcminute scales. *MNRAS*, 370:1057–1105.

Shibuya, T., Kashikawa, N., Ota, K., Iye, M., Ouchi, M., Furusawa, H., Shimasaku, K., and Hattori, T. (2012). The First Systematic Survey for Lyα Emitters at z = 7.3 with Red-sensitive Subaru/Suprime-Cam. *ApJ*, 752:114.

Shimizu, I., Yoshida, N., and Okamoto, T. (2011). Lyman α emitters in cosmological simulations - I. Lyman α escape fraction and statistical properties at z= 3.1. *MNRAS*, 418:2273–2282.

Silva, L., Granato, G. L., Bressan, A., and Danese, L. (1998). Modeling the Effects of Dust on Galactic Spectral Energy Distributions from the Ultraviolet to the Millimeter Band. *ApJ*, 509:103–117.

Simpson, J. M., Swinbank, A. M., Smail, I., Alexander, D. M., Brandt, W. N., Bertoldi, F., de Breuck, C., Chapman, S. C., Coppin, K. E. K., da Cunha, E., Danielson, A. L. R., Dannerbauer, H., Greve, T. R., Hodge, J. A., Ivison, R. J., Karim, A., Knudsen, K. K., Poggianti, B. M., Schinnerer, E., Thomson, A. P., Walter, F., Wardlow, J. L., Weiß, A., and van der Werf, P. P. (2014). An ALMA Survey of Submillimeter Galaxies in the Extended Chandra Deep Field South: The Redshift Distribution and Evolution of Submillimeter Galaxies. *ApJ*, 788:125.

Siringo, G., Kreysa, E., Kovács, A., Schuller, F., Weiß, A., Esch, W., Gemünd, H.-P., Jethava, N., Lundershausen, G., Colin, A., Güsten, R., Menten, K. M., Beelen, A., Bertoldi, F., Beeman, J. W., and Haller, E. E. (2009). The Large APEX BOlometer CAmera LABOCA. *A&A*, 497:945–962.

Skibba, R. A., Engelbracht, C. W., Dale, D., Hinz, J., Zibetti, S., Crocker, A., Groves, B., Hunt, L., Johnson, B. D., Meidt, S., Murphy, E., Appleton, P., Armus, L., Bolatto, A., Brandl, B., Calzetti, D., Croxall, K., Galametz, M., Gordon, K. D., Kennicutt, R. C., Koda, J., Krause, O., Montiel, E., Rix, H.-W., Roussel, H., Sandstrom, K., Sauvage, M., Schinnerer, E., Smith, J. D., Walter, F., Wilson, C. D., and Wolfire, M. (2011). The Emission by Dust and Stars of Nearby Galaxies in the Herschel KINGFISH Survey. *ApJ*, 738:89.

Sklias, P., Zamojski, M., Schaerer, D., Dessauges-Zavadsky, M., Egami, E., Rex, M., Rawle, T., Richard, J., Boone, F., Simpson, J. M., Smail, I., van der Werf, P., Altieri, B., and Kneib, J. P. (2014). Star formation histories, extinction, and dust properties of strongly lensed z ˜ 1.5-3 star-forming galaxies from the Herschel Lensing Survey. *A&A*, 561:A149.

Smail, I., Ivison, R. J., and Blain, A. W. (1997). A Deep Sub-millimeter Survey of Lensing Clusters: A New Window on Galaxy Formation and Evolution. *ApJ*, 490:L5–L8.

Smail, I., Ivison, R. J., Blain, A. W., and Kneib, J.-P. (2002). The nature of faint submillimetre-selected galaxies. *MNRAS*, 331:495–520.

Smith, D. J. B., Dunne, L., da Cunha, E., Rowlands, K., Maddox, S. J., Gomez, H. L., Bonfield, D. G., Charlot, S., Driver, S. P., Popescu, C. C., Tuffs, R. J., Dunlop, J. S., Jarvis, M. J., Seymour, N., Symeonidis, M., Baes, M., Bourne, N., Clements, D. L., Cooray, A., De Zotti, G., Dye, S., Eales, S., Scott, D., Verma, A., van der Werf, P., Andrae, E., Auld, R., Buttiglione, S., Cava, A., Dariush, A., Fritz, J., Hopwood, R., Ibar, E., Ivison, R. J., Kelvin, L., Madore, B. F., Pohlen, M., Rigby, E. E., Robotham, A., Seibert, M., and Temi, P. (2012). Herschel-ATLAS: multi-wavelength SEDs and physical properties of 250 μm selected galaxies at z < 0.5. *MNRAS*, 427:703–727.

Solomon, P. M., Downes, D., and Radford, S. J. E. (1992). Dense molecular gas and starbursts in ultraluminous galaxies. *ApJ*, 387:L55–L59.

Stacey, G. J., Geis, N., Genzel, R., Lugten, J. B., Poglitsch, A., Sternberg, A., and Townes, C. H. (1991). The 158 micron C II line - A measure of global star formation activity in galaxies. *ApJ*, 373:423–444.

Stacey, G. J., Hailey-Dunsheath, S., Ferkinhoff, C., Nikola, T., Parshley, S. C., Benford, D. J., Staguhn, J. G., and Fiolet, N. (2010). A 158 μm [C II] Line Survey of Galaxies at z ˜ 1-2: An Indicator of Star Formation in the Early Universe. *ApJ*, 724:957–974.

Staguhn, J. G., Benford, D. J., Allen, C. A., Maher, S. F., Sharp, E. H., Ames, T. J., Arendt, R. G., Chuss, D. T., Dwek, E., Fixsen, D. J., Miller, T. M., Moseley, S. H.,

Navarro, S., Sievers, A., and Wollack, E. J. (2008). Instrument performance of GISMO, a 2 millimeter TES bolometer camera used at the IRAM 30 m Telescope. In *Society of Photo-Optical Instrumentation Engineers (SPIE) Conference Series*, volume 7020 of *Society of Photo-Optical Instrumentation Engineers (SPIE) Conference Series*.

Stanway, E. R., Bremer, M. N., Davies, L. J. M., and Lehnert, M. D. (2010). Constraining the thermal dust content of Lyman break galaxies in an overdense field at z ˜ 5. *MNRAS*, 407:L94–L98.

Stark, D. P., Ellis, R. S., Chiu, K., Ouchi, M., and Bunker, A. (2010). Keck spectroscopy of faint $3 < z < 7$ Lyman break galaxies - I. New constraints on cosmic reionization from the luminosity and redshift-dependent fraction of Lyman α emission. *MNRAS*, 408:1628–1648.

Swinbank, A. M., Karim, A., Smail, I., Hodge, J., Walter, F., Bertoldi, F., Biggs, A. D., de Breuck, C., Chapman, S. C., Coppin, K. E. K., Cox, P., Danielson, A. L. R., Dannerbauer, H., Ivison, R. J., Greve, T. R., Knudsen, K. K., Menten, K. M., Simpson, J. M., Schinnerer, E., Wardlow, J. L., Weiß, A., and van der Werf, P. (2012). An ALMA survey of submillimetre galaxies in the Extended Chandra Deep Field-South: detection of [C II] at $z = 4.4$. *MNRAS*, 427:1066–1074.

Symeonidis, M., Vaccari, M., Berta, S., Page, M. J., Lutz, D., Arumugam, V., Aussel, H., Bock, J., Boselli, A., Buat, V., Capak, P. L., Clements, D. L., Conley, A., Conversi, L., Cooray, A., Dowell, C. D., Farrah, D., Franceschini, A., Giovannoli, E., Glenn, J., Griffin, M., Hatziminaoglou, E., Hwang, H.-S., Ibar, E., Ilbert, O., Ivison, R. J., Floc'h, E. L., Lilly, S., Kartaltepe, J. S., Magnelli, B., Magdis, G., Marchetti, L., Nguyen, H. T., Nordon, R., O'Halloran, B., Oliver, S. J., Omont, A., Papageorgiou, A., Patel, H., Pearson, C. P., Pérez-Fournon, I., Pohlen, M., Popesso, P., Pozzi, F., Rigopoulou, D., Riguccini, L., Rosario, D., Roseboom, I. G., Rowan-Robinson, M., Salvato, M., Schulz, B., Scott, D., Seymour, N., Shupe, D. L., Smith, A. J., Valtchanov, I., Wang, L., Xu, C. K., Zemcov, M., and Wuyts, S. (2013). The Herschel census of infrared SEDs through cosmic time. *MNRAS*, 431:2317–2340.

Tacconi, L. J., Genzel, R., Smail, I., Neri, R., Chapman, S. C., Ivison, R. J., Blain, A., Cox, P., Omont, A., Bertoldi, F., Greve, T., Förster Schreiber, N. M., Genel, S., Lutz, D., Swinbank, A. M., Shapley, A. E., Erb, D. K., Cimatti, A., Daddi, E., and Baker, A. J. (2008). Submillimeter Galaxies at z ˜ 2: Evidence for Major Mergers and Constraints on Lifetimes, IMF, and CO-H_2 Conversion Factor. *ApJ*, 680:246–262.

Tacconi, L. J., Neri, R., Genzel, R., Combes, F., Bolatto, A., Cooper, M. C., Wuyts, S., Bournaud, F., Burkert, A., Comerford, J., Cox, P., Davis, M., Förster Schreiber,

N. M., García-Burillo, S., Gracia-Carpio, J., Lutz, D., Naab, T., Newman, S., Omont, A., Saintonge, A., Shapiro Griffin, K., Shapley, A., Sternberg, A., and Weiner, B. (2013). Phibss: Molecular Gas Content and Scaling Relations in z ˜ 1-3 Massive, Main-sequence Star-forming Galaxies. *ApJ*, 768:74.

Taniguchi, Y., Ajiki, M., Nagao, T., Shioya, Y., Murayama, T., Kashikawa, N., Kodaira, K., Kaifu, N., Ando, H., Karoji, H., Akiyama, M., Aoki, K., Doi, M., Fujita, S. S., Furusawa, H., Hayashino, T., Iwamuro, F., Iye, M., Kobayashi, N., Kodama, T., Komiyama, Y., Matsuda, Y., Miyazaki, S., Mizumoto, Y., Morokuma, T., Motohara, K., Nariai, K., Ohta, K., Ohyama, Y., Okamura, S., Ouchi, M., Sasaki, T., Sato, Y., Sekiguchi, K., Shimasaku, K., Tamura, H., Umemura, M., Yamada, T., Yasuda, N., and Yoshida, M. (2005). The SUBARU Deep Field Project: Lymanα Emitters at a Redshift of 6.6. *PASJ*, 57:165–182.

Vallini, L., Gallerani, S., Ferrara, A., and Baek, S. (2013). Far-infrared line emission from high-redshift galaxies. *MNRAS*, 433:1567–1572.

Valtchanov, I., Virdee, J., Ivison, R. J., Swinyard, B., van der Werf, P., Rigopoulou, D., da Cunha, E., Lupu, R., Benford, D. J., Riechers, D., Smail, I., Jarvis, M., Pearson, C., Gomez, H., Hopwood, R., Altieri, B., Birkinshaw, M., Coia, D., Conversi, L., Cooray, A., de Zotti, G., Dunne, L., Frayer, D., Leeuw, L., Marston, A., Negrello, M., Portal, M. S., Scott, D., Thompson, M. A., Vaccari, M., Baes, M., Clements, D., Michałowski, M. J., Dannerbauer, H., Serjeant, S., Auld, R., Buttiglione, S., Cava, A., Dariush, A., Dye, S., Eales, S., Fritz, J., Ibar, E., Maddox, S., Pascale, E., Pohlen, M., Rigby, E., Rodighiero, G., Smith, D. J. B., Temi, P., Carpenter, J., Bolatto, A., Gurwell, M., and Vieira, J. D. (2011). Physical conditions of the interstellar medium of high-redshift, strongly lensed submillimetre galaxies from the Herschel-ATLAS. *MNRAS*, 415:3473–3484.

van de Voort, F., Schaye, J., Booth, C. M., Haas, M. R., and Dalla Vecchia, C. (2011). The rates and modes of gas accretion on to galaxies and their gaseous haloes. *MNRAS*, 414:2458–2478.

Vanzella, E., Pentericci, L., Fontana, A., Grazian, A., Castellano, M., Boutsia, K., Cristiani, S., Dickinson, M., Gallozzi, S., Giallongo, E., Giavalisco, M., Maiolino, R., Moorwood, A., Paris, D., and Santini, P. (2011). Spectroscopic Confirmation of Two Lyman Break Galaxies at Redshift Beyond 7. *ApJ*, 730:L35.

Venemans, B. P., McMahon, R. G., Walter, F., Decarli, R., Cox, P., Neri, R., Hewett, P., Mortlock, D. J., Simpson, C., and Warren, S. J. (2012). Detection of Atomic Carbon [C II] 158 μm and Dust Emission from a z = 7.1 Quasar Host Galaxy. *ApJ*, 751:L25.

Wagg, J., Carilli, C. L., Wilner, D. J., Cox, P., De Breuck, C., Menten, K., Riechers, D. A., and Walter, F. (2010). [CII] line emission in BRI 1335-0417 at z = 4.4. *A&A*, 519:L1.

Wagg, J., Wiklind, T., Carilli, C. L., Espada, D., Peck, A., Riechers, D., Walter, F., Wootten, A., Aravena, M., Barkats, D., Cortes, J. R., Hills, R., Hodge, J., Impellizzeri, C. M. V., Iono, D., Leroy, A., Martín, S., Rawlings, M. G., Maiolino, R., McMahon, R. G., Scott, K. S., Villard, E., and Vlahakis, C. (2012). [C II] Line Emission in Massive Star-forming Galaxies at z = 4.7. *ApJ*, 752:L30.

Walter, F., Brinks, E., de Blok, W. J. G., Bigiel, F., Kennicutt, Jr., R. C., Thornley, M. D., and Leroy, A. (2008). THINGS: The H I Nearby Galaxy Survey. *AJ*, 136:2563–2647.

Walter, F., Decarli, R., Carilli, C., Bertoldi, F., Cox, P., da Cunha, E., Daddi, E., Dickinson, M., Downes, D., Elbaz, D., Ellis, R., Hodge, J., Neri, R., Riechers, D. A., Weiss, A., Bell, E., Dannerbauer, H., Krips, M., Krumholz, M., Lentati, L., Maiolino, R., Menten, K., Rix, H.-W., Robertson, B., Spinrad, H., Stark, D. P., and Stern, D. (2012a). The intense starburst HDF 850.1 in a galaxy overdensity at z$\sim$5.2 in the Hubble Deep Field. *Nature*, 486:233–236.

Walter, F., Decarli, R., Carilli, C., Riechers, D., Bertoldi, F., Weiß, A., Cox, P., Neri, R., Maiolino, R., Ouchi, M., Egami, E., and Nakanishi, K. (2012b). Evidence for Low Extinction in Actively Star-forming Galaxies at z > 6.5. *ApJ*, 752:93.

Walter, F., Riechers, D., Cox, P., Neri, R., Carilli, C., Bertoldi, F., Weiss, A., and Maiolino, R. (2009). A kiloparsec-scale hyper-starburst in a quasar host less than 1gigayear after the Big Bang. *Nature*, 457:699–701.

Walter, F., Weiß, A., Downes, D., Decarli, R., and Henkel, C. (2011). A Survey of Atomic Carbon at High Redshift. *ApJ*, 730:18.

Wang, R., Wagg, J., Carilli, C. L., Walter, F., Lentati, L., Fan, X., Riechers, D. A., Bertoldi, F., Narayanan, D., Strauss, M. A., Cox, P., Omont, A., Menten, K. M., Knudsen, K. K., Neri, R., and Jiang, L. (2013). Star Formation and Gas Kinematics of Quasar Host Galaxies at z ˜ 6: New Insights from ALMA. *ApJ*, 773:44.

Wang, W.-H., Cowie, L. L., Barger, A. J., and Williams, J. P. (2011). SMA Observations of GOODS 850-11 and GOODS 850-13: First Examples of Multiple Submillimeter Sources Resolved by an Interferometer. *ApJ*, 726:L18.

Wardlow, J. L., Smail, I., Wilson, G. W., Yun, M. S., Coppin, K. E. K., Cybulski, R., Geach, J. E., Ivison, R. J., Aretxaga, I., Austermann, J. E., Edge, A. C., Fazio, G. G.,

Huang, J., Hughes, D. H., Kodama, T., Kang, Y., Kim, S., Mauskopf, P. D., Perera, T. A., and Scott, K. S. (2010). An AzTEC 1.1-mm survey for ULIRGs in the field of the Galaxy Cluster MS0451.6-0305. *MNRAS*, 401:2299–2317.

Weiß, A., Downes, D., Neri, R., Walter, F., Henkel, C., Wilner, D. J., Wagg, J., and Wiklind, T. (2007). Highly-excited CO emission in APM 08279+5255 at z = 3.9. *A&A*, 467:955–969.

Willott, C. J., Omont, A., and Bergeron, J. (2013). Redshift 6.4 Host Galaxies of 10^8 Solar Mass Black Holes: Low Star Formation Rate and Dynamical Mass. *ApJ*, 770:13.

Zheng, W., Postman, M., Zitrin, A., Moustakas, J., Shu, X., Jouvel, S., Høst, O., Molino, A., Bradley, L., Coe, D., Moustakas, L. A., Carrasco, M., Ford, H., Benítez, N., Lauer, T. R., Seitz, S., Bouwens, R., Koekemoer, A., Medezinski, E., Bartelmann, M., Broadhurst, T., Donahue, M., Grillo, C., Infante, L., Jha, S. W., Kelson, D. D., Lahav, O., Lemze, D., Melchior, P., Meneghetti, M., Merten, J., Nonino, M., Ogaz, S., Rosati, P., Umetsu, K., and van der Wel, A. (2012). A magnified young galaxy from about 500 million years after the Big Bang. *Nature*, 489:406–408.

Zitrin, A., Moustakas, J., Bradley, L., Coe, D., Moustakas, L. A., Postman, M., Shu, X., Zheng, W., Benítez, N., Bouwens, R., Broadhurst, T., Ford, H., Host, O., Jouvel, S., Koekemoer, A., Meneghetti, M., Rosati, P., Donahue, M., Grillo, C., Kelson, D., Lemze, D., Medezinski, E., Molino, A., Nonino, M., and Ogaz, S. (2012). CLASH: Discovery of a Bright z ˜= 6.2 Dwarf Galaxy Quadruply Lensed by MACS J0329.6-0211. *ApJ*, 747:L9.

List of Figures

1.1 Example of how the negate K-correction affects the observation of high redshift galaxies. The predicted flux density of a dusty galaxy template as a function of redshift in various submm atmospheric windows. Each color line represent the flux density observed at a given wavelength. For observations at wavelength longer than 250 μm the flux density is almost independent of redshift (**?**). 4

1.2 The UV luminosity density (*right axis*) and star formation rate density (*left axis*) versus redshift (extracted from Bouwens et al. (2014)). These luminosity densities and SFR densities are only considered down to a limiting luminosity of -17.7 AB mag. The UV luminosity is converted into a star formation rate using the canonical UV-to-SFR conversion factors. The upper set of points at every given redshift and orange contour show the dust-corrected SFR densities, while the lower set of points and blue contours show the inferred SFR densities before dust correction. The data is been taken from Bouwens et al. (2007, 2011b); Coe et al. (2013); Ellis et al. (2013); Oesch et al. (2012, 2013, 2014); Reddy and Steidel (2009); Schiminovich et al. (2005); Zheng et al. (2012). 6

1.3 Example of a fit to the FIR continuum emission in a submillimeter galaxy HFLS3 at $z = 6.34$. HFLS3 was identified as a very high redshift candidate, as it appears red between the Herschel/SPIRE 250, 350, and 500 μm bands (inset). The SED of the source (black data points) is fitted with a modified black body (MBB; solid line) and spectral templates for the starburst galaxies Arp 220, M82, HR10, and the Eyelash (broken lines, see key) (Riechers et al., 2013). 7

1.4 The ratio $L[CII]/L_{FIR}$ as a function of L_{FIR} for some observed galaxies. The dashed horizontal line indicates a value of $3 \times 10^{-3} \sim$ Milky Way value. This plot shows how bright is the $[CII]$ emission with respect to the total FIR emission of some galaxies. (Carilli and Walter, 2013). . . . 9

2.1 Spectra of the LAEs with a velocity resolution of 50 $\mathrm{km\,s^{-1}}$. The relative velocities are with respect to the frequency expected for the [C II] line including absorption by the IGM (150 $\mathrm{km\,s^{-1}}$ to the blue of $z_{\mathrm{Ly}\alpha}$). The redshifts of the target are z=6.965 for IOK-1, z=6.541 for SDF J132415.7+273058 and z=6.554 for SDF J132408.3+271543 17

2.2 Spectrum of MACS0647-JD . The spectrum shows the added fluxes measured on the positions of the two lensed images JD1 and JD2 (combined magnification $\mu \sim 15$). The spectra of the two images were corrected by the primary beam pattern before combination. The 4 setups are plotted in different colors, blue, red, green and orange the colors for the setups A, B, C and D respectively. The error bars correspond to the quadrature of the errors of the individual measurement of the fluxes for JD1 and JD2 in each frequency channel. For display purposes, the spectrum is sampled at a channel resolution of 200 $\mathrm{km\,s^{-1}}$, but the search of the [C II] line as well as the analysis was made with the spectrum sampled to 50 $\mathrm{km\,s^{-1}}$. 18

2.3 Rest-frame 158 μm continuum maps of the LAEs. Each contour level represents 1σ steps ($\pm 1\sigma$ levels are not shown). Solid contours are positive signal and dashed contour are negative signals. The 1σ levels are 0.75 $\mathrm{mJy\,beam^{-1}}$ for SDF J132408.3+271543 , 0.37 $\mathrm{mJy\,beam^{-1}}$ for SDF J132415.7+273058 and 0.19 $\mathrm{mJy\,beam^{-1}}$ for IOK-1. The blue crosses represent the position of each LAE as given in Tab. 2.1. 18

2.4 Continuum map of the field of MACS0647-JD . Each contour level represents 1σ steps ($\pm 1\sigma$ levels are not shown). Solid contours are positive signal and dashed contour are negative signals. The 1σ level is 93 $\mu\mathrm{Jy\,beam^{-1}}$. The blue plus signs represent the positions of the two lensed images MACS0647-JD1 and MACS0647-JD2 as given in Tab. 2.2. 20

2.5 *Top:* Spectral energy distribution of IOK-1. The photometric points correspond to those measured by Cai et al. (2011); Iye et al. (2006); Ono et al. (2012); Ota et al. (2010). The red triangle corresponds to the 3σ upper limit given by the CARMA observations. The colored lines correspond to the SEDs of local galaxies shifted to the redshift of IOK-1 and scaled to the observations in the UV band. The dashed lines correspond to the observed SED of the local galaxies after the effects of the CMB on the observations are taken into account. *Bottom:* Spectral energy distribution of MACS0647-JD. The photometric points correspond to those presented by Coe et al. (2013). The SED of the galaxies follow the same prescription as in the upper panel. The red triangle corresponds to the 3σ upper limit calculated as the quadrature of the errors of the individual fluxes of JD1 and JD2, in the same way as the errors presented by Coe et al. (2013). The 1σ photometric uncertainty of the observations is 0.093 mJy, and the error of the added fluxes is 0.13 mJy. 21

2.6 Ratio of the [C II] luminosity to the FIR luminosity vs the FIR luminosity (integrated from 42.5μm to 122.5μm rest frame) for galaxies at different redshifts. The green symbols correspond to the upper limits of the LAEs presented here. The blue hexagon corresponds to the upper limit of MACS0647-JD using the most sensitive setup. The FIR luminosities for the galaxies are upper limits estimated from the observations including the CMB effects. The black diamond corresponds to the upper limit for Himiko with ALMA observations (Ouchi et al., 2013). The horizontal dashed line is the average value for $L_{[C\,II]}/L_{\mathrm{FIR}}$ on the local galaxies. (Cox et al., 2011; De Breuck et al., 2011; Iono et al., 2006; Ivison et al., 2010; Luhman et al., 2003; Maiolino et al., 2009; Malhotra et al., 2001; Negishi et al., 2001; Ouchi et al., 2013; Riechers et al., 2013; Stacey et al., 2010; Swinbank et al., 2012; Venemans et al., 2012; Wagg et al., 2010; Walter et al., 2012a, 2009; Wang et al., 2013) 28

2.7 Relation of the [C II] luminosity with the UV-derived star formation rate of galaxies. The black solid lines correspond to the relation found by de Looze et al. (2011), with the gray area corresponding to 2σ of the scatter in the relation. The black dots with error bars correspond to the data used to find the relation of [C II] - SFR. The green circle, square and pentagon correspond to the LAEs with the [C II] upper limits presented in this paper assuming the star formation rate estimated from the UV fluxes. The blue hexagon corresponds to the [C II] upper limit of MACS0647-JD with based in the most sensitive setup and the star formation rate estimated from the UV fluxes. The red star corresponds to the LAE detected with ALMA at $z \sim 4.7$ (Carilli et al., 2013). The black triangle corresponds to the upper limit of the [C II] emission found for HCM-6A by Kanekar et al. (2013). The black diamond corresponds to the upper limit of the [C II] emission found for Himiko by Ouchi et al. (2013). 29

2.8 Simulated [C II] spectrum of a galaxy similar to IOK-1 at $z \sim 7$. The parameters set for this simulation were a SFR of $20 M_{\odot} yr^{-1}$, and stellar population age of 10 Myr and a solar metallicity. The blue spectrum corresponds to the emission produced in the cold neutral medium, the orange spectrum corresponds to the emission produced in the warm neutral medium and the green spectrum corresponds to the emission produced in the ionized medium. The main peak (at ~ 80 km s^{-1}) of the cold neutral medium has a FWHM of ~ 50 km s^{-1}. For more details on the simulations of [C II] emission in high redshift galaxies see Vallini et al. (2013). 31

2.9 Contour plot of the integrated [C II] flux of IOK-1 in mJy km s^{-1} for different simulation conditions. As comparison, our upper limit for integrated flux of IOK-1 is 175 mJy km s^{-1}. The two independent parameters are the stellar population age and the metallicity of the gas. The flux is integrated over the whole area of the cube and in a channel resolution of 500 km s^{-1} around the peak of the emission. The integrated flux is a conservative upper limit for the different parameters. We can see from the contour plot that the [C II] emission is very sensitive to the metallicity of the galaxy, and in a less significant way to the age of the stellar population. The different ages correspond to a different amount of heating photons coming from the young stars, which is critical for the cooling of the gas. 32

3.1 Continuum map of one pointing in the galaxy cluster MACS0329. The synthesized beam is of $1.85'' \times 0.55''$. The contour levels are in step of 1σ, starting in $-2\sigma, 2\sigma$, with $\sigma = 121.3$ μJy b^{-1} in the phase center. The contours are corrected by the primary beam sensitivity. Two detections are found with $sn > 3\sigma$ and no negative detection of similar significance. One of them is outside the HPBW and no optical counterpart is found. The second detection corresponds to a lensed galaxy at $z \sim 3.5$. 40

3.2 Rest-frame 158 μm continuum map of the region around MACS0329-iD. Each contour level represents 1σ steps. Solid contours represent positive signal and dashed contour represent negative signal. The panel to the left shows the nominal resolution and the one in the right shows the extended resolution. In the left panel, the 1σ levels are of 121.3 μJy b^{-1}in the phase center and are corrected by the PB. In the right panel, the 1σ levels are of 176.5 μJy b^{-1}in the phase center and are corrected by the PB as in the left panel. The black solid line represent the ALMA HPBW. The red crosses are the position of the brightest regions of each image of the lensed galaxy. The red ellipse is the synthesized beam, $1.85'' \times 0.55''$ for the left panel and $2.23'' \times 1.26''$ for the right panel. 41

3.3 Signal-to-noise spectrum of the combination of the two lensed images (D1 and D2) of the galaxy. Using the a channel resolution of 50 km s^{-1} and the extended resolution. The blue line correspond to the photometric redshift of 6.18 estimated for the galaxy. We recall two features that need further study; the channel with a $sn = 2.3$ just to the right of the line that represents the frequency expected for the [C II] emission line for the photometric redshift and what appears to be an emission line at 266 GHz. 42

3.4 Spectral energy distribution of MACS0329-iD together with several templates of local galaxies. The black points represent the HST and Spitzer photometry while the red triangle is the ALMA upper limit to the FIR continuum. All the templates has been corrected by the effect of the CMB following the procedures presented in da Cunha et al. (2013) and extended in González-López et al. (2014). The dashed line correspond to the sed templates of local galaxies. 44

3.5 Spectrum extracted in the the position of the emission found at 266 GHz in Fig. 3.3 using the a channel resolution of 26.5 km s^{-1} and the extended resolution. 45

3.6 Map of the emission associated with the yellow channels in Fig. 3.5 with the two spatial resolutions. The left panel shows the nominal resolution and the right panel shows the extended resolution. Each line corresponds to a 1σ level starting at -2σ and $+2\sigma$. The emission appears to be related to a galaxy near the MACS0329-iD2. The fact that the emission is not observed in MACS0329-iD1 discards the possibility of this emission being [C II] for the MACS0329-iD. The emission in the left panel appear to not be related with any optical detected galaxies, making difficult to associated the possible emission to a galaxy and therefore identifying the emission line. 45

3.7 Zoom in to the positive signal found in Fig. 3.3 but showing the flux density units instead of signal-to-noise. The red line correspond to a gaussian function adjusted to the data. The best-fit parameters of the gaussian function are in Table 3.1. 47

3.8 Map of the three central channels of the tentative [C II] emission shown in Fig. 3.7. The contour levels are in step of 1σ, starting in $-1\sigma, 1\sigma$. The tentative emission line is observed, at least in low signal-to-noise, in both lensed images D1 and D2, supporting the hypothesis that this emission could correspond to the [C II] in MACS0329-iD. 49

3.9 Stack of the four position of the brightest regions of the lensed images in the channels around the tentative [C II] detection (marked as yellow channels in Fig. 3.7). The total signal-to-noise of the line is of 3.64σ. . . 50

3.10 Simulated [C II] emission for a galaxy at a similar redshift of MACS0329-iD and with similar characteristics. We use a SFR= 3.2 $M_{\odot}yr^{-1}$, a magnification of $\mu = 29.2$, and a metallicity of $0.2Z_{\odot}$. The yellow lines represent the simulated emission, the black lines is the emission binned to match the observed spectral resolution of ~ 8.85 km s^{-1}. The red line is the best fit gaussian function to the binned emission, resulting in a line width of ~ 30 km s^{-1}. 51

3.11 Relation of the [C II] luminosity with the UV-derived star formation rate of galaxies. The black solid lines correspond to the relation found by de Looze et al. (2011), with the gray area corresponding to 2σ of the scatter in the relation. The black dots with error bars correspond to the data used to find the relation of [C II] - SFR. We present our tentative detection in MACS0329-iD (red star) together with the 3σ upper limit (red square, displaced for display purposes). We also present the upper limits and observations of [C II] in normal star-forming galaxies at $z > 4$ (Carilli et al., 2013; González-López et al., 2014; Kanekar et al., 2013; Ota et al., 2014; Ouchi et al., 2013; Riechers et al., 2013; Schaerer et al., 2014). For each galaxy, the symbol correspond to the SFR estimated from the UV observations and the error bar in SFR correspond to the range of values allowed by the FIR non detections. 52

3.12 Ratio of the [C II] luminosity to the FIR luminosity vs the FIR luminosity (integrated from 42.5μm to 122.5μm rest frame) for galaxies at different redshifts. The horizontal dashed line is the average value for $L_{[C\,II]}/L_{\rm FIR}$ on the local galaxies. The galaxy MACS0329-iD is represented with the red star together with the 3σ upper limit (red circle, displaced for display purposes). (Carilli et al., 2013; Cox et al., 2011; De Breuck et al., 2011; González-López et al., 2014; Iono et al., 2006; Ivison et al., 2010; Kanekar et al., 2013; Luhman et al., 2003; Maiolino et al., 2009; Malhotra et al., 2001; Negishi et al., 2001; Ota et al., 2014; Ouchi et al., 2013; Riechers et al., 2013, 2014; Schaerer et al., 2014; Stacey et al., 2010; Swinbank et al., 2012; Venemans et al., 2012; Wagg et al., 2010; Walter et al., 2012a, 2009; Wang et al., 2013) 54

3.13 Continuum detection of a galaxy at $z \sim 3.5$. The contour levels are in step of 1σ, starting in $-1\sigma, 1\sigma$. 55

3.14 Probability distribution of the redshift for the galaxy detected in continuum with ALMA. The distribution was calculated using Bayesian Photometric Redshifts and the 16 HST filters used in the CLASH survey. The low redshift secondary peak is low in comparison to the main higher redshift peak. The high redshift peak is also supported by the ALMA 1.1 mm detection. 56

3.15 Spectral energy distribution of the galaxy detected with ALMA. The red points are the detection in each filter, from HST and ALMA. The upper limits are plotted as downward triangles, and correspond to the UV filter from HST, Spitzer channels 1 and 2 at 3.6 and 4.5 μm, Herschel cameras PACS and SPIRES, and APEX/LABOCA bolometer. The red dashed line corresponds to the stellar emission in the galaxy and the blue continuum line corresponds to the stellar emission absorbed by dust and re-emitted in the FIR. The physical quantities distribution obtained from the fit can be found in Table 3.2. 57

3.16 Likelihood distribution of the physical parameters fitted by MAGPHYS to photometry of the galaxy at $z \sim 3.5$. The parameters are, first row in the top; fraction of the total infrared luminosity contributed by dust in the ambient inter stellar medium (ISM) associated to the stellar population (f_{μ}^{SFR}); fraction of the total infrared luminosity contributed by dust in the ambient ISM associated to the IR spectrum (f_{μ}^{IR}), the total fraction of the total infrared luminosity contributed by dust in the ambient ISM (f_{μ}) is estimated as the average of the previous values, $f_{\mu} = 0.5 \times (f_{\mu}^{SFR} + f_{\mu}^{IR})$; fraction of the total V-band absorption optical depth of the dust contributed by the ambient ISM (μ); total effective V-band absorption optical depth of the dust ($\hat{\tau}_{V}$); second row from the top; specific star formation rate (sSFR); stellar mass (M_{*}); total infrared luminosity of the dust (L_{d}^{Tot}); equilibrium temperature of cold dust in the ambient ISM (T_{C}^{ISM}); third row; equilibrium temperature of warm dust in stellar birth clouds (T_{W}^{BC}); contribution by cold dust in thermal equilibrium to the total infrared luminosity (ξ_{C}^{Tot}); global contributions (i.e. including stellar birth clouds and the ambient ISM) by polycyclic aromatic hydrocarbons (PAHs); global contributions by the hot mid-infrared continuum (ξ_{MIR}^{Tot}); fourth row; global contributions by the warm dust in thermal equilibrium (ξ_{W}^{Tot}); effective V-band absorption optical depth of the dust in the ambient ISM ($\mu\hat{\tau}_{V}$); dust mass (M_{d}); Star formation rate (SFR). 58

3.17 Comparison of the dust mass, stellar mass and star formation rate for the detected galaxy (red star) with the local galaxies of the KINGFISH survey sample (black dots). In the lower red corner is the median of the errors for the KINGFISH sample. The blue squares are the low-metallicity blue compact dwarfs (BCDs) studied in Hunt et al. (2005). The green pentagons are the lensed galaxies studied as part of the Herschel Lensing Survey (Sklias et al., 2014), we are only showing the galaxies that have similar values to the KINGFISH sample. The galaxy detected in our observations agrees very well with the fit to the KINGFISH sample (black line) in the dust mass to SFR relation. In the lower panel, the dust mass appears to be slightly higher in comparison to the galaxies of the KINGFISH sample with similar stellar mass. In general, the BCDs sample, the lensed galaxies appears to be above the relation found between dust mass and stellar mass for the KINGFISH sample. 59

3.18 Distribution of photometric redshift of the galaxies found within the ALMA HPWB. We separate the group to do a stacking searching for continuum emission. The group G5 is the galaxy found at $z = 6.17$ discussed above. G1 corresponds to the members of the galaxy cluster. . . . 60

3.19 R values for different channel resolutions and different angular resolution. The top row represent the native spectral resolution and the bottom row the search in the data cube where the channel resolution was set to 50 $\mathrm{km\,s^{-1}}$. For each row, each color represents the search for emission lines with a given line width, set by the σ value assigned in the legend of the plot. For each row, the left panel is the one with the nominal resolution, the middle is the one with the extended resolution and the right panels are for the third angular resolution reached by using a smaller uv-tapering. In the top row, the green and magenta lines in the middle and right panel follow the trends that indicate a possible emission line. The same behavior is observed for some lines in the bottom row. It is important to note that one candidate to emission line can be detected in several panels at the same time. 62
3.20 Spectra of the 4 candidate to emission lines found in the data cube. The list from L1 to L4 is in decreasing signal to noise value. 64
3.21 Emission line 1. Each contour represent 1σ (starting in $\pm 2\sigma$) of the emission integrated in the yellow channels in Fig. 3.20. The red and green circles are the positions of the detection made with CLASH. The red circles represent the detections made using the optical images and the green circles the ones made with the IR images in the CLASH survey. . . 64
3.22 Map of the two peaks found in Line 1 in Fig. 3.20. The contours are in step of 1σ starting in $\pm 2\sigma$. The blue contours represent the line with the peak at the higher frequency. 65
3.23 Emission line 2. Each contour represent 1σ (starting in $\pm 2\sigma$) of the emission integrated in the yellow channels in Fig. 3.20. The red and green circles are the positions of the detection made with CLASH. The red circles represent the detections made using the optical images and the green circles the ones made with the IR images. 67
3.24 Emission line 3. Each contour represent 1σ (starting in $\pm 2\sigma$) of the emission integrated in the yellow channels in Fig. 3.20. The red and green circles are the positions of the detection made with CLASH. The red circles represent the detections made using the optical images and the green circles the ones made with the IR images. 68
3.25 Emission line 4. Each contour represent 1σ (starting in $\pm 2\sigma$) of the emission integrated in the yellow channels in Fig. 3.20. The red and green circles are the positions of the detection made with CLASH. The red circles represent the detections made using the optical images and the green circles the ones made with the IR images. 69
3.26 Redshift probability distribution of the possible counterparts to the emission lines detected in the data cube. Each probability distribution is normalized to the peak of the distribution. For each distribution, the vertical lines corresponds to the redshift that the galaxy would be if the detected line corresponds to the one in the label. The closest the line to the peak of the distribution higher are the chances that the observed line corresponds to that. 70

3.27 Offset between the optical detected galaxies nearest to the continuum and line emission detected in our ALMA observation vs the distance to the critical curve of the galaxy cluster at $z = 2$. The offsets and distances were calculated between the center of the optical galaxies and the brightest pixel of the mm source. The errors of the points correspond to the size of the pixel in the ALMA observations of 0.1". The point label as C1 corresponds to the continuum detection of the galaxy at $z_{\rm ph} = 3.5$ and the other points correspond to the emission lines. The blue line correspond to a power law fit with an index of -0.46. 73

4.1 Histogram of the pixels in signal-to-noise for the LABOCA observations. The red line corresponds to a gaussian noise. In the bottom of the plot we can see the ratio of the data and the gaussian noise. The error bars in the upper plot correspond to the square root of the number of pixel per interval. The error bars in the bottom plot correspond to the error propagation of the errors in the counts. At signal-to-noise higher to 3 we can see how the data is clearly departing from the gaussian model, indicating the existence of real sources. 79
4.2 LABOCA signal-to-noise map towards the galaxy cluster MACS0416. Each detected source is marked as black circle with the corresponding name. 80
4.3 LABOCA signal-to-noise map towards the galaxy cluster Abell209. Each detected source is marked as black circle with the corresponding name. . 81
4.4 LABOCA signal-to-noise map towards the galaxy cluster Abell383. Each detected source is marked as black circle with the corresponding name. . 82
4.5 LABOCA signal-to-noise map towards the galaxy cluster MACS0329. Each detected source is marked as black circle with the corresponding name. 83
4.6 LABOCA signal-to-noise map towards the galaxy cluster MACS0429. Each detected source is marked as black circle with the corresponding name. 84
4.7 LABOCA signal-to-noise map towards the galaxy cluster MACS1149. Each detected source is marked as black circle with the corresponding name. 85
4.8 LABOCA signal-to-noise map towards the galaxy cluster MACS1931. Each detected source is marked as black circle with the corresponding name. 86
4.9 LABOCA signal-to-noise map towards the galaxy cluster MACS2129. Each detected source is marked as black circle with the corresponding name. Here are also plotted the GISMO detection. 87
4.10 LABOCA signal-to-noise map towards the galaxy cluster MS2137. Each detected source is marked as black circle with the corresponding name. . 88
4.11 LABOCA signal-to-noise map towards the galaxy cluster RXJ1347. Each detected source is marked as black circle with the corresponding name. . 89
4.12 LABOCA signal-to-noise map towards the galaxy cluster RXJ2129. Each detected source is marked as black circle with the corresponding name. . 90
4.13 LABOCA signal-to-noise map towards the galaxy cluster RXJ2248. Each detected source is marked as black circle with the corresponding name. . 91

4.14 LABOCA signal-to-noise map towards the galaxy cluster MACS1115. Each detected source is marked as black circle with the corresponding name. 92
4.15 GISMO signal-to-noise map towards the galaxy cluster MACS0647. Each detected source is marked as black circle with the corresponding name. . 93
4.16 GISMO signal-to-noise map towards the galaxy cluster MACS2129. Each detected source is marked as black circle with the corresponding name. Here are also plotted the LABOCA detection. 94
4.17 GISMO signal-to-noise map towards the galaxy cluster MACS0717. Each detected source is marked as black circle with the corresponding name. . 95
4.18 We show the PFD for MACS1931-870.2 (black solid line), the likelihood of observing the data $p(S_m, \sigma_m|S_i)$ (green dash line), the simulated flux distribution $p(S_i)$ (blue line) together with the Schechter function (red solid line). The vertical lines show the observed flux density (vertical green dash line) and the deboosted flux density (vertical black line). For this source we found a slightly lower deboosted flux density with a similar associated error. 100
4.19 We show the PFD for MACS0329-870.3 (black solid line), the likelihood of observing the data $p(S_m, \sigma_m|S_i)$ (green dash line), the simulated flux distribution $p(S_i)$ (red blue line) together with the Schechter function (red solid line). The vertical lines show the observed flux density (vertical green dash line) and the deboosted flux density (vertical black line). Fro this source we are not able to estimate a deboosted flux density since the PFD does not have a local maximum for $S_\nu > 0$. 101
4.20 False color image of the CLASH galaxy clusters at the position of LABOCA and GISMO detections. The central red cross represent the position of the LABOCA/GISMO detection and the red circle is the 14" radius allowed for the search for counterparts (16.7" in the case of the GISMO detections). The yellow circles show the galaxies that were selected as possible counterparts. For each galaxy is also presented the value of ξ^2 from the MAGPHYS fit and the photometric redshift estimated from the CLASH observations. The orange cross shows the center of the lower wavelength detection of the source in either PACS or SPIRE instruments in Herschel shown in Figs. 4.25-4.28. 112
4.21 Continuation of Fig. 4.20. 113
4.22 Continuation of Fig. 4.20. 114
4.23 Continuation of Fig. 4.20. 115
4.24 Continuation of Fig. 4.20. 115
4.25 Spectral energy distribution of the best fit model made with MAGPHYS for the candidates to counterparts of the LABOCA and GISMO detections. The red points correspond to the observed photometry from the CLASH catalogs and from the archive images of PACS/SPIRE in Herschel and in the LABOCA/GISMO observations, the orange triangles show the upper limits of the observations. The green lines corresponds to the stellar un-attenuated emission and the blue line corresponds to the observed emission after the stellar emission is attenuated by the dust and re-emitted in the FIR. In the box we show the ID of the candidate, the χ^2 value for the fit and the assumed redshift. 116
4.26 Continuation of Fig. 4.25. 117

4.27 Continuation of Fig. 4.25. 118
4.28 Continuation of Fig. 4.25. 119
4.29 False color image of the galaxy cluster MACS1931 in the position of the detected LABOCA source MACS01931-870.1. Each white line corresponds to a 1σ emission starting at $\pm 2\sigma$ with $\sigma = 2.7$ mJy b^{-1}. The LABOCA detection is clearly over the BCG of the galaxy cluster, being this known by hosting a powerful AGN. The red ellipses corresponds to the radio cavities identified by Ehlert et al. (2011). This cavities are aligned with the X-ray cavities, being the latter of smaller size than the ones shown in the image. The BCG is known by having powerful jets, which push the cavities in each directions. The extension of the LABOCA emission could be an indication of the emitting dust following the direction of the jets, more observations are needed to confirm this relation. The extended emission could also be a residual of the Sunyaev-Zel'dovich effect, although the extended emission should be filtered out by the mapping algorithm. 120
4.30 Spectral energy distribution of the best fit model made with MAGPHYS. The red points correspond to the observed photometry from the CLASH catalogs and from the archive images of PACS/SPIRE in Herschel and in the LABOCA observations. The green lines corresponds to the stellar unattenuated emission the blue line corresponds to observed emission, after the stellar emission is attenuated by the dust and re-emitted in the FIR. In the box we shoes the χ^2 value for the fist and the assumed redshift, being this the redshift of the galaxy cluster MACS1931. 121
4.31 IR luminosities estimates for the list our list of candidates given by MAGPHYS and their photometric redshift. As comparison to our sample we also plot a number of SMGs detected in previous surveys in different colors. The black squares correspond to our sample candidates that are first priority to be the unique counterpart to the LABOCA and GISMO emission, the magenta sample correspond to the B and C priorities. For the Symeonidis et al. (2013) sample we present the region with a 1σ dispersion (yellow regions). It is important to note that the purple and green stars correspond to the lensed SMGs studied in Combes et al. (2012) and in Johansson et al. (2010). The down blue triangles correspond to a sample of lensed SMGs studied with Herschel. The other points correspond to the references: Sklias et al. (2014). (Elbaz et al., 2011; Magdis et al., 2010; Magnelli et al., 2012). Our sample of galaxies at $z < 2$ is located in the same region as other surveys. For the galaxies at $z > 2$ of our sample, they have very low IR luminosities in comparison to other observed SMGs showing that despite of our galaxies with low magnification they are still intrinsically fainter than previous studies. 122

4.32 Comparison of the SED fit derived SFR and stellar mass of our candidates with a sample of other SMGs. The solid red line corresponds to the fit to the main sequence of galaxies at $z \sim 2$ done by Rodighiero et al. (2011), the dashed red lines corresponds to 1σ range in the α index from the red line. The purple line corresponds to the MS estimated by Daddi et al. (2007). The green line corresponds to the multiplication of the red line by $\times 4$ and it represents a separation between the MS and the starburst galaxies. The black squares correspond to our sample candidates that are first priority to be the unique counterpart to the LABOCA and GISMO emission, the magenta sample correspond to the B and C priorities. Most of our sample galaxies fall well within the 1σ range of the MS sequence, showing that the nature of these galaxies appears to be that of the main-sequence normal star-forming phase. These results are different as some of the SMGs in other surveys have SFR above the MS line, showing how some SMGs are better represented as galaxies in starburst phase. Reference of the SMGs are Johansson et al. (2010); Magnelli et al. (2012); Michałowski et al. (2010); Sklias et al. (2014). 123

4.33 Comparison of the SED fit derived dust and stellar masses of our candidates with a sample of other SMGs. The solid green line corresponds to the fit to a sample of galaxies at $z < 0.5$ done by Smith et al. (2012). The dashed red lines corresponds to the KINGFISH survey of nearby galaxies (Skibba et al., 2011). The red continuum line corresponds to the maximum amount of dust estimated for a given value of stellar mass assuming the highest efficiency in the production of dust by stars in a 'closed box' scenario (Santini et al., 2014). The black squares correspond to our sample candidates that are first priority to be the unique counterpart to the LABOCA and GISMO emission, the magenta sample correspond to the B and C priorities. The spirals, ULIRGs and high-z SMGs sample were taken from Santini et al. (2010). Here we see that a big part of the SMGs fall in the regions around the solid green line, showing similarities with the $z < 0.5$ population of galaxies. A second part of the SMGs in our sample and in the other surveys fall well above the red line, showing a large amount of dust in comparison to their stellar mass. We see that at the lower values of stellar masses higher is the difference between the local relation (green lines) and the estimated dust masses for our and other samples. Reference of the SMGs are Johansson et al. (2010); Magnelli et al. (2012); Michałowski et al. (2010); Sklias et al. (2014). 124

List of Tables

2.1 Summary of Observations and Results for the LAEs 16
2.2 Summary of Observations and Results for MACS0647JD 19

3.1 Summary of Observations and Results for MACS0329-iD 43
3.2 Best fit parameters from MAGPHYS for the galaxy detected in continuum 59
3.3 Groups of galaxies searched for stacked continuum emission. 60
3.4 List of candidates to emission lines. 63

4.1 Properties of the galaxy clusters observed with LABOCA/APEX 96
4.2 Properties of the galaxy clusters observed with GISMO 96
4.3 Properties of the galaxy clusters observed with PACS/Herschel and SPIRE/Herschel 97
4.4 List of sources detected in the LABOCA and GISMO observations. 102
4.4 List of sources detected in the LABOCA and GISMO observations. 103
4.5 List of candidates to be the counterpart of the LABOCA and GISMO detections. 108
4.6 FIR photometry of the candidates to counterparts of LABOCA. 109
4.7 FIR photometry of the candidates to counterparts of GISMO. 110
4.8 Properties estimated using the SED fit for the the candidates to counterparts. 111